Theory and simulation of low-pressure plasma transport phenomena : Application to the PEGASES Thruster

Romain Lucken

université PARIS-SACLAY

NNT : 2019SACLX046

Thèse de doctorat

THEORY AND SIMULATION OF LOW-PRESSURE PLASMA TRANSPORT PHENOMENA

Application to the PEGASES Thruster

Thèse de doctorat de l'Université Paris-Saclay
préparée à l'École polytechnique

École doctorale n°572 Ondes et Matière (EDOM)
Spécialité de doctorat: Physique des Plasmas

Thèse présentée et soutenue à Paris, le 27 septembre 2019, par

ROMAIN LUCKEN

Composition du Jury :

Gerjan Hagelaar Directeur de Recherche. CNRS, LAPLACE, Université Toulouse III	Rapporteur
Nicolas Plihon Chargé de recherche. CNRS, Laboratoire de Physique ENS Lyon	Rapporteur
Sébastien Galtier Professeur. Université Paris-Sud	Président du jury
Julian Schulze Professeur chargé de cours. Ruhr-Universität Bochum	Examinateur
Trevor Lafleur Consultant. Plasma Potential	Examinateur
Pascal Chabert Directeur de Recherche. CNRS, LPP, École polytechnique	Directeur de thèse
Anne Bourdon Directeur de Recherche, CNRS, LPP, École polytechnique	Co-directrice de thèse

To my friends and to my family

À mes amis et à ma famille

THEORY AND SIMULATION OF LOW-PRESSURE PLASMA TRANSPORT PHENOMENA

Application to the PEGASES Thruster

Romain Lucken

PhD Thesis
December 3, 2019

Laboratoire de Physique des Plasmas, UMR CNRS 7648, École polytechnique, Sorbonne Université, Université Paris-Sud, Observatoire de Paris, Université Paris-Saclay, PSL Research University
Route de Saclay 91128 Palaiseau, FRANCE

Contact: romain.lucken@lpp.polytechnique.fr

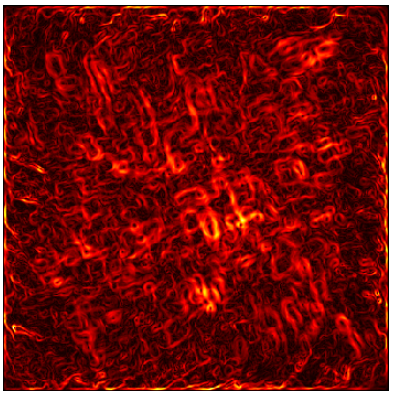

THÉORIE ET SIMULATION DE PHÉNOMÈNES DE TRANSPORT DU PLASMA À BASSE PRESSION
Application au propulseur PEGASES

Résumé substantiel en Français

Le domaine de la physique des plasmas froids a émergé avec les premières découvertes fondamentales en physique atomique et en physique des plasmas il y a plus d'un siècle. Toutefois, ce domaine a été rapidement orienté vers les applications. L'une des applications les plus importantes dans la première moitié du XX^{eme} siècle est le "Calutron" (California University Cyclotron), inventé par E. Lawrence à Berkeley, qui faisait partie du projet Manhattan, et utilisé comme un spectromètre de masse pour séparer les isotopes de l'uranium. Dans un rapport du projet Manhattan daté de 1949, D. Bohm fait deux observations qui sont fondamentales pour la physique des plasmas froids : (i) Les ions doivent avoir une énergie cinétique minimale lorsqu'ils entrent dans la gaine du plasma, estimée à $T_e/2$, T_e étant la température électronique en électron-volts. (ii) Le transport du plasma à travers un champ magnétique est augmenté par des instabilités.

La propulsion électrique par plasma est utilisée pour des satellites militaires et des sondes spatiales depuis les années 1960 et a suscité un intérêt grandissant ces vingt dernières années avec le développement des applications commerciales des technologies spatiales. Néanmoins, les mêmes questions que celles auxquelles D. Bohm était confronté, c'est-à-dire le transport multidimensionnel, l'interaction plasma-gaine, et les instabilités, se posent toujours. La théorie et les simulations sont d'autant plus importantes pour la conception des systèmes de propulsion électrique que les tests en conditions réelles nécessitent le lancement d'un satellite dans l'espace. Le Laboratoire de Physique des Plasmas (LPP) de l'École polytechnique (UMR CNRS 7648) a développé une expertise sur les systèmes de propulsion de satellite par plasma depuis le début des années 2000, avec initialement une forte composante expérimentale. Le premier concept original développé au LPP est le propulseur à grilles PEGASES, qui a été breveté en 2005.

Les premières simulations des plasmas de type particulaires ont émergé dès les années 1970. Dans un premier temps, ces simulations ont permis de résoudre l'équation de Boltzmann et ainsi valider des hypothèses théoriques. Parmi les simulations particulaires, les simulations « particule en cellule » (particle-in-cell, PIC) font interagir une population de macro-particules qui ont chacune un certain poids statistique, typiquement un million de particules physiques, avec un champ électrique, à chaque pas de temps. Ces simulations permettent d'avoir accès, avec une très grande résolution temporelle, à toutes les propriétés statistiques du plasma, à chaque cellule. L'émergence du calcul haute performance permet aujourd'hui d'utiliser la simulation PIC dans des conditions proches des conditions expérimentales, ce qui permet d'extraire des informations très précises sur les propriétés du transport dans les plasmas de laboratoire.

Dans ce travail, nous utilisons le code PIC bi-dimensionnel (2D) parallélisé LP-Pic qui a été partiellement développé dans le cadre du projet et qui fait suite aux travaux de V. Croes à l'École polytechnique. Toutes les dérivations théoriques sont motivées et validées par un grand nombre de simulations PIC qui sont présentées en détail tout au long du manuscrit.

Dans un premier temps, nous rappelons les définitions de la plupart des quantités importantes pour la modélisation des plasmas à basse pression. Quelques premiers résultats de simulation PIC sont présentés. Ensuite, nous établissons les équations du transport multidimensionnel dans un plasma isotherme, en généralisant la théorie du transport ambipolaire au régime de basse pression, avec une approche originale. Le chapitre 3 est dédié à la simulation en 2D d'une colonne magnétisée. L'instabilité de dérive résistive qui s'y développe est étudiée en détail. Nous proposons un nouveau critère de gaine qui permet de rendre compte de la saturation du champ magnétique dans un plasma froid et faiblement ionisé. Au chapitre 4, nous modélisons le refroidissement des électrons à travers le filtre magnétique du propulseur PEGASES (Plasma Propulsion with Electronegative Gases), fonctionnant avec l'argon. Enfin, les cas de simulation sont étendus à une décharge inductive à plasma dans l'iode, avec un nouvel ensemble de sections efficaces de réaction. Différentes ondes et instabilités sont observées, même en l'absence de champ magnétique. Ces nouvelles simulations permettent de faire le pont entre certains modèles théoriques développés ces vingt dernières années et des expériences de laboratoires antérieures.

THEORY AND SIMULATION OF LOW-PRESSURE PLASMA TRANSPORT PHENOMENA

Application to the PEGASES Thruster

Abstract

The field of low-temperature plasma physics has emerged from the first fundamental discoveries in atom and plasma physics more than a century ago. However, it has soon become driven by applications. In the first half of the XX^{th} century, one of the most important application is the "Calutron" (California University Cyclotron) invented by E. Lawrence in Berkeley. It was part of the Manhattan project, and operated as a mass spectrometer to separate uranium isotopes. In a 1949 report of the Manhattan project, D. Bohm makes two observations that are fundamental for low-temperature plasma physics: (i) The ions must have minimum kinetic energy when they enter the plasma sheath estimated to $T_e/2$, T_e being the electron temperature in eV ; (ii) plasma transport across a magnetic field is enhanced by instabilities.

Plasma electric propulsion is used on military satellites and space probes since the 1960s and has gained more and more interest in the last twenty years as space commercial applications were developing. However, the same questions as the ones D. Bohm was faced with, namely multi-dimensional transport, plasma sheath interaction, and instabilities, arise. Theory and simulation are even more important for electric space propulsion systems design since testing in real conditions involves to launch a satellite into space.

In this work, (i) we derive the equations of the multi-dimensional isothermal plasma transport, (ii) we establish a sheath criterion that causes the magnetic confinement to saturate in low-temperature, weakly ionized plasmas, and (iii) we model the electron cooling through the magnetic filter of the PEGASES (Plasma Propulsion with Electronegative Gases) thruster. All the theories are driven and validated with extensive two-dimensional particle-in-cell (PIC) simulations, using the LPPic code that was partially developed in the frame of this project. Finally, (iv) the simulation cases are extended to an iodine inductively coupled plasma (ICP) discharge with a new set of reaction cross sections.

PUBLICATIONS

The works presented in this thesis were partially published in the following journal articles.

Chapter 1

V. Croes, A. Tavant, R. Lucken, R. Martorelli, T. Lafleur, A. Bourdon, and P. Chabert. The effect of alternative propellants on the electron drift instability in Hall-effect thrusters: Insight from 2D particle-in-cell simulations. Physics of Plasmas, 25(6):063522, 2018.

A. Tavant, R. Lucken, A. Bourdon, and P. Chabert. Non-isothermal sheath model for low pressure plasmas. Plasma Sources Science and Technology, 28(7):075007, 2019.

Chapter 2

R. Lucken, V. Croes, T. Lafleur, J.-L. Raimbault, A. Bourdon, and P. Chabert. Edge-to-center plasma density ratios in two-dimensional plasma discharges. Plasma Sources Science and Technology, 27(3):035004, 2018.

Chapter 3

R. Lucken, A. Bourdon, M. A. Lieberman, and P. Chabert. Instability-enhanced transport in low temperature magnetized plasma. Physics of Plasmas, 26(7):070702, 2019.

R. Lucken, A. Tavant, A. Bourdon, M. A. Lieberman, and P. Chabert. Saturation of the magnetic confinement in weakly ionized plasma. Accepted in Plasma Sources Science and Technology, 2019.

The above list includes neither articles that are not at the core of the thesis, nor conference papers. Other publications of the author are cited in the text and

referenced in the bibliography section. The contents of Chapters 4 and 5 have not been published yet.

REMERCIEMENTS

On ne fait rien tout seul.

C'est le moment pour moi de dire à tout ceux qui m'ont entouré pendant ces trois ans de vie combien je leur suis reconnaissant. Mes remerciements vont d'abord à mes directeurs de thèse Pascal Chabert et Anne Bourdon qui ont créé en quelques années de collaboration une belle famille de chercheurs dont je suis fier de faire partie. Merci à tous les deux pour votre confiance, merci Anne pour ta vigilance et ton soutien, merci Pascal d'avoir amplifié ma joie de faire de la physique et de m'avoir guidé. De tous mes autres collègues du LPP, je dois d'abord mentionner Antoine Tavant. J'ai vraiment eu le sentiment de progresser en travaillant avec toi ; merci pour ta rigueur et pour ton humilité. Ces trois ans de thèses auraient été très différents si je n'avais pas pendant mes 12 premiers mois, partagé le bureau 425 de Jussieu avec Trevor Lafleur et Vivien Croes. Merci Trevor pour ta patience et ton assurance. Pour schématiser, tout ce que je n'ai pas appris dans le Lieberman [100], je l'ai appris grâce à toi. Vivien, tu seras toujours mon grand frère de thèse et c'est en bonne partie grâce à toi que je veux continuer à travailler dans le spatial. Merci de m'avoir communiqué ton énergie et ton ambition. Florian Marmuse, merci pour notre collaboration sur le modèle global de décharge à l'iode. Je t'ai toujours vu comme dans un miroir : tu étais toujours à Palaiseau quand j'étais à Jussieu, et tu faisais toujours des expériences quand je faisais des simulations. Mais nos sujets de recherche sont très proches et nos aspirations semblables. Je ne désespère pas de travailler davantage avec toi dans le futur. Merci à toi Thomas Charoy de si bien assurer la relève sur le code PIC et merci pour ton implication dans la vie du laboratoire.

Je suis très reconnaissant envers Mike Lieberman et Allan Lichtenberg qui m'ont accueilli à l'Université de Berkeley. Votre aide a été très précieuse et vos méthodes de travail sont tout simplement exemplaires. À mon arrivée au LPP, Ane Aanesland et Dmytro Rafalskyi étaient en train de réaliser ce que je n'osais même pas rêver en créant ThrustMe. Vous êtes toujours des modèles pour moi et je suis admiratif du succès de votre entreprise.

Les post docs recrutés par Anne, Roberto Martorelli, Alejandro Alvarez Laguna, Sergey Shcherbanev et Victor Desangles ont bien sûr beaucoup contribué à

mes travaux. Vous n'avez pas la part facile du travail et vous avez fait et faites remarquablement bien avancer l'équipe. Alejandro, je resterai complètement fan de ton aisance dans la jungle des schémas numériques. Il faut encore mentionner tous les chercheurs du LPP et d'ailleurs qui m'ont débloqué quand j'en ai eu besoin et qui m'ont consacré de leur temps précieux. Merci Özgür Gürcan, merci Jean - Luc Raimbault, merci Zdenvek Bonaventura, merci Dan Goebel, merci Thierry Magin, merci Nicolas Sissourat. Vous êtes tous, chacun avec votre spécialité, de formidables représentants du monde de la recherche. Merci également à Nicolas Aunai d'avoir organisé la première édition du hackathon du LPP à Belle-Île-en-Mer. J'ai enfin eu la chance de travailler avec Yannis Laplace à l'élaboration et à l'encadrement des travaux pratiques du nouveau bachelor de l'École polytechnique.

Je dois également remercier les stagiaires qui sont passés par le laboratoire et qui ont contribué au projet. Merci Wahid Mainassara d'avoir toujours été disponible pour la maintenance du code LPPic, et merci David Tordeux d'avoir apporté ta pierre à l'édifice. Merci à toi Guillaume Bogopolsky pour ton enthousiasme pour la physique et pour la programmation. Merci Benjamin Estèves de prendre la suite sur PEGASES. En quelques mois, tu as déjà considérablement amélioré le modèle fluide.

Les équipes administrative et technique du LPP, à Jussieu comme à Palaiseau, sont toujours très dévouées aux étudiants. Je voudrais en particulier remercier Christiane Chevalier, Catherine Jegu, Nicolas Marsac, Stéphane Ravenel et Véronique Bouzid.

Ces travaux doctoraux ont été réalisés dans d'excellentes conditions matérielles. Tout d'abord, grâce aux locaux de Sorbonne Université, tutelle du LPP, les conditions de travail étaient idéales. Ensuite, grâce à la chaire ANR Industrielle en partenariat avec le groupe Safran et portée par Anne Bourdon (ANR-16-CHIN-0003-01), j'ai pu participer à un grand nombre de conférences et de séminaires. Enfin, les simulations particulaires des plasmas recquièrent d'importantes ressources de calcul qui dépassent les ressources du LPP et de Polytechnique. La plupart de mes simulations ont été réalisées sur la machine OCCIGEN du CINES à Montpellier dans le cadre des contrats 2017-A0020510092, 2018-A0040510092, 2018-A0040510439, et 2019-A0060510439 avec le GENCI. Certains calculs ont été réalisés au CERFACS à Toulouse, ce qui a été possible grâce à la chaire ANR Industrielle.

L'équipe du futur c'est l'équipe de Share My Space et du projet PADME. Un grand merci à toi Damien Giolito pour ton énergie débordante et pour ta créativité. Merci Delphine Ly pour ta détermination et ton dévouement. Merci Louis Cid pour ces conversations téléphoniques sans fin pour définir le trente-sixième business model de Share My Space. Merci Vincent Marsat pour ton inventivité et ta force de réalisation. Merci Dominique Fontaine pour tes conseils avisés pour la préparation du dossier de PADME. Merci Anne-Laure Doireau et Delphine Marcillac pour tout ce que j'ai appris grâce à vous sur le monde du transfert de technologie. Je me

réjouis de continuer à travailler avec vous tous.

Ces remerciements s'éternisent mais il faut encore mentionner les personnes qui m'ont accompagné sur le plan personnel pendant ces trois ans et bien au-delà. Merci à mes parents Isabelle et Mike de m'avoir toujours aimé et de m'avoir laissé si libre depuis mes 18 ans. Merci Alice et Édouard pour votre tendresse et votre complicité d'adultes. Merci Jean-Pierre et Michèle d'être toujours le coeur de la famille et de nous rappeler qu'il existe une vie en dehors de Paris. Merci Dana et Leroy pour votre accueil à Berkeley. Merci Jo et Yana d'être deux individus si extraordinaires. Merci Paul pour ton amitié sans faille. Merci Pierre pour l'amour de la nature et du sport que l'on partage ensemble, et merci pour les vacances de la décénie. Merci Marion pour ta grandeur historique. Merci Réda pour ces trois ans de jogging et de franches discussions qui donnent foi en la vie. Merci Thomas pour toutes ces conversations intimes ou professionnelles qui m'ont tant fait progresser.

Merci Claudia d'être si douce et joyeuse. Je crois en toi et j'espère pouvoir te rendre aussi heureuse que tu me rends heureux.

ACKNOWLEDGMENTS

You cannot do anything on your own.

It is time for me to tell how grateful I am to all the people who supported me during this three-year lifetime. My acknowledgments are first due to my PhD supervisors Pascal Chabert and Anne Bourdon who created in just a few years of partnership a beautiful family of researchers I am proud to belong to. Thank you for your trust, thank you, Anne for your care and support, thank you, Pascal for amplifying my joy of doing Physics and for your remarkable guidance. Out of all my LPP colleagues, I should mention first Antoine Tavant. I had the feeling that I could improve by working with you ; thank you for being so rigorous and humble. These three years of PhD would have been very different if I had not shared office number 425 of Jussieu with Trevor Lafleur and Vivien Croes during the first 12 months. Thank you, Trevor for your patience and your confidence. To put it simply, everything I did not learn in Lieberman [100], I could learn it thanks to you. Vivien, you will always be my PhD big brother and if I want to keep working in aerospace, it is to a great extent thanks to you. Thank you for communicating your energy and your ambition. Florian Marmuse, thank you for our collaboration on the global model of an iodine discharge. I have always seen you like in a mirror: you were always at Palaiseau when I was in Jussieu, and you were always doing experiments when I was running my simulations. But our research subjects are very close and our yearnings similar. I do not give up on the idea of collaborating with you more in the future. Thank you Thomas Charoy for taking over so well on the PIC code and thank you for your commitment to the life of the laboratory.

I am very grateful to Mike Lieberman and Allan Lichtenberg who welcomed me at the University of Berkeley. Your help was very precious and your working methods are just exemplary. When I arrived at LPP, Ane Aanesland and Dmytro Rafalskyi were achieving what I could not even imagine in my dreams by creating ThrustMe. You are always role models for me and I look up to the success of your company.

Anne's post docs, Roberto Martorelli, Alejandro Alvarez Laguna, Sergey Shcherbanev and Victor Desangles also significantly contributed to my works. You do not have the easiest part of the work and you still make the team improve so much. Ale-

jandro, I will always look up to how easy it is for you to find your way in the jungle of numerical schemes. I still have to mention all the researchers from LPP and elsewhere who debugged me when I needed it and dedicated some of their precious time to me. Thank you Özgür Gürcan, thank you, Jean-Luc Raimbault, thank you, Zdenvek Bonaventura, thank you, Dan Goebel, thank you, Thierry Magin, thank you, Nicolas Sissourat. All of you are, each with your specialties, great ambassadors of the world of research. Thank you as well Nicolas Aunai for organizing the first edition of the LPP hackathon at Belle-Île-en-Mer. Finally, I was lucky to work with Yannis Laplace to set up and supervise the Physics laboratory sessions of the new bachelor program of École polytechnique.

I also need to acknowledge the contribution of the interns who visited the lab. Thank you, Wahid Mainassara, for always making yourself available for the maintenance of the LPPic code, and thank you David Tordeux for adding one more straw to the haystack. Thank you, Guillaume Bogopolsky, for being so enthusiastic about physics and programming. Thank you, Benjamin Estèves, for taking over on PEGASES. In just a few months, you already vastly improved the fluid model.

The administrative and technical teams, either at Jussieu or Palaiseau, are always very much devoted to the students. I want to thank in particular Christiane Chevalier, Catherine Jegu, Nicolas Marsac, Stéphane Ravenel and Véronique Bouzid.

These doctoral works were performed in excellent material conditions. First of all, thanks to the offices of Sorbonne Université, which is one of the laboratory supports, the working conditions were perfect for me. Moreover, thanks to the *Agence Nationale pour la recherche* (French National Research Funding Institution) (ANR) *Chaire Industrielle* in partnership with Safran Group and lead by Anne Bourdon (ANR-16-CHIN-0003-01), I could take part in many conferences and workshops. Finally, plasma particle simulations require computational resources that surpass those of the LPP and of École polytechnique. Most simulations were run on the OCCIGEN machine of *Centre Informatique National de l'Enseignement Supérieur* (French national computing center for higher education) (CINES) with contract agreements 2017-A0020510092, 2018-A0040510092, 2018-A0040510439, et 2019-A0060510439 made by *Grand Équipement National de Calcul Intensif* (Large French national facility for intensive computing) (GENCI). Some of my computations were also made at the *Centre Européen de Recherche et de Formation Avancée en Calcul Scientifique* (European research and training center for scientific computing) (CERFACS) in Toulouse, which was made possible by the ANR *Chaire Industrielle*.

The team of the future is the team of Share My Space and of the Plasma Applications for Debris Mitigation around Earth (PADME) project. Great thanks to you, Damien Giolito, for your overwhelming energy and your creativity. Thank you Delphine Ly for being so strong-minded and devoted to the project. Thank you, Louis Cid, for these endless online conversations to define the thirty-sixth business

model of Share My Space. Thank you, Vincent Marsat, for your inventive mind and your achievement capacity. Thank you, Dominique Fontaine, for your sharp advice when we were preparing for the PADME project. Thank you Anne-Laure Doireau and Delphine Marcillac for all the things I have learnt about technology transfer thanks to you. I am looking forward to working with you all.

These acknowledgments are getting endless but I must still mention the people who supported me at personal level during these three years and beyond. Thank you to my parents Isabelle and Mike for loving me always and for leaving me so free since I was 18. Thank you, Alice and Édouard, for your tenderness and for growing up so well as adults. Thank you, Jean-Pierre and Michèle, for being always the heart of the family and for reminding us that there is a life outside Paris. Thank you, Dana and Leroy, for welcoming me so nicely in Berkeley. Thank you, Jo and Yana, for being such extraordinary individuals. Thank you, Paul, for your flawless friendship. Thank you, Pierre-Antoine, for the love of nature and sport that we share, and thank you for this once-in-a-decade trip. Thank you, Marion, for your historical greatness. Thank you, Réda, for these three years of jogging and sincere discussions that give hope for life. Thank you, Thomas, for these intimate or professional conversations that made me improve so much.

Thank you, Claudia, for being so sweet and joyful. I believe in you and I hope that I can make you as happy as you make me happy.

CONTENTS

SYMBOLS AND ABBREVIATIONS

List of Acronyms

0D zero-dimensional

1D one-dimensional

2D two-dimensional

3D three-dimensional

AC alternative current

ANR *Agence Nationale pour la recherche* (French National Research Funding Institution)

amu atomic mass unit

ASDEX Axially Symmetric Divertor Experiment

BATMAN Bavarian Test Machine for Negative Ions

CAD computer aided design

CERFACS *Centre Européen de Recherche et de Formation Avancée en Calcul Scientifique* (European research and training center for scientific computing)

CINES *Centre Informatique National de l'Enseignement Supérieur* (French national computing center for higher education)

CCP capacitively-coupled plasma

CFL Courant – Friedrichs – Lewy

CMF center of mass frame

CNRS *Centre National de la Recherche Scientifique* (French National Center for Scientific Research)

CPU central processing unit

CS cross section

DC direct current

DSHT double stage Hall thruster

EEDF electron energy distribution function

EEPF electron energy probability function

ELISE Extraction from a Large Ion Source Experiment

EP electric propulsion

EVDF electron velocity distribution function

FT Fourier transform

GENCI *Grand Équipement National de Calcul Intensif* (Large French national facility for intensive computing)

GIT gridded ion thruster

HT Hall thruster

ICP inductively-coupled plasma

ITER International Thermonuclear Experimental Reactor

IEPC International Electric Propulsion Conference

JPL Jet Propulsion Laboratory

LEO low Earth orbit

LHS left-hand side

LPP *Laboratoire de Physique des Plasmas*

LTP low-temperature plasma

GEO geostationary Earth Orbit

MANITU Multi Ampere Negative Ion Test Unit

MHD magnetohydrodynamics

MITICA Megavolt ITER Injector and Concept Advancement

MRFEA magnetized retarding field energy analyzer

MCC Monte-Carlo collision

NBI neutral beam injector

PADME Plasma Applications for Debris Mitigation around Earth

PDE partial differential equation

PEGASES Plasma Propulsion with Electronegative Gases

PIC particle-in-cell

PPU power processing unit

PSST Plasma Sources Science and Technology Journal

RHS right-hand side

RF radio-frequency

SC spacecraft

SEE Secondary Electron Emission

sccm standard cubic centimeters per minute

SI International System of Units

SPIDER Source for the Production of Ions of Deuterium Extracted from a Radio-frequency plasma

RADI former RADIal injector of Wendelstein 7 Advanced Stellarator

SPT stationary plasma thruster

UMR *Unité Mixte de Recherche* (CNRS Joint Research Unit)

W7-X Wendelstein 7 Advanced Stellarator-X

Nomenclature

Physical Constants

k_B	Boltzmann constant	$1.38064852 \times 10^{-23}$	J/K
e	Elementary charge	$1.60217662 \times 10^{-19}$	C
ϵ_0	Vacuum permittivity	$8.854187817 \times 10^{-12}$	F/m
g	Gravitational acceleration on the ground	9.81	m/s^2
c	Speed of light	299 792 458	m/s
m_e	Electron mass	9.109×10^{-31}	kg
m_H	Hydrogen atom mass	$1.6726219 \times 10^{-27}$	kg

Dimensional Quantities

Unless otherwise stated, all the dimensional quantities are in the International System of Units (SI). Vector quantities are in bold font.

n	Density	m^3
$\mathbf{v}$	Velocity	m/s
v_T	Thermal velocity	m/s
u_B	Bohm speed	m/s
Γ	Flux	$m^{-2}s^{-1}$
ρ	Charge density	C/m^3
$\boldsymbol{J}$	Electric current density	A/m^2
$\boldsymbol{T}$	Temperature, in K	K
T_e	Electron temperature, in V	eV
$\mathbf{Q}$	Heat flux	W/m^2
ϕ	Electrostatic potential	V
$\mathbf{E}$	Electric field	V/m
$\mathbf{B}$	Magnetic field	T
ν	Collision frequency	s^{-1}
ω	Angular frequency	rad/s
ξ	Growth rate	s^{-1}
ω_{pe}, ω_{pi}	Plasma frequencies	s^{-1}
λ_{De}, λ_{Di}	Debye lengths	m
ω_{ce}, ω_{ci}	Cyclotron frequencies	s^{-1}
$\boldsymbol{K}$	Reaction rate	m^3s^{-1}
m	Particle mass	kg
$\mathcal{E}$	Reaction threshold energy	eV
$\mathcal{W}$	Injected power	W
w	Volume density of injected power	W/m^3
l	Discharge length	m
$\boldsymbol{L}$	Gradient length	m

$\mathbf{k}$	Wavevector	m^{-1}
λ	Wavelength	m
λ_e, λ_i	Electron and ion mean free paths	m
ρ_L	Larmor radius	m
σ	Collision cross section	m^2
p	Pressure, (gas pressure if no subscript)	Pa or mTorr
F	Thrust	N
I_{sp}	Specific impulse	s
I_d	Discharge current	A
f	Velocity distribution function	$\mathrm{s}^3\mathrm{m}^{-3}$
f_ϵ	Energy distribution function	eV^{-1}
f_P	Probability distribution function	$\mathrm{eV}^{-3/2}$

Dimensionless Quantities

$\mathcal{M}$	Mach number
η	Hall parameter
h	Edge-to-center plasma density ratio
μ	Ratio of the electron mass over the ion mass
η	Efficiency
γ	Polytropic coefficient
γ_s	Wall recombination ("sticking") coefficient
q_f	Particle weight factor

Subscripts

$_{\mathrm{max}}$	Maximum
$_{av}$	Average
$_e$	Electrons
$_i$	Positive ions
$_n$	Negative ions
$_g$	Gas
$_x$	x axis
$_y$	y axis
$_z$	z axis
$_d$	Electron drift
$_*$	Electron diamagnetic drift
$_{E\times B}$	Electron $E \times B$ drift
$_a$	Instability-enhanced ("anomalous")
$_{\mathrm{eff}}$	Effective
$_{\mathrm{loss}}$	Loss energy or power
$_{iz}$	Ionization

$_{el}$	Elastic momentum transfer
$_{ex}$	Inelastic momentum transfer
$_{LH}$	Lower hybrid
$_{1D}$	One-dimensional model
$_{2D}$	Two-dimensional model
$_{s}$	Sheath boundary
$_{\mathrm{B\,ref}}$	Reference quantities for the dispersion relation (see Chapter 3)
$_{\mathcal{E}\,\mathrm{ref}}$	Reference quantities for the global and one-dimensional (1D) fluid model (see Chapter 4)

Normalization

$\tilde{x}$	x variable normalized to $x_{\mathrm{B\,ref}}$ (see Chapter 3)
X	x variable normalized to $x_{\mathcal{E}\,\mathrm{ref}}$ (see Chapter 4)

Derivatives

∇	Gradient
∇^2	Laplace operator
$\nabla\cdot$	Divergence operator
$\nabla\times$	Rotational operator
∂_x	Derivative along x
∂_y	Derivative along y
∂_z	Derivative along z
∂_t	Time derivative
$\frac{df}{dt}$	Total (Lagrangian) derivative
f', f''	First and second order derivatives of a single variable function

Integrals

$\oiint_S \cdot\,\mathbf{dS}$	Integral over the discharge surface
$\iiint_V \cdot\,dV$	Integral over the discharge volume
$\langle\cdot\rangle$	Average over a distribution function

Taylor Expansion

The i-th term of the Taylor expansion of the variable X is X_i.

Vector Norm

The vector norm is either $\|\cdot\|$, or just the vector quantity in light font.

Real and Imaginary Parts

$\mathfrak{R}$ Real part
$\mathfrak{I}$ Imaginary part

INTRODUCTION

Contents

Plasma Physics for Space Propulsion

At the beginning of the XX^{th} century, when airplanes were hardly flying, Rutherford evidenced the role of electrons and protons as constituents of atoms, opening the way to a new discipline: Plasma Physics [129] . Plasma Physics deals with the collective behavior of electric charges carried by electrons, ions or striped atoms. The neutrality of atoms, that is widely observed at the Earth surface, happens to be just an exception at the scale of the universe. In most conditions of pressure and temperature observed outside of our planet, electrons are not bounded enough to the nuclei, such that matter behaves as a plasma, and not as a standard gas or liquid. The plasma can be accelerated by electric fields, confined by magnetic fields, and heated by electromagnetic waves. These phenomena are essential to understand the structure of astrophysical objects, and in particular, the sun and its interaction with the planets of the solar system. For example, on Earth, the confinement of ions of the solar wind around the Earth magnetic field lines can be observed in auroras, and high electric fields trigger ionization fronts in lightning.

Plasma Physics lies at the crossing of hydrodynamics, statistical physics, particle physics and quantum chemistry. It inherently tackles physical problems at a *mesoscopic* scale. The observation of natural phenomena was very important for the progress of plasma physics,. But perhaps at an equally important level, the fact that ionized matter can be accelerated, confined and heated by electric and magnetic fields gave birth to many technological applications. The application that has

drawn the most interest from the scientific community and the governments in the past seventy years is nuclear fusion. Nuclear energy is the densest source of energy currently available. The typical energy released in a chemical reaction is 1 eV while the typical energy released in a nuclear reaction is 1 MeV. So the nuclear energy density per mass unit is typically one million times higher than the chemical energy density per mass unit. This is of great interest both for civilian energy supply, and military applications, including propulsion and weapons. While fission reactions rely on high energy neutron impactors, nuclear fusion of light elements is sustained by the energy of the elements themselves. The typical fusion reaction between deuterium and tritium nuclei can be sustained only under very high temperatures and very high pressures, where the gas behaves as a fully ionized plasma. Research on nuclear fusion has been fundamental for the development of the theories of plasma physics since World War II, both for magnetic confinement fusion (mostly civilian), and inertial confinement fusion (mostly military) applications.

The motivation of the present work is spacecraft (SC) electric propulsion (EP). EP is perhaps less fundamental to the future of human kind than nuclear fusion but is a crucial element for the development of space exploration and the commercial use of the outer space. It has been successfully tested in the 1960s in Cold War United States and USSR. The idea of using charged particles to generate thrust instead of hot gases appeared almost at the same time as the discovery of the very existence of these particles [39]. In 1920, at the very early stage of plasma physics and soon after the fundamental discoveries of electrons and ions, the first concepts of electric propulsion were patented by Robert H. Goddard [65]. The original idea comes from the very high velocity that ions can reach when accelerated through a moderate electrostatic potential. While the thermal expansion of neutral gases leads to velocities that are typically

$$v_{Tg} = \left(\frac{k_B T_g}{m_g} \right)^{1/2}, \tag{1}$$

the velocity reached by an ion accelerated by an electrostatic potential $\Delta\phi$ is

$$v_i = \left(\frac{2e\Delta\phi}{m_i} \right)^{1/2}. \tag{2}$$

For xenon (131.29 atomic mass unit (amu)), with $T_g = 1\,000\,\mathrm{K}$ and $\phi = 100\,\mathrm{V}$, $v_{Tg} = 0.25\,\mathrm{km/s}$ and $v_i = 12\,\mathrm{km/s}$. The velocity achieved by electrostatic acceleration is easily one or two orders of magnitude higher than those reached through thermal expansion. This difference comes from the ratio between the elementary charge and the Boltzmann constant $e/k_B = 11\,605\,\mathrm{K/V}$: while it is relatively easy to generate a 1 V electrostatic potential, it is much more challenging to sustain a gas reactor at 11 605 K.

The outer space cannot provide the external forces that could be used for propulsion purposes like on the ground, in the air or the sea. On the contrary, the mass

used for propulsion has to be carried on board the SC. According to Newton's third law, the thrust generated by a mass flow at velocity v_{ex} is

$$F = \dot{m} v_{ex} \tag{3}$$

where v_{ex} is the exhaust velocity of the propellant and $\dot{m}$ is the mass flow rate. This equation can be integrated over time to yield the Tsiolkovsky equation for the velocity budget Δv of a space mission

$$\Delta v = v_{ex} \ln \left(\frac{m_0 + m_p}{m_0} \right) \tag{4}$$

where m_0 is the "dry mass" of the SC (its mass without the propellant) and m_p is the mass of propellant available at the beginning of the mission. The two previous equations put emphasis on the critical role of the propellant outlet velocity for space propulsion purposes. At a given mass flow rate, a higher thrust can be achieved if the exhaust velocity is higher. Conversely, a lower mass flow rate can be used to achieve the same thrust, which means that less propellant needs to be carried to space from the ground. Tsiolkovsky equation also shows that a greater velocity budget can be achieved with a greater exhaust velocity, which makes EP a good candidate for deep space exploration. In SC propulsion, the exhaust velocity is usually estimated through the specific impulse

$$I_{sp} = v_{ex}/g \tag{5}$$

where $g = 9.81$ is the gravitational acceleration on the ground. This quantity is particularly convenient for rocket propulsion: when $I_{sp}\dot{m} = m_R$, m_R being the total mass of the rocket, the rocket can take off.

Of course, like for any propulsion technology, an energy source is needed. For most scientific and commercial space missions, the electrical energy is provided by solar panels. The USSR has also flown stationary plasma thruster (SPT) technologies powered by a nuclear reactor through a thermionic converter, for example on the Kosmos 1818 surveillance satellite launched in 1987. The development of nuclear electric propulsion systems has slowed down since the end of the Cold War and the consensus on the peaceful use of the outer space and of nuclear energy. The power budget for most electric propulsion systems today is limited by the size of the solar panels (typically 1 kW/m^2) such that most electric thrusters commercially available are in the 1-10 kW range. The current trend is to miniaturize satellites to build constellations of hundreds or thousands of satellites that can provide global connectivity or Earth imaging with a very short revisit period. In-orbit servicing or extra-terrestrial resource extractions tend to draw interest from the public and private investors since 2016. These applications may require the development of new high power propulsion systems in a not-too-distant future.

The rough characteristics of a plasma thruster can be estimated through very simple analytical models. The main parameters are the discharge current I_d, the

acceleration voltage $\Delta\phi$, the mass flow rate $\dot{m}$, and the type of propellant. In an ideal plasma thruster with only singly-charged ions of mass m_i, each atom that enters the discharge chamber has to be ionized and accelerated, such that

$$\mathcal{W} = \Delta\phi \times I_d = (\mathcal{E}_{\text{ion}} + e\Delta\phi)\frac{\dot{m}}{m_i} \tag{6}$$

where $\mathcal{W}$ is the electrical power and $\mathcal{E}_{\text{ion}}$ is the mean energy required to create one ion. The exhaust velocity is estimated by Eq. (2). The specific impulse is

$$I_{sp} = \frac{1}{g}\left(\frac{2e\Delta\phi}{m_i}\right)^{1/2}, \tag{7}$$

and the thrust

$$F = \frac{\mathcal{W}}{\mathcal{E}_{\text{ion}} + e\Delta\phi}\left(2e\Delta\phi m_i\right)^{1/2}. \tag{8}$$

This equation shows that the propellant should have a high ion mass and a low ionization energy to maximize the thrust. The kinetic power of the plasma plume is

$$\mathcal{W}_{kin} = \frac{1}{2}\dot{m}{v_i}^2 = \frac{\mathcal{W}}{1 + \mathcal{E}_{\text{ion}}/(e\Delta\phi)} \tag{9}$$

such that the thruster efficiency is

$$\eta = \frac{1}{1 + \mathcal{E}_{\text{ion}}/(e\Delta\phi)}. \tag{10}$$

In this simple model, the thruster efficiency only depends on the mean energy required to generate one ion $\mathcal{E}_{\text{ion}}$, which is typically of the order of magnitude of the ionization potential $\mathcal{E}_{iz}$ of the propellant (molecule or atom). Due to its inert nature, its high mass, and low ionization energy, xenon is the most commonly used propellant in the field of plasma propulsion.

This model is very much simplified and the art of plasma thruster design is to obtain performances that are close to the ideal situation depicted by Eqs. (7), (8) and (10).

The original designs of gridded ion thruster (GIT) and Hall thruster (HT) (equivalent to the SPT), which are the two main families of plasma thrusters, are the results of decades of research and technological development mainly in the US and the former Soviet Union. Nowadays, new thruster designs, even when they are not revolutionary, need to be validated through expensive test campaigns where the thrusters are fired for over 10 000 hours in a vacuum chamber on the ground. One of the first approaches of plasma thruster design via modeling was established by D. Goebel and I. Katz at the Jet Propulsion Laboratory (JPL) [68]. Among the main parameters that limit the thruster performances, we can mention

(1) The *plume angle*. Only the kinetic energy of the beam directed along the thrust axis is useful for the thrust generation. Designing a thruster where the ion beam is narrow is quite essential. The GIT technology is typically more efficient to this respect than the HT.

(2) The *multi-ion generation* also deteriorates the thruster efficiency. A significant amount of doubly-ionized ions can be generated when the electron temperature is too high.

(3) The most important source of performance losses holds in the discrepancy between $\mathcal{E}_{\text{ion}}$ and the ionization energy $\mathcal{E}_{iz}$. The energy required per ion generated $\mathcal{E}_{\text{ion}}$ is necessarily greater than the ionization potential energy $\mathcal{E}_{iz}$, and it can eventually be much higher. The power conversion from the power processing unit (PPU) to the plasma may not be ideal, which yields what is called in the literature the electrical efficiency. A significant amount of the energy is lost in atomic or molecular excitation levels that naturally decay to the fundamental state by emitting light at various frequencies, including in the visible spectrum, or remain in metastable states. Some of the energy is also lost through elastic collisions with the neutral gas and contributes to gas heating. Finally, the loss of energetic particles at the inner reactor walls may deteriorate the thruster performances as well. The same questions of plasma confinement and transport arise as in problems related to fusion technologies.

An investigation of the phenomena mentioned above requires a deep understanding of low-temperature plasma (LTP) Physics. In this work, we will focus mainly on point (3), with great emphasis set on transport and power loss phenomena involved in GIT technologies, both with and without magnetic fields.

Low-temperature Plasma

LTP Physics is a theoretical framework that covers a quite wide range of experiments and applications. The pressure can vary between atmospheric pressure or above to very low pressures of a fraction of milli-Torr (mT). The milli-Torr will be the typical unit of pressure used throughout this work. In our simulations, the pressure is varied between 0.3 and 100 mTorr. We remind that the Torr unit is defined by

$$1\,\text{Torr} = 1/760\,\text{atm} \approx 1\,\text{mmHg} \approx 133.32\,\text{Pa}. \tag{11}$$

The type of power injection in LTP experiments can be radio-frequency (RF), microwave, helicon, or through a direct current (DC) discharge. The nature and the applications of LTP vary very widely. However, a few properties are common to every LTP systems. The most fundamental property is that electrons are not in thermal equilibrium with the gas and with the ions. The electron temperature has to be high enough to sustain the discharge through electron impact ionization. In practice, the electron temperature has to be greater than a fraction of the ionization potential, typically a few electron-volts. The temperature of heavy species (gas and ions) is typically lower than 1 eV. If there is such a temperature gap between electrons and ions, it means that electrons and ions cannot be thermalized through Coulomb collisions. This implies that the plasma density cannot be too high. The issue will be

addressed more carefully in Section 1.2. Transport processes are driven by collisions between charged particles and neutrals, but the residence time of a particle inside the discharge is not high enough to achieve thermal equilibrium with the gas. Since interactions between charged particles and neutrals dominate over Coulomb collisions, the gas is often weakly ionized: the electron density is smaller or comparable to the gas density. This also means that the electron temperature cannot be much higher than the ionization potential.

Many chemical processes are enhanced by temperature. However, only the energy of the electrons plays a role in the reactivity of a gas because they are responsible for molecular bounds. In LTP, instead of heating a gas to a high temperature to enhance reactivity, only electrons are targeted, which potentially yields a much better power efficiency for chemical processes, and the generation of metastable species and ions.

At pressures down to 10^3 Pa, the collisional processes are so strong that the fluid velocity of charged species does not exceed the thermal velocity. The properties of the plasma are considered to be local and they can be parametrized by the reduced electric field E/n, where E is the local electric field and n is the gas density. At lower pressure, the particles are more freely accelerated by the electric field, and space derivatives become important to predict correctly the plasma properties.

Particle-in-Cell Simulation

As said previously, Plasma Physics consists in investigating the collective behavior of charged particles. One approach is to treat the plasma as a fluid to derive equations for the statistical properties of this fluid, for instance its local density, fluid velocity, and temperature. As computer power increased in the early 1990's, it became possible to a certain extent to extract these collective properties by simulating the motion of charged particles interacting together. The description of $1\,\mathrm{cm}^3$ of a plasma of $10^{11}\,\mathrm{cm}^{-3}$ of electron density by pair interactions leads to the computation of $2^{10^{11}}$ interactions at each time step which is completely out of reach even by today's most powerful computing systems. The particle-in-cell (PIC) simulation is based on two fundamental assumptions that allow reducing massively the computation resources required.

1. The collective behavior of the plasma can be described by the motion of *super-particles* that obey the same physical laws as the particles that they represent but with a statistical weight factor q_f such that the mass of a super-particle that represents q_f electrons of mass m_e and charge $-e$, is $q_f m_e$ and its charge is $-q_f e$. In PIC simulations, no real particle is tracked individually, only sets of hundred thousands of particles are. If the number of super-particles simulated is too low, numerical noise can appear very quickly.

2. The interaction between charged particles is well represented by computing an electric field and sometimes also a magnetic field according to Maxwell's

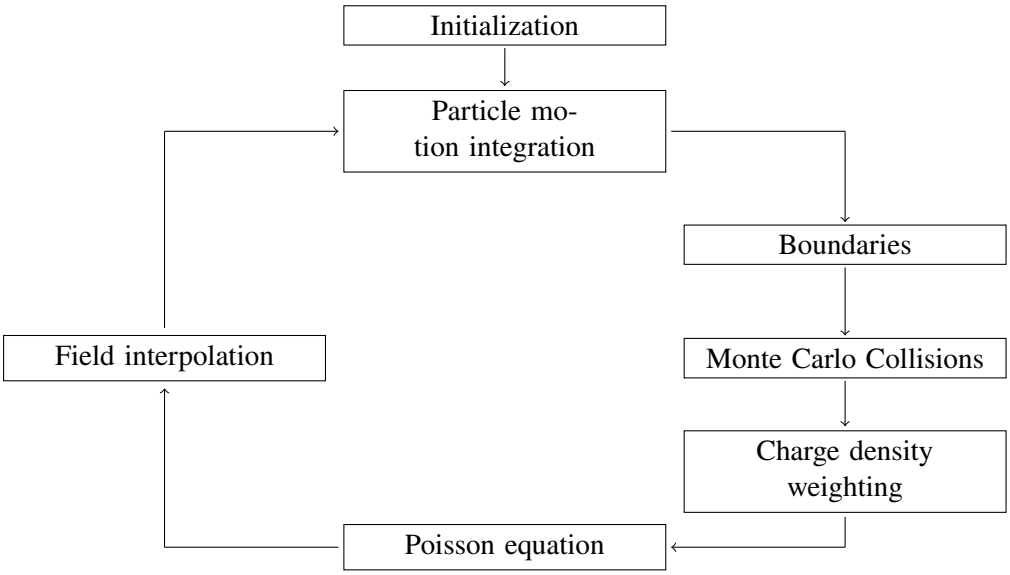

Figure 1: Diagram of the PIC time loop.

equations from a density of charge and of current. While this seems an obvious consequence of Maxwell's equations, the implementation of this method necessarily underestimates the role of short-range Coulomb interactions, due to grid discretization.

The motion of super-particles is directed by the Lorentz force

$$m\frac{d\mathbf{v}}{dt} = q(\mathbf{E} + \mathbf{v} \times \mathbf{B}) \tag{12}$$

where m and q are respectively the mass and the charge of the super-particle.

As illustrated in Fig. 1, all PIC simulations start with an initialization stage where super-particles are distributed in a simulation domain, with initial values of the electric and magnetic fields. Eq. (12) is then integrated over one time step dt. After this initial time step, some of the particles may be collected on the boundaries of the simulation, and subsequently absorbed or re-injected. Depending on reaction cross sections, a subset of the super-particles can undergo collisions leading to scattering, energy loss, and new particle generation. The new distribution of super-particles leads to a new charge density map obtained by weighting the particle positions with their charges on grid points. The field equations are then solved (Poisson's equation in the electrostatic case treated in this work) to obtain new electric and magnetic fields that are in turn interpolated at each particle's position to initialize the next time step. The first PIC algorithms for electrostatic simulation of plasmas were implemented in the 1960s and a comprehensive monograph was published by Birdsall and Langdon in 1985 [16].

The present work is the continuation of the doctoral work carried out by V. Croes [41], and his effort to develop a two-dimensional (2D) PIC code at *Laboratoire*

de Physique des Plasmas (LPP) that would be suited for the simulation of plasma thrusters. This code is called *LPPic* and has been developed since 2014 under the supervision of T. Lafleur, P. Chabert and A. Bourdon. Most of the algorithms implemented in *LPPic* come from Birdsall and Langdon [16]. Nevertheless, the Monte-Carlo algorithms used to describe the collisions between charged particles and the neutral background were developed in the 1990's by Vahedi [161]. Collisions between super-particles and the background of neutral gas necessarily make the simulation stochastic. PIC simulation is a remarkably powerful tool because all the properties of the super-particles and the plasma as a fluid can be extracted. However, the amount of data processed and generated can be overwhelming, and it needs to be carefully selected and sorted. Up to the 1990's PIC simulation was mostly used to investigate fundamental processes and was often limited to 1D [156]. Only since the 2000's, 2D and three-dimensional (3D) PIC simulation of real systems has become more and more accessible [42, 24], but they also demand more computer engineering to run with massively parallelized codes, and require careful benchmarking [157], validation [25], and convergence study [83].

The PEGASES Thruster

The work carried out during these three years was motivated mainly by the investigation of the Plasma Propulsion with Electronegative Gases (PEGASES) thruster, a concept patented at LPP by P. Chabert in 2005 [28]. This thruster is a GIT designed to operate with strongly electronegative gases.

The space environment itself is a plasma at very low density ($10^9 - 10^{10}\,\mathrm{m}^{-3}$). The surfaces of the satellites form space charge sheaths of several meters with electric fields that tend to accelerate the ions towards the surfaces of the satellite, affecting the local charging of the satellite, and causing erosion on some surfaces [102], and contamination.

On classical electric propulsion systems, the beam of ion is neutralized by a cathode, which is an external electron source that maintains the charge balance with the ion beam [68]. However, this device does not prevent ions from being collected on the surfaces, and their lifetime is limited [67]. Most commonly used cathodes are hollow cathodes, and their Physics require a dedicated treatment [132, 131]. Moreover, they can be expensive and difficult to miniaturize.

The main idea of the PEGASES thruster is to generate thrust with two ion beams of opposite sign. The design would tackle at the same time the issues of ion recollection, the plume angle, and would allow one to get rid of the cathode subsystem. As illustrated in Fig. 2(a), the design comprises a planar RF antenna which is located on the side of the gas injection. The inner walls of the thruster are made out of dielectric materials (ceramic and Pyrex). The plasma is generated inductively near the RF antenna and transported towards the double acceleration grid located on the right-hand side (RHS) of Fig. 2(a) through the magnetic filter formed by permanent

magnets. The double grid is polarized alternately positively and negatively in order to accelerate the positive and negative ions. The ion fluxes were analyzed by a specially designed magnetized retarding field energy analyzer (MRFEA) [95]. The role of the magnetic filter is to cool down the electrons through magnetic confinement. The thruster was made to operate with iodine (I_2), which is a promising candidate for future electric propulsion systems (see Chapter 5), but experiments were also carried out with argon and SF_6. The thruster can be split into three stages:

- The ionization stage where the electron temperature needs to be high enough to produce ionization;
- The magnetic filter where the electron temperature decreases due to magnetic confinement, such that they can produce dissociative attachment on the I_2 molecule;
- The acceleration stage where the ions are extracted and expelled at high velocity.

The objective is to guarantee that the positive and negative ions can recombine in the plasma plume to form a neutral beam.

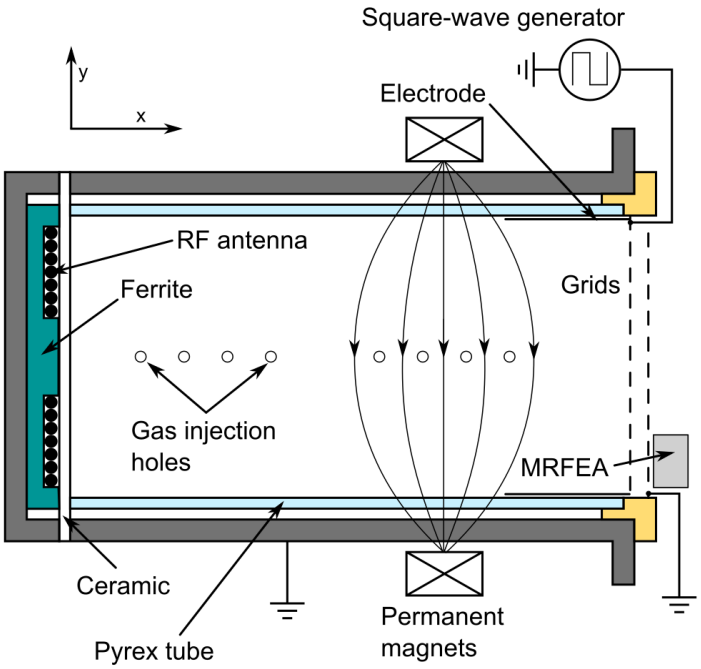

(a)

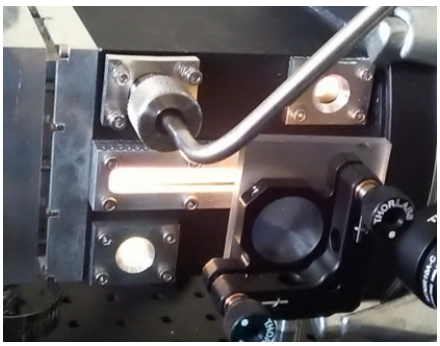

(b)

Figure 2: The PEGASES thruster at LPP. (a) Diagram of the system, from Lafleur *et al.* (2014) [95]. (b) Picture of the system operated with iodine (Experiment by T. Courtois in 2017)

Outline of the Thesis

The first four chapters of the thesis will be dedicated to theory and simulation of transport phenomena in plasmas of noble gas discharges, with a particular emphasis set on the case of argon. In Chapter 1 we introduce the basic definitions and concepts that will be used throughout the thesis. The general equations of the transport are provided, the PIC simulation method and global models of plasma discharges are described. First simulation results of a helium inductively-coupled plasma (ICP) discharge are qualitatively discussed to illustrate fundamental plasma theories.

In Chapter 2, some analytical solutions of the isothermal plasma transport in 1D and 2D are given. The 2D theory is compared to the PIC simulation results, and generalized to 3D geometries. Parametric studies with respect to the pressure and the aspect ratio are performed.

Chapter 3 investigates the cross-field transport phenomena with a study of the effect of resistive drift instabilities in low pressure, weakly ionized plasmas. It is shown in this chapter that the magnetic confinement of the plasma completely saturates at high magnetic fields.

In Chapter 4, we present simulations of a magnetic filter in both realistic and reduced geometries and compare it to a 1D quasineutral model. The results are also compared with experimental results and 2D fluid simulations performed by other authors.

Chapter 5 is dedicated to the study of an iodine ICP with no magnetic field. The state-of-the-art regarding low-pressure iodine plasmas is summarized and a CS set relevant to low-pressure, low temperature plasmas is presented. Relaxation oscillations observed in the transient of the PIC simulation are analyzed, and used to partially validate the model.

Chapter 1

MODELING OF WEAKLY IONIZED PLASMAS

Contents

In this first chapter of the thesis, we introduce the particle motion equations, the kinetic equations and the fluid conservation equations that will be used throughout this work. This includes a description of the collision processes between charged particles and atoms in noble gas plasma discharges. Cross section sets and reaction rates are provided for helium, argon, krypton and xenon. The principles underlying low-temperature plasma simulation by the PIC method are also presented and the first simulation results of a low-density

helium ICP discharge are discussed. The equations of global models (zero-dimensional (0D)) of low-temperature plasma discharges are derived.

1.1 Particle Approach: Theory and Simulation

The motion of a non-relativistic charged particle is described by the integration of Newton's second law with the Lorentz force given by Eq. (12). If there is no electric field, the trajectory of a charged particle is a circle, and the angular velocity of the particle is the cyclotron frequency

$$\omega_c = qB/m \tag{1.1}$$

where q and m are the charge and the mass of the charged particle respectively, and B is the intensity of the magnetic field. The radius of the circular trajectory is called the Larmor radius ρ_L. If the projection of the particle velocity vector in the plane perpendicular to the magnetic field is $v_\perp$, then the Larmor radius is

$$\rho_L = v_\perp/\omega_c = \frac{v_\perp m}{qB} \tag{1.2}$$

The magnetic field cannot accelerate a particle in the parallel direction, such that the trajectory of a charged particle in a magnetic field is a helix. This motion is called the cyclotron motion. When an electric field is added, one can retrieve the same type of equation as for the cyclotron motion by noticing that

$$\frac{d\left(\mathbf{v} - \mathbf{v}_{E\times B}\right)}{dt} = \frac{q}{m}\left(\mathbf{v} - \mathbf{v}_{E\times B}\right) \times \mathbf{B} \tag{1.3}$$

where

$$\mathbf{v}_{E\times B} = \frac{\mathbf{E}\times\mathbf{B}}{B^2} \tag{1.4}$$

is the $E \times B$ drift. The motion of a charged particle in constant and uniform electric and magnetic fields is the sum between the cyclotron motion (helix) and a drift in the direction perpendicular both to $\mathbf{E}$ and $\mathbf{B}$. The reader can refer to the monograph by Chen [37] for more details about the basics of single particle motion.

The electric and magnetic fields are the sum of the fields generated by each particle, following Coulomb's law for the electric field and Biot-Savart's law for the magnetic field. Computing the binary interactions of each charged particles is very computationally expensive. In practice, the field generated by a large number of particles is calculated using Maxwell's equations using a continuous description of the charge and current densities ρ and $\mathbf{j}$.

$$\nabla \cdot \mathbf{E} = \rho/\epsilon_0 \tag{1.5}$$

$$\nabla \cdot \mathbf{B} = 0 \tag{1.6}$$

$$\nabla \times \mathbf{E} + \partial_t \mathbf{B} = 0 \tag{1.7}$$

$$\nabla \times \mathbf{B} - \frac{1}{c^2}\partial_t E = \mu_0 \mathbf{j} \tag{1.8}$$

The plasma densities considered throughout this work do not exceed 10^{17} m^{-3} with electron temperatures that remain below 20 eV. The fluid velocities were always smaller than the electron thermal velocity

$$v_{Te} = \left(\frac{k_B T_e}{m_e}\right)^{1/2} \sim 10^7 \text{ m/s} \tag{1.9}$$

The resulting current density is always lower than 1.5×10^4 A/m^2. For a system of typically 1 cm of size, the induced magnetic field is about 0.2 mT, which corresponds to a Larmor radius of about 3 cm for electrons moving at the electron thermal velocity (Eq. (1.9)), which is of the same order of magnitude as the systems investigated in this work. The magnetic field induced by the electron motion is weak and does not affect much the particle trajectory. The effect is even weaker for the ions due to their lower typical velocity. Most often, the fluid velocity of the electrons is at least one order of magnitude lower than the thermal velocity, except in the high magnetic field case that will be discussed in Chapter 3, where the fluid velocity of the electrons comes close to the electron thermal velocity. Moreover, the frequencies investigated are in the range of 1-100 MHz such that the term $\frac{1}{c^2}\partial_t E$ remains low and does not influence the magnetic field either. In all the models developed in this work, we stand in the magnetostatic assumption, and we further assume that the magnetic field is decoupled from the particle motion equations. The electric field is coupled to the particle motion equations through Gauss' law (Eq. (1.5)). In the magnetostatic limit, Maxwell-Faraday's equation (1.7) is equivalent to $\nabla \times E = 0$, which means that an electrostatic potential ϕ exists such that

$$\mathbf{E} = -\nabla\phi. \tag{1.10}$$

PIC simulation codes feature two co-existing data structures: the particles, which are defined by their charge, position and velocity, and a grid of cells. Each cell contains at least the charge density, the electrostatic potential and the electric field. The `particle` and `grid` types implemented in the *LPPic* code are given below as an illustration.

```
type particle
    !-------------------------------------------------------
  integer                     :: numero = 0     !ID number
  integer                     :: charge = 1000  !charge
  real(dbleprc), dimension(3) :: V    = [0,0,0] !velocity (normalized)
```

```
  real(dbleprc)              :: X     = 8880   !Position along x
  real(dbleprc)              :: Y     = 8880   !Position along y
  real(dbleprc)              :: Z     = 8880   !Position along z
end type particle
    !-------------------------------------------------------


type grid
    !-------------------------------------------------------
  ! De-normalized charge density
  real(dbleprc)                                :: Rho = 0
  ! Normalized electric field
  real(dbleprc), dimension(2)                  :: Ej  = [0,0]
  ! Normalized electrostatic potential
  real(dbleprc)                                :: Phi = 0
  ! Normalized charge density
  real(dbleprc)                                :: p   = 0
  ! Normalized magnetic field
  real(dbleprc), dimension(3)                  :: B   = [0,0,0]
  ! Normalized electron density
  real(dbleprc)                                :: Nume = 0
  ! Normalized density of heavy species tracked
  real(dbleprc), dimension(:), allocatable     :: Numh
end type grid
    !-------------------------------------------------------
```

The particle position is interpolated at the grid cells using a linear weighting method. The contribution of all the charged particles at all the grid cells provides values of the charge density at each grid cell. Eq. (1.5) combined with Eq. (1.10) yields Poisson's equation:

$$\nabla^2 \phi = -\rho/\epsilon_0 \tag{1.11}$$

which is the fundamental law of electrostatics. The Poisson's equation is solved using either HYPRE [54] or PETSC [7] numerical solvers in 2D, with either closed boundary conditions in the x and y directions or periodic boundary conditions in the x direction and closed boundary conditions in the y direction. The solvers are interfaced in C programming language and provide a value of the potential at each grid cell. The electric field is estimated from the electrostatic potential using simple finite differences. The value of the electric potential at each particle's position is interpolated using again a linear interpolation algorithm. The particles are then displaced by integrating Eq. (12) over one time-step dt. In case of a magnetized plasma, the classical Boris scheme is used [19, 16, 41], which consists in splitting the particle motion in two halves, and the rotation due to the magnetic field is performed at $t + dt/2$. In their motion, particles can eventually undergo collisions of various sorts that will be investigated in the next section. The current version of *LPPic* uses a completely explicit scheme [16].

In general the weight factor q_f is defined by

$$q_f = \frac{nV_{simu}}{N_{part}} \tag{1.12}$$

where N_{part} is the number of particles for the considered species, n the initialized density, and V_{simu} is the simulation domain. In 3D, V_{simu} is the simulation volume, and the weight factor represents exactly the ratio between the number of physical particles and the number of numerical super-particles. However, in lower dimension, the super-particles are not exactly points but straight lines (in 2D) or planes (in 1D) because the simulation volume is either a surface area (2D) or a line segment (1D). In the 2D PIC simulations presented here, the weight factor is therefore in m^{-1}.

1.2 Kinetic Theory and Collisions

1.2.1 Boltzmann Equation

The kinetic theory of plasmas is based on equations that apply on the distribution function of each species of a given system. In 3D, the velocity distribution function f takes seven arguments x, y, z, v_x, v_y, v_z, and t, such that $f(\mathbf{x}, \mathbf{v}, t)\, d^3x\, d^3v$ is the number of particles inside a six-dimensional phase space volume $d^3x\, d^3v$ at $(\mathbf{r}, \mathbf{v})$ at time t, where $d^3x = dxdydz$ and $d^3v = dv_x dv_y dv_z$ [100]. If the distribution of particles is not affected by any collision, the distribution function f follows a continuity equation

$$\partial_t f + \mathbf{v} \cdot \nabla f + \mathbf{a} \cdot \nabla_{\mathbf{v}} f = 0 \tag{1.13}$$

where $\mathbf{a} = \frac{d\mathbf{v}}{dt}$ and $\mathbf{v} = \frac{d\mathbf{x}}{dt}$ are the acceleration and the velocity vectors of the flow, respectively, and $\nabla_{\mathbf{v}}$ is the gradient operator with respect to the velocity variables:

$$\nabla_{\mathbf{v}} = \mathbf{e}_x \frac{\partial}{\partial v_x} + \mathbf{e}_y \frac{\partial}{\partial v_y} + \mathbf{e}_z \frac{\partial}{\partial v_z}\,. \tag{1.14}$$

Assuming that the particles at the position $\mathbf{x}$ all undergo a force field $\mathbf{F}$, Newton's second law imposes that $\mathbf{F} = m\,\mathbf{a}$. Moreover, collisions can affect the velocity of some particles, create or destroy particles at very short time scales. These effects are accounted for by introducing a collision term in Eq. (1.13)

$$\partial_t f + \mathbf{v} \cdot \nabla f + \frac{\mathbf{F}}{m} \cdot \nabla_{\mathbf{v}} f = \partial_t f\big|_c\,. \tag{1.15}$$

Eq. (1.15) is called the Boltzmann equation or the Vlasov equation when $\partial_t f\big|_c = 0$. While the Vlasov equation can be solved by the method of characteristics, the Boltzmann equation (including collisions) is much more challenging to solve, especially

due to the collision term, which is difficult to estimate. The *LPPic* code contains a Monte-Carlo collision (MCC) subroutine that describes the collisions between charged particles and the neutral gas.

In the following, the density n, and the fluid velocity $\mathbf{u}$ are defined for each species by integrating the distribution functions in the velocity space

$$n(\mathbf{x},t) = \iiint f \, d^3v \tag{1.16}$$

$$\mathbf{u}(\mathbf{x},t) = \frac{1}{n} \iiint \mathbf{v} f \, d^3v \,. \tag{1.17}$$

The kinetic definition of the temperature is also used

$$T(\mathbf{x},t) = \frac{m}{3k_B n} \iiint (\mathbf{v}-\mathbf{u})^2 f \, d^3v \,. \tag{1.18}$$

These definitions can be naturally used in the PIC code to extract macroscopic information (either local or global) from the simulation. Isotropic distribution functions can be described using the energy distribution function $f_\epsilon(\epsilon)$ or the energy probability distribution function f_P where $\epsilon = \frac{1}{2}m\mathbf{v}^2$ is the kinetic energy of the particle. These functions are connected to the velocity distribution function by

$$f_\epsilon(\mathbf{x},\epsilon,t)\, d\epsilon = f(\mathbf{x},\mathbf{v},t)\, d^3v \tag{1.19}$$

$$f_P(\mathbf{x},\epsilon,t) = \epsilon^{-1/2} f_\epsilon(\mathbf{x},\epsilon,t) \tag{1.20}$$

The energy distribution function

$$f_\epsilon(\epsilon) = \frac{2N\epsilon^{1/2}}{(k_B T)^{3/2}\pi^{1/2}} \exp\left[-\frac{q\phi+\epsilon}{k_B T}\right] \tag{1.21}$$

is called the Maxwell-Boltzmann distribution function. The probability distribution function f_P is proportional to $\exp(-\frac{\epsilon}{k_B T})$ for a Maxwell-Boltzmann distribution function, which makes it a convenient variable to estimate if a population extracted from experimental or simulation data is Maxwellian.

In terms of velocity, Eq. (1.21) is

$$f(\mathbf{v}) = N\left(\frac{m}{2\pi k_B T}\right)^{3/2} \exp\left[-\frac{q\phi + mv^2/2}{k_B T}\right] \,. \tag{1.22}$$

This function is a solution of the (stationary) Vlasov equation (1.13) where the only force term is the electrostatic force $qE = -q\nabla\phi$. In Eq. (1.21), N is the density at the position corresponding to $\phi = 0$. One can also show (Lieberman and Lichtenberg 2nd ed. Appendix B [100]) that this distribution function corresponds to the solution of the Boltzmann equation (1.15) with only elastic collisions.

1.2.2 Electron-Neutral Reactions

The elastic scattering of electrons, electron impact-induced excitations and ionization were implemented by V. Croes during his thesis [41] for helium and xenon in two different codes. In this thesis, the code was generalized to read cross section data files exported from the LXCat database, allowing to explore various cross section sets, and with various gases where the chemistry is limited to the same types of reactions as for noble gases. The cross sections are tabulated against the collision energy in eV. All the electron-neutral collision cross sections come from the Biagi database retrieved from LXCat [10]. In 2017, the collision module was used for the study of the instability-enhanced electron mobility in the direction of the thrust axis of an HT using PIC simulations in the radial - azimuthal plane, and published in Croes *et al.* [44, 43]. Similar investigations were also presented with a simplified cross section set for iodine, involving only the same reactions as in the case of a noble gas, in V. Croes' thesis [41]. More complete cross section sets for the iodine chemistry will be detailed in Chapter 5.

The momentum transfer from electrons to the gas is neglected. Therefore, when elastic scattering occurs, the impinging electron keeps the same kinetic energy. The direction of its velocity vector is randomized following a uniform probability function over a solid angle of 4π sterad. Ionization and excitation reactions are inelastic collisions, so a fraction of the kinetic energy of the impinging electron is transferred to internal energy levels of the target atom in the case of excitation, and used to detach an electron in the case of ionization. After an excitation reaction takes place, the atoms should release their energy by photon emission or remain in a metastable state. Ionization or excitation from excited atomic levels is neglected such that we always make the assumption that the neutral species are in the majority in their fundamental state. After atom excitation, the electron is scattered with a random velocity angle and a kinetic energy which is simply $\epsilon - \mathcal{E}_{e,x}$. Here, ϵ is the kinetic energy of the impinging particle and $\mathcal{E}_{e,x}$ is the energy loss corresponding to the excitation reaction. In the case of an ionization collision, the remaining kinetic energy $\epsilon - \mathcal{E}_{e,x}$ is divided in half between the two secondary electrons, which are both scattered with a random velocity angle.

Some cross section sets available on the LXCat database contain many excitation levels that each correspond to real electronic states. However, it is possible to average some neighboring excitation levels into fewer effective inelastic collisions that represent the electron transport correctly. Such simplifications were made by Biagi [10] and all the electron cross section sets used by default in *LPPic* contain between 1 and 4 inelastic collisions with various energy thresholds that do not represent well-identified excitation levels of the atom. As shown in the next section, this simplification does not affect the local electron temperature and the electron density.

The cross sections can be integrated over the whole energy space and weighted against a distribution function to yield the reaction rate or reaction rate factor

$$K(\mathbf{x},t) = \frac{1}{n}\left(\frac{2}{m}\right)^{1/2} \int f_\epsilon(\epsilon)\,\sigma(\epsilon)\epsilon^{1/2} d\epsilon \tag{1.23}$$

It is also useful to introduce the collision frequency defined for particles colliding with a gas of density n_g.

$$\nu = n_g K \tag{1.24}$$

For a Maxwellian distribution function, the reaction rate is

$$K = \left(\frac{2}{k_B T}\right)^{3/2} \frac{1}{(m\pi)^{1/2}} \int \sigma(\epsilon)\epsilon e^{-\frac{\epsilon}{k_B T}} d\epsilon \tag{1.25}$$

The CS of electron-atom processes selected for *LPPic* are summarized in Fig. 1.1. The MCC subroutine uses the "null collision" method as described in the original article by V. Vahedi [161] and in V. Croes' thesis [41]. The reaction rates for Maxwellian distribution functions are also provided in Fig. 1.2. These reaction rates are the ones used in the global model of noble gas discharges described in this work. For the sake of comparison, the set of reaction rates for argon estimated by V. Vahedi is provided in Fig. 1.3. It is sometimes convenient to have access to analytical fits of the reaction rates. Some of the fits available in the literature are summarized in Fig. 1.4.

1.2.3 Ion-Neutral Reactions

The collisional transport of ions across a neutral background can be modeled by decomposing the collisions in two categories: isotropic scattering and backscattering [113]. This decomposition is a projection of the space of differential cross sections on a two-vector basis. For argon, this projection was found to match very well the macroscopic transport properties of ions through a neutral gas. The cross sections for xenon and argon were validated against experimental data [114, 113], but a simple assumption of Langevin collision cross section using atomic polarizability was chosen in the paper of Piscitelli *et al.* [114] for xenon. Helium data was also released on LXCat by the group of Phelps, but no data was available for krypton. The Langevin capture cross section corresponds to the polarization of an atom or a molecule by the close approach of an ion [100]:

$$\sigma_L = \frac{1}{v_R}\left(\frac{\pi\alpha_P e^2}{\epsilon_0 \mu_R}\right)^{1/2} \tag{1.26}$$

where v_R is the relative velocity between the two particles, $\mu_R = m_1 m_2/(m_1+m_2)$ is the reduced mass, and α_P is the relative polarizability of the atom. The values of polarizabilities for noble gases are provided in Table 1.1. Lieberman and Lichtenberg

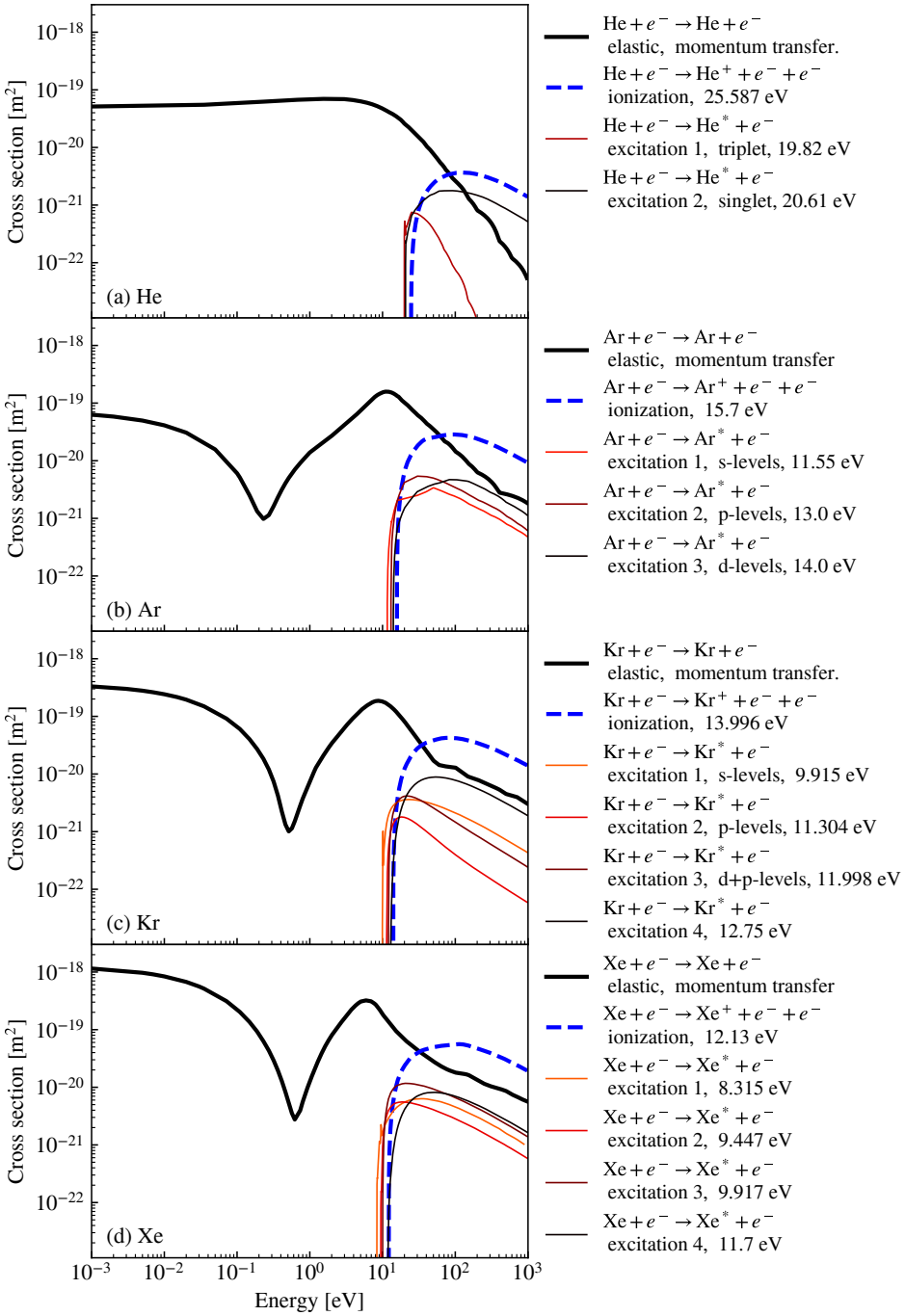

Figure 1.1: Electron-neutral collision CSs for noble gases used by default in the simulations performed in this work [10].

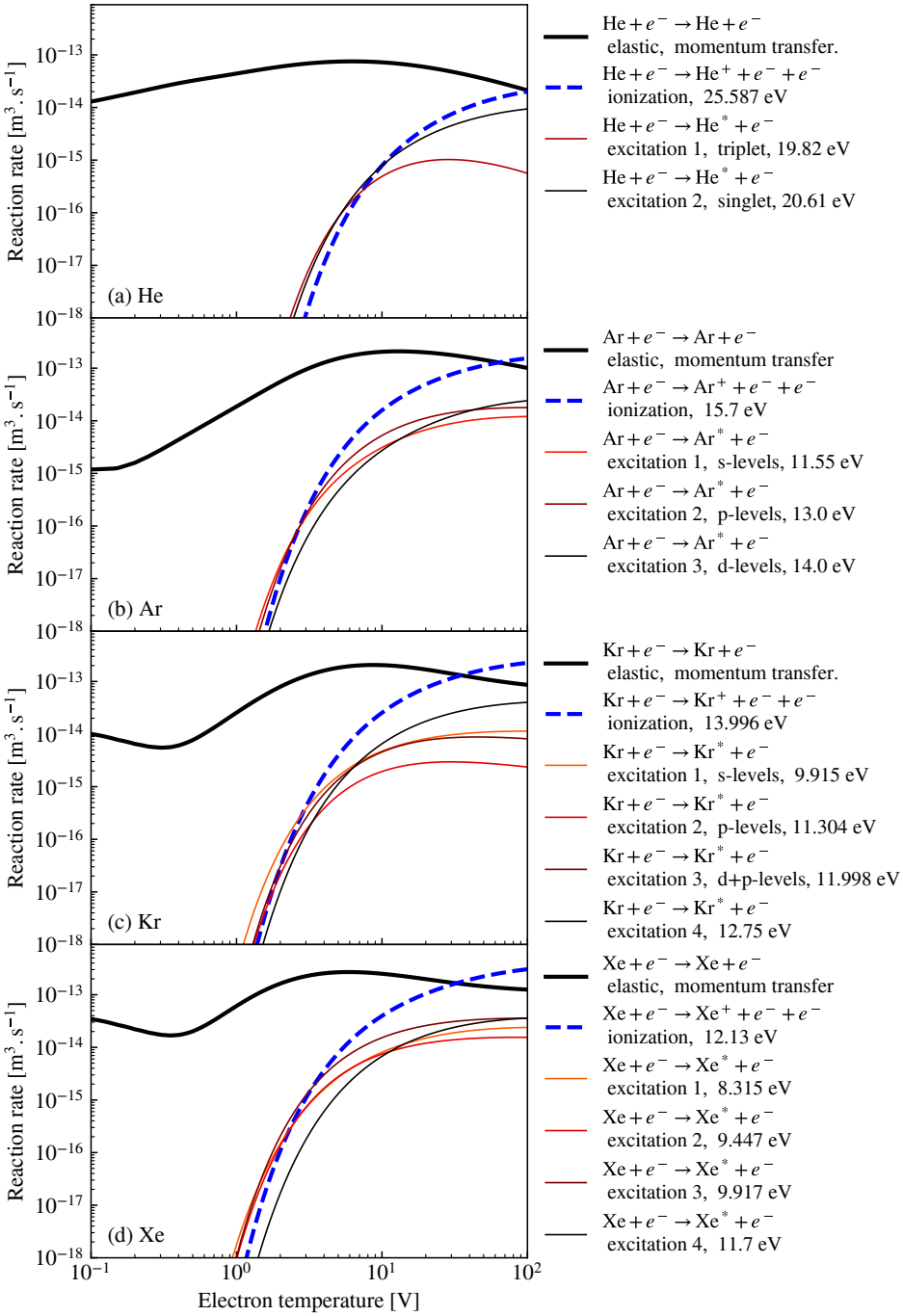

Figure 1.2: Electron-neutral reaction rates for a Maxwellian EEDF and neutral atoms at rest. Numerical integration was performed over the data of Fig. 1.1.

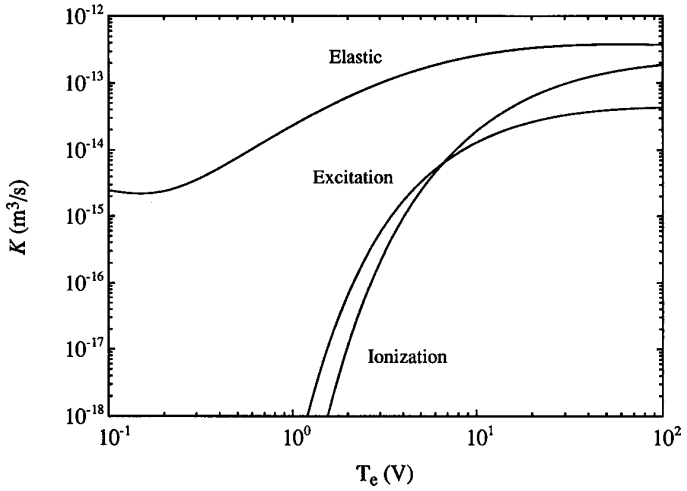

Figure 1.3: Electron-neutral reaction rates for argon [100].

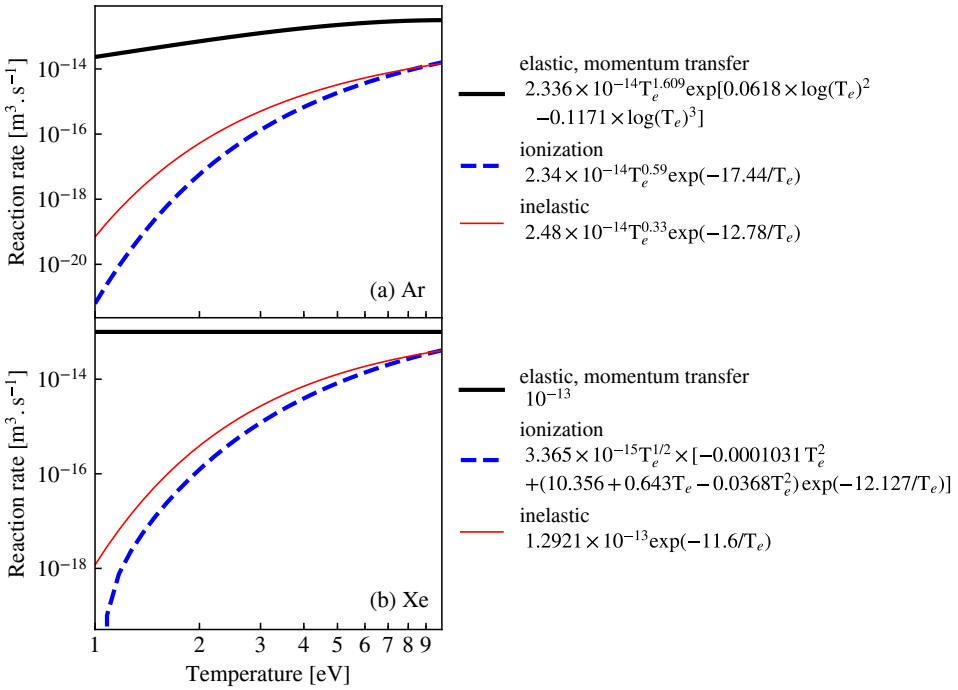

Figure 1.4: Analytical formulas to estimate the electron-neutral reaction rates for argon (a) [100] and xenon (b) [30].

Gas	He	Ar	Kr	Xe
Atomic mass [amu]	4.003	39.95	83.8	131.3
Ionization potential [eV]	24.59	15.7	21.75	12.13
Relative polarizability	1.383	11.08	16.74	27.06

Table 1.1: Atomic masses and relative polarizabilities of the noble gases implemented in *LPPic* . From Radzig and Smirnov (1985) [120].

propose an estimate of the charge exchange cross section based on a semi-classical quantum tunneling theory

$$\sigma_{\mathrm{BS}} \approx \frac{9}{16\pi}\left(\frac{e}{\epsilon_0 \mathcal{E}_{i,z}}\right)^2 \tag{1.27}$$

where $\mathcal{E}_{i,z}$ is the ionization potential of the atom in electron-volts. This estimate has the advantage of being independent of the impact energy.

Sakabe *et al.* [130] (1992) proposed an analytical formula that is an improvement of the earlier work of Rapp and Francis (1962) [124], validated with a large set of experimental data for quite high relative impact velocities ($> 10^3$ m/s). The backscattering cross section is, in cm^2:

$$\sigma_{\mathrm{BS}} \approx (A - B\log_{10} v_R)(\mathcal{E}_{i,z}/\mathcal{E}_{i,z,0})^{-3/2} \tag{1.28}$$

where $A = 1.81\times10^{-14}\,\mathrm{cm}^2$, $B = 2.12\times10^{-15}\,\mathrm{cm}^2$, and v_R is the relative velocity in cm/s. $\mathcal{E}_{i,z} = 13.6\,\mathrm{eV}$ is the ionization potential of the hydrogen atom. Fig. 1.5 summarizes the various estimates of reaction cross sections for isotropic scattering and resonant backscattering in noble gas plasmas. Sakabe formula (1.28) provides reasonable estimates of the backscattering cross section for helium, argon, and xenon, except at low energy where it does not apply well for xenon. Sakabe formula was used to run the simulations with krypton in Croes *et al.* [44]. The constant cross section estimate (Eq. (1.27)) also provides a reasonable order of magnitude but seems to systematically underestimate the backscattering cross section.

The cross sections of two-body collisions provided by the LXCat database are functions of the total energy in the center of mass frame (CMF) of the collision $\mathcal{E}_{CM}$. However, the collision frequency is calculated from the velocity of the charged species in the reference frame of the neutrals v, by the formula :

$$\nu = \sigma n_g v \tag{1.29}$$

where n_g is the density of the neutral gas. The aim here is to determine the relationship between $\mathcal{E}_{CM}$ and v in order to calculate the collision frequency correctly and in a general case.

Let v_{CM}, m_g, and m be respectively the center of mass velocity, the neutral mass, and the charged particle mass. By definition of the center of mass, and since

the neutral velocity is zero in the neutral frame (by definition):

$$(m + m_g)v_{CM} = mv \Rightarrow v_{CM} = \frac{m}{m + m_g}v \tag{1.30}$$

The total kinetic energy in the CMF is the sum of the kinetic energy of the charged particle and the neutral.

$$\begin{aligned}\mathcal{E}_{CM} &= \frac{1}{2}m(v - v_{CM})^2 + \frac{1}{2}m_g v_{CM}^2 \qquad (1.31)\\ &= \frac{v^2}{2\left(1 + m_g/m\right)^2}\left(\frac{m_g^2}{m} + m_g\right)\\ \mathcal{E}_{CM} &= \frac{m_g v^2}{2\left(1 + m_g/m\right)} \qquad (1.32)\end{aligned}$$

The velocity of the charged particle in the neutral frame hence writes:

$$v = \left[2\mathcal{E}_{CM}\left(\frac{1}{m_g} + \frac{1}{m}\right)\right]^{1/2} \tag{1.33}$$

And using Eq. (1.29),

$$\boxed{\nu = \sigma n_g \left[2\mathcal{E}_{CM}\left(\frac{1}{m_g} + \frac{1}{m}\right)\right]^{1/2}}. \tag{1.34}$$

Two limiting cases can be of interest.

- When the impinging particle is an electron, the term $\frac{1}{m_g}$ in Eq. (1.33) is negligible, the velocity becomes $v = \left(\frac{2\mathcal{E}_{CM}}{m_e}\right)^{1/2}$ and the collision frequency:

$$\nu = \sigma n_g \left(\frac{2\mathcal{E}_{CM}}{m_e}\right)^{1/2}. \tag{1.35}$$

- When the impinging particle has the same mass as the neutral, $m = m_g$, $v = 2\left(\mathcal{E}_{CM}/m_g\right)^{1/2}$, and

$$\nu = 2\sigma n_g \left(\frac{\mathcal{E}_{CM}}{m_g}\right)^{1/2}. \tag{1.36}$$

1.2.4 Momentum Transfer Collision Frequency

In PIC simulations, the cross sections used are the (real) reaction cross sections, while momentum transfer cross sections are usually implemented in fluid models. The relevant quantity for the momentum balance equations of fluid models is the *effective momentum transfer cross section* that includes both the elastic and the inelastic processes. As seen in Figs. 1.1 and 1.2, the elastic collisions dominate over all inelastic processes at electron temperatures below a few electron-volts.

The ion dynamics is influenced by isotropic and backscattering collision processes. In order to better understand these concepts, we propose here a simple explanation for the theoretical framework used in the works of the group of Phelps [113, 114]. More details about binary collisions can also be found in Lieberman and Lichtenberg (2005) [100]. In reality, the scattering angle of a particle colliding with a target particle depends on the impact parameter, and every angle does not have the same probability. This effect is taken into account by introducing a differential cross section $I(\upsilon, \theta)$. The quantity

$$I(\upsilon, \theta)\, d\theta\, n_g\, \upsilon\, dt \tag{1.37}$$

is the probability for a particle to be scattered with an angle between θ and $\theta + d\theta$ in the time lapse dt against the particles of the gas of density n_g. Only one angular parameter θ is chosen because a binary collision system features a cylindrical symmetry. The cross section σ is the integral over all the scattering angles of the differential cross section.

$$\sigma(\upsilon) = 2\pi \int_0^\pi I(\upsilon, \theta)\, \sin\theta\, d\theta. \tag{1.38}$$

When a process is assumed to be isotropic, the differential cross section does not depend on the angle θ and is

$$I_{\text{isotropic}} = \frac{\sigma}{4\pi}. \tag{1.39}$$

For an elastic process, the kinetic energy of the fictitious particle in the CMF is conserved, and the momentum transfer in the direction of the initial velocity vector $\mathbf{v}$ in the CMF is $(1 - \cos\theta)\mathbf{v}$. The *momentum transfer cross section* is therefore defined as

$$\sigma_p = 2\pi \int_0^\pi (1 - \cos\theta)\, I(\upsilon, \theta)\, \sin\theta\, d\theta\ . \tag{1.40}$$

For an isotropic process

$$\sigma_p = \sigma \tag{1.41}$$

since $\int_0^\pi \cos\theta \sin\theta\, d\theta = 0$. All the electron-neutral processes are assumed to be isotropic, such that for all of them, using σ_p or σ is equivalent. Due to charge exchange mechanisms that are particularly important at low ion energy, the ion-atom

(or ion-molecule) elastic interactions cannot be modeled with an isotropic cross section. The idea of Phelps [113] is to use a differential cross section

$$I = I_{\text{isotropic}} + I_{\text{BS}} \tag{1.42}$$

where

$$I_{\text{BS}} = \frac{\sigma_{\text{BS}}\,\delta(\theta - \pi)}{2\pi \sin\theta} \tag{1.43}$$

where δ is the Dirac delta function, and I_{BS} and σ_{BS} are the backscattering differential cross section and cross section respectively. σ_{BS} is just chosen to satisfy Eq. (1.38). At high ion energy, a charge exchange reaction is equivalent to a backscattering reaction, since the ion produced at very low velocity in the laboratory reference frame has just the velocity $-\mathbf{v}$ in the CMF. Direct integration of Eq. (1.40) leads to the momentum cross section associated with a backscattering reaction

$$\sigma_{p,\text{BS}} = 2\sigma_{\text{BS}}\ . \tag{1.44}$$

Therefore, it is important to make a difference between collision cross sections and *momentum transfer* cross sections for charge exchange reactions.

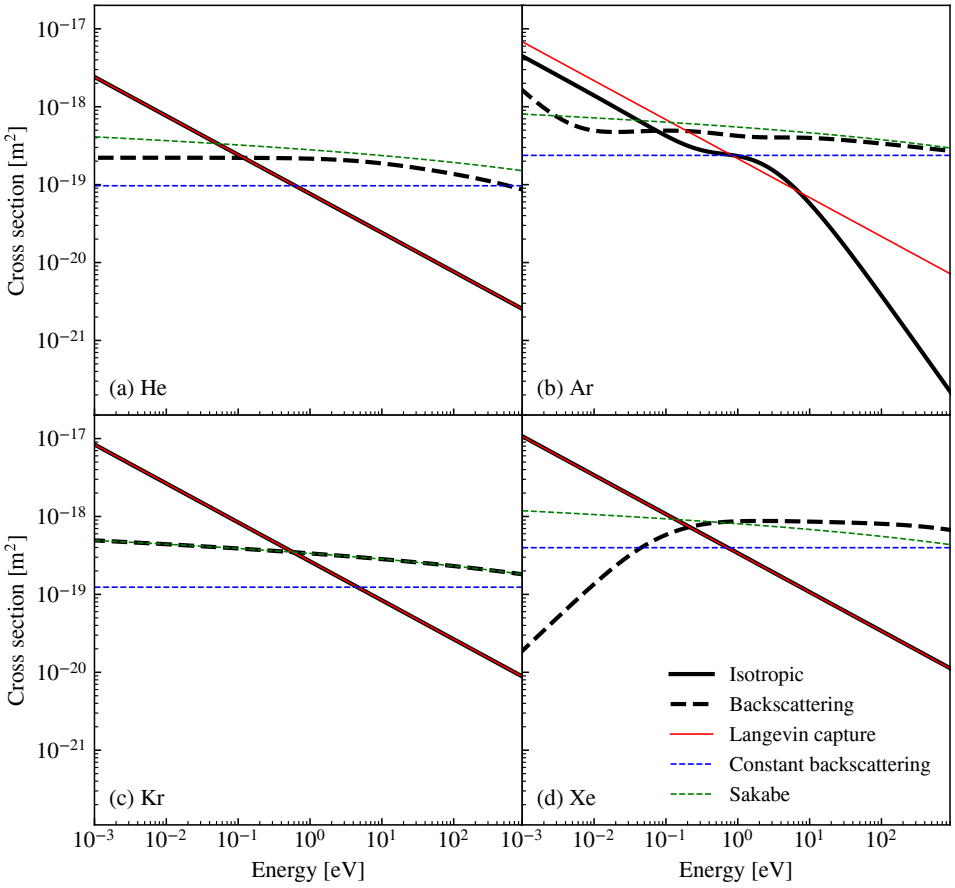

Figure 1.5: Ion-neutral collision cross sections for noble gases. The thick black lines represent the values implemented in the *LPPic* simulation code. The solid lines represent estimations of the elastic scattering, and the dashed lines represent resonant charge exchange. The cross sections for xenon and argon were validated against published experimental data [114, 113]. Helium data was also released on LXCat by the group of Phelps. For krypton, the backscattering cross section is chosen equal to the Sakabe formula [130]. The choice of Langevin capture cross section for isotropic scattering is made arbitrarily for argon, helium and krypton.

1.3 Introduction to ICP Modeling

1.3.1 Heating Mechanism

The main driver of this work is the simulation of the PEGASES thruster. The PEGASES source used at LPP is an ICP source with a planar antenna. The planar coil is powered with a sinusoidal RF voltage and produces a magnetic field that can be estimated through Maxwell-Ampere's law (Eq. (1.8)). A sinusoidal electric field is, in turn, generated in the plasma, according to Faraday's law (Eq. (1.7)). The induced electric field vector is typically in a plane parallel to the planar coil. It accelerates the electrons that gain enough energy to produce ionization and sustain the discharge. The amplitude of the oscillatory electric field decreases with the distance x to the coil due to two factors:

1. The magnetic field generated by a planar coil typically decreases as $1/x^3$ when the distance x becomes larger than the radius of the coil;

2. The electric field penetrates only through a typical distance δ_s called the skin depth that depends on the plasma conductivity. This length is also called London's length and is a characteristic of the plasma response to an electromagnetic perturbation [125]

$$\delta_s = c/\omega_{pe} = c\left(\frac{\epsilon_0 m_e}{n_e e^2}\right)^{1/2} \tag{1.45}$$

where c is the speed of light, and

$$\omega_{pe} = \left(\frac{n_e e^2}{\epsilon_0 m_e}\right)^{1/2} \tag{1.46}$$

is the electron plasma frequency. For a homogeneous plasma, the amplitude of the heating electric field satisfies

$$E \propto e^{-x/\delta_s}\,. \tag{1.47}$$

The skin depth is 5.3 cm at $10^{16}\,\mathrm{m}^{-3}$ of plasma density, and 5.3 mm for a plasma density of $10^{18}\,\mathrm{m}^{-3}$. Therefore, for the simulations of small ICP discharges of 3 cm at low plasma density, the geometrical decrease of the electromagnetic field is more important than the skin depth effect, whereas for the real system at high density and with large dimensions ($\approx$ 10 cm), the skin depth effect is the main cause of the limitation of the induced electric field amplitude.

These considerations are very important for the electrostatic simulation of ICP because the shape of the induced electric field cannot be resolved in a self-consistent manner. The only way to resolve it would be to use a solver for the full set of Maxwell's equations (Eqs. (1.5) to (1.8)), and not only a Poisson's equation solver.

The coupling between the electric circuit and the plasma is not investigated in depth here; the reader can refer to the book of P. Chabert and N. Braithwaite [31] for more details about concepts such as plasma impedance, matchboxes, or power coupling efficiency that are very important experimentally. The method implemented in *LPPic* uses an electric E_z field imposed in the z direction perpendicular to the simulation plane. In order to represent a joint effect of the geometrical decrease of the electromagnetic field produced by the coil, and the skin effect, the magnitude of E_z can vary with the distance x from the coil.

$$E_z = E_0 \max\left[0, \left(1 - \frac{\alpha x}{x_{\max}}\right)\right] \cos(\omega t) \tag{1.48}$$

where ω is the RF frequency, set to $2\pi \times 13.56\,\text{MHz}$ in all simulation conditions. InEq. (1.48), $x_{\max}$ is the distance at the end of the simulation domain (near the acceleration grid), and α sets the linear decrease of the heating electric field with distance. Three different values were tested for α:

- $\alpha = 0$: This corresponds to the situation where the heating electric field is uniform.
- $\alpha = 1$: The electric field reaches 0 right at the end of the simulation domain.
- $\alpha = 3$: The heating occurs only in one-third of the simulation domain.

The amplitude of the electric field E_0 is updated at the end of each RF cycle to keep the total power absorbed by the plasma equal to a fixed parameter $\mathcal{W}_{\text{abs}}$. The aim is to reach

$$\frac{l_z \omega_{RF}}{2\pi} \int_t^{t+\frac{2\pi}{\omega_{RF}}} \iint J_z E_z \, dx \, dy \, dt = \mathcal{W}_{\text{abs}} \tag{1.49}$$

at steady state. The simulation starts with a first estimate of E_0 provided as an input parameter, that should be approximately consistent with the initial plasma density imposed, in order to avoid a too violent behavior of the plasma during the first RF periods that can cause the simulation to crash. This effect can be particularly visible at low pressure and when the heating electric field is more localized. Adjusting the right initial condition can require a little bit of engineering, but once the steady state is reached, the amplitude of the heating electric field does not vary anymore, and the state of the system does not depend on the initial condition.

$$E_0 = \frac{2\pi \mathcal{W}_{\text{abs}}}{l_z \omega_{RF}} \left(\int_t^{t+\frac{2\pi}{\omega_{RF}}} \iint J_z \max\left[0, \left(1 - \frac{\alpha x}{x_{\max}}\right)\right] \cos(\omega t) \, dx \, dy \, dt \right)^{-1} \tag{1.50}$$

While the heating electric field is in the z direction, the x and y components of the electric field are solved through the solution of Poisson's equation. The particles are

free to move in the three directions, such that the electrons respond to the heating electric field and generate a current that can be monitored to keep the power as imposed by Eq. (1.49).

One should keep in mind that this method to model the inductive plasma does not accurately represent the local power balance, because the profile of the heating electric field is fixed *a priori*, but it does preserve the global power balance. Moreover, the instantaneous heating electric field could also vary along the y coordinate, and this effect was ignored entirely here.

The configurations simulated in this work are represented in Fig. 1.6 where the RF antenna is schematically represented on the left. Fig. 1.6(a) and (d) correspond to the case $\alpha = 0$, Fig. 1.6(b), (e) and (h) correspond to the case $\alpha = 1$, and Fig. 1.6(c), (f), and (i) correspond to the case $\alpha = 3$.

The scheme can be subject to oscillations during the transient and over-shooting is observed. This can be fixed by adding a successive under-relaxation coefficient r to the numerical method, such that the electric field is updated the following way:

$$E_{n+1} = rE_n + (1 - r)E_0 \tag{1.51}$$

where E_0 is defined by Eq. (1.50). We found a significantly smoother transient at low pressure by choosing, for example $r = 2/3$, with no significant loss on the convergence time. When the electrons are well confined, either by a relatively high gas pressure or by an external magnetic field, r can be equal to 0.

1.3.2 Fluid Equations of the Plasma Transport

Plasma transport covers all the collective phenomena where electrons and ions move inside a discharge domain, and how they reach the discharge walls. In general, these phenomena can be described by a set of conservation equations, field equations (a subset of Maxwell's equations), and closure equations. The equations presented below are the fluid equations of the plasma, that come from the integration of the various moments of the Boltzmann equation [9]. The *continuity equation* for electrons and ions is

$$\partial_t n + \nabla \cdot \mathbf{\Gamma} = S \tag{1.52}$$

where S represents the local particle source term (or loss term) due to collisions, and $\mathbf{\Gamma} = n\mathbf{v}$ is the particle flux vector. In this context, $\mathbf{v}$ is the fluid velocity vector, that is, the mean velocity of the particles at a given position. Eq. (1.52) is valid for both electrons and ions, and can be used with the corresponding density and source terms. If the only volume mechanism responsible for charged species production or destruction is electron impact ionization,

$$\partial_t n_i + \nabla \cdot \mathbf{\Gamma}_i = \partial_t n_e + \nabla \cdot \mathbf{\Gamma}_e = n_e \nu_{iz} \tag{1.53}$$

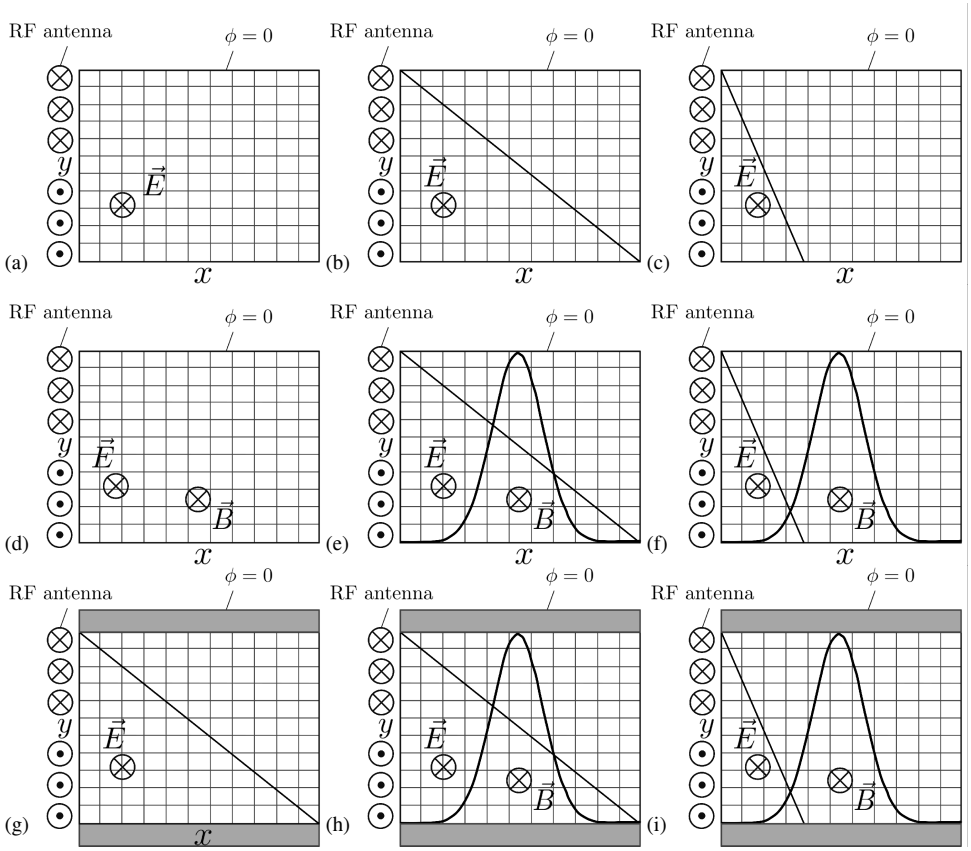

Figure 1.6: Sketches of the various ICP configurations investigated with the 2D PIC model.

where ν_{iz} is the electron impact ionization frequency. The momentum conservation equation contains all the force terms that drive the plasma motion.

$$m\left(\partial_t \mathbf{v} + \mathbf{v}\cdot\nabla\mathbf{v}\right) = q\left(\mathbf{E} + \mathbf{v}\times\mathbf{B}\right) - \frac{\nabla p}{n} - m\mathbf{v}\nu_{tot} \tag{1.54}$$

where ν_{tot} is the total momentum transfer collision frequency, and

$$p = nk_B T \tag{1.55}$$

is the pressure of the considered species. Eq. (1.54) can be used either for the electrons or the ions. The loss of momentum due to collisions can be quite complicated to take into account. It is assumed that the plasma is weakly ionized, such that the frequency of charged species is much lower than the density of the neutral gas. Similarly to the PIC model, Coulomb collisions are neglected and only collisions with high-density neutral species are taken into account. In general, the collision frequency depends on the energy, and thus the fluid velocity. Furthermore, viscosity is neglected. However, for electrons, the thermal velocity is usually much higher than the fluid velocity, such that the collision frequency becomes a function of the local electron temperature and the neutral gas density. The situation is more complicated for ions because the fluid velocity can be higher than the thermal velocity. As described in Section 1.2.3, collision cross sections between ions and atoms are quite poorly characterized. However, Langevin capture cross sections that describe the isotropic scattering of ions on neutral atoms are proportional to v^{-1}. An approximation that is often made in analytical models is to assume a constant collision cross section (typically $10^{-18}\,\mathrm{m}^2$ for argon) and to assume that the ion thermal velocity is the reference velocity for the computation of the total momentum transfer collision frequency.

In the quasistatic approximation, the magnetic field has only a DC component that is imposed by a coil powered in DC or permanent magnets, as it is the case in the PEGASES experiment. Combined with Poisson's equation for the electric field, this set of equations can already be enough to determine the plasma density if an assumption is made on the electron temperature. The simplest assumption is the isothermal assumption where electrons and ions are assumed to be at a constant temperature, still with $T_e \gg T_i$. Another model that can be used but which is less spread in the community of LTP technologies is the *polytropic* model. This model consists in assuming a relationship between the density and the temperature under the form

$$Tn^{1-\gamma} = cst \tag{1.56}$$

where γ is called the polytropic coefficient. The polytropic law is associated with adiabatic processes for ideal monoatomic gases with three degrees of freedom and has then the value of 5/3 [9]. The polytropic coefficient can also be used as an empirical coefficient that accounts for first order variations of the temperature inside a discharge due in particular to non-Maxwellian distribution functions.

An energy equation may also be added to the system, for instance to account more precisely for local heating phenomena. It can be written either in terms of total energy or internal energy only. We provide here the form given by P. Bellan, integrated from the Boltzmann equation [9]:

$$\frac{3}{2}\partial_t(nk_BT) + \frac{3}{2}\mathbf{v}\cdot\nabla(nk_BT) + \frac{5}{2}nk_BT\nabla\cdot v = -\nabla\cdot\mathbf{Q} + \nu_{tot}n\mathbf{v}^2 - \partial_t w\big|_c \quad (1.57)$$

where $\partial_t w\big|_c$ is the rate at which the species transfers its energy through collisions, and

$$\mathbf{Q} = \frac{m}{2}\iiint (\mathbf{v}-\mathbf{u})^2(\mathbf{v}-\mathbf{u}) f\, d^3v \quad (1.58)$$

is the heat flux. The electron and ion heat fluxes are neglected in the models developed in this work but may be of high interest for future investigations.

1.3.3 Numerical Parameters of the PIC Simulation

The Debye length

$$\lambda_D = \left(\frac{\epsilon_0 k_B T}{ne^2}\right)^{1/2} \quad (1.59)$$

represents the typical screening distance between charged particles [37] and can be defined for each species. The electron Debye length has to be resolved to guarantee the stability and accuracy of the simulation. For similar reasons, the time step is constrained by the plasma frequency (Eq. (1.46)). The conditions imposed on the time step and the cell size in plasma simulations using particles result from extensive numerical experiments [16, 80] and depend on various numerical choices such as the particle weighting scheme, or physical parameters, such as the drift velocity. A bilinear weighting scheme is used in *LPPic* , and the commonly accepted criteria in the LTP community are [157]

$$\boxed{\begin{aligned} \Delta x &< \lambda_{De}/2 \quad (1.60)\\ \Delta t &< 0.2/\omega_{pe} \quad (1.61)\end{aligned}}$$

where λ_{De} and ω_{pe} are the electron Debye length, and electron plasma frequency respectively.

Another stability condition that is not exclusive to PIC simulation is the Courant – Friedrichs – Lewy (CFL) condition that imposes that the typical velocity is not such that particles would "jump" over one cell in a single time step.

$$v\Delta t < \Delta x \quad (1.62)$$

Particles have a velocity distribution function that is not bounded in velocity. The highest typical velocity in LTP is the electron thermal velocity v_{Te} (Eq. (1.9)), such

that if the CFL condition has to be fulfilled approximately by a fraction α of the electron population, one can estimate a maximal velocity v_α for the CFL condition. For a Maxwellian distribution function defined by Eq. (1.22), the velocity v_α satisfies

$$\int_0^{v_\alpha} \left(\frac{m_e}{2\pi k_B T_e}\right)^{3/2} \exp\left[\frac{m_e v^2}{2\pi k_B T_e}\right] 4\pi v^2 dv = \alpha \tag{1.63}$$

which is also

$$\mathrm{erf}\left(\frac{v_\alpha}{\sqrt{2}v_{Te}}\right) - \left(\frac{2}{\pi}\right)^{1/2} \frac{v_\alpha}{v_{Te}} \exp\left[-\frac{1}{2}\left(\frac{v_\alpha}{v_{Te}}\right)^2\right] = \alpha \tag{1.64}$$

where erf is the error function defined by

$$\mathrm{erf}(x) = \frac{2}{\sqrt{\pi}} \int_0^x \exp\left(-x^2\right)\, dx \tag{1.65}$$

One should typically aim for a ratio $v_\alpha / v_{Te} = 2.5$ which fulfills the CFL conditions for $\alpha = 90\,\%$ of the electrons. The CFL condition of interest for the PIC simulation is therefore

$$\boxed{v_{Te}\Delta t < 0.4\Delta x} \tag{1.66}$$

1.4 Main Features of a Plasma Discharge

1.4.1 First Run Example

We conclude this section by presenting 2D PIC simulation results of an ICP discharge. The numerical and physical parameters are inspired by the 1D benchmark of a helium capacitively-coupled plasma (CCP) discharge published by Turner *et al.* [157]. The idea of this simulation case is to work towards a series of benchmarks for the 2D PIC simulation of LTP. The helium cross section set described in the previous section is the same as in the case of Turner *et al.* [157]. The numerical parameters of the simulation are summarized in Table 1.2. An excitation frequency of 13.56 MHz is retained because it is the standard frequency delivered by many experimental power supplies. The aim is not to reach exact experimental conditions but to have a simulation case that is clearly defined and whose numerical results can be verified independently by other groups. While some plasma reactors for industrial processing can be quite well described by 1D models due to their large aspect ratio, plasma thrusters usually have at least an intrinsically 2D geometry. We hence present here first results for a square simulation domain of 3×3 cm size. The absorbed power is $10\,\mathrm{kW/m^3}$, which is relatively low for laboratory plasmas, and yields a plasma density comprised between 10^{14} and $10^{15}\,\mathrm{m^{-3}}$. This low density

	Physical parameters		
Discharge sizes	$l_x = l_y$	30	mm
Neutral pressure	p	30	mTorr
Neutral density	n_g	9.578×10^{20}	m^{-3}
Neutral temperature	T_g	300	K
Frequency	f_{RF}	13.56	MHz
Power density	w	10.0	kW/m^3
Physical time of the simulation	$t_{\text{simulation}}$	$300/f_{RF} = 22.12$	µs
Averaging time	t_{average}	$3/f_{RF} = 0.2212$	µs
	Initial conditions		
Plasma density	$n_e = n_i$	1×10^{14}	m^{-3}
Electron temperature	T_e	4.0	eV
Ion temperature	T_i [eV]	0.026	eV
Particles per cell	$N_{\text{part./cell}}$	100	
Heating electric field amplitude	E_0	1.0	kV/m
	Numerical parameters		
Cell size	Δx	150	µm
Time step	Δt	$(2000 f_{RF})^{-1} = 3.6873 \times 10^{-11}$	s
Steps to execute	$N_{\text{simulation}}$	600 000	
Steps to average	N_{average}	6 000	
Weighting factor	q_f	22 500	m^{-1}

Table 1.2: Main physical and numerical input parameters of the 2D PIC simulation.

allows using a time step and cell sizes that are not too small, which reduces the computation time.

Gas heating and gas depletion phenomena are neglected, and the neutral gas is assumed to be of uniform and constant density n_g and temperature T_g. We assume that the gas behaves as an ideal gas, such that the pressure in mTorr is provided as an input parameter:

$$n_g = \frac{0.133 p\,[\text{mTorr}]}{k_B T_g}. \tag{1.67}$$

The plasma is initialized with uniform densities of electrons and ions of 10^{14} m^{-3}. The super-particles representing electrons are distributed with a Maxwellian distribution function at 4.0 eV, while the ions are initialized with a Maxwellian distribution function at temperature 0.026 eV. All the new ions created by ionization are generated at the same temperature of 0.026 eV, which is approximately equal to the gas temperature (300 K). As illustrated in Fig. 1.7(a), the electrons first leave the plasma before being regenerated by ionization after approximately 0.5 µs. There are always slightly more ions than electrons in the discharge. The exceeding ion frac-

Physical characteristics			*Numerical characteristics*	
			$\omega_{pe}\Delta t$	0.053
$n_{i\max} \times 10^{14}$	[m^{-3}]	6.21	$\lambda_D/\Delta x$	7
$n_{e\max} \times 10^{14}$	[m^{-3}]	5.87	$\nu_e \Delta t$	0.0085
T_e	[eV]	12.81	$\nu_i \Delta t$	1.4×10^{-5}
J_e	[A/m^2]	1.12	N_D	26 566
			N_P	19 760 461

Table 1.3: Physical and numerical characteristics extracted from the results of the simulation.

tion typically depends on the ratio between the Debye length and the system size. Fig. 1.7(b) shows the mean kinetic energy of the electrons in the three directions. Since the electrons are accelerated by the heating RF electric field in the z direction, their kinetic energy is higher in the z direction. The kinetic energy of the electrons is transferred from the z direction to the x and y directions through collisions. The system is perfectly symmetrical with respect to x and y, so it can be verified that the mean kinetic energy has the same value along x and y directions. The discrepancy in kinetic energy between the heating direction and the others was observed in all simulation conditions, and the effect was more visible at low pressure. The amplitude of the heating electric field oscillates during the first RF cyles and converges to 543 V/m after 3 µs. The value of the heating electric field amplitude is updated every 2 000 time steps, while the number of particles and the mean kinetic energy are extracted every $N_{\text{average}} = 6\,000$ time steps. The oscillations that are visible in the curve of E_0 should be more visible in the curves showing the number of super particles if the sampling time was the same.

A few numerical parameters are shown in Table 1.3. The maximum ion density is 6.21×10^{14} m^{-3} while maximum electron density is 5.87×10^{14} m^{-3}. N_P represents the number of super-particles (both ions and electrons) in memory at the end of the simulation. There are, on average, 494 particles per cell (both ions and electrons) at steady state. The Debye length is 1.1 mm and the number of super-particles in a Debye square is $N_D = 25\,566$. The nominal simulation runs in 12 hours on 160 central processing unit (CPU), due to the relatively large number of super-particles.

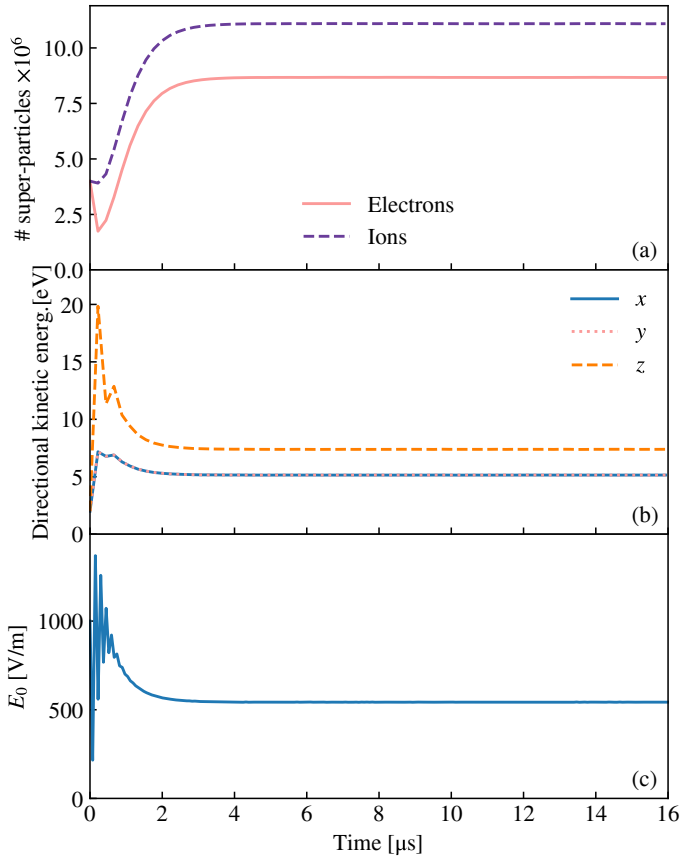

Figure 1.7: Temporal evolution of (a) the number of super-particles of electrons and ions (He^+), (b) the electron kinetic energy along each axis, and (c) the amplitude of the heating electric field (Eq. (1.50)).

1.4.2 Numerical Tests and Influence of the Reaction Scheme

Fig. 1.8 shows that both the electron and the ion densities decrease smoothly from the center of the discharge to the edges, and the electron density is always below the ion density. Fig. 1.9(c) shows the plasma potential (the walls are grounded to $\phi = 0$) spatial distribution. The plasma potential ϕ is positive, which means that the electrons are confined inside the plasma discharge while the ions are accelerated towards the edge. The plasma potential and the electron temperature (Fig. 1.9) are almost uniform in the middle of the discharge and decrease strongly near the edge, in a region that is called the *sheath*. While the electron and ion densities are almost equal in the center of the discharge, the electrons are repelled by the strong electric field in the sheath, and their density becomes much lower than that of the ions. The electron temperature reaches 12.81 eV at the discharge center and drops to approximately 6 eV at the wall. Fig. 1.9(d) shows a map of the electron currents. The background color map represents the norm of the current and the arrows represent the direction of the current. The electrons flow from the center of the discharge to the walls, the current points inward due to the negative electron charge. The deceleration of the electrons in the sheath is quite visible.

A few tests were performed to assess the sensitivity of this run to several parameters:

Case (1) the number of particles per cell;

Case (2) the reaction scheme used for inelastic collisions;

Case (3) the presence of inelastic collisions.

The electron and ion densities, the electron temperature, and the electron energy probability function (EEPF) for the 4 cases (including the reference Case (0) presented in the above paragraph) are shown together in Fig. 1.8(a-c). Fig. 1.8(a) and (b) show cuts at $y = 15$ mm of the plasma density and the electron temperature. For Case (1), the initial number of particles per cell was divided by 4. This increases the noise level visible in the ion density and the electron temperature profiles. As expected, the tail of the EEPF is less well resolved as in the reference Case (0). More interestingly, the gradient in the electron temperature profile is sharper than in the reference case: it is higher in the center and lower at the walls. The mean kinetic energy of the particles and the density profiles are not much affected by the number of particles, but the local temperature is affected. Since we know that the local power balance is not necessarily well resolved in the heating scheme used in the electrostatic PIC simulation as a uniform heating electric field is assumed, this is not a major problem.

In Case (2), we used a more recent version of the Biagi database for inelastic collisions between electrons and helium atoms [12], and the number of particles per cell was fixed to 100 when the simulation is initialized, as in Case (0). This set of cross sections includes 49 excitation states that are all detailed in Appendix A.

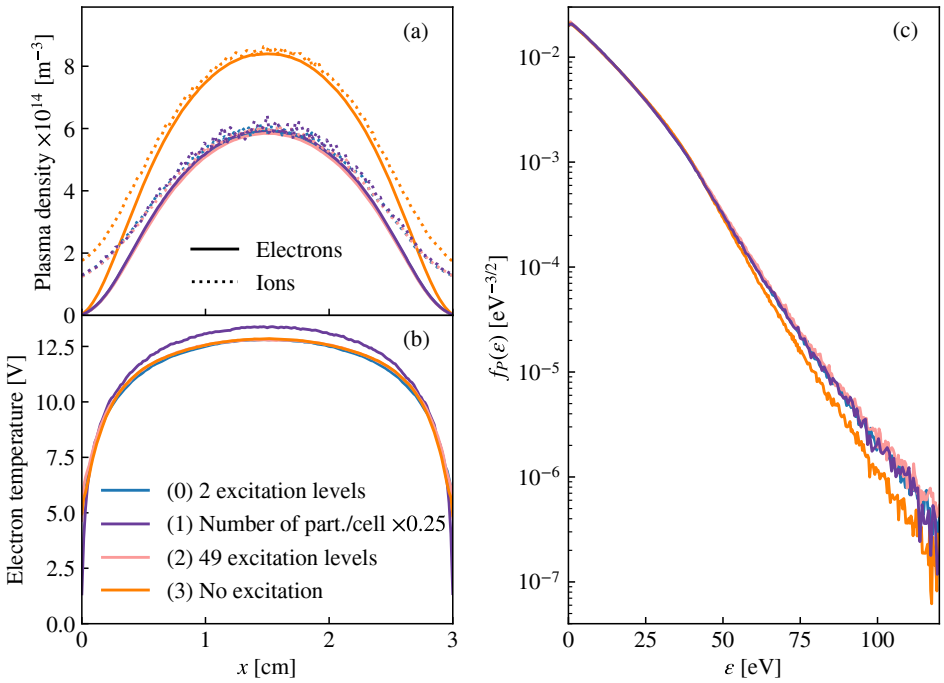

Figure 1.8: PIC simulation results of an ICP helium discharge with various models: a refined model with 49 excitation levels, an approximate model with two excitation levels, and a model with no inelastic collisions except ionization. (a) Electron and ion densities, (b) electron temperatures, (c) EEPF.

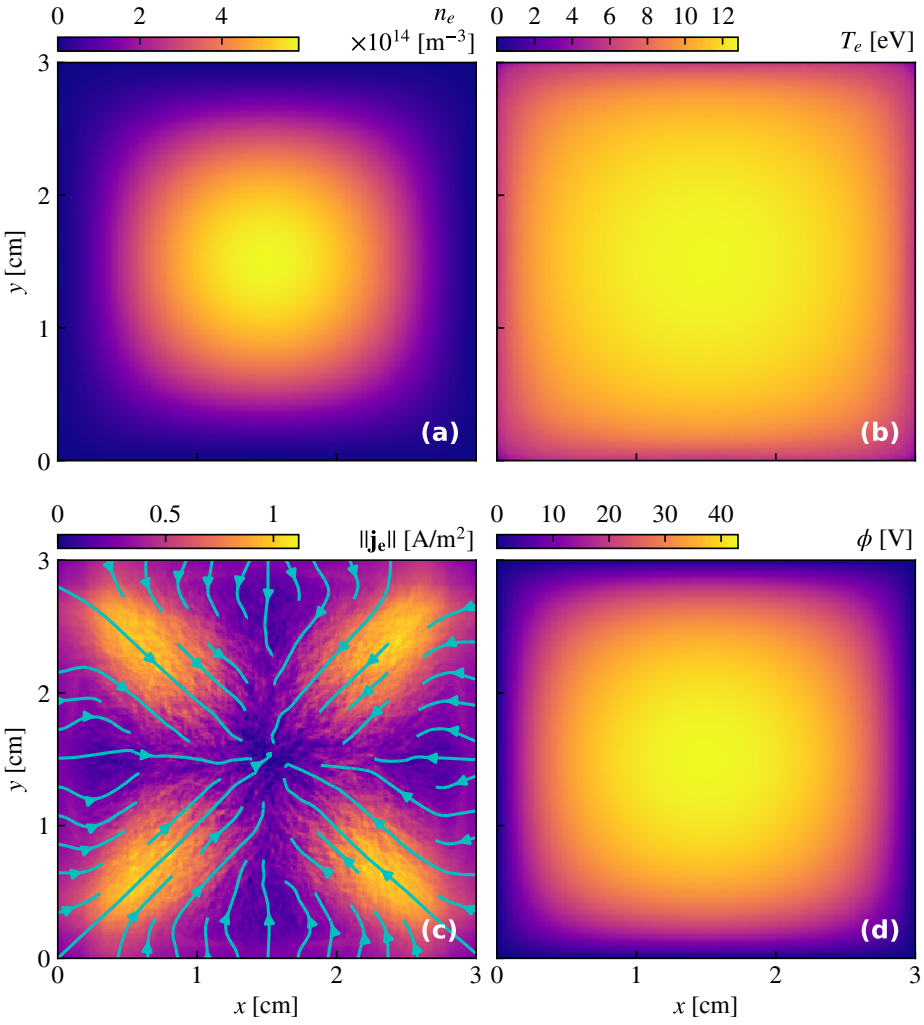

Figure 1.9: 2D plots of the electron density (a), the electron temperature (b), the electron current (c), and the plasma potential (d). The streamlines represent the line of electron currents in the simulation plane. All the data are averaged over the last 6 000 time steps of the simulation.

This set of cross section was designed to model the transport of the helium plasma correctly. We remind that the excitation states are not tracked in the PIC model used here, and each excitation reaction is treated as isotropic scattering with an energy loss for the electron that corresponds to an excitation energy of the atom. Fig. 1.8(a) shows that the ion and the electron densities are statistically the same in the Cases (0) and (2). The electron temperature profile is also very similar to the reference case. Even the EEPF shown in Fig. 1.8 are quite indistinguishable down to $10^{-6}\,\mathrm{eV}^{-3/2}$. Comparing the EEPF could be used as a method to validate a cross section set that is aggregated from multiple sources.

In order to better sense the role of inelastic collisions, we chose to present a simulation with no excitation reactions at all in Case (3), where the number of particles per cell was kept to 100 at initialization. This simulation case does not characterize any possible realistic plasma but aims at pointing out the role of inelastic collisions in the transport equations. As illustrated in Fig. 1.8(a), the ion and electron density profiles have the same shape as in Case (0), but the maximum density is approximately 30 % higher. This can be explained by the fact that less energy is dissipated in internal levels of the atom and a higher fraction of the injected power is converted into ionization of the helium atoms. Nevertheless, Fig. 1.8(b) shows that the electron temperature has locally almost exactly the same value as in the reference Case (0). To the first order, one can interpret this observation by saying that the electron temperature results from a balance between ionization and ion losses to the walls. This global model approach will be discussed in Section 1.5.2. All the EEPF presented in Fig. 1.8(c) feature the same shape with a knee at approximately 40 eV. Even in Case (3), when no excitation levels are present, the knee is still visible. This indicates that the knee in the EEPF does not come from excitation reactions, but it should rather come here from wall absorption of electrons whose kinetic energy in volts is higher than the plasma potential.

1.5 Analytical Models and Their Limitations

In this section, two important analytical models of a single-ion plasma discharge are presented. The last paragraph stresses the limitations of these approaches for the modeling of the PEGASES source.

1.5.1 Non-Isothermal Sheath Theory

In Section 1.4, we have mentioned a region called the *sheath* where the ion density becomes higher than the electron density. This is a fundamental characteristic of LTP. The sheath is a region that separates a quasineutral plasma region from the reactor walls. Quasineutral models are very convenient to handle but break in the sheath region. It is therefore very important to understand how the sheath behaves to feed quasineutral models with the right boundary conditions at the sheath edge.

Due to their low mass and high temperature, the electrons have typical velocities that are much greater than the ion velocity. If electron and ion densities remained equal up to the walls, the flux of electrons would be much higher than the ion flux, and it would not be possible to sustain a discharge steady state. At steady state, in all the simulation conditions studied in this work, the total current leaving the plasma has to be zero on average. The primary characteristic of the sheath is therefore to feature a charge difference between electrons and ions, and subsequently a strong space charge electric field. We have seen in the previous section, for example, in Fig. 1.9(b), that the sheath can also be associated with a significant temperature drop. In the next paragraph, we propose to describe a 1D model of a DC sheath with a temperature gradient described by a *polytropic* law.

Polytropic sheath model

In a 1D plasma, a polytropic coefficient can always be locally defined for the electrons by

$$\gamma = 1 + \frac{n_e dT_e}{T_e dn_e} \tag{1.68}$$

In some plasma conditions reached by the PIC simulations, this polytropic coefficient is notably constant throughout the discharge and the value of this constant can lead to a much more accurate description of the plasma properties than classically used isothermal models while keeping the mathematical framework quite simple. In this case, the electron density and temperature are bounded by the relation

$$T_e/T_0 = (n/N)^{\gamma-1} \tag{1.69}$$

where N and T_0 are reference electron density and temperature respectively, for example, taken at the sheath edge. Note that the isothermal limit is recovered when $\gamma = 1$. In this paragraph, the role of the magnetic field is neglected.

In a collisionless plasma, the electron momentum conservation equation at steady state is

$$en_e\nabla\phi - \nabla(k_B T_e n_e) = 0 \tag{1.70}$$

where electron inertia has been neglected and where ϕ is the plasma potential. Eq. (1.70) can be rearranged as

$$\frac{e\nabla\phi}{k_B T_e} = \frac{\nabla T_e}{T_e} + \frac{\nabla n_e}{n_e} \tag{1.71}$$

So

$$e\nabla\phi = \frac{\gamma k_B \nabla T_e}{\gamma - 1} \tag{1.72}$$

which can be integrated into

$$e\phi = \frac{\gamma}{\gamma - 1} k_B (T_e - T_0) \tag{1.73}$$

where it was assumed that the plasma potential is zero at the sheath edge.

The electron density is hence:

$$\boxed{n_e = N\left[1 + \frac{(\gamma-1)e\phi}{\gamma k_B T_0}\right]^{\frac{1}{\gamma-1}}} \tag{1.74}$$

Eqs. (1.69) and (1.70) provide two equations for the three unknown variables n_e, T_e, and ϕ. Additional equations are required in order to solve for the sheath properties. In the sheath ($x > 0$), the plasma is not quasineutral, so Poisson's equation (Eq. (1.11)) needs to be solved. The simplest way to describe the plasma sheath is to neglect ion collision and temperature, which reduces the ion momentum conservation equation (Eq. (1.54)) to the energy conservation for one ion:

$$\frac{1}{2}m_i({v_i}^2 - v_0^2) = -e\phi \tag{1.75}$$

where v_0 is the ion velocity when they enter the sheath. Moreover, ionization is neglected in the sheath because the electron density is expected to be very low (the electrons are repelled by the space charge field). Therefore, the continuity equation has no source term:

$$\nabla \cdot (n_i v_i) = 0 \tag{1.76}$$

which reduces to flux conservation

$$n_i v_i = N v_0 \tag{1.77}$$

In Eq. (1.77), it was assumed that the plasma is quasineutral at the sheath edge:

$$n_e(0) = n_i(0) = N \tag{1.78}$$

The set of equations to be solved is then made of Eqs. (1.11), (1.69), (1.70), (1.75) and (1.77) for the five variables n_e, n_i, T_e, ϕ, and v_i.

The ion velocity v_i can immediately be eliminated by combining Eqs. (1.75) and (1.77). This leads to an expresion of n_i as a function of the plasma potential

$$n_i = N\left(1 - \frac{2e\phi}{m_i v_0^2}\right)^{-1/2} \tag{1.79}$$

Replacing n_i, n_e, and T_e with Eqs. (1.73), (1.74) and (1.79) respectively in Poisson's equation leads to the second order differential equation in 1D

$$\frac{d^2\phi}{dx^2} = N\left[\left\{1 + \frac{(\gamma-1)e\phi}{\gamma k_B T_0}\right\}^{\frac{1}{\gamma-1}} - \left(1 - \frac{2e\phi}{m_i v_0^2}\right)^{-1/2}\right] \tag{1.80}$$

Let us introduce the normalized potential $\chi = -\frac{e\phi}{k_B T_0}$, the Mach number $\mathcal{M} = v_0\left(\frac{m_i}{k_B T_0}\right)^{1/2}$, and the normalized position $X = x/\lambda_{De}$, where λ_{De} is the electron

Debye length at the sheath edge defined by Eq. (1.59). Eq. (1.80) can then be expressed in the normalized form:

$$\chi'' = \left(1 + \frac{2\chi}{\mathcal{M}^2}\right)^{-1/2} - \left[1 - \frac{(\gamma-1)\chi}{\gamma}\right]^{\frac{1}{\gamma-1}} \tag{1.81}$$

where the symbol $''$ represents the second derivative with respect to the normalized dimension X. After multiplying this equation by the first derivative of the normalized electric field χ', integration yields

$$\frac{\chi'^2 - \chi'(0)^2}{2} = \mathcal{M}^2 \left[\left(1 + \frac{2\chi}{\mathcal{M}^2}\right)^{1/2} - 1\right] + \left[1 - \frac{(\gamma-1)\chi}{\gamma}\right]^{\frac{\gamma}{\gamma-1}} - 1 \tag{1.82}$$

where $\chi'(0)$ is the normalized electric field at the sheath edge. In Eq. (1.82), the second term of the right-hand side (RHS) tends towards $e^{-\chi}$ when γ tends towards 1^+, which is the classical exponential factor when the EEDF is assumed to be Maxwellian with a uniform temperature. In the isothermal electrons limit corresponding to $\gamma \to 1^+$, Eq. (1.82) becomes:

$$\frac{\chi'^2 - \chi'(0)^2}{2} = \mathcal{M}^2 \left[\left(1 + \frac{2\chi}{\mathcal{M}^2}\right)^{1/2} - 1\right] + e^{-\chi} - 1 \tag{1.83}$$

which is in agreement with classical isothermal sheath models [128].

We assume that the electric field increases in the sheath, which means that $\chi'^2 > \chi'(0)^2$ for $X > 0$, such that the RHS of Eq. (1.82) has to be positive for all χ. Hence, a second order Taylor expansion in χ provides the relation

$$\mathcal{M}^2 > \gamma \tag{1.84}$$

As a result, the ions must enter the polytropic sheath with a speed larger than the ion acoustic speed

$$\boxed{u_0 > \gamma^{1/2} u_B \quad ;} \tag{1.85}$$

where

$$u_B = \left(\frac{k_B T_e}{m_i}\right)^{1/2} \tag{1.86}$$

is the Bohm speed. This criterion is the *polytropic Bohm sheath criterion*.

We find again the more classical isothermal Bohm sheath criterion [128, 46] in the case where $\gamma = 1$. In the same way as for the isothermal Debye sheath, we will assume that the sheath criterion is saturated

$$\mathcal{M}^2 = \gamma \tag{1.87}$$

The potential drop ϕ_s in the sheath can then be obtained by equating electron and ion fluxes at the wall. The electron flux can be found by integrating a Maxwellian distribution function over half a sphere. This is called the thermal flux

$$\Gamma_e = \frac{1}{4} n_{e,wall} \left(\frac{8 k_B T_{e,wall}}{\pi m_e}\right)^{1/2} \tag{1.88}$$

where the $n_{e,wall}$ and $T_{e,wall}$ are given by Eqs. (1.73) and (1.74) respectively. In this steady state model, the ion flux is conserved through the sheath, which can be obtained by integrating Eq. (1.52) with no source term. Therefore,

$$\Gamma_i = N \left(\frac{\gamma k_B T_0}{m_i} \right)^{1/2} \tag{1.89}$$

The steady state current equality condition

$$\Gamma_e = \Gamma_i \tag{1.90}$$

yields

$$\left[1 + \frac{(\gamma - 1)}{\gamma} \frac{e\phi_s}{k_B T_0} \right]^{\frac{2}{\gamma - 1}} \left[1 - \frac{(\gamma - 1)}{\gamma} \frac{e\phi_s}{k_B T_0} \right] = \frac{4\gamma\pi m_e}{m_i} \tag{1.91}$$

This equation can be solved numerically to find the sheath drop as a function of the electron temperature at the sheath edge T_0 and the polytropic coefficient. A numerical fit was proposed by A. Tavant *et al.* for argon [150]

$$\boxed{\frac{e\phi_s}{k_B T_0} \approx 0.70 + 4.1 \times \gamma^{-1.7}} \tag{1.92}$$

In the limit where γ equals 1, Eq. (1.91) becomes

$$\frac{e\phi_s}{k_B T_0} = \frac{1}{2} \ln \left(\frac{m_i}{2\pi m_e} \right) \tag{1.93}$$

which is approximately 4.8 for argon. PIC simulation results have shown that γ was always between 1.2 and 1.8.

In summary, when an ion is created in the plasma bulk, it is accelerated to the sheath edge where it reaches the speed $\gamma^{1/2} u_B$. The potential drop that produces the ion acceleration is related to a decrease of the electron density. At the sheath edge, the plasma density is lower than at the discharge center, and the space charge electric field becomes very strong.

The electron temperature drop in the sheath is often neglected in fluid models but can be crucial to account correctly for electron impact Secondary Electron Emission (SEE) as shown by the work of Tavant *et al.* [149]. The temperature drop mainly comes from an EEDF effect: as the walls absorb high energy electrons, the EEDF is a concave function of the energy, which implies that mean electron energy decreases when the plasma potential decreases. This effect was investigated in details in Tavant *et al.* using the above polytropic model and 1D-3V PIC simulations [150].

1.5.2 Global Models of a Plasma Discharge

Global models rely on volume-averaged balance equations for the particle densities and energy. The variables are typically the electron and ion densities at the discharge center, the electron temperature, the gas density, and in some cases the gas temperature. All the global models studied here assume two temperatures: one for the electrons, and one for the heavy species ($T_g = T_i$). The models are always quasineutral, such that we will assume in this section

$$n_e = n_i = n\,. \tag{1.94}$$

The set of equations here is applicable for a plasma with only one ion species, following, for instance, the work of P. Chabert *et al.* [30]. More details about global models of thrusters operated with molecular gases (e.g. iodine) will be given in Chapter 5 and can also be found in Grondein *et al.* [71].

The particle balance equation is obtained by integrating the continuity equation (Eq. (1.53))

$$\iiint_V \partial_t n\, dV + \oiint_S \mathbf{\Gamma_i} \cdot \mathbf{dS} = \iiint_V n\nu_{iz}\, dV \tag{1.95}$$

and illustrated in Fig. 1.10(a). Let N be the plasma density at the discharge center. The ion flux at the walls is normalized to the Bohm flux SNu_B through the h factor defined by

$$\boxed{h = \frac{\oiint_S \mathbf{\Gamma_i} \cdot \mathbf{dS}}{SNu_B}} \tag{1.96}$$

where S is the surface of the inner reactor walls. We also introduce the normalized mean plasma density

$$\tilde{n} = \frac{1}{V} \iiint_V \frac{n}{N}\, dV \tag{1.97}$$

such that Eq. (1.95) becomes

$$\frac{dN}{dt} = n_g K_{iz} N - \frac{hSu_B}{V\tilde{n}} N \tag{1.98}$$

where we have substituted the collision frequency by its expression $K_{iz} n_g$, K_{iz} being the reaction rate factor provided for instance by Fig. 1.2 as a function of the electron temperature.

Low-pressure global models often assume of a Maxwellian electron velocity distribution function (EVDF). The equation for the internal energy of the electrons is an integral form of Eq. (1.58)

$$\partial_t \iiint_V \frac{3}{2} n k_B T_e\, dV = \mathcal{W}_{\text{abs}} - \mathcal{W}_{\text{loss}} \tag{1.99}$$

where $\mathcal{W}_{\text{abs}}$ stands for the power absorbed by the plasma which can be seen as a control parameter, and $\mathcal{W}_{\text{loss}}$ aggregates all the volume and surface power losses

$$\mathcal{W}_{\text{loss}} = \iiint_V n\nu_{iz} e\mathcal{E}_{iz}\gamma_i + 3\frac{m_e}{m_g}k_B(T_e - T_g)n_e\nu_e \, dV + \oiint_S e\mathcal{E}_w \mathbf{\Gamma}_i \cdot \mathbf{dS} \quad (1.100)$$

In Eq. (1.100),

$$\gamma_i = 1 + \frac{1}{K_{i,z}\mathcal{E}_{iz}} \sum K_{ex}\mathcal{E}_{ex} \quad (1.101)$$

is the ratio between the energy losses of all electron-neutral inelastic collisions and the energy lost for ionization only, and $\nu_{iz} = n_g K_{iz}$. The quantity $\mathcal{E}_w$ is the mean electron energy when they reach the wall. According to Chabert and Braithwaite [31],

$$\mathcal{E}_w = 2\mathrm{T}_e + \Delta\phi \quad (1.102)$$

for a Maxwellian EVDF, where $\Delta\phi$ represents the potential difference between the plasma and the wall, and T_e is the electron temperature in volts. The potential drop ϕ_s in the sheath is given by Eq. (1.93). The plasma potential drops in the pre-sheath region to accelerate the ions by approximately $\mathrm{T}_e/2$. One can therefore estimate

$$\phi_s < \Delta\phi < \phi_s + \mathrm{T}_e/2 \quad (1.103)$$

Since the isothermal model tends to overestimate the sheath drop slightly, it is reasonable to assume

$$\Delta\phi \approx \phi_s = \frac{\mathrm{T}_e}{2} \ln\left(\frac{m_i}{2\pi m_e}\right) \quad (1.104)$$

Hence,

$$\mathcal{E}_w = \mathrm{T}_e \left[2 + \frac{1}{2}\ln\left(\frac{m_i}{2\pi m_e}\right)\right] . \quad (1.105)$$

The second term of the RHS of Eq. (1.100) is the energy transferred from the electron population to the neutral gas through elastic collisions. Its expression is given, for instance, by Liard *et al.* [99]. The ratio m_e/m_i is very small, but since the elastic collision rate is much larger than the rate for inelastic collisions, the contribution of this term can be significant. At each collision, the electrons transfer some momentum to the neutral gas and lose a fraction of their energy. The expression $3\frac{m_e}{m_g}k_B(T_e - T_g)n_e\nu_e$ comes from an average over Maxwellian distribution functions. The power balance equation is represented schematically in Fig. 1.10(b).

In our PIC simulations, the background gas is fixed at a given pressure. Conversely, global models allow one to consider a gas balance equation easily. The discharge chamber is filled at a certain rate Q_0 (in standard cubic centimeters per minute (sccm) or particles per second). The gas leaves the discharge chamber with a thermal flux through an open surface S_g. The gas population is regenerated by the ions that reach the inner walls and depleted by electron impact ionization. Moreover, the gas density is assumed uniform here, which can be a strong assumption if the

power becomes too high. Following Chabert *et al.* [30], the gas balance equation is

$$\frac{dn_g}{dt} = \frac{Q_0}{V} + hnu_B\frac{S}{V} - nn_gK_{iz} - \frac{1}{4}n_g\left(\frac{8k_BT_g}{\pi m_g}\right)^{1/2}\frac{S_g}{V} \tag{1.106}$$

The balance equation for the neutral gas density is illustrated in Fig. 1.10(c).

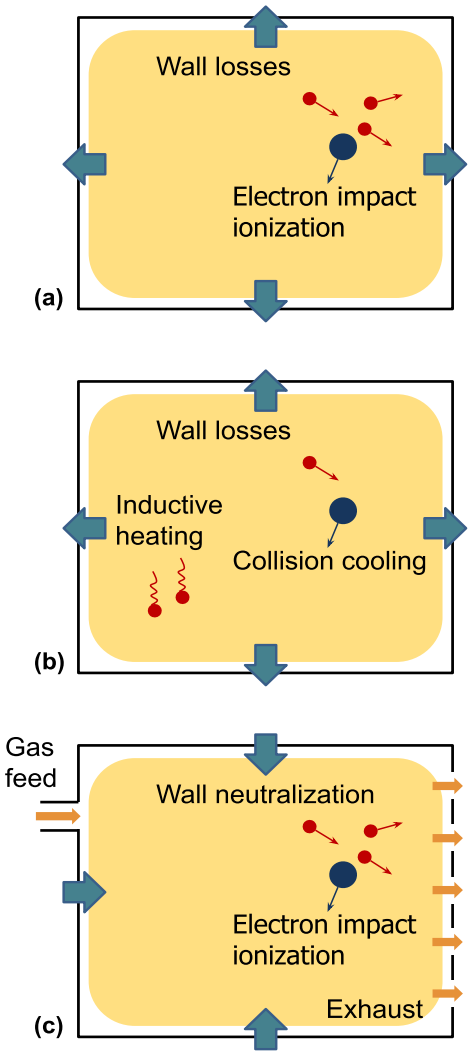

Figure 1.10: Illustration of the equations of the global models of a plasma discharge for (a) particles (electron or ion), (b) the electron temperature, and (c) the neutral gas.

An additional equation for the gas temperature was included in former models [30, 99]. This last equation is subject to some approximations that are not the main focus of this work, so the gas heating phenomenon is not included here.

Global models can be very efficient for the modeling of a discharge because all the physics is reduced to a system of a few temporal equations. However, it has several limitations because it depends on parameters that are not necessarily easy to estimate. First, the reaction rates rely on more or less direct experiments or some quantum chemistry simulations, for example through the R-matrix method [151] to compute the reaction cross sections. The cross sections are then integrated over a certain distribution function to yield the reaction rates. At higher pressure (typically greater than 100 mTorr for laboratory plasmas), the Boltzmann equation can be solved in the two-term approximation, for example with the Bolsig+ solver [74]. In the range of pressure of interest here, these methods do not apply, mainly because ion inertia plays a crucial role at low pressure. The easier assumption that was made in the global models used for this work is taking Maxwellian EEDF, although this is not the case in general (see Fig. 1.8(c)). A finer approach would be to feed the global model solver with distribution functions measured experimentally or found by PIC simulation. This would, however, break the predictive nature of the global model.

Secondly, some of the mechanisms at the walls are not very well known for most plasmas and wall materials. Here, it was assumed that the ions that reach the walls are released in the reactor as neutral atoms. We have neglected SEE from the surface that can be the consequence of high energy electron or ion impacts. At the low electron temperatures observed in the simulations, this effect should not be dominant but may depend on the wall material.

Finally, in the global model presented above, all the plasma transport processes are contained solely in the h factor that is not easy to estimate in general. More insights on the h factor can be provided by PIC simulation and fluid theory, as will be shown in Chapter 2.

1.5.3 Limitations of Simplified Models for the Modeling of PEGASES

The models presented above are examples of analytical models that can apply to LTP. In some cases, they are effective and can capture the relevant plasma properties. However, they rely on a number of input parameters, such as the reaction rate coefficients, and closure equations (isothermal or polytropic). In the case of global models, the h factor, the mean normalized density $\tilde{n}$, or the mean energy lost per electron lost $\mathcal{E}_w$ come from somehow ad-hoc estimates, experimental measurements, or numerical simulation. In the case of the polytropic sheath model, the polytropic coefficient also has to be estimated by external means, and it may not be constant across the discharge in some cases. Moreover, the assumptions made in the simplified models may not be verified. For example, collisions were neglected in the sheath model, the global model assumes a uniform heating power source term that is uniform and well known, which may not be the case in experiments. Plasma chemistry and magnetic field effects were also entirely ignored in the previous paragraphs.

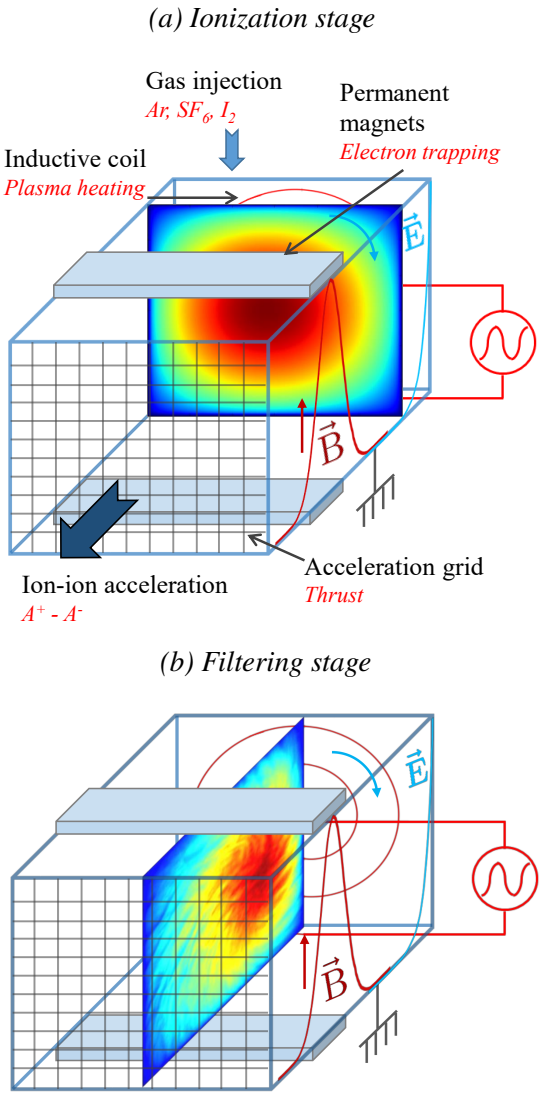

Figure 1.11: The PEGASES configuration with the simulated electron density maps in (a) the ionization region (see Chapter 2), and (b) the filter region (see Chapter 4)

Each of the next chapters will tackle one (or a few) of these limitations, with the ultimate aim of modeling the PEGASES thruster operated with iodine correctly. The challenges are the following

- The PEGASES ion source depicted in Fig. 2 has inherently a 3D geometry ($l_x \sim l_y \sim l_z$). Therefore, the parameters that come from 1D models (typically the h factor) need to be challenged in 2D or 3D. The ionization region, where the magnetic field is very low, can be modeled on its own in a first approximation. This approach is represented schematically in *Fig. 1.11(a)*. The

2D PIC simulation and the derivation of the quasineutral, isothermal theory are achieved in *Chapter 2*.

- In the high magnetic field region of the PEGASES filter, the very rich effects of magnetic fields on low pressure ionized gases need to be investigated. This is first done with a uniform magnetic field in *Chapter 3*. The cross-field plasma transport is studied from a *fundamental point of view*. Magnetized plasmas are known for producing instabilities. Most of these instabilities are electrostatic and can be simulated with the *LPPic* code.

- The PEGASES configuration couples the ionization region with the magnetic filter region. Hence, accurate modeling requires to account for both regions at the same time. This requires to include non-uniform power deposition and spatial variations of the magnetic field in the model. *Fig. 1.11(b)* provides an illustration of the simulation case investigated in *Chapter 4*. As the main direction is the thrust axis x, where the heating power, the magnetic field, as well as the electron temperature and density vary strongly, the simplest model of the PEGASES thruster should be at least 1D. But the particle and power losses in the y and z directions need to be modeled correctly.

- Up to Chapter 4, all the simulations are performed assuming an argon discharge. All the work should be performed again to account correctly for the specific features of an *iodine plasma*. In particular, an iodine plasma has multiple positive ion species (at least I^+ and I_2^+), and also at least one negative ion species I^-, that change the discharge behavior entirely. When the negative ion density is about twice higher than the electron density, which is typically the case in the high magnetic field region of the PEGASES thruster [20], the presheath region of the discharge can be unstable, even with no magnetic fields [27]. It means that in the filter region, these effects combine with the magnetic drift instabilities, to drive the plasma transport across the filter. The balance between both neutral species I and I_2 can also be a challenge for modeling. These aspects are partially investigated in *Chapter 5*.

Summary

This chapter has mainly defined the framework in which the present work is performed. The concepts of sheath, quasineutrality, reaction rate, global models, that can vary in the literature, are defined. The general features of the electrostatic PIC/MCC code LPPic are described, and the cross section sets used for noble gas modeling are given. The heating algorithm employed to model the ICP generation is explained, and the various simulation configurations that will be used in the next chapters are introduced. The results of a 2D PIC simulation of a helium ICP at low plasma density are presented and discussed.

We have shown that the electron temperature decreases in the sheath, and that the cooling mechanism is affected by the number of super-particles used in the PIC simulation. We verified that all the excitation reactions can be modeled with only a few effective inelastic electron-neutral collisions. This is valid, at least, as long as excited states are not tracked in the simulation. Furthermore, a 1D model of a polytropic sheath was proposed, which provides a significant improvement to the more common isothermal model, as it can account for the drop of electron temperature in the sheath. We generalize the definition of the h factor (edge-to-center density ratio in 1D) as the ratio between the mean ion flux collected at the inner walls of the reactor and the Bohm flux.

Most of the analytical models available in the literature are 0D or 1D, and apply to a very limited number of experimental situations. The next chapters will aim at improving the modeling of the ionization and the filtering stages of the PEGASES thruster, with argon and iodine. This will be mainly achieved through 2D PIC simulation and fluid theory.

Chapter 2

ISOTHERMAL TRANSPORT MODELS

Contents

Following the general picture provided in Chapter 1, the bulk plasma region is modeled using an isothermal closure. The transport equations of a quasineutral plasma are solved in several conditions. Due to the isothermal assumption, the plasma transport can generally be reduced to a single scalar equation for the electron temperature. We first treat the general 1D case for a wide range of pressures and magnetic fields. We then focus on the non-magnetized 2D case. The 2D analytical solution is validated by PIC simulations, and the general 2D h factor, that represents the ion losses at the reactor walls is correctly predicted. The analytical solutions rely on the assumption of a spatially uniform collision frequency between charged particles and neutrals. This assumption is also discussed.

2.1 Motivation

The h factor introduced in Chapter 1 is often known in the literature as the pre-sheath drop or edge-to-center density ratio, and it characterizes the ratio between the plasma density in the center of a discharge and the density at the sheath edge, where the quasineutrality becomes violated. In the literature, this factor has been labeled h_L for 1D Cartesian geometries or h_R for 1D cylindrical geometries. In a 1D system, this definition coincides with the more general definition proposed in Eq. (1.96) for the 1D case. In 2D or 3D, the plasma density at the sheath edge is not necessarily the same everywhere.

We have proposed a generalization of Eq. (1.96) in a journal article (Lucken *et al.*, PSST 2018 [105]) and successfully implemented the corrected h factor in a simplified global model (Lucken *et al.* IEPC 2017)[104]). The main results of both articles are reproduced in Section 2.3 of this thesis, without the application to the simplified global model presented at the IEPC 2017 [104].

Several authors provided theoretical estimates of the h factor in various pressure regimes, based on asymptotic solutions of the 1D transport equations of a quasineutral, isothermal plasma with no magnetic field [100, 31]. The low-pressure regime was investigated in the early days of plasma physics, in the 1920s, by Tonks and Langmuir [155]. Ion and electron collisions are entirely neglected in this case, and the h factor is independent of pressure. Schottky [134] studied the higher pressure regime where the ion thermal velocity dominates over the ion fluid velocity and found that the plasma density profile follows a Helmholtz equation

$$n'' = -\frac{\nu_{iz}}{D} n \tag{2.1}$$

where ν_{iz} is the electron impact ionization frequency and D is a diffusion coefficient that is inversely proportional to the pressure. It can be shown that the h factor decreases in $1/p$ as well in this case. The intermediate pressure regime is of particular interest because ion collisions cannot be neglected in this regime, but the typical velocity of the ions is driven by the mean fluid velocity and not by the thermal velocity of the ions. V. Godyak successfully described this transport regime and found that the h factor should be proportional to $p^{-1/2}$ [66]. The effect of neutral gas depletion in this intermediate transport regime was studied by J.-L. Raimbault *et al.* [123]. Lafleur and Chabert [94] confirmed by PIC simulation the validity of heuristic models over the entire pressure range for weakly-ionized 1D plasmas.

All these theories are some limit cases of the *ambipolar* 1D transport of the plasma. In the next paragraph, we introduce the *ambipolar* transport of an isothermal plasma with one ion species, in a quite general context.

2.2 One-Dimensional Transport Solutions

2.2.1 Differential Equation for the Plasma Velocity

One of the fundamental assumption of ambipolar transport is the plasma neutrality

$$n_e = n_i = n \tag{2.2}$$

It is assumed that the plasma properties only depend on the x direction, and that the magnetic field $\mathbf{B} = B\mathbf{e}_z$ is uniform and along z. Both electrons and ions can be magnetized, and can potentially drift in the y direction.

The continuity equation (Eq. (1.53)) is in 1D

$$(nv_{ix})' = (nv_{ex})' = n\nu_{iz} \tag{2.3}$$

the prime $'$ denotes the derivative with respect to x. Eq. (2.3) says that the electric current $en(v_i - v_e)$ is constant. We further assume that no current is drawn at the discharge center. By symmetry, electron and ion fluid velocities are equal to 0 at the discharge center. It follows then that

$$nv_{ix} = nv_{ex} \tag{2.4}$$

everywhere. The fact that $v_{ex} = v_{ix} = v_x$ is called the *ambipolarity* condition, and it is a simple consequence of quasineutrality in 1D.

The projections of Eq. (1.54) on the x and y axis with constant electron and ion temperatures are respectively

$$-k_B T_e \frac{n'}{n} - eE - ev_{ey}B - m_e\nu_e v_x = 0 \tag{2.5}$$

$$ev_x B - m_e\nu_e v_{ey} = 0 \tag{2.6}$$

for the electrons, and

$$-k_B T_i \frac{n'}{n} + eE + ev_{iy}B - m_i\nu_{i,tot}\, v_x = m_i v_x v_x' \tag{2.7}$$

$$-ev_x B - m_i\nu_{i,tot}\, v_{iy} = 0 \tag{2.8}$$

for the ions. Again, electron inertia has been neglected in Eq. (2.5). In Eqs. (2.7) and (2.8), $\nu_{i,tot}$ is the total momentum loss term for the ion population. This term includes momentum transfer due to elastic collisions (both isotropic and backscattering) with the neutral atoms, and the inertia of newly created ions, produced by electron impact ionization [31]:

$$\nu_{i,tot} = \nu_i + \nu_{iz} \tag{2.9}$$

The y component of electron and ion velocities can be eliminated to yield

$$-k_B T_e \frac{n'}{n} - eE - m_e\nu_e(1 + \eta_e{}^2)v = 0 \tag{2.10}$$

and

$$-k_B T_i \frac{n'}{n} + eE - m_i \nu_{i,tot}(1+\eta_i{}^2)v = m_i v v' \tag{2.11}$$

where we have replaced v_x by v since it is now the only velocity variable, and where

$$\eta_e = \frac{\omega_{ce}}{\nu_e} = \frac{eB}{m_e \nu_e} \tag{2.12}$$

and

$$\eta_i = \frac{\omega_{ci}}{\nu_{i,tot}} = \frac{eB}{m_i \nu_{i,tot}} \tag{2.13}$$

are the Hall parameters of electrons and ions, respectively. By introducing the Bohm speed

$$u_B = \left[\frac{k_B(T_e + T_i)}{m_i}\right]^{1/2} \tag{2.14}$$

Eqs. (2.10) and (2.11) can be summed up to eliminate the electric field,

$$-\frac{n'}{n} - \frac{v}{D_a} = \frac{vv'}{u_B{}^2} \tag{2.15}$$

where

$$D_a = \frac{k_B(T_e + T_i)}{m_e \nu_e(1+\eta_e{}^2) + m_i \nu_{i,tot}(1+\eta_i{}^2)} \tag{2.16}$$

is a general *ambipolar diffusion* coefficient. This equation is combined with the continuity equation $(nv)' = n\nu_{iz}$ to yield

$$\boxed{\left(1 - \frac{v^2}{u_B{}^2}\right) v' = \nu_{iz} + \frac{v^2}{D_a}} \tag{2.17}$$

2.2.2 The Problem of Ion-Neutral Momentum Transfer Collision Frequency

The integration of Eq. (2.17) is possible when the ambipolar diffusion coefficient is constant. If the magnetic field is uniform, the only question is on the collision frequencies which are given by Eq. (1.24). We will assume that the gas density is uniform, which is a reasonable approximation for weakly ionized plasmas. The rate for momentum transfer between electrons and neutrals is a function of the electron temperature, which is assumed uniform. For the momentum transfer between ions and neutral atoms, the rate depends on the CS, which is almost constant within the range of energy considered (typically 0.03 - 0.3 eV), and on the typical velocity of the ions. The latter quantity should, in general, depend on the plasma fluid velocity v. By assuming that the neutral atoms are at rest,

$$\nu_i \approx n_g \sigma_i \langle \| \mathbf{v}_i \| \rangle \tag{2.18}$$

Computing the mean velocity for a Maxwellian distribution function shifted by a drift velocity $\mathbf{v_0}$

$$f(\mathbf{v}) = n\left(\frac{m}{2\pi k_B T}\right)^{3/2} \exp\left[-\frac{m(\mathbf{v}-\mathbf{v}_0)^2}{2k_B T}\right] \tag{2.19}$$

is thus useful for the accurate modeling of ion collisions in fluid simulations. The integral is

$$\langle \|\mathbf{v}\| \rangle = \left(\frac{m}{2\pi k_B T}\right)^{3/2} \iiint \|\mathbf{v}\| \exp\left[-\frac{m(\mathbf{v}-\mathbf{v}_0)^2}{2k_B T}\right] d^3v\,. \tag{2.20}$$

Assuming that $\mathbf{v}_0$ is along the z axis of spherical coordinates,

$$\langle \|\mathbf{v}\| \rangle = \frac{1}{{v_T}^3\sqrt{2\pi}} \int_0^{+\infty}\int_0^{\pi} v^3 \exp\left[-\frac{v^2+v_0^2-2vv_0\cos\theta}{2{v_T}^2}\right] \sin\theta\, d\theta\, dv\,. \tag{2.21}$$

where $v_0 = \left\|\mathbf{v_0}\right\|$ and $v = \|\mathbf{v}\|$. By introducing the normalized velocities $u = v/v_T$ and $u_0 = v_0/v_T$,

$$\langle \|\mathbf{v}\| \rangle = \frac{v_T}{\sqrt{2\pi}} \int_0^{+\infty}\int_0^{\pi} u^3 \exp\left[-\frac{u^2+u_0^2-2uu_0\cos\theta}{2}\right] \sin\theta\, d\theta\, du\,. \tag{2.22}$$

Since

$$\int_0^{\pi} e^{uu_0\cos\theta} \sin\theta\, d\theta = \frac{e^{uu_0}-e^{-uu_0}}{uu_0}\,, \tag{2.23}$$

$$\langle \|\mathbf{v}\| \rangle = \frac{v_T e^{-u_0^2/2}}{u_0\sqrt{2\pi}} \int_0^{+\infty} u^2 e^{-u^2/2}\left(e^{uu_0}-e^{-uu_0}\right) du\,. \tag{2.24}$$

We find

$$\boxed{\langle \|\mathbf{v}\| \rangle = v_T\left[\frac{1+u_0^2}{u_0}\mathrm{erf}\left(\frac{u_0}{\sqrt{2}}\right)+\left(\frac{2}{\pi}\right)^{1/2} e^{-u_0^2/2}\right]} \tag{2.25}$$

which satisfies the limits

$$\langle \|\mathbf{v}\| \rangle \approx \left(\frac{8}{\pi}\right)^{1/2} v_T \qquad \text{when } u_0 \ll 1, \tag{2.26}$$

$$\langle \|\mathbf{v}\| \rangle \approx v_0 \qquad \text{when } u_0 \gg 1. \tag{2.27}$$

The gas velocity was neglected here. The derivation could also be done by integrating over a given gas velocity distribution function, for example a Maxwellian distribution function at temperature T_g.

2.2.3 Boundary Conditions and Mathematical Solution

In order to make analytical derivations, we now assume a constant ambipolar diffusion coefficient D_a and that ν_i is uniform. Eq. (2.17) has separate variables

$$\frac{(1 - v^2/{u_B}^2)dv}{\nu_{iz} + v^2/D_a} = dx \tag{2.28}$$

and can be integrated into

$$\boxed{\left(1 + \frac{\nu_{iz} D_a}{{u_B}^2}\right) \arctan\left[\frac{v}{(\nu_{iz} D_a)^{1/2}}\right] - \frac{(\nu_{iz} D_a)^{1/2}}{{u_B}^2} v = \left(\frac{\nu_{iz}}{D_a}\right)^{1/2} x} \tag{2.29}$$

This equation can be inverted numerically to yield a plasma velocity profile $v(x)$. The plasma density is also retrieved by arranging Eqs. (2.15) and (2.17):

$$\frac{n'}{n} = -\frac{v}{{u_B}^2 - v^2}\left(\frac{{u_B}^2}{D_a} + \nu_{iz}\right) \tag{2.30}$$

Under integral form

$$n(x) = N \exp\left[-\int_0^x \frac{v(X)}{{u_B}^2 - v(X)^2}\left(\frac{{u_B}^2}{D_a} + \nu_{iz}\right) dX\right] \tag{2.31}$$

$$= N \exp\left[-\left(1 + \frac{\nu_{iz} D_a}{{u_B}^2}\right) \int_0^{v(x)} \frac{\zeta d\zeta}{\nu_{iz} D_a + \zeta^2} d\zeta\right] \tag{2.32}$$

This integral is

$$\boxed{n(x) = N\left(1 + \frac{v(x)^2}{\nu_{iz} D_a}\right)^{-\frac{1}{2}\left(1 + \frac{\nu_{iz} D_a}{{u_B}^2}\right)}} \tag{2.33}$$

To be consistent with the isothermal approximation, the polytropic coefficient has to be equal to 1, such that the sheath criterion applicable here is the simple Bohm criterion $v = u_B$. If the sheath thickness is neglected, Eq. (2.29) becomes at the sheath edge defined by $x = l/2$

$$\boxed{f\left(\frac{u_B}{(\nu_{iz} D_a)^{1/2}}\right) = \frac{u_B l}{2 D_a}} \tag{2.34}$$

where the function f is defined by

$$\boxed{f(x) = \left(x + \frac{1}{x}\right) \arctan(x) - 1} \tag{2.35}$$

The graph of f is provided in Appendix D. Eq. (2.34) can be seen as the equation for the electron temperature, which will play the role of an eigen value of the system. f has the following asymptotes

$$f(x) \underset{x\to 0}{\sim} \frac{2}{3}x^2 + \mathcal{O}\left(x^4\right) \tag{2.36}$$

$$f(x) \underset{x\to +\infty}{\sim} \frac{\pi}{2}x - 2 + \mathcal{O}\left(x^{-1}\right) \tag{2.37}$$

The inverse function f^{-1}, therefore, has the following asymptotic expansions

$$f^{-1}(x) \underset{x\to 0}{\sim} \left(\frac{3}{2}x\right)^{1/2} + \mathcal{O}\left(x^{3/2}\right) \tag{2.38}$$

$$f^{-1}(x) \underset{x\to +\infty}{\sim} \frac{2}{\pi}(x+2) + \mathcal{O}\left(x^{-1}\right) \tag{2.39}$$

and is plotted in Fig. 2.1(a) in logarithmic scales. The two asymptotic limits can provide the following approximate equation

$$f^{-1}(x) \approx \left[\frac{4}{\pi^2}x^2 + \frac{3}{2}x\right]^{1/2} \tag{2.40}$$

that preserves the first term of each asymptotic expansion. The formula provided by Eq. (2.40) approximates the numerical solution shown in Fig. 2.1(a) with a relative mean square error of only 0.77% in the interval $[10^{-3}, 10^4]$. Similarly, estimating Eq. (2.33) at the sheath edge provides an estimate of the h factor in 1D

$$h = \left(1 + \frac{{u_B}^2}{\nu_{iz} D_a}\right)^{-\frac{1}{2}\left(1+\frac{\nu_{iz} D_a}{{u_B}^2}\right)} \tag{2.41}$$

where $\frac{{u_B}^2}{\nu_{iz} D_a}$ is given by Eq. (2.34). The function

$$g(x) = \left(1 + \frac{1}{x}\right)^{-\frac{1}{2}(1+x)} \tag{2.42}$$

has the following asymptotes

$$g(x) \underset{x\to 0}{\sim} x^{1/2} + \mathcal{O}(x^{3/2}\ln(x)) \tag{2.43}$$

$$g(x) \underset{x\to +\infty}{\sim} e^{-1/2} + \mathcal{O}(x^{-1}) \tag{2.44}$$

Using the function

$$F : x \longrightarrow g\left(\left[f^{-1}(x)\right]^{-2}\right) \tag{2.45}$$

the h parameter is

$$h = F\left(\frac{u_B l}{2D_a}\right) \tag{2.46}$$

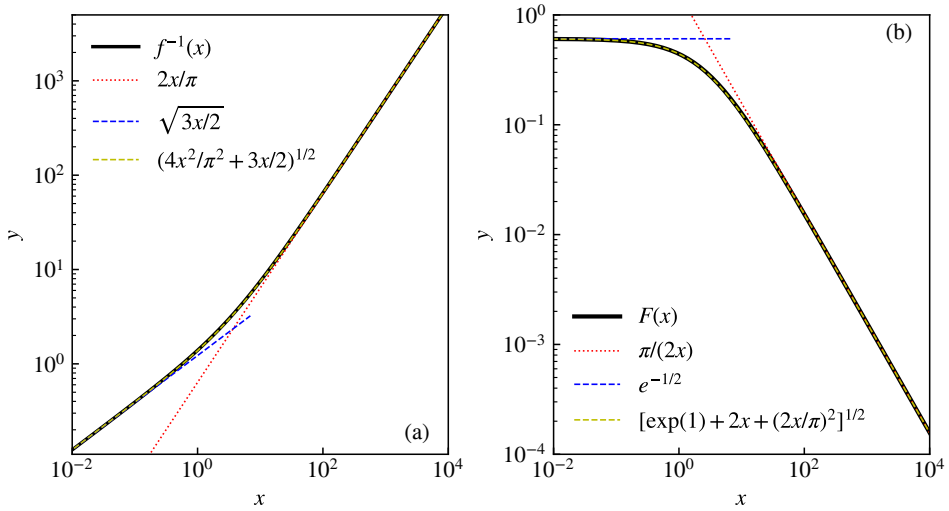

Figure 2.1: Graphs of the mathematical solutions of the quasineutral transport model with the asymptotes and the approximate formulas.

The function F has the limits

$$F(x) \underset{x\to 0}{\sim} e^{-1/2} \tag{2.47}$$

$$F(x) \underset{x\to +\infty}{\sim} \frac{\pi}{2x} \tag{2.48}$$

F is very well approximated by

$$F(x) \approx \left[\exp(1) + 2x + \left(\frac{2x}{\pi}\right)^2\right]^{-1/2} \tag{2.49}$$

with a relative error of less than 1.3 % in the interval $[10^{-3}, 10^4]$. The function F is plotted in Fig. 2.1(b) together with its asymptotes.

This implies for the h factor that

$$h \approx e^{-1/2} \qquad \text{when } \frac{u_B l}{2D_a} \ll 1 \tag{2.50}$$

$$h \approx \frac{\pi D_a}{u_B l} \qquad \text{when } \frac{u_B l}{2D_a} \gg 1 \tag{2.51}$$

and

$$\boxed{h \approx \left[\exp(1) + \frac{u_B l}{D_a} + \left(\frac{u_B l}{\pi D_a}\right)^2\right]^{-1/2}} \tag{2.52}$$

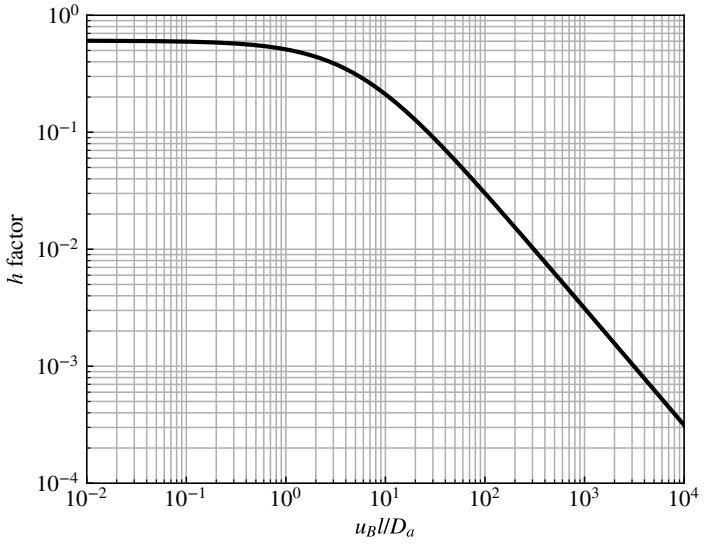

Figure 2.2: Graphs of the numerical solution for the h factor as a function of $u_B l/D_a$.

The mean normalized density profile

$$\tilde{n} = \frac{2}{l}\int_0^{l/2} n(x)\,dx \tag{2.53}$$

also has a simple general expression. Integrating the 1D continuity equation $(nv)' = n\nu_{iz}$ between the center and the edge gives

$$hu_B = \nu_{iz}\tilde{n}l/2 \tag{2.54}$$

which is, of course, equivalent to the particle balance used in global models (see Eq. (1.98)) and yields

$$\tilde{n} = \frac{2hu_B}{l\nu_{iz}}\,. \tag{2.55}$$

The numerical solution of h is shown in Fig. 2.2. We want to emphasize the fact that Eq. (2.52) includes the electron and ion collisions, ion temperature, and the magnetic field effects through the general ambipolar diffusion coefficient D_a, given by Eq. (2.16). Since the h factor is sometimes difficult to measure directly, knowing a general expression between the ambipolar diffusion coefficient and the h factor can be very useful. This expression can also be applied to turbulent transport regimes, provided that we assume an instability-enhanced diffusion coefficient, as will be seen in Chapter 3. This expression is consistent with more classical heuristic formulas as the ones given by Chabert at al. [31] that incorporates, in particular, the

intermediate pressure regime studied by Godyak [66]

$$h = h_0 = 0.86 \left[3 + 0.5 \frac{l}{\lambda_i} + 0.2 \frac{T_i}{T_e} \left(\frac{l}{\lambda_i} \right)^2 \right]^{-1/2} . \tag{2.56}$$

where λ_i is the ion mean free path. The second term of Eq. (2.56) accounts for an ion collision frequency that incorporates the ion fluid velocity, as it was suggested with Eq. (2.25). Few direct measurements of the h factor exist. To the knowledge of the author, only Kim *et al.* [85] provided some experimental values of the h factor in argon ICP discharges for pressures between 3 and 30 mTorr. The experimental values were in good agreement with the classical models. Eq. (2.56) was also validated using 1D PIC simulations of ICP and CCP discharges by T. Lafleur. [94]. The main difference between the models described above and the classical models is that no assumption was made on any particular form of the ambipolar diffusion coefficient. All the terms of Eq. (2.16) were retained. In particular, D_a depends on the ionization frequency at low pressure, which makes comparison with other models not so straightforward.

We now investigate two limit cases, the low pressure case and the high pressure case, where $D_a/(u_B l) \ll 1$

2.2.4 Asymptotic Regimes

The High D_a Limit (Low Pressure *and* Low Magnetic Field)

The low pressure non-magnetized limit is slightly intricate because the ambipolar diffusion coefficient depends on the electron impact ionization frequency through $\nu_{i,tot}$ (Eq. (2.9)). By neglecting ion magnetization, the ambipolar coefficient is written

$$D_a = \frac{{u_B}^2}{\nu_m + \nu_{iz}} \tag{2.57}$$

where ν_m accounts for both ion and electron transport processes

$$\nu_m = \nu_i + \frac{m_e}{m_i} \nu_e (1 + {\eta_e}^2) \tag{2.58}$$

Instead of treating D_a as a parameter, Eqs. (2.34) and (2.57) can be seen as two equations for the two variables ν_{iz} and D_a, that can be re-arranged into

$$\frac{\nu_m D_a}{{u_B}^2} f \left(\left[1 - \frac{\nu_m D_a}{{u_B}^2} \right]^{-1/2} \right) = \frac{l \nu_m}{2 u_B} \tag{2.59}$$

At very low pressure, the *collisionless ambipolar diffusion coefficient* involves $f(1) = \pi/2 - 1$ and is

$$\boxed{D_a = \frac{l u_B}{\pi - 2}} . \tag{2.60}$$

This expression is quite interesting because it gives a diffusion coefficient that represents only the inertia of the newly created ions that are instantly coupled to the electrons through the ambipolar electric field. The diffusion coefficient is quite large at low pressure such that the second term of the left-hand side (LHS) in Eq. (2.15) is rather small, but not negligible. Since we also have $D_a = {u_B}^2/\nu_{iz}$ in this low pressure regime, we find a straightforward equation for the electron temperature

$$\nu_{iz} = (\pi - 2)u_B/l \tag{2.61}$$

In this regime, Eq. (2.41) yields

$$h = 0.5 \tag{2.62}$$

which is consistent with the low-pressure limit of Eq. (2.56).

As a consequence, the left-hand side of the curve of Fig. 2.2, where $u_B l/D_a$ is smaller than $\pi - 2$, is not physical.

The Low D_a Limit (High Pressure *or* High Magnetic Field)

At high pressure ($l\nu_m/u_B \gg 1$), Eq. (2.59) yields

$$D_a = {u_B}^2/\nu_m \tag{2.63}$$

This is consistent with classical non-magnetized diffusion coefficients in the high pressure case [100], where $T_i \ll T_e$ and $\nu_i = (8/\pi)^{1/2} v_{Ti}/\lambda_i$

$$D_a = (\pi/8)^{1/2}\, u_B \lambda_i (T_e/T_i)^{1/2} \tag{2.64}$$

Finally, the low D_a limit provides an interesting behavior at the sheath edge because the electric field has a finite value in $1/D_a$. If $\nu_{iz} D_a/{u_B}^2 \ll 1$, Eq. (2.29) yields

$$v = (\nu_{iz} D_a)^{1/2} \tan\left(\frac{\nu_{iz}^{1/2}}{D_a^{1/2}} x\right) = -D_a \frac{n'}{n} \tag{2.65}$$

Therefore,

$$n = N \cos\left(\frac{\nu_{iz}^{1/2}}{D_a^{1/2}} x\right) \tag{2.66}$$

so the density n is the solution of a Helmholtz equation. Moreover, the electron temperature equation Eq. (2.34) provides the boundary condition

$$\nu_{iz} = \pi^2 D_a/l^2 \,. \tag{2.67}$$

which is equivalent to the so-called *Schottky boundary condition* that states that the plasma density drops to zero at the wall. In this case,

$$v' = \frac{\nu_{iz}}{\cos^2\left(\nu_{iz}^{1/2} x/D_a^{1/2}\right)} = \frac{v^2/D_a}{\sin^2\left(\nu_{iz}^{1/2} x/D_a^{1/2}\right)} \tag{2.68}$$

So at the sheath edge ($v = u_B$), the plasma acceleration is

$$v_s' = {u_B}^2 / D_a \tag{2.69}$$

Hence, Eqs. (2.10) and (2.11) taken at the sheath edge provide a system of equations for the electric field E_s and the density gradient length $\Lambda_s = -n/n'|_s$ at the sheath edge

$$k_B T_e \Lambda_s^{-1} - eE_s - m_e \nu_e (1 + {\eta_e}^2) u_B = 0 \tag{2.70}$$

$$k_B T_i \Lambda_s^{-1} + eE_s - m_i \nu_{i,tot} (1 + {\eta_i}^2) u_B = m_i {u_B}^3 / D_a \tag{2.71}$$

This system leads to

$$\Lambda_s = \frac{D_a}{2u_B} \tag{2.72}$$

and

$$E_s = \frac{m_i {u_B}^3}{eD_a} \left(1 + \left[1 + \frac{m_e \nu_e (1 + {\eta_e}^2)}{m_i \nu_i (1 + {\eta_i}^2)} \right]^{-1} - \frac{2T_i}{T_e + T_i} \right) \tag{2.73}$$

The second term of this expression is equal to 1 when the transport is limited by the ions, as it is usually the case in non-magnetized plasmas, and is small when the transport is limited by the electrons, as in a strongly magnetized plasma for example. The third term is just a correction related to the ion temperature and can be neglected in most cases.

$$\boxed{E_s = \begin{cases} 2m_i {u_B}^3/(eD_a) & \text{at high pressure} \\ m_i {u_B}^3/(eD_a) & \text{at high magnetic field} \end{cases}} \tag{2.74}$$

2.3 Two-Dimensional Transport Model with no Magnetic Field

In this section, we first go on with the analytical description of the quasineutral isothermal plasma transport, but now in a 2D Cartesian geometry with no magnetic field. The electron collisions are usually negligible in this case so they will be neglected. The plasma is bounded by walls located at $x = \pm l_x/2$ and $y = \pm l_y/2$. The analysis is quite analogous to the work performed by Sternberg and Godyak [145] in cylindrical coordinates but with several validations and improvements enabled by the use of the *LPPic* code.

2.3.1 Equations of Ion Transport

The electron momentum conservation is just the Boltzmann equation

$$-k_B T_e \nabla n/n - e\mathbf{E} = 0 \tag{2.75}$$

It is important to note that the electron fluid velocity does not appear in this equation. The ion momentum conservation equation is projected along both x and y axis

$$m_i(v_x\partial_x + v_y\partial_y)v_x = eE_x - k_B T_i \partial_x n/n - m_i(\nu_i + \nu_{iz})v_x \tag{2.76}$$

$$m_i(v_x\partial_x + v_y\partial_y)v_y = eE_y - k_B T_i \partial_y n/n - m_i(\nu_i + \nu_{iz})v_y \tag{2.77}$$

where $\mathbf{v}$ is now the *fluid velocity of the ions*. Combined with the electron momentum equation, this leads to

$$(v_x\partial_x + v_y\partial_y)v_x/{u_B}^2 = -\partial_x n/n - v_x/D_a \tag{2.78}$$

$$(v_x\partial_x + v_y\partial_y)v_y/{u_B}^2 = -\partial_y n/n - v_y/D_a \tag{2.79}$$

where the ambipolar diffusion coefficient D_a is here ${u_B}^2/(\nu_i + \nu_{iz})$. Moreover, the 2D ion continuity equation is

$$\partial_x(nv_x) + \partial_y(nv_y) = \nu_{iz} n \tag{2.80}$$

The plasma is not ambipolar in this case and we do not need to use the electron continuity equation. Eqs. (2.78) to (2.80) form a set of 3 first order partial differential equation (PDE) for the 3 unknown variables v_x, v_y, and n. The boundary condition is fixed by the Bohm criterion. By neglecting the sheath thickness, we also assume that the ions are always accelerated perpendicularly to the walls, such that

$$\mathbf{v}\left(x = \pm\frac{l_x}{2}, y = 0\right) = \begin{pmatrix} \pm u_B \\ 0 \end{pmatrix} \tag{2.81}$$

$$\mathbf{v}\left(x = 0, y = \pm\frac{l_y}{2}\right) = \begin{pmatrix} 0 \\ \pm u_B \end{pmatrix} \tag{2.82}$$

The plasma density cannot be calculated without the power balance equation. So the solution of the model will be a density profile that can be multiplied by any constant, depending on the heating power conditions. We look for solutions by separation of variables

$$n = N n_x(x) n_y(y) \tag{2.83}$$

$$\mathbf{v} = \begin{bmatrix} v_x(x) \\ v_y(y) \end{bmatrix} \tag{2.84}$$

where n_x and n_y are arbitrary dimensionless functions of x and y respectively, and N is the plasma density at the discharge center ($x = y = 0$). The normalization implies that $n_x(0) = n_y(0) = 1$. Due to the symmetry of the system, n_x and n_y are

even functions, and v_x and v_y are odd functions, with $v_x(0) = v_y(0) = 0$. Eq. (2.80) becomes

$$v_x \frac{n_x'}{n_x} + v_x' + v_y \frac{n_y'}{n_y} + v_y' = \nu_{iz} \tag{2.85}$$

All the functions have only one variable, so the prime $'$ denotes here the derivative with respect to x for the functions that depend on x and y for the functions that depend on y. By taking the derivatives of Eq. (2.85) with respect to x and y:

$$\left(v_x \frac{n_x'}{n_x} + v_x' \right)' = 0 \tag{2.86}$$

$$\left(v_y \frac{n_y'}{n_y} + v_y' \right)' = 0 \tag{2.87}$$

We can, therefore, introduce the constants ν_x and ν_y such that

$$v_x \frac{n_x'}{n_x} + v_x' = \nu_x \tag{2.88}$$

$$v_y \frac{n_y'}{n_y} + v_y' = \nu_y \tag{2.89}$$

and

$$\nu_x + \nu_y = \nu_{iz} \tag{2.90}$$

With the assumption of Eq. (2.84), the second term of the LHS drops for Eq. (2.78) and the first term of the LHS drops for Eq. (2.79). Combined with Eqs. (2.88) and (2.89), Eqs. (2.78) and (2.79) yield two first order differential equations for v_x and v_y

$$(1 - v_x/{u_B}^2) v_x' = \nu_x + v_x^2/D_a \tag{2.91}$$

$$(1 - v_y/{u_B}^2) v_y' = \nu_y + v_y^2/D_a \tag{2.92}$$

which have the same form as the equation that describes the 1D case (Eq. (2.17)) and can be solved the same way, for uniform D_a, ν_x and ν_y:

$$\left(1 + \frac{\nu_x D_a}{{u_B}^2}\right) \arctan\left[\frac{v_x}{(\nu_x D_a)^{1/2}}\right] - \frac{(\nu_x D_a)^{1/2}}{{u_B}^2} v_x = \left(\frac{\nu_x}{D_a}\right)^{1/2} x \tag{2.93}$$

$$\left(1 + \frac{\nu_y D_a}{{u_B}^2}\right) \arctan\left[\frac{v_y}{(\nu_y D_a)^{1/2}}\right] - \frac{(\nu_y D_a)^{1/2}}{{u_B}^2} v_y = \left(\frac{\nu_y}{D_a}\right)^{1/2} y \tag{2.94}$$

2.3.2 The Temperature Equation

As in the 1D case that is summarized in Eqs. (2.34) and (2.35), the boundary conditions (Bohm criterion) impose that

$$f\left(\frac{u_B}{(\nu_x D_a)^{1/2}}\right) = \frac{u_B l_x}{2D_a} \tag{2.95}$$

$$f\left(\frac{u_B}{(\nu_y D_a)^{1/2}}\right) = \frac{u_B l_y}{2D_a} \tag{2.96}$$

and the electron temperature equation is given by Eq. (2.90):

$$\boxed{\left[f^{-1}\left(\frac{u_B l_x}{2D_a}\right)\right]^{-2} + \left[f^{-1}\left(\frac{u_B l_y}{2D_a}\right)\right]^{-2} = \frac{\nu_{iz} D_a}{{u_B}^2}} \tag{2.97}$$

The density profiles can also be integrated

$$n_x(x) = \left(1 + \frac{v_x^2}{\nu_x D_a}\right)^{-\frac{1}{2}\left(1+\frac{\nu_x D_a}{{u_B}^2}\right)} \tag{2.98}$$

$$n_y(x) = \left(1 + \frac{v_y^2}{\nu_y D_a}\right)^{-\frac{1}{2}\left(1+\frac{\nu_y D_a}{{u_B}^2}\right)} \tag{2.99}$$

As discussed before, D_a may also depend on the ionization frequency at low pressure, which makes Eq. (2.97) harder to solve, especially since it depends here on two parameters l_x and l_y.

In the low-pressure limit, the only important collision type is ionization, so $\frac{\nu_{iz} D_a}{{u_B}^2} = 1$. Let us introduce the angle θ such that

$$\tan^2\theta = l_y/l_x \tag{2.100}$$

and the variable

$$\delta = \frac{2D_a}{u_B(l_x + l_y)} \tag{2.101}$$

such that Eq. (2.97) becomes at low pressure

$$\left[f^{-1}\left(\cos^2\theta/\delta\right)\right]^{-2} + \left[f^{-1}\left(\sin^2\theta/\delta\right)\right]^{-2} = 1 \tag{2.102}$$

This equation can be inverted to give δ as a function of θ. As shown in Fig. 2.3, the solution is very well approximated by

$$\delta = \frac{\sin^2(2\theta)}{2f(\sqrt{2})} \tag{2.103}$$

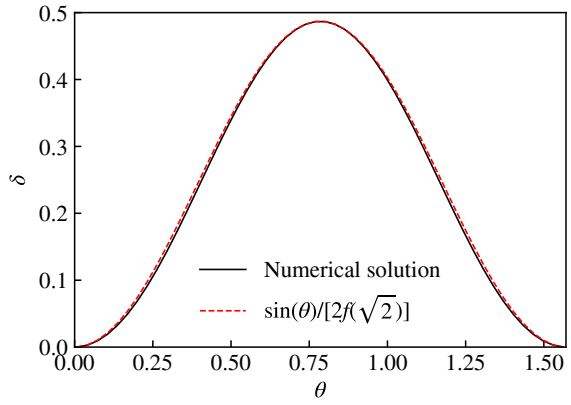

Figure 2.3: Graph of the geometrical dependence of the collisionless ambipolar diffusion coefficient. See Eqs. (2.100) and (2.101) for the definitions of the dimensionless axis.

where $f\left(\sqrt{2}\right) \approx 1.027$.

So for D_a:

$$D_a = \frac{u_B(l_x + l_y)}{\beta_{xy}} \tag{2.104}$$

where

$$\beta_{xy} = \frac{4f(\sqrt{2})}{\sin^2\left[2\arctan\left(\sqrt{l_y/l_x}\right)\right]} \approx \frac{4.11}{\sin^2\left[2\arctan\left(\sqrt{l_y/l_x}\right)\right]}\,. \tag{2.105}$$

contains the role of the aspect ratio at low pressure. The properties of the sin and arctan functions imply that $\beta_{xy} = \beta_{yx}$. Moreover, β_{xy} becomes large for large aspect ratios.

At higher pressure, the dimensions l_x and l_y do not affect the ambipolar diffusion coefficient. We hence propose the following heuristic formula

$$D_a = \frac{{u_B}^2}{\nu_i}\left[1 + \frac{u_B\beta_{xy}}{\nu_i(l_x + l_y)}\right]^{-1} \tag{2.106}$$

that matches very well the numerical solution of the model for all pressure and aspect ratios (see Fig. 2.11). This general formula is injected in Eq. (2.97), that gives directly ν_{iz} as a function of the discharge parameters, and the Bohm speed. For convenience, this solution is also approximated by

$$\nu_{iz} = \nu_i\left[\frac{\nu_i(l_x + l_y)}{\beta_{xy}u_B} + \frac{{\nu_i}^2}{\pi^2{u_B}^2(1/l_x^2 + 1/l_y^2)}\right]^{-1} \tag{2.107}$$

This heuristic formula is shown in Fig. 2.11 and compared with the numerical solution. This expression is a quite simple electron temperature equation for the 2D Cartesian system with no magnetic field.

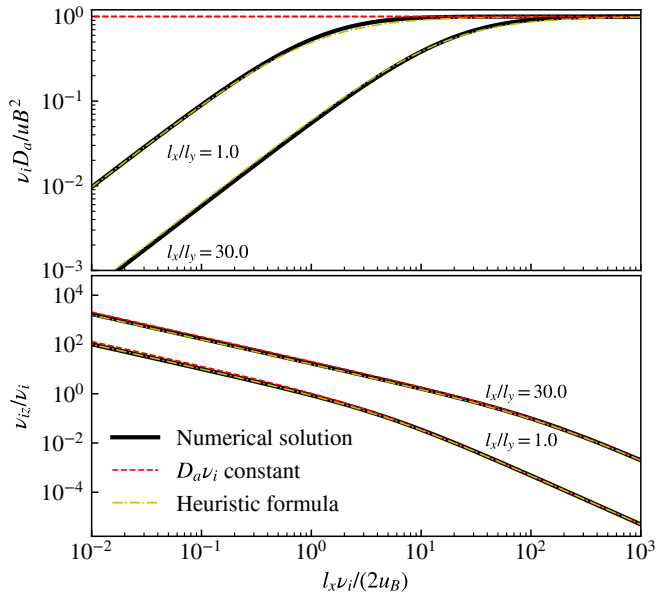

Figure 2.4: Comparison between the numerical solution, the heuristic formula, and the simple high-pressure model for the ambipolar diffusion coefficient. (a) The normalized ambipolar diffusion coefficient, (b) The normalized ionization frequency.

2.3.3 The h factor in 2D

Now that the interdependence between the x and y directions is solved thanks to the low-pressure limit of the ambipolar diffusion coefficient, we can give some useful estimates of the h factor as a function of the ion collision frequency.

First, we should notice that the ion flux collected at a wall, for example at $x = l_x/2$, is not uniform

$$\Gamma_i(l_x/2, y) = N n_{xs} n_y(y) u_B \tag{2.108}$$

where $n_{xs} = n_x(l_x/2)$ (similarly $n_{ys} = n_y(l_y/2)$) is the edge-to-center density ratio in the x direction. Therefore,

$$\int_{-l_y/2}^{l_y/2} \Gamma_i(l_x/2, y)\, dy = N n_{xs} u_B \int_{-l_y/2}^{l_y/2} n_y(y)\, dy \tag{2.109}$$

Integrating Eq. (2.89), as it was made to obtain Eq. (2.55), leads to

$$\int_{-l_y/2}^{l_y/2} \Gamma_i(l_x/2, y)\, dy = 2N {u_B}^2 n_{xs} n_{ys} / \nu_y \tag{2.110}$$

According to the definition of Eq. (1.96), in 2D Cartesian coordinates, the h factor is

$$\boxed{h_{2D} = \frac{2u_B n_{xs} n_{ys}}{l_x + l_y}\left(\frac{1}{\nu_x} + \frac{1}{\nu_y}\right)} \tag{2.111}$$

Using Eqs. (2.95) and (2.96) and the approximate formula of f^{-1},

$$\frac{1}{\nu_x} = \frac{l_x^2}{\pi^2 D_a} + \frac{3}{4}\frac{l_x}{u_B} \tag{2.112}$$

$$\frac{1}{\nu_y} = \frac{l_y^2}{\pi^2 D_a} + \frac{3}{4}\frac{l_y}{u_B} \tag{2.113}$$

Replacing D_a from Eq. (2.106),

$$\frac{1}{\nu_x} = \frac{l_x^2 \nu_i}{\pi^2 {u_B}^2} + \frac{l_x}{u_B}\left(\frac{3}{4} + \frac{\beta_{xy}}{\pi^2}\right) \tag{2.114}$$

$$\frac{1}{\nu_y} = \frac{l_y^2 \nu_i}{\pi^2 {u_B}^2} + \frac{l_y}{u_B}\left(\frac{3}{4} + \frac{\beta_{xy}}{\pi^2}\right) \tag{2.115}$$

The solutions of the 1D model can be rigorously applied to each direction x and y, provided that the ambipolar diffusion coefficient D_a is taken from the solution of the 2D electron temperature equation. Therefore,

$$n_{xs} = \left[\exp(1) + \frac{u_B l_x}{D_a} + \left(\frac{u_B l_x}{\pi D_a}\right)^2\right]^{-1/2} \tag{2.116}$$

$$n_{ys} = \left[\exp(1) + \frac{u_B l_y}{D_a} + \left(\frac{u_B l_y}{\pi D_a}\right)^2\right]^{-1/2} \tag{2.117}$$

Replacing again D_a,

$$n_{xs} = \left[\exp(1) + \frac{\beta_{xy} l_x^2}{(l_x + l_y)^2}\left(1 + \beta_{xy} + \frac{l_y}{l_x}\right) + \frac{\nu_i l_x^2}{u_B (l_x + l_y)}\left(1 + \frac{2\beta_{xy}}{\pi^2} + \frac{l_y}{l_x}\right) + \frac{{\nu_i}^2 l_x^2}{\pi^2 {u_B}^2}\right]^{-1/2} \tag{2.118}$$

$$n_{ys} = \left[\exp(1) + \frac{\beta_{xy} l_y^2}{(l_x + l_y)^2}\left(1 + \beta_{xy} + \frac{l_x}{l_y}\right) + \frac{\nu_i l_y^2}{u_B (l_x + l_y)}\left(1 + \frac{2\beta_{xy}}{\pi^2} + \frac{l_x}{l_y}\right) + \frac{{\nu_i}^2 l_y^2}{\pi^2 {u_B}^2}\right]^{-1/2} \tag{2.119}$$

2.3.4 Comparison with 2D PIC Simulation

Input Parameters

In order to validate this new 2D model, we run several PIC simulations for a rectangular argon discharge of an ICP with a uniform heating electric field, corresponding to the configuration of Fig. 1.6(a). In order to satisfy quasineutrality over most of the simulation domain, the Debye length, that is supposed to be a fraction of the sheath thickness [100], should be much smaller than the size of the discharge. Hence, the aim is to simulate a plasma at reasonably high density, typically higher than $10^{16}\,\mathrm{m}^{-3}$. As explained in the discussion relative to global models, the density in a weakly ionized plasma is typically controlled by the absorbed power, which is an input of the simulation. It is here fixed to $19.1\,\mathrm{kW/m}^{-3}$. Since we are not focusing on the heating process but more on the transport, this parameter is kept constant. The mesh has between 4×10^4 and 4×10^5 cells. The most relevant input parameters are provided in Table 2.1.

Physical parameters			
Gas type		Ar	
Discharge size in x direction	l_x	7.5 – 75	mm
Discharge size in y direction	l_y	30	mm
Neutral pressure	p	0.3 – 100	mTorr
Neutral density	n_g	$9.6 \times 10^{18} - 3.2 \times 10^{21}$	m^{-3}
Neutral temperature	T_g	0.026	eV
Frequency	f_{RF}	13.56	MHz
Power density	w	19.1	kW/m^3
Physical time of the simulation	$t_{\text{simulation}}$	12 – 48	µs
Averaging time	t_{average}	0.03 – 0.09	µs
Initial conditions			
Plasma density	$n_e = n_i$	1×10^{15}	m^{-3}
Electron temperature	T_e	4.0	eV
Ion temperature	T_i [eV]	0.026	eV
Particles per cell	$N_{\text{part./cell}}$	100	
Heating electric field amplitude	E_0	1.0	kV/m
Numerical parameters			
Cell size	Δx	75	µm
Time step	Δt	$1 \times 10^{-11} - 3 \times 10^{-11}$	s
Steps to execute	$N_{simulation}$	> 450 000	
Steps to average	N_{average}	3 000	
Weighting factor	q_f	$1.5 \times 10^6 - 3.75 \times 10^6$	m^{-1}
Number of CPU	N_{CPU}	200 – 400	
Initial number of super-particles	$N_{part,0}$	$1.5 \times 10^5 - 1.2 \times 10^6$	

Table 2.1: Main physical and numerical input parameters of the 2D PIC simulation.

Verification of the Assumptions of the Model

We summarize here the assumptions made in the model and verify it against the PIC simulation results.

1. The sum of the electron temperature and the ion temperature is the same everywhere in the plasma bulk.

2. The plasma is quasineutral in the region where the ion speed is lower than the Bohm speed.

3. The plasma density and the velocity profiles can be described by separation of variables (see Eqs. (2.83) and (2.84))

4. The sheath thickness is small.

5. Electron and ion collision frequencies are uniform in the bulk plasma.

First, the pressure is varied from 0.3 to 100 mTorr for a square geometry where $l_x = l_y = 3$ cm. The electron and ion density profiles are plotted in Fig. 2.5(a). The electrons and the ions have almost the same densities, except in the sheath region which is localized very close to the walls. In this region, the electron density becomes lower than the ion density, as predicted by the classical sheath theory (see Section 1.5.1). The quasineutral assumption seems reasonable for the bulk plasma region. As shown in Fig. 2.5(b), the plasma potential, which is set to zero at the walls, decreases from the center to the edge, and it accelerates the ions.

Fig. 2.6 shows the region of the discharge close to the wall for $y = l_y/2$. The plasma is quasineutral with a good approximation up to the location were the ions reach the Bohm speed. The Bohm speed is computed at each cell using the local electron temperature. The electron fluid velocity is more sensitive to the numerical noise and was here averaged over 10 cells around $y = l_y/2$. The quantities shown in this figure are averaged over 8 µs at steady state. The sheath thickness is approximately $s = 2$ mm in this case. When the model equations are applied, the dimension of the plasma should not be $l_x \times l_y$ but $(l_x - 2s) \times (l_y - 2s)$. In Fig. 2.7 we aim at justifying the assumption made in the model that the plasma density could be described by variable separation. Here, we compute the ion density along both slices $x = l_x/2$ and $y = l_y/2$ and reconstruct a 2D map as a convoluted solution

$$n_{conv} = \frac{n\left(x, \frac{l_y}{2}\right) n\left(\frac{l_x}{2}, y\right)}{n\left(\frac{l_x}{2}, \frac{l_y}{2}\right)} \tag{2.120}$$

The convoluted solution and the real solution should, of course, be equal in the slices $x = l_x/2$ and $y = l_y/2$. In Fig. 2.7, the convoluted solution is compared with the real solution at 1.5 mm from the wall, near the sheath edge, where the discrepancy

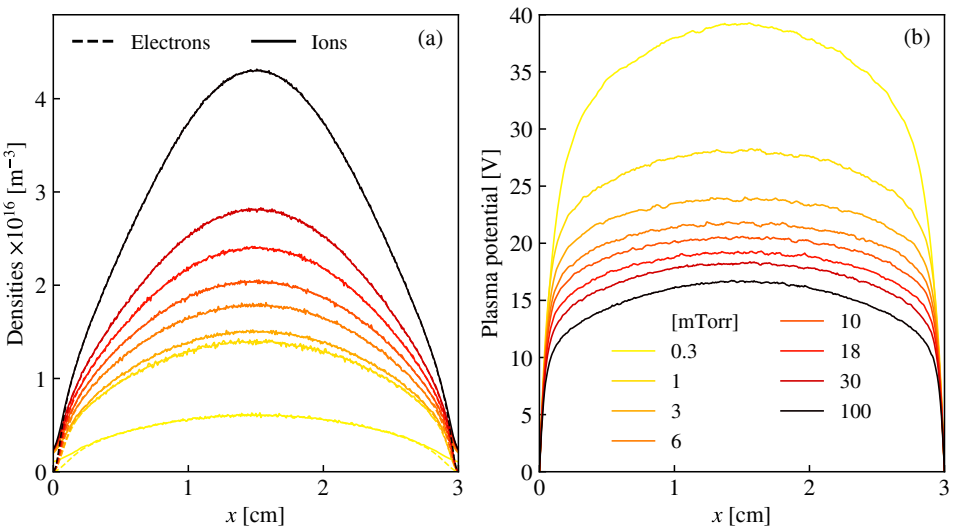

Figure 2.5: Properties of the plasma at steady state for a square box (3×3 cm), at $y = l_y/2$, and 19.1 kW/m^3 of absorbed power density. The pressure is varied from 0.3 to 100 mTorr. (a) Electron and ion densities, (b) plasma potential.

is the largest (we are not interested in the sheath behavior as the model is quasineutral). The convoluted solution tends to underestimate the density at the sheath edge slightly but in general, shows a very good agreement with the real solution.

The temperature profiles are analyzed in Fig. 2.8 at low pressure (0.3 mTorr) and relatively high pressure (100 mTor). The ion temperature was multiplied by ten to scale with the electron temperature – it always remains below the electron temperature. The sum of the two temperatures is approximately constant in the plasma bulk, and the isothermal assumption seems reasonable. The model could perhaps be improved by adding a polytropic coefficient γ, as it was done in the description of the sheath in Section 1.5.1, but the isothermal assumption is much more accurate in the bulk than in the sheath. At high pressure, the ion temperature reaches 0.6 eV near the wall because a large part of the directional kinetic energy of the ions gained by the sheath electric field is transfered to thermal energy through collisions. This effect is also visible at low pressure, but less acute.

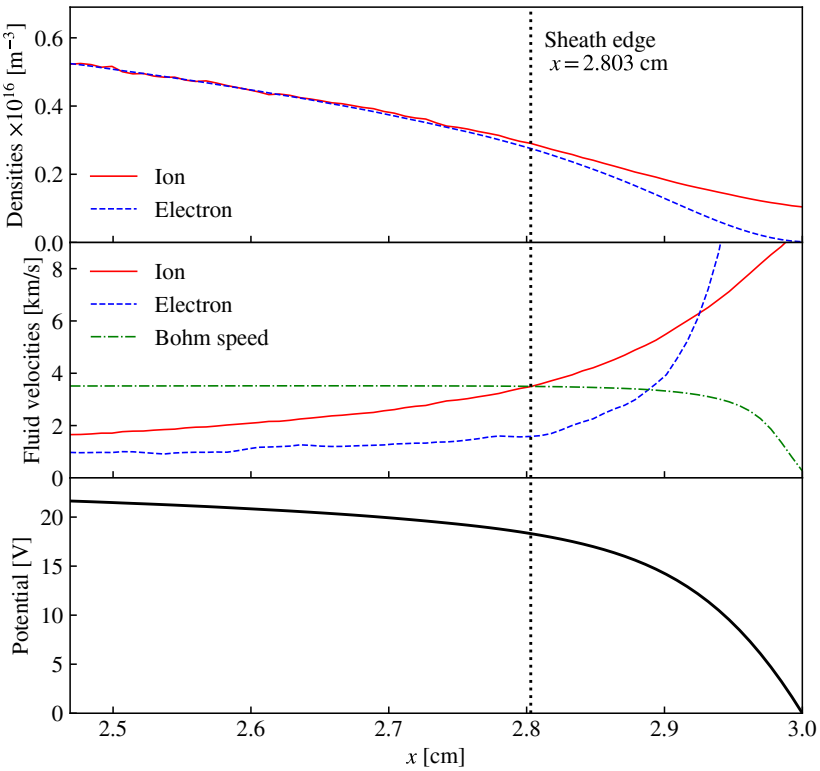

Figure 2.6: Sheath profiles at $y = l_y/2$ for a square (3×3 cm) discharge at 3 mTorr. In this case, the power is 9.6 kW/m^3.

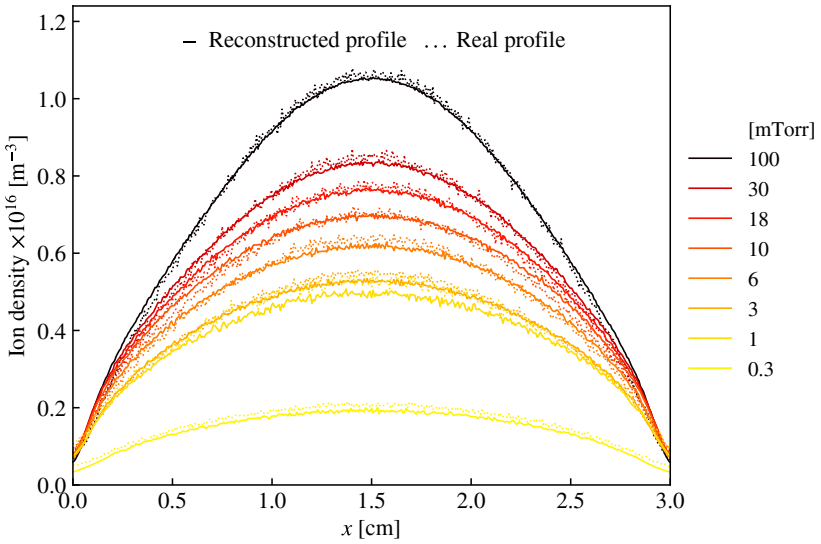

Figure 2.7: Plasma density profiles at steady state for discharges between 0.3 and 100 mTorr, at 1.5 mm from the wall. The real simulation profiles (solid line) of ion density are compared with the convoluted profiles (dotted line). The simulation conditions are: 3×3 cm, at 19.1 kW/m^3.

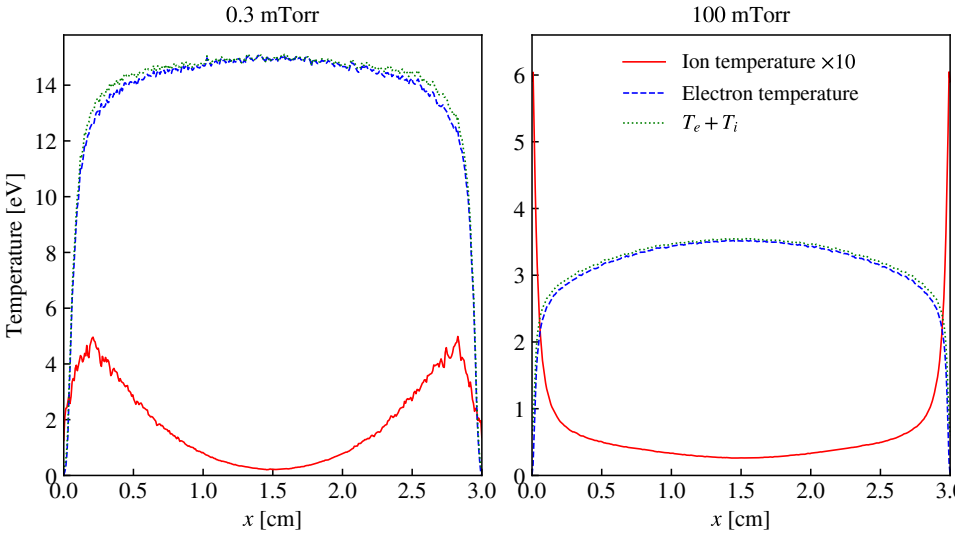

Figure 2.8: Electron and ion temperature profiles at $y = l_y/2$ for a 3×3 cm discharge at 0.3 mTorr (left) and 100 mTorr (right) of gas pressure. The ion temperature was multiplied by a factor ten to scale with the electron temperature.

A Parametric Study with Pressure

We now investigate the role of pressure on the discharge properties in order to verify the solutions of the model. The ions have more difficulty to reach the walls at higher pressure due to collisions with neutrals. The losses are hence reduced, and the electron temperature needed to sustain the discharge through ionization decreases, as predicted by the theory. The quantity measured in the PIC simulation is based on the mean energy of the electrons inside the simulation domain, including the flow energy, multiplied by 2/3. This effective electron temperature is hence slightly higher than the kinetic temperature of Eq. (1.18). Since the electron fluid velocity is neglected in the fluid model, we will compare the electron temperature of the fluid model with this effective electron temperature measured in the PIC simulation. The effective electron temperature drops from 18.7 eV at 0.3 mTorr to 3.21 eV at 100 mTorr. Below 0.3 mTorr, the discharge was very hard to sustain and would require a smaller time step to preserve the CFL condition for the energetic electrons. Since the plasma is better confined at high pressure for the same injected power, the plasma density rises at high pressure. This result matches the general picture that was established in the section on global models.

To allow comparison with theory, we need to choose the ion-neutral collision frequency. The easiest way the evaluate the typical ion-neutral momentum transfer collision frequency is to assume a constant CS (10^{-18} m^2 for argon) and multiply it by the mean thermal velocity:

$$\nu_i = n_g \sigma_i \overline{v}_i \tag{2.121}$$

where

$$\overline{v}_i = \left(\frac{8 k_B T_{i0}}{\pi m_i} \right)^{1/2} \tag{2.122}$$

Here, $T_{i0} = 300$ K is the injection ion temperature in the PIC simulation, which is also the ion temperature measured at the discharge center. However, Fig. 2.8 shows that the ion temperature increases away from the discharge center. Moreover, the ions are accelerated, such that their fluid velocity also has an important role in the mean velocity (see Eq. (2.25)). The typical ion velocity is therefore significantly affected by the electric field, as they have to reach the Bohm speed at the sheath edge. At high pressure, the acceleration is very localized at the sheath edge, but at low pressures, it is much smoother, such that the typical ion fluid velocity in the bulk is a fraction of the Bohm speed at low pressure. We have proposed [105] to correct this effect by introducing a dependence of the typical ion velocity $v_{i,ref}$ on the Bohm speed

$$\nu_i = n_g \sigma_i v_{i,ref} \tag{2.123}$$

The reference velocity should be typically $\overline{v}_i$ at high pressure where the ion energy is dominated by the thermal motion, and of the order of $u_B/2$ at low pressures where most of the ion energy is directional (towards the wall). We chose

$$v_{i,ref} = \overline{v}_i + b(\alpha) u_B/2 \tag{2.124}$$

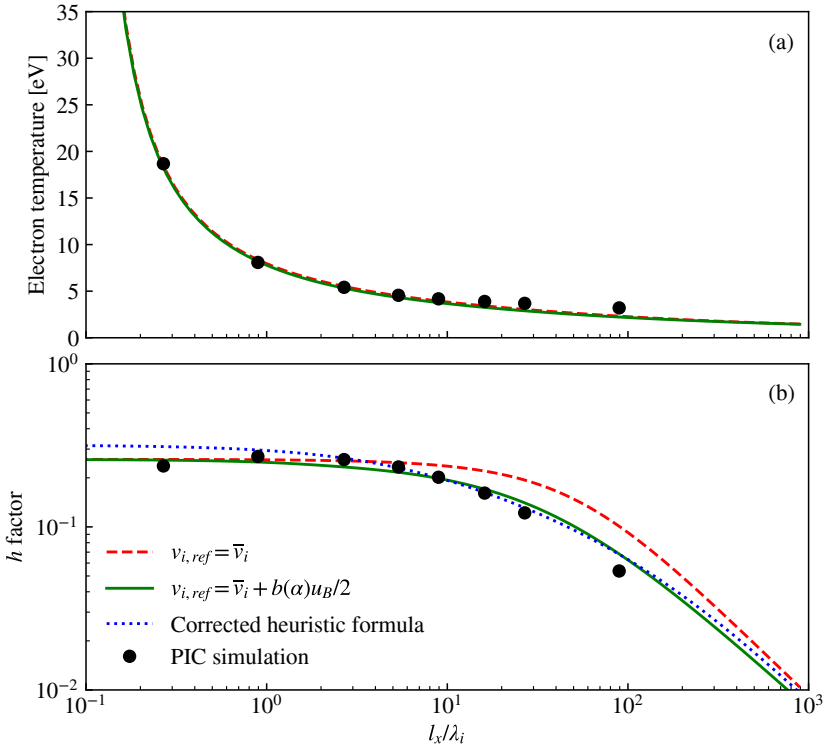

Figure 2.9: Parametric study with pressure varying from 0.3 to 100 mTorr for a 3×3 cm argon discharge. (a) Electron temperature. (b) h factor. The PIC simulation results (black circles) are compared with the solutions of the fluid model, with Eq. (2.121) (red dashed line) and Eq. (2.124) (solid green line), and the heuristic formula given by Eq. (2.130).

where $\alpha = 4{\lambda_i}^2/(l_x l_y)$ is inversely proportional to the pressure squared, and

$$b(\alpha) = \tanh^{0.2}(\alpha) \tag{2.125}$$

satisfies the conditions $b(0) = 0$ and $\lim_{\alpha\to\infty} b(\alpha) = 1$. By this means, do not need to solve the non-linear equation where Eq. (2.25) is taken into account, while keeping a good prediction capability. The model equations can also be used with PIC simulation or experimental data of the mean ion energy, but the solution would have to be numerical in this case.

In Fig. 2.9, the electron temperature and the h factor are plotted against the inverse Knudsen number in the x direction l_x/λ_i, which is proportional to the pressure. Here, l_x is fixed to 3 cm, and the ion mean free path is

$$\lambda_i = (\sigma_i n_g)^{-1} \tag{2.126}$$

As shown in Fig. 2.9(a) the electron temperature is very well predicted by the model and the choice for the ion collision frequency does not play a major role. There is

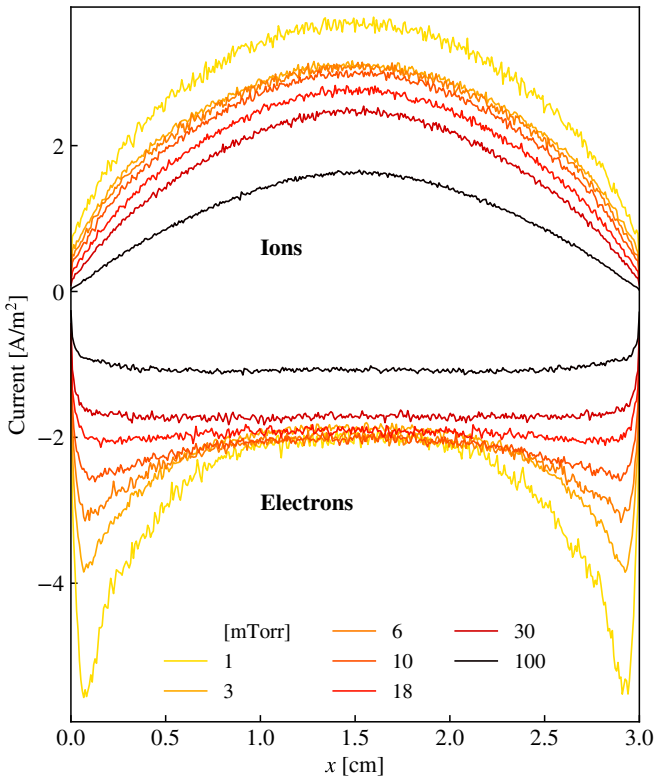

Figure 2.10: Electron (bottom, negative) and ion (top positive) currents collected at the bottom wall ($y = 0$) of the simulation domain for simulation cases between 1 and 100 mTorr.

however a significant discrepancy at high pressure, probably because the isothermal assumption is less valid at pressures of the order of 100 mTorr, see Fig. 2.8. The h factor is not very well predicted by the model with $v_{i,ref} = \overline{v}_i$ for pressures higher than 10 mTorr because the ion collision frequency is predicted poorly. The low-pressure regime is correctly described because it corresponds to a collisionless model where the only momentum loss in the ion momentum conservation equation comes from the newly created ions, and is hence proportional to ν_{iz} and not ν_i anymore. Using Eq. (2.124) yields good prediction of the h factor.

The heuristic formula proposed by Chabert and Braithwaite [31] (Eq. (2.56)) can be corrected to take into account the first order corrections induced by the 2D geometry. The correction factor essentially depends on the mean density profile in the direction perpendicular to the ion velocity vector. At high pressure, as in the 1D case, the density profile has a cosine shape in both directions, such that the mean normalized density profile is $2/\pi$. The corrected heuristic formulas hence become

$$h_{L,heur,x} = 0.55 \left[3 + 0.5\frac{l_y}{\lambda_i} + 0.2\frac{T_i}{T_e}\left(\frac{l_y}{\lambda_i}\right)^2 \right]^{-1/2} \tag{2.127}$$

$$h_{L,heur,y} = 0.55 \left[3 + 0.5\frac{l_x}{\lambda_i} + 0.2\frac{T_i}{T_e}\left(\frac{l_x}{\lambda_i}\right)^2 \right]^{-1/2} \tag{2.128}$$

where $0.55 \approx (2/\pi) \times 0.86$. It should be noted that $h_{L,heur,x}$ – which is the h factor relative to the flux of ions collected on $y = \pm l_y/2$ – depends on l_y, and not l_x. The global heuristic h factor is then

$$h_{2D,heur} = \frac{l_x h_{L,heur,x} + l_y h_{L,heur,y}}{l_x + l_y} \tag{2.129}$$

For a square, ($l_x = l_y = l$)

$$h_{2D,heur} = 0.55 \left[3 + 0.5\frac{l}{\lambda_i} + 0.2\frac{T_i}{T_e}\left(\frac{l}{\lambda_i}\right)^2 \right]^{-1/2} . \tag{2.130}$$

This formula was also compared with the PIC simulation results and the solutions of the model in Fig. 2.9. It shows a good agreement for the whole range of pressures investigated. In Eqs. (2.127) and (2.128), the electron temperature is the solution of Eq. (2.107).

The local currents collected at the walls of the PIC simulation domain are plotted in Fig. 2.10. The discharge is clearly not ambipolar as the electron and ion fluxes differ very significantly. The electrons tend to move towards low electrostatic potential regions, while the ions are accelerated straight to the walls. The profile for the ion flux resembles the density profile in the center of the discharge. On the contrary, the electron current profile is flatter at high pressure, where it reminds of the plasma potential profile, and features a minimum at the center for pressures below 18 mTorr.

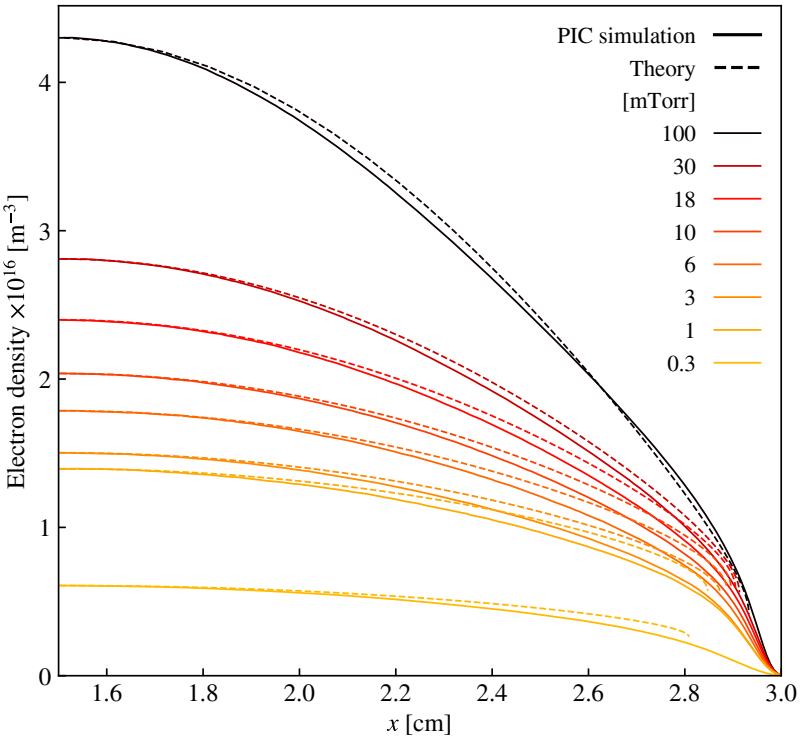

Figure 2.11: Comparison between the simulation results and the theoretical solution with predicted electron temperature and profiles. The electron density is plotted at $y = l_y/2$ of a square discharge with pressure varying between 0.3 and 100 mTorr.

At low pressures, the electron current has very sharp peaks near the corner of the simulation domain. However, the spatially integrated electron and ion currents are equal, which is a necessary condition for the steady state.

We noted that the h factor determined by PIC simulation slightly decreases from 1 mTorr to 0.3 mTorr. At low pressure, the EEDF is strongly anisotropic, which might affect the sheath formation and hence the ion flux.

A Parametric Study with Dimension l_x

We now perform a parametric study with the aspect ratio while keeping the pressure fixed to 10 mTorr. The size l_y is set to 3 cm and the size l_x is varied from 0.75 to 7.5 cm. The density profiles are plotted in Fig. 2.13. The density generally increases with the size of the discharge. In the case where $l_x = 0.75$ cm, the plasma potential is not uniform across y such that quasineutrality is not satisfied anymore in most of the simulation domain. The sheath dimension becomes of the same order of magnitude as the discharge size, which gives the concave shape to the electron density profile at $l_x = 0.75$ cm in Fig. 2.13(a). The quasineutral model does not seem to strictly apply for aspect ratios greater than 4. However, as the aspect ratio increases,

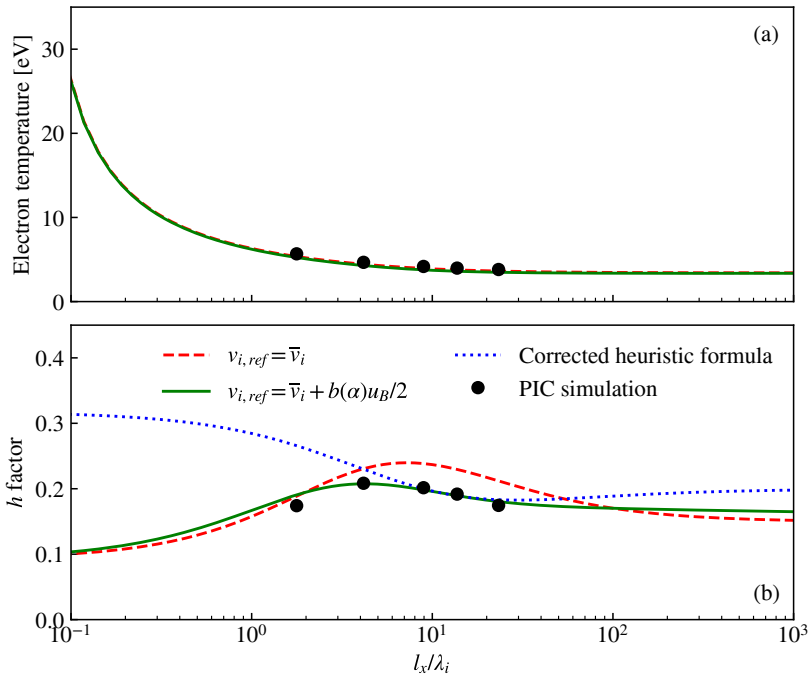

Figure 2.12: Electron temperature (a) and h factor (b) investigated for different discharge geometries. l_y is fixed to 3 cm ,and l_x varied from 0.75 to 7.5 cm. The pressure is 10 mTorr. The PIC simulation results (black circles) are compared with the solutions of the fluid model, with Eq. (2.121) (red dashed line) and Eq. (2.124) (solid green line), and the heuristic formula given by Eq. (2.129).

the 2D effects become minor and the plasma can essentially be described with the single x direction. As confirmed by the good agreements found in Fig. 2.9, the 2D quasineutral model derived above accounts for the large aspect ratio limit correctly.

As emphasized by the ratio l/λ_i that characterizes the properties of a non-magnetized 1D discharge, increasing the size of the system should play approximately the same role as increasing the pressure, such that the electron temperature should decrease for larger systems. Fig. 2.12(a) shows that this is also generally true for a 2D system. The h factor measured from the PIC simulation is compared with the solutions of the model and the corrected heuristic formula described in the previous paragraph in Fig. 2.12(b). For l_x/λ_i higher than 4, the h factor decreases with the system size and the three formulas are reasonably accurate. However, below typically $l_x/\lambda_i = 4$, and for an aspect ratio higher than 2, the effect of the coupling of x and y direction through the β_{xy} factor becomes important and the h factor decreases again. This effect seems to be well captured by the model, both with $v_{i,ref} = \overline{v}_i$ and $v_{i,ref} = \overline{v}_i + b(\alpha)u_B/2$, but the corrected heuristic formula does not show this trend, although the order of magnitude seems correct for all the conditions investigated.

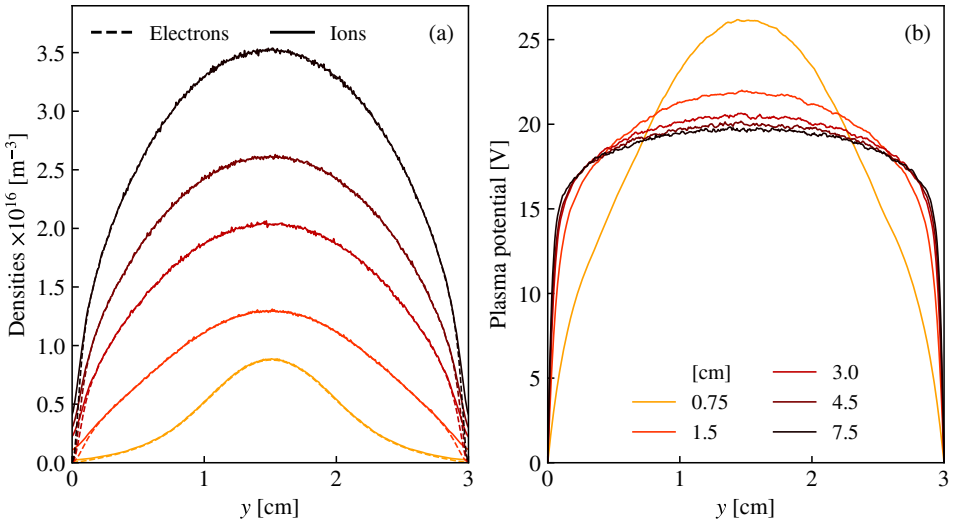

Figure 2.13: Properties of a 10 mTorr plasma at steady state at $x = l_x/2$, and 19.1 kW of absorbed power. l_y is fixed to 3 cm and l_x is varied between 0.75 and 7.5 cm. (a) Electron and ion densities, (b) plasma potential.

2.3.5 Discussion

The ambipolar assumption is not necessary to derive the equation of the plasma transport as long as electron inertia and collisions are neglected. *A posteriori*, we can verify if the ion and the electron fluxes are equal. Fig. 2.10 has already shown that this is not the case for the particles collected at the wall. We now examine the ambipolar nature of the plasma outside of the sheath. Therefore, Fig. 2.14 presents the electron and ion currents in the bulk plasma. We can observe the same patterns as in the curve of the currents collected at the walls of the discharge: while the ions are going straight to the walls with short streamlines, the electrons tend to first escape towards the corners where the potential is higher. They still enter the sheath with a velocity vector that is almost everywhere perpendicular to the sheath surface.

The assumption of variable separation can also be questioned for large aspect ratio discharges. Fig. 2.15(a) and (b) show the profiles of the electron and ion density along the x and y axis respectively for a 10 mTorr argon discharge with $l_x = 0.75$ cm and $l_y = 3$ cm. While the plasma is quasineutral in the main direction (y), the space charge sheaths are quite large in the x direction. It seems that the larger the dimension, in a given axis, the smaller the sheath. The space charge sheaths are relatively large and cover almost half of the discharge. This observation affects very much the reconstructed plasma density profiles shown in Fig. 2.15(c) and (d). The reconstructed profiles seem to match the electron density (in red) quite accurately, but the assumption of variable separation seems to break up for the ions. A more accurate model of this type of plasma would require to solve the Poisson's equation in 2D, as

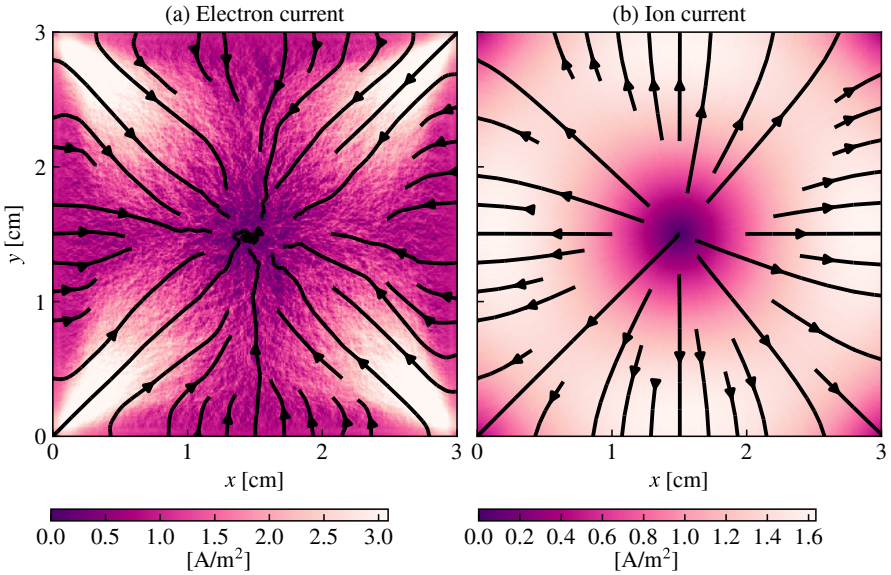

Figure 2.14: Maps of the norm of the electric current generated by electron (a) and ion (b) motion, for a pressure of 3 mTorr. The arrows represent the streamlines.

it is done in the PIC simulation.

The limitation of the model being acknowledged, it is probably of some interest to mention the 3D generalization of the method developed in this section. If one assumes that the variable separation method is applicable in 3D, the model equations can be solved exactly the same way and provide a 3D electron temperature equation for an isothermal, quasineutral, electropositive plasma bounded by space charge sheaths with no magnetic field:

$$\boxed{\left[f^{-1}\left(\frac{u_B l_x}{2D_a}\right)\right]^{-2} + \left[f^{-1}\left(\frac{u_B l_y}{2D_a}\right)\right]^{-2} + \left[f^{-1}\left(\frac{u_B l_z}{2D_a}\right)\right]^{-2} = \frac{\nu_{iz} D_a}{{u_B}^2}} \quad (2.131)$$

which is a generalization of Eq. (2.97). Again, this equation can be solved if some assumptions are made about the ambipolar diffusion coefficient D_a. For inverse Knudsen number l_x/λ_i higher than 1, and if the aspect ratio is not too large. The 2D analysis suggests that $D_a = {u_B}^2/\nu_i$ is a good approximation. It would be however useful to perform some probe measurements to check these predictions experimentally.

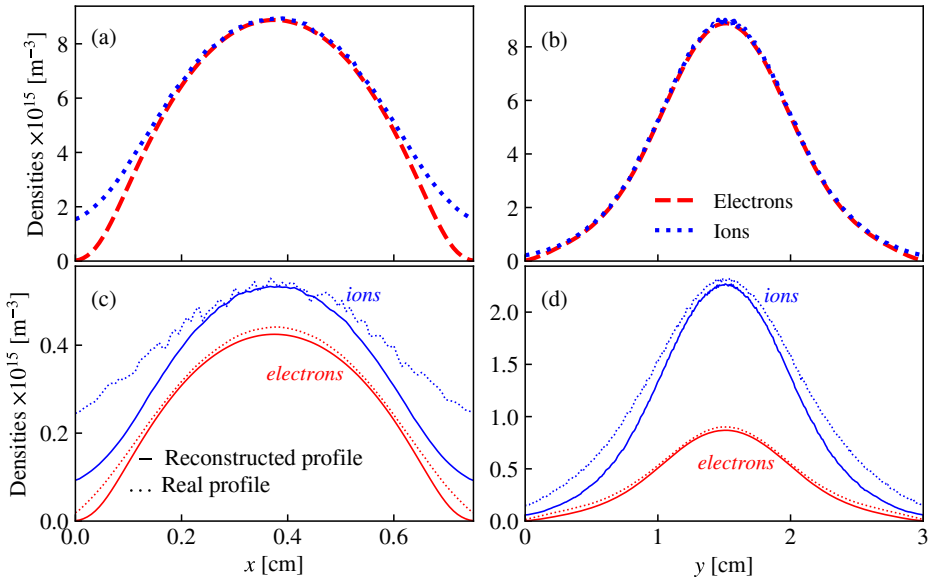

Figure 2.15: Plasma density profiles for a discharge at 10 mTorr with $l_x = 3$ cm and $l_y = 0.75$ cm. The following slices are shown: (a) $y = l_y/2$, (b) $x = l_x/2$, (c) $y = 0.052$ cm, (d) $x = 0.225$ cm. In (c) and (d), the real ion and electron density profiles (dotted lines) are compared with the reconstructed ones (solid lines) $n(x, l_y/2)n(l_x/2, y)/n(l_x/2, l_y/2)$.

Summary

In this chapter, we have presented a set of isothermal models for quasineutral, weakly ionized plasmas. In 1D, the discharge is ambipolar and analytical solutions can always be found to these models, under the assumption of constant ion mobility. The discharge behavior is parametrized by the ambipolar diffusion coefficient, the electron impact ionization frequency, and the Bohm sheath criterion. Analytical formulas of the electric field at the sheath edge are provided.

In 2D, the discharge is non-ambipolar and no general solution exists. However, assuming a Boltzmann electron distribution, a solution can be found by variable separation when no magnetic field is applied. In particular, the effect of geometry on the ambipolar diffusion coefficient at low pressures is estimated correctly. Multiple 2D PIC simulations of a non-magnetized argon discharge were performed for pressures between 0.3 and 100 mTorr and l_x/l_y ratios between 0.25 and 2.5. The PIC simulation results are compared with the theory using two different models for the ion-neutral collision frequency. (i) If the ion-neutral collision frequency is driven by the thermal ion speed, then the electron temperature of the discharge is correctly predicted but the h factor is overestimated by a factor two in the intermediate pressure range. (ii) If the ion-neutral frequency also accounts for the ion acceleration, the correct discharge h factor can be recovered. We proposed an empirical formula for the ion-neutral collision frequency based on the assumptions that the typical ion velocity should be close to the thermal speed at high pressure, and of the order of $u_B/2$ in the free fall regime at low pressure.

For large aspect ratios, the sheaths become relatively larger along the smaller dimension, which is one of the main limitations of the model because the quasineutral assumption becomes no longer valid. Finally, the effects of the magnetic fields on the 2D plasma transport involves other phenomena that will be explained in the next chapter.

Chapter 3

CROSS-FIELD TRANSPORT IN A UNIFORM MAGNETIC FIELD

Contents

This chapter contains the core of the theoretical results of this work. When a magnetic field perpendicular to the simulation plane is added to the simulation setup, plasma drifts and instabilities are observed. Dispersion relations coming from uniform and non-uniform fluid plasma theories of linear perturbations are compared with the PIC simulation data. We investigate the onset of the

instability with pressure and magnetic field and propose a theory of instability-enhanced plasma transport.

3.1 Two-dimensional PIC Simulation of a Magnetized Plasma Column

3.1.1 Context

The magnetized plasma column is a classic of plasma physics. Experimentally, several methods exist to sustain a magnetized plasma column. Among them, one can cite the Penning discharge that features an external electron source, or inductive discharges. An experimental study on the combination of both plasma generation techniques was recently performed by V. Desangles [51]. Our work focuses on ICP generation. In a magnetized plasma column, the length of the axis is typically larger than the radial dimensions, such that 2D simulations in the plane perpendicular to the main axis are well-suited to the geometry. The magnetic field is along the main axis of the magnetized plasma column (z).

Several theoretical and experimental studies have investigated the magnetized LTP column. Fruchtman *et al.* [59] performed an experimental study of the 2D (radial-axial) transport in a cylindrical discharge. In the configuration of this article, the ion losses along the axis (and along the magnetic field lines) are thought to be dominant. The classical fluid model developed does not show a good agreement with the experiments. When an empirical Bohm mobility is included, the model predictions yield a correct order of magnitude for the plasma density, but still with up to 100% discrepancy with the experimental results at magnetic fields between 10 and 20 mT. Curreli and Chen [45] provided a comprehensive review of the historical studies on cross-field diffusion. The classical theories are presented together with their limits, and the qualitative effects of the resistive drift wave instability are described. The resistive drift instability can be triggered by collisions in systems where the axial dimension is extremely long or where the magnetic surfaces are closed, as shown already by Birdsall in 1953 [15]. However,

- the conditions needed for collisions to trigger an instability are not identified in the literature.
- Moreover, few theories were able to quantify the corresponding instability-enhanced transport.

The main results of this chapter concerning the resistive drift instability were published in Lucken *et al.* (Physics of Plasmas, 2019) [103], and the results concerning the new instability-enhanced transport model were submitted to Plasma Sources Science and Technology Journal (PSST) journal [108].

3.1.2 Simulation Parameters

In our configuration, the CS of the magnetized plasma column is a square that has the same dimensions as the system that was described in the previous chapter. The walls remain conductive, and we keep the same CS set for argon as previously. The simulation parameters used for the results presented in this chapter are reported in Table 3.1. Most of the runs were performed on 220 CPU and lasted between 12 and 24 hours on the OCCIGEN machine (CINES, Montpellier, France) so the parallel capability of the *LPPic* code is fully utilized.

The typical lengths and frequencies that characterize the simulation conditions are summarized in Tables 3.2 and 3.3. The ion mean free path is a fraction of the size of the discharge, which is a characteristic of intermediate pressure regimes. The Larmor radius for the ions thermalized at 300 K can be as low as 5 mm at 40 mT. The typical ion speed, however, increases away from the discharge center, both due to ion collisional heating, and ion flow acceleration, in a similar fashion as in the non-magnetized case. These effects cause the typical ion Larmor radius to increase as well. In general, the ion mean free path is not smaller than the size of the discharge and can often be neglected. In most of the simulation runs, the Lorentz force on the ions is neglected. Some tests were performed with magnetized ions as well, with minor effects on the discharge properties.

3.1.3 Description of the Steady State

We have seen in the 1D model described in Chapter 2 that a permanent magnetic field perpendicular to the direction of the transport can considerably confine the plasma, and hence reduce the wall losses. The magnetic field is, however, known for generating plasma instabilities that can, in turn, influence the plasma transport. There are hence two time-scales to be considered. The larger time-scale is the one that corresponds to the equilibrium observed in experiments. At this time-scale, for each value of the magnetic field, one can define the mean values of the plasma properties, for example, ϕ, n_e, n_i, $\mathbf{\Gamma}_e$, $\mathbf{\Gamma}_i$, T_e and T_i, at each position in space. On the shorter time-scale, these properties may fluctuate with a wide range of frequencies, and with more or less well defined spatial structures. When only the longer time-scale is considered, and for reasonable values of the magnetic field (this will be specified later), some of the discharge characteristics have qualitatively the same aspect as the non-magnetized equilibrium. For example, the discharge domain can still be split into a quasineutral region near the center, and a sheath region near the wall where the electron density becomes lower than the ion density. As in the non-magnetized case, the ion and electron densities decrease from the center to the walls, and the electron temperature is almost uniform in the plasma bulk and decreases significantly in the sheath. The mean plasma potential also decreases smoothly from the center to the walls, which indicates that the space charge always remains positive (on average).

Physical parameters			
Gas type		Ar	
Discharge size in x direction	l_x	30	mm
Discharge size in y direction	l_y	30	mm
Neutral pressure	p	3.0, 6.0, 12.0	mTorr
Transverse magnetic field	B	0 – 40	mT
Neutral density	n_g	$0.96 \times 10^{20} - 3.83 \times 10^{20}$	m^{-3}
Neutral temperature	T_g	0.026	eV
Frequency	f_{RF}	13.56	MHz
Power density	w	9.6	kW/m^3
Physical time of the simulation	$t_{\text{simulation}}$	27 – 98	µs
Averaging time	t_{average}	0.033 – 0.099	µs
Initial conditions			
Plasma density	$n_e = n_i$	1×10^{15}	m^{-3}
Electron temperature	T_e	4.0	eV
Ion temperature	T_i [eV]	0.026	eV
Particles per cell	$N_{\text{part./cell}}$	7 – 400	
Heating electric field amplitude	E_0	0.1 – 1	kV/m
Numerical parameters			
Cell size	Δx	75	µm
Time step	Δt	3.3×10^{-11}	s
Steps to execute	$N_{simulation}$	> 818 000	
Steps to average	N_{average}	1 000 – 3 000	
Weighting factor	q_f	$2.53 \times 10^6 - 1.05 \times 10^7$	m^{-1}
Number of CPU	N_{CPU}	220	
Initial number of super-particles	$N_{part,0}$	$8 \times 10^6 - 3.2 \times 10^7$	

Table 3.1: Main physical and numerical input parameters for the parametric study in pressure and magnetic field of the magnetized plasma column.

Lengths		[mm]
Typical wavelength	λ	$0.6 - 3$
Ion Debye length	λ_{Di}	$7 - 14 \times 10^{-3}$
Ion mean free path	λ_i	$2.6 - 10$
Thermal ion Larmor radius	ρ_{Li}	$5 - \infty$
Electron Debye length	λ_{De}	$0.08 - 0.2$
Electron mean free path (elastic)	λ_e	$30 - 120$
Thermal electron Larmor radius	ρ_{Le}	$0.4 - \infty$
Discharge sizes	$l_x = l_y$	30
Cell size	dX	0.075

Table 3.2: Characteristic lengths of the system, in mm.

Frequencies		[Hz]
Drift wave	$\omega/2\pi$	$1 - 10 \times 10^6$
Electron impact ionization	ν_{iz}	$1 - 7 \times 10^4$
Ion collision	ν_i	$1 - 4 \times 10^4$
Ion cyclotron	$\omega_{ci}/2\pi$	$0 - 8 \times 10^3$
Ion plasma	$\omega_{pi}/2\pi$	$0.5 - 1 \times 10^7$
Electron elastic collision	ν_e	$0.5 - 2 \times 10^7$
Electron cyclotron	$\omega_{ce}/2\pi$	$0 - 1 \times 10^9$
Electron plasma	$\omega_{pe}/2\pi$	$1 - 2 \times 10^9$
RF heating antenna	f_{RF}	1.356×10^7
Sampling frequency	$1/(N_A dT)$	$0.3 - 1 \times 10^7$
Time resolution	$1/dT$	3×10^{10}

Table 3.3: Characteristic frequencies of the system, in Hz.

In the simulations performed in this chapter, instabilities in the range of 1 to 5 MHz were observed. The two time-scales that are investigated are hence typically 50 ns for the shorter one and 10 µs for the longer one. Fig. 3.1 shows the maps of the electron density and the electron current for a run at 3 mTorr of pressure and 20 mT of magnetic field. We can see in Fig. 3.1(a) that the time-averaged electron density looks qualitatively similar to the non-magnetized case, in spite of the strong electron magnetization. On the shorter time-scale, the map of the electron density features a very distinct instability pattern that rotates in the anti-clockwise direction, with a motion that is close to solid body motion. The typical wavelength seems to be about 2 mm. As shown in Fig. 3.1(c), the electron fluid rotates in the same direction as the instability. This drift motion is typical from magnetized plasma, and it is here opposed to the $E \times B$ drift.

3.1.4 Magnetic Drifts

Similarly to what was done to obtain Eq. (1.4) for the $E \times B$ drift, the collisionless momentum conservation equation

$$m_e \frac{d\mathbf{v}_e}{dt} = -e(\mathbf{E} + \mathbf{v} \times \mathbf{B}) - \frac{\nabla p_e}{n_e} \tag{3.1}$$

can be written

$$\frac{d(\mathbf{v}_e - \mathbf{v}_{E\times B} - \mathbf{v}_*)}{dt} = -\frac{e}{m_e}(\mathbf{v}_e - \mathbf{v}_{E\times B} - \mathbf{v}_*) \times \mathbf{B} \tag{3.2}$$

where

$$\mathbf{v}_* = \frac{\nabla p_e \times B}{e n_e B^2} \tag{3.3}$$

is the diamagnetic drift. Eq. (3.2) implies that the electron fluid velocity can be split into a translation by $v_{E\times B} + v_*$ and a cyclotron motion at frequency $\omega_{ce} = eB/m_e$. The diamagnetic drift v_* is only present in the fluid momentum conservation equations and not in the equation of motion of a single particle. This term cannot be interpreted as particle transport, but it can be captured in the PIC simulation without difficulty due to grid discretization. The reader can refer to the monograph by Chen [37] for more details about the diamagnetic drift interpretation and the measurement. The electron flux found in Fig. 3.1(c) is in the same direction as the diamagnetic drift and has the same order of magnitude.

To validate the idea that the electron fluid motion is driven by the diamagnetic drift, the electron fluid velocity along y measured from the PIC simulation at $y = l_y/2$ is plotted as a function of x together with the $E \times B$ drift and the diamagnetic drift in Fig. 3.2. The $E \times B$ and the diamagnetic drifts were computed using Eqs. (1.4) and (3.3) respectively. The gas pressure is 3 mTorr, and the power is 9.6 kW/m^3. The velocity terms are averaged over more than 4 µs since we are interested in the properties of the plasma equilibrium here. Two cases are investigated:

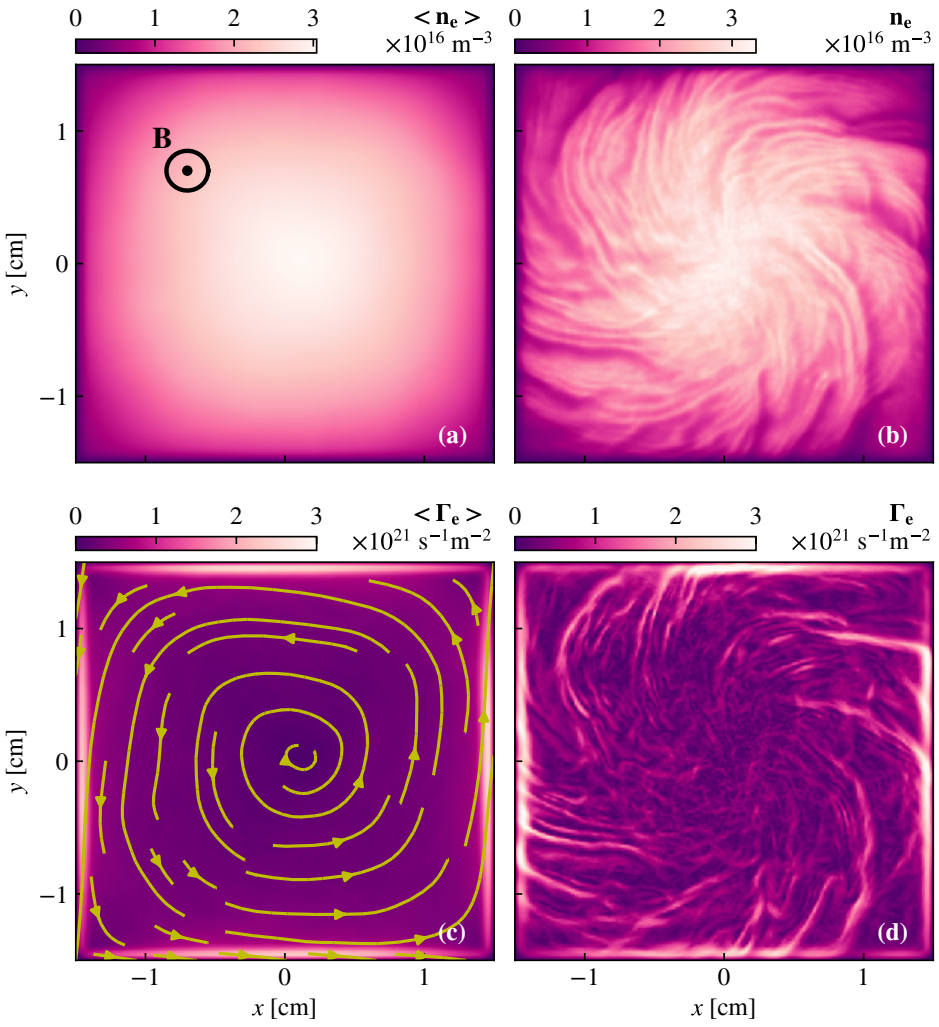

Figure 3.1: Electron density and norm of the electron flux at 91 µs (b, d), and averaged over the last 27 µs of the simulation (a, c). In (c), the spiral streamlines represent the electron flux. The data come from a 3 mTorr, 20 mT LPPic simulation.

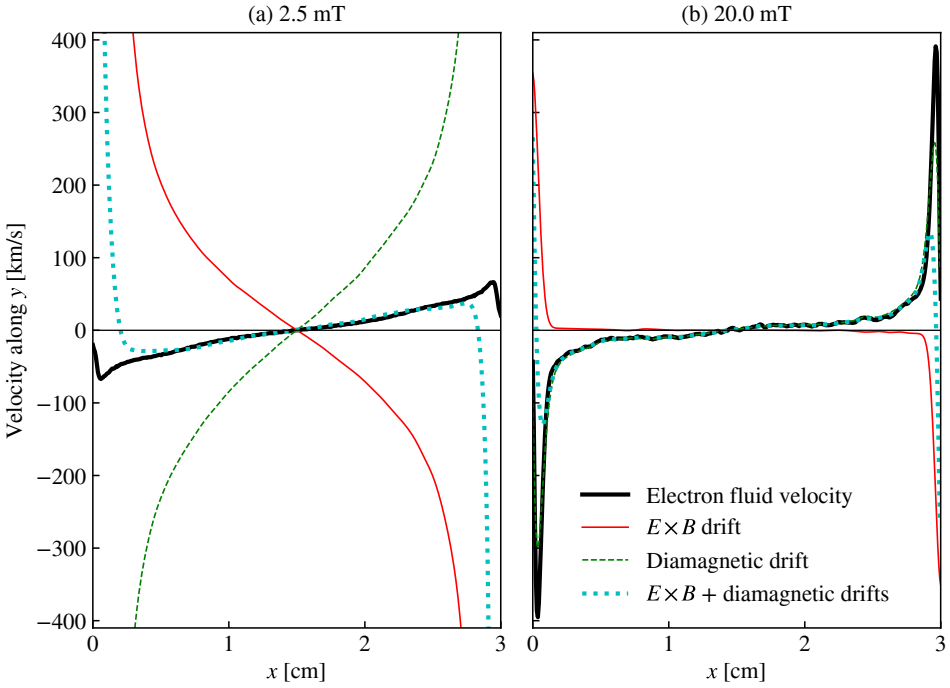

Figure 3.2: The electron fluid velocity along y extracted from the PIC simulation (solid black line) is compared to the diamagnetic drift (green dashed line) and the $E \times B$ drift (solid red line). The sum of the diamagnetic drift and the $E \times B$ drift is represented in cyan dotted line. The simulation data are averaged over a time greater than 4 µs. The pressure is 3 mTorr, and the magnetic field is 2.5 mT (a) and 20 mT (b).

(a) 2.5 mT. At low magnetic field, both the $E \times B$ and the diamagnetic drifts are very large because of the $1/B$ dependency but cancel each other to produce a total drift that is typically one order of magnitude lower.

(b) 20 mT. At higher magnetic field, the $E \times B$ drift becomes negligible and the electron drift velocity is almost equal to the diamagnetic drift velocity everywhere in the bulk plasma.

Both in Fig. 3.2(a) and (b), the sum of the diamagnetic drift and the $E \times B$ drift represented with a cyan dotted line matches the measured fluid velocity in the plasma bulk. In the sheath, this condition breaks because the electron fluid velocity becomes very high, so the electron inertia can no longer be neglected.

On the shorter time-scale, the electron fluid velocity is also perturbed by the instability, as illustrated in Fig. 3.1(d). The amplitude of the instability seems lower in the central region of the discharge and increases closer to the walls.

3.1.5 Magnetized Sheath

Before further development, it may be useful to focus on the sheath that characterizes the plasma equilibrium. Fig. 3.3 is analog to Fig. 2.6 with a magnetic field of 20 mT. Again, all the quantities are averaged over more than 5µs. One can first notice that the plasma density is generally higher for the same injected power, so the magnetic field does have a significant confining effect. The plasma density is typically 3 to 4 times higher at 20 mT than at 0 mT. This discrepancy translates into a smaller sheath region near the wall. The qualitative descriptions of section Section 3.1.3 are generally validated. The electron velocity along x is very much perturbed by the instability such that a smooth electron velocity profile could not be obtained at 20 mT, even when large temporal averages are considered. It is suspected that these patterns partially remain at steady state, as will be indicated later when the wall currents will be studied. The plasma potential is quite flat far away from the walls, and the ions accelerate smoothly towards the walls.

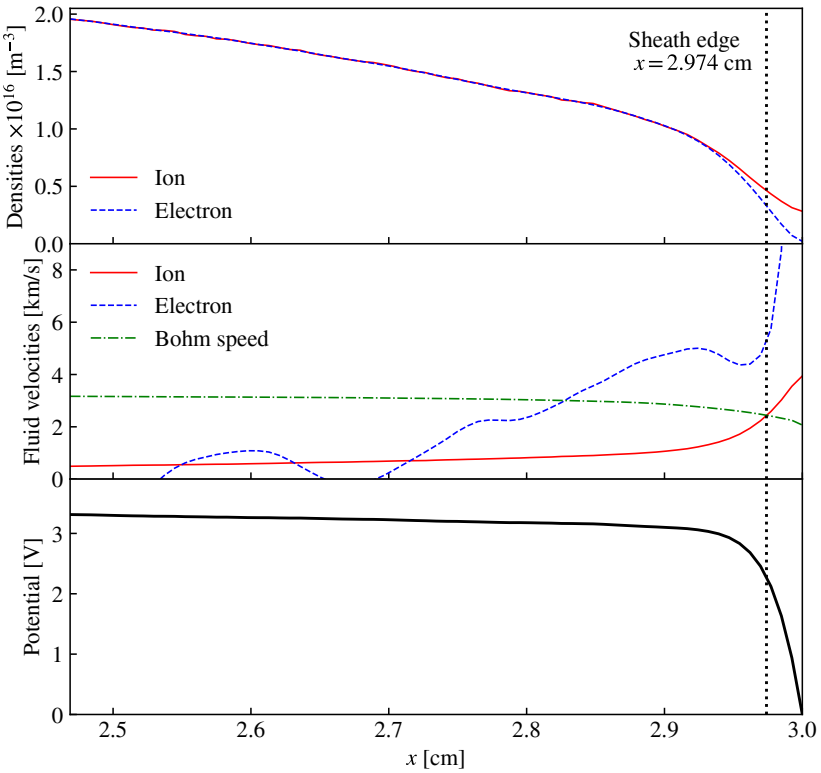

Figure 3.3: Magnetized sheath profiles at $y = l_y/2$ for a square (3×3 cm) discharge at 3 mTorr, 9.6 kW/m^3 and with a uniform magnetic field of 20 mT along z.

We have seen in Chapter 2 that the Bohm criterion that states that the ion velocity should be equal to the Bohm speed at the sheath edge is a necessary condition that

appears naturally in the 1D quasineutral fluid model. This can be seen, for example, in Eq. (2.30) which is entirely valid in the magnetized case. The Bohm sheath criterion was observed experimentally in magnetized plasma already in the original studies of Bohm [46]. Several authors have investigated the validity of the Bohm sheath criterion in magnetized plasmas. Allen and Holgate (2016) have investigated the 1D cylindrical case with a fluid model and has retrieved the usual Bohm criterion from a Boltzmann gradient condition for the electrons [4]. The effect of the angle between the magnetic field vector and the wall was also studied separately by Chodura [38], Stangeby [142], and Yankun *et al.* [163]. The situation investigated in the present work is restricted to the case where the magnetic field is parallel to the wall, but the plasma's unstable behavior is taken into account here, which was not possible with the equilibrium fluid models employed in previous studies.

The Bohm criterion is supposed to define the boundary between the quasineutral plasma region and the sheath region. Fig. 3.3 shows that the electron density is already about 30% lower than the ion density when the ion velocity reaches the Bohm speed. This is in contrast with the non-magnetized case where the electron density is only about 6% lower than the ion density at the sheath edge (see Fig. 2.6). It reveals that the Bohm criterion is somewhat arbitrary and it suggests that the accuracy of quasineutral models could be improved by selecting as a boundary condition a pre-sheath velocity that would be slightly lower than the Bohm speed. However, changing the Bohm criterion also affects the sheath size with two consequences: (i) the sheath size might become of the same order of magnitude as the system size, and (ii) the ionization in the sheath region might not be negligible anymore.

3.1.6 Parametric Studies with the Magnetic Field and the Pressure

Already earlier than Bohm, it was found that collisions were not the right mechanism to describe the transport of the electrons away from the magnetic field lines where they are trapped. The high-frequency oscillations in more or less random directions were suspected to be responsible for local electric fields that generate drifts pushing the electrons to the discharge walls. This effect was first described qualitatively by experimentalists [46]. In an article by Yoshikawa and Rose [165] it is assumed that the direction of plasma oscillations is completely random and that the relative density fluctuations do not depend on the magnetic field at strong magnetic field. Under these conditions, the diffusion coefficient is inversely proportional to the magnetic field, which seemed in reasonable agreement with experimental observations. These previous works conclude that the effective Hall parameter for the electrons should saturate at a value that is of the order of 10 to 100. The value of 16 is often used in the literature [165, 100].

In Fig. 3.4(a, b, c), the time-averaged electron density is plotted as a function of x, at the discharge center ($y = l_y/2 = 1.5\,\mathrm{cm}$) for many values of the magnetic field and three values of the pressure. The electron density increases with the magnetic

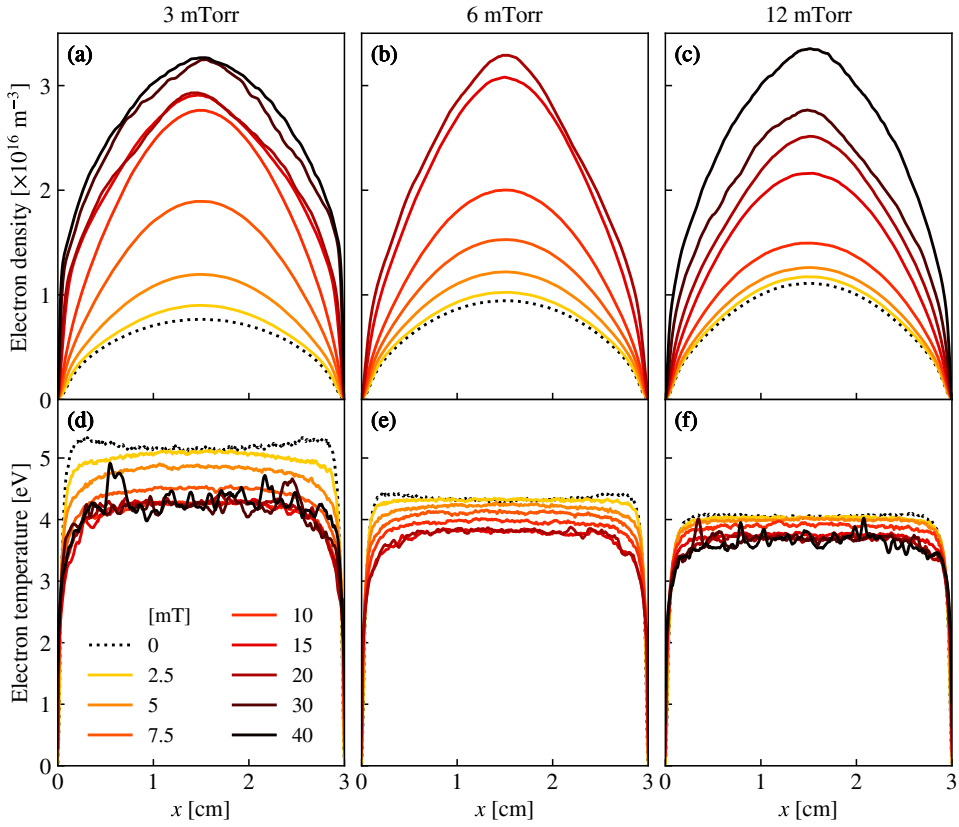

Figure 3.4: Curves of the time-averaged electron density (a, b, c) and the electron temperature (d, e, f) at $y = 1.5$ cm. The density is averaged over at least 5 µs of simulation while the electron temperature is only averaged over $N_{\text{average}} dT \approx 0.1$ µs.

field, and then seems to saturate when the magnetic field becomes large enough. Moreover, the shape of the profile is not much affected, and the typical cosine profile appears to be a reasonable solution. The electron temperature profiles are shown in Fig. 3.4(d, e, f). The assumption that the electron temperature is uniform in the bulk plasma seems to be satisfied as well. The electron temperature first decreases with the magnetic field, which is in agreement with the classical theory, and then saturates to a specific value that weakly depends on the pressure. When the magnetic field is above 30 mT, fluctuations are visible in the electron temperature. According to the global particle balance equation taken at steady state (Eq. (1.98)), the fact that the plasma density saturates at high magnetic field is a hint that the h factor and the diffusion coefficient should reach minimum values, whatever the magnetic field.

Fig. 3.5 shows the electric currents collected along the bottom wall of the simulation domain due to electrons (negative currents) and ions (positive currents) for various simulation runs at 6 mTorr. The ion current features a cosine shape that resembles the density profiles of Fig. 3.4. The ion current is remarkably constant with

the magnetic field. The magnetic confinement tends both to increase the plasma density and to reduce the ion speed at the sheath edge because the electron temperature decreases. These two effects seem to cancel out in the ion flux. This unexpected feature could be subject to further investigations. The profiles of electron currents are much more complex. First, the mean electron current over all the walls of the discharge is always exactly opposite to the mean ion current, which ensures that the plasma has reached a steady state. This observation is a consequence of the global charge balance of the discharge at steady state. At low magnetic fields, we could find the same patterns as in previous works [93, 105]. In the high pressure limit with no magnetic field, one could show that the electron flux should be uniform along the wall, except near the corner where the sheath is distorted. At high magnetic field, the electrons rotate in the azimuthal direction. The mean motion of the particles is in the $E \times B$ direction, while the electron *fluid* current is always in the direction of the diamagnetic drift. The simulations showed that at high magnetic field, the electron flux at the wall is locally equal to the ion flux, which is equivalent to the ambipolar condition found in previous publications [93, 89]. In between these two asymptotic regimes, the electrons are magnetized but they do not yet dominate the transport process, such that the electron flux is distorted with surprising patterns that look like stationary waves. As shown in Fig. 3.3 (center), these patterns can also be detected with the electron current diagnostics in volume, but the noise is quite large due to both the large drift velocity in the azimuthal direction, and the instability.

The 2D maps of the normalized density are plotted in Fig. 3.6 for various values of the pressure and the magnetic field. The instability seems to play an essential role in the discharge aspect only when the magnetic field is higher than a certain threshold that depends on the pressure. Once the threshold is passed, the 2D density profiles are more and more distorted by the magnetic field. The instability develops first mainly in the azimuthal direction. When the magnetic field further increases, more complex structures with smaller wavelengths appear.

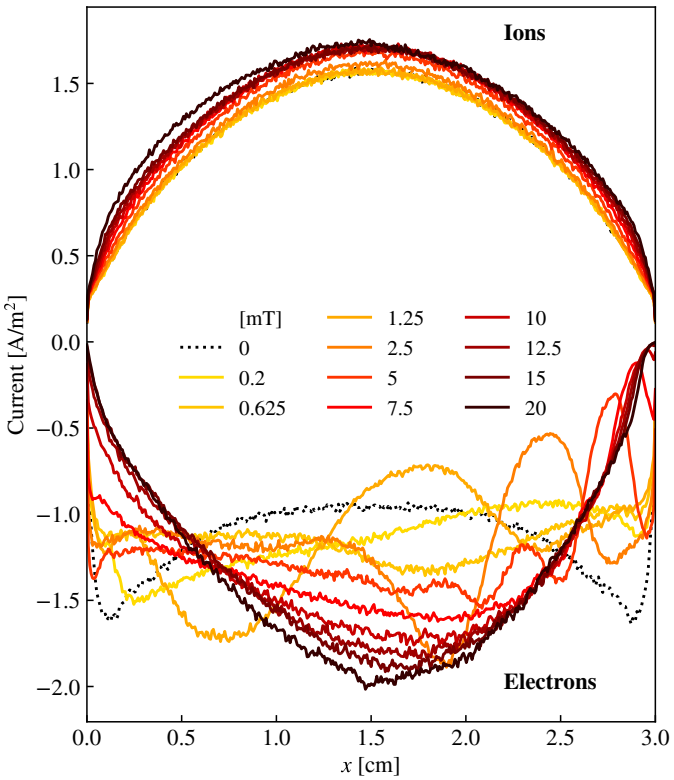

Figure 3.5: Electron currents (bottom, negative) and ions (top, positive) collected at the bottom wall of the simulation ($y = 0\,\text{cm}$) and averaged over at least 5 µs of simulation.

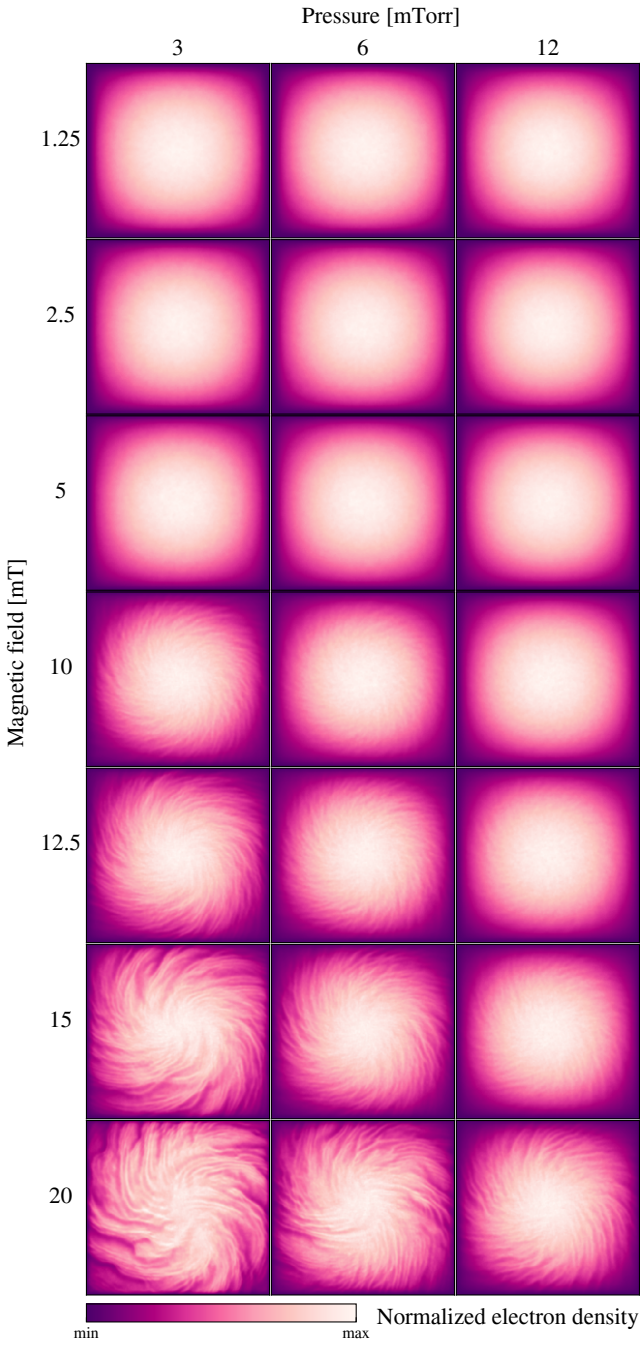

Figure 3.6: Normalized density map for 21 *LPPic* simulation runs after instability saturation for various values of the pressure (vertical axis) and the magnetic field (horizontal axis). The sampling time is lower than 100 ns in each case.

3.2 The Collisional Resistive Drift Instability

This section aims to describe the linear propagation of oscillatory modes in the direction of the electron drift using isothermal fluid theory.

3.2.1 Model Introduction

The effect of curvature is neglected, and it is assumed that the wave propagation is purely 1D. The electron temperature is assumed uniform and the ion temperature is neglected. It is further assumed that the ions are not magnetized.

All the frequencies are normalized to the electron cyclotron frequency, and the distances are normalized to the thermal electron Larmor radius. The plasma potential is normalized to the electron temperature in volts. The plasma density is normalized to the plasma density in the discharge center n_0. The whole set of normalized quantities is listed below.

$$\begin{aligned}
\tilde{n} &= n/n_0 \\
\tilde{l} &= l/\rho_{Le} \\
\tilde{\nu}_e &= \nu_e/\omega_{ce} \\
\tilde{\nu}_i &= \nu_i/\omega_{ce} \\
\tilde{\omega}_{ce} &= 1 \\
\tilde{\omega} &= \omega/\omega_{ce}\tilde{\omega}_{ci} && = m_e/m_i \\
\tilde{t} &= \omega_{ce}t \\
\tilde{\omega}_{pe} &= \omega_{pe}/\omega_{ce} \\
\tilde{\mathbf{k}} &= \rho_{Le}\mathbf{k} \\
\tilde{\mathbf{x}} &= \mathbf{x}/\rho_{Le} \\
\tilde{\mathbf{v}} &= \mathbf{v}/v_{Te} \\
\tilde{\nabla} &= \rho_{Le}\nabla
\end{aligned} \tag{3.4}$$

Poisson's equation in normalized units is

$$\frac{\tilde{\nabla}^2\tilde{\phi}}{\tilde{\omega}_{pe}} = \tilde{n}_e - \tilde{n}_i \tag{3.5}$$

We consider small perturbations of the plasma potential and the electron and ion densities:

$$\tilde{n}_e = \tilde{n}_{e0}(\tilde{x}) + \tilde{n}_{e1}(\tilde{y},\tilde{t})\ ;\ \tilde{n}_i = \tilde{n}_{i0}(\tilde{x}) + \tilde{n}_{i1}(\tilde{y},\tilde{t})\ ;\ \tilde{\phi} = \tilde{\phi}_0(\tilde{x}) + \tilde{\phi}_1(\tilde{y},\tilde{t}) \tag{3.6}$$

with $n_{e1} \ll n_{e0}$, $n_{i1} \ll n_{i0}$ and $\tilde{\phi}_1 \ll \tilde{\phi}_0$. The perturbations n_1 and $\tilde{\phi}_1$ are assumed proportional to $\exp(-i\tilde{\omega}\tilde{t} + i\tilde{k}\tilde{y})$.

To the first order, Eq. (3.5) implies

$$-\frac{\tilde{k}^2}{{\tilde{\omega}_{pe}}^2}\tilde{\phi}_1 = \tilde{n}_{e1} - \tilde{n}_{i1} \tag{3.7}$$

which can be written under the form

$$1 + \chi_e + \chi_i = 0 \tag{3.8}$$

where

$$\chi_e = \frac{{\tilde{\omega}_{pe}}^2 \tilde{n}_{e1}}{\tilde{k}^2 \tilde{\phi}_1} \text{ and } \chi_i = -\frac{{\tilde{\omega}_{pe}}^2 \tilde{n}_{i1}}{\tilde{k}^2 \tilde{\phi}_1} \tag{3.9}$$

are the electron and ion susceptibilities.

3.2.2 Dispersion Relation in a Homogeneous Plasma

In this paragraph, it is assumed that the equilibrium quantities $\tilde{n}_{e0}$, $\tilde{n}_{i0}$ and $\tilde{\phi}_1$ have slow variations with respect to $\tilde{x}$.

The ion momentum conservation equation is

$$\frac{d\tilde{\mathbf{v}}_\mathbf{i}}{d\tilde{t}} = -\mu\tilde{\nabla}\tilde{\phi} - \tilde{\nu}_i\tilde{\mathbf{v}}_\mathbf{i}. \tag{3.10}$$

where $\frac{d}{d\tilde{t}}$ is the total time derivative. The $\tilde{y}$ axis projection of Eq. (3.10) yields to the first order, in the referential of the drift motion of the ions ($\tilde{\mathbf{v}}_i = 0$)

$$-i\tilde{\omega}\tilde{v}_{i_{y_1}} = -i\mu\tilde{k}\tilde{\phi}_1 - \tilde{\nu}_i\tilde{v}_{i_{y_1}} \tag{3.11}$$

We assume that the frequency of the perturbations is much greater than the electron impact ionization frequency, such that the ion continuity equation is

$$\partial_{\tilde{t}}\tilde{n}_i + \tilde{\nabla}\cdot(\tilde{n}_i\tilde{\mathbf{v}}_i) = 0 \tag{3.12}$$

which becomes to the first order

$$-i\tilde{\omega}\tilde{n}_{i1} + i\tilde{k}\tilde{n}_{i0}\tilde{v}_{i_{y_1}} = 0 \tag{3.13}$$

Eqs. (3.11) and (3.13) are combined and lead to

$$\chi_i = -\frac{\mu{\tilde{\omega}_{pe}}^2}{\tilde{\omega}(\tilde{\omega} + i\tilde{\nu}_i)} \tag{3.14}$$

The picture is similar for the electrons, but the resolution is slightly more complicated due to the magnetic field and the pressure term. In normalized quantities, the electron momentum conservation equation is

$$\frac{d\tilde{\mathbf{v}}_e}{d\tilde{t}} = \tilde{\nabla}\tilde{\phi} - \tilde{\mathbf{v}}_e \times \mathbf{b} - \frac{\tilde{\nabla}\tilde{n}_e}{\tilde{n}_e} - \tilde{\nu}_e\tilde{\mathbf{v}}_e. \tag{3.15}$$

where **b** is a unit vector in the direction of the magnetic field. The analysis is first performed in the electron reference frame where $\tilde{\mathbf{v}}_e = 0$. The two components of Eq. (3.15) are to the first order

$$-i\tilde{\omega}\tilde{v}_{ex1} = -\tilde{v}_{ey_1} - \tilde{\nu}_e\tilde{v}_{ex1} \tag{3.16}$$

$$-i\tilde{\omega}\tilde{v}_{ey_1} = i\tilde{k}\tilde{\phi}_1 + \tilde{v}_{ex1} - \frac{i\tilde{k}\tilde{n}_{e1}}{\tilde{n}_{e0}} - \tilde{\nu}_e\tilde{v}_{ey_1} \tag{3.17}$$

Eliminating $\tilde{v}_{ex1}$,

$$(i\tilde{\omega} - \tilde{\nu}_e)\tilde{v}_{ey_1} + i\tilde{k}\tilde{\phi}_1 + \frac{\tilde{v}_{ey_1}}{i\tilde{\omega} - \tilde{\nu}_e} - \frac{i\tilde{k}\tilde{n}_{e1}}{\tilde{n}_{e0}} = 0 \tag{3.18}$$

The continuity equation writes exactly the same way as for the ions (Eq. (3.13)) and leads to

$$\chi_e = -\frac{\tilde{\omega}_{pe}{}^2(\tilde{\omega} + i\tilde{\nu}_e)}{(\tilde{\omega} + i\tilde{\nu}_e)^2\tilde{\omega} - \tilde{k}^2(\tilde{\omega} + i\tilde{\nu}_e) - \tilde{\omega}} \tag{3.19}$$

Let us now assume that the wave frequency and the collision frequency are both smaller than the electron cyclotron frequency

$$|\tilde{\omega} + i\tilde{\nu}| \ll 1 \tag{3.20}$$

The computation will be performed to the first order in $|\tilde{\omega} + i\tilde{\nu}|$. In this approximation

$$\chi_e = \frac{\tilde{\omega}_{pe}{}^2(\tilde{\omega} + i\tilde{\nu}_e)}{\tilde{k}^2(\tilde{\omega} + i\tilde{\nu}_e) + \tilde{\omega}} \tag{3.21}$$

Let us now assume that the electrons are drifting with respect to the ions with a velocity $\tilde{v}_d$. If $\tilde{\omega}$ is the wave frequency in the ion referential, it has to be shifted to $\tilde{\omega} - \tilde{\omega}_d$ in the referential of the ions, where $\tilde{\omega}_d = \tilde{k}\tilde{v}_d$, such that the electron susceptibility is $\chi_e = \frac{\tilde{\omega}_{pe}{}^2(\tilde{\omega}-\tilde{\omega}_d+i\tilde{\nu}_e)}{\tilde{k}^2(\tilde{\omega}-\tilde{\omega}_d+i\tilde{\nu}_e)+\tilde{\omega}-\tilde{\omega}_d}$ In this case, the perturbed Poisson's equation (3.8) is

$$P(\tilde{\omega}) = P_0(\tilde{\omega}) + i\tilde{\nu}_e Q(\tilde{\omega}) + i\tilde{\nu}_i Q_i(\tilde{\omega}) - \tilde{\nu}_e\tilde{\nu}_i R(\tilde{\omega}) = 0 \tag{3.22}$$

where

$$P_0(\tilde{\omega}) = (\tilde{\omega} - \tilde{\omega}_d)\left[(1 + \tilde{k}^2 + \tilde{\omega}_{pe}{}^2)\tilde{\omega}^2 - \mu\tilde{\omega}_{pe}{}^2(1 + \tilde{k}^2)\right] ; \tag{3.23}$$

$$Q(\tilde{\omega}) = (\tilde{k}^2 + \tilde{\omega}_{pe}{}^2)\tilde{\omega}^2 - \mu\tilde{\omega}_{pe}{}^2\tilde{k}^2 ; \tag{3.24}$$

$$Q_i(\tilde{\omega}) = \tilde{\omega}(\tilde{\omega} - \tilde{\omega}_d)(1 + \tilde{k}^2 + \tilde{\omega}_{pe}{}^2) ; \tag{3.25}$$

$$R(\tilde{\omega}) = (\tilde{k}^2 + \tilde{\omega}_{pe}{}^2)\tilde{\omega} . \tag{3.26}$$

If there are no collisions, the modes that can exist in the plasma are the roots of P_0:

$$\tilde{\omega}_0 = \tilde{\omega}_d \text{ and } \tilde{\omega}_\pm = \pm\tilde{\omega}_{pe}\left[\frac{\mu(1 + \tilde{k}^2)}{1 + \tilde{k}^2 + \tilde{\omega}_{pe}{}^2}\right]^{1/2} \tag{3.27}$$

which are purely stable modes, with with no damping nor growth. Since the phase velocity of the $\tilde{\omega} = \tilde{\omega}_d$ mode is the electron drift velocity, it is called an electron beam mode. Three asymptotic regimes are of interest for the $\tilde{\omega}_\pm$ mode:

- If $\tilde{k} \ll 1$, $\tilde{\omega}_\pm = \pm\frac{\mu^{1/2}}{(1+\tilde{\omega}_{pe}{}^{-2})^{1/2}}$, which corresponds to the lower hybrid modes.
- If $1 \ll \tilde{k} \ll \tilde{\omega}_{pe}$, $\tilde{\omega}_\pm = \pm\tilde{k}\mu^{1/2}$, which corresponds to the ion acoustic modes.
- If $\tilde{k} \gg \tilde{\omega}_{pe}$, $\tilde{\omega}_\pm = \pm\tilde{\omega}_{pe}\mu^{1/2}$, which corresponds to the ion plasma frequency.

We are now interested in the perturbation of these modes by collisions, under the assumption $\tilde{\nu}, \tilde{\nu}_i \ll \tilde{\omega}$. Except in exceptional cases, $Q(\tilde{\omega})$ and $Q_i(\tilde{\omega})$ are of the same order of magnitude. Moreover, since the electron collision frequency is, in general, higher than the ion collision frequency, due to the higher electron speed, the contribution of Q_i can be neglected. Since $\tilde{\nu}_i < \tilde{\nu}$, the contribution of $R(\tilde{\omega})$ is of order 2. The only perturbation of P_0 taken into account comes therefore from the electron collisions. Let $\tilde{\omega}_r$ be a root of P_0, and $\tilde{\omega}_r + i\tilde{\nu}\delta$ the corresponding perturbed root of P (when there are no collisions $P = P_0$ and the roots are equal).

$$0 = P(\tilde{\omega}_r + i\tilde{\nu}\delta) \tag{3.28}$$

$$= P_0(\tilde{\omega}_r) + i\tilde{\nu}\delta P_0'(\tilde{\omega}_r) + i\tilde{\nu}Q(\tilde{\omega}_r) + \mathcal{O}\left(\tilde{\nu}^2\right) \tag{3.29}$$

To the 0-th order in $\tilde{\nu}$,

$$\delta = -\frac{Q(\tilde{\omega}_r)}{P_0'(\tilde{\omega}_r)} \tag{3.30}$$

And the normalized growth rate of the wave is

$$\tilde{\xi} = \Re(\tilde{\nu}\delta)\,. \tag{3.31}$$

where $\Re(\cdot)$ is the real part. The stability of the perturbed mode $\tilde{\omega}_r$ is hence determined by the sign of δ. If $\delta > 0$, the mode is unstable, and if $\delta < 0$, the mode is stable.

$$\begin{aligned} P_0'(\tilde{\omega}_d) &= (1 + \tilde{k}^2 + \tilde{\omega}_{pe}{}^2)\tilde{\omega}_d^2 - \mu\tilde{\omega}_{pe}{}^2(1 + \tilde{k}^2) \\ &= (1 + \tilde{k}^2 + \tilde{\omega}_{pe}{}^2)(\tilde{\omega}_d^2 - \tilde{\omega}_+^2) \end{aligned} \tag{3.32}$$

$$P_0'(\tilde{\omega}_\pm) = 2\tilde{\omega}_+(1 + \tilde{k}^2 + \tilde{\omega}_{pe}{}^2)(\tilde{\omega}_\pm - \tilde{\omega}_d) \tag{3.33}$$

Moreover,

$$Q(\tilde{\omega}_d) = (\tilde{k}^2 + \tilde{\omega}_{pe}{}^2)\tilde{\omega}_d^2 - \mu\tilde{\omega}_{pe}{}^2\tilde{k}^2 \tag{3.34}$$

$$Q(\tilde{\omega}_\pm) = \frac{\mu\tilde{\omega}_{pe}{}^4}{1 + \tilde{k}^2 + \tilde{\omega}_{pe}{}^2} > 0 \tag{3.35}$$

We define

$$\delta_0 = -\frac{Q(\tilde{\omega}_d)}{P_0'(\tilde{\omega}_d)} \text{ and } \delta_\pm = -\frac{Q(\tilde{\omega}_\pm)}{P_0'(\tilde{\omega}_\pm)} \tag{3.36}$$

δ_+ has the sign of $\tilde{\omega}_d - \tilde{\omega}_+$ and δ_- has the sign of $-\tilde{\omega}_d - \tilde{\omega}_+$. Hence:

- If $\tilde{\omega}_d^2 > \tilde{\omega}_+^2$, either the $\tilde{\omega}_+$ mode or the $\tilde{\omega}_-$ mode is unstable.
- If $\tilde{\omega}_d^2 < \tilde{\omega}_+^2$, then $\tilde{\omega}_+$ and $\tilde{\omega}_-$ modes are both stable. Furthermore,

$$\delta_0 = \frac{\mu\tilde{\omega}_{pe}{}^2\tilde{k}^2 - (\tilde{k}^2 + \tilde{\omega}_{pe}{}^2)\tilde{\omega}_d^2}{(1 + \tilde{k}^2 + \tilde{\omega}_{pe}{}^2)(\tilde{\omega}_d^2 - \tilde{\omega}_+^2)} \tag{3.37}$$

has the same sign as $(\tilde{k}^2+\tilde{\omega}_{pe}{}^2)\tilde{\omega}_d^2-\mu\tilde{\omega}_{pe}{}^2\tilde{k}^2$. Hence, $\tilde{\omega} = \tilde{\omega}_d$ mode is stable if

$$\tilde{\omega}_d^2 < \frac{\mu\tilde{\omega}_{pe}{}^2\tilde{k}^2}{\tilde{k}^2 + \tilde{\omega}_{pe}{}^2} \tag{3.38}$$

In summary, since the inequality $\frac{\mu\tilde{\omega}_{pe}{}^2\tilde{k}^2}{\tilde{k}^2+\tilde{\omega}_{pe}{}^2} < \tilde{\omega}_+^2$ is always true, the plasma is stable if and only if condition (3.38) is satisfied. The stability criterion is:

$$\boxed{\tilde{\omega}_d < \frac{\mu^{1/2}\tilde{k}}{\left(1 + \tilde{k}^2/\tilde{\omega}_{pe}{}^2\right)^{1/2}}} \tag{3.39}$$

where the sign of $\tilde{k}$ is chosen to match $\tilde{v}_d$'s sign. In the case where the drift velocity is higher than the Bohm speed ($\tilde{v}_d^2 > \mu$), this condition is never satisfied, and the plasma is unstable for all wavenumbers. This instability is not an ion acoustic wave, in the sense that its phase velocity is not constant and is not equal to the Bohm speed. If the drift velocity is lower than the Bohm speed, stability occurs for low wavenumbers

$$\tilde{k}^2 < \tilde{\omega}_{pe}{}^2\left(\frac{\mu}{\tilde{v}_d^2} - 1\right) \tag{3.40}$$

In the limit of low collisionality, the most unstable modes are when δ_0 or $\delta_\pm$ becomes infinite, that is when $P_0'(\tilde{\omega}_d) = 0$ or $P_0'(\tilde{\omega}_\pm) = 0$ according to Eq. (3.36). This occurs when $\tilde{\omega}_d$ or $\tilde{\omega}_\pm$ become multiple roots of P_0. Since the $\tilde{\omega}_+$ and $\tilde{\omega}_-$ modes do not intersect, the most unstable mode has to satisfy $\tilde{\omega}_d = \tilde{\omega}_\pm$. Consequently, the instability comes from the coupling between the beam mode $\tilde{\omega}_d$ and one of the modes $\tilde{\omega}_\pm$, by collisions. For $\tilde{\omega}_d = \tilde{\omega}_\pm$, the maximum growth rate cannot be estimated by Eq. (3.30) because $P_0'(\tilde{\omega}_d) = P_0'(\tilde{\omega}_+) = 0$ at $\tilde{k} = \tilde{k}_{\max}$. For positive $\tilde{\omega}_d$, the maximum growth rate can hence be estimated by taking the second order perturbation of the dispersion relation $P(\tilde{\omega}) = 0$:

$$(\tilde{\omega} - \tilde{\omega}_d)(\tilde{\omega} - \tilde{\omega}_+)(\tilde{\omega} + \tilde{\omega}_+) = -\frac{i\tilde{\nu}\left[\left(\tilde{k}_{\max}^2 + \tilde{\omega}_{pe}{}^2\right)\tilde{\omega}^2 - \mu\tilde{\omega}_{pe}{}^2\tilde{k}_{\max}^2\right]}{1 + \tilde{k}_{\max}^2 + \tilde{\omega}_{pe}{}^2} \tag{3.41}$$

$\tilde{k}_{\max}$ is here the wavenumber where $\tilde{\omega}_d = \tilde{\omega}_\pm$. The perturbation of the mode intersection writes $\tilde{\omega} = \tilde{\omega}_+ + i\tilde{\nu}\delta_{\max} = \tilde{\omega}_d + i\tilde{\nu}\delta_{\max}$, which yields

$$2\tilde{\omega}_+\tilde{\nu}^2\delta_{\max}^2 = \frac{i\tilde{\nu}\left[\left(\tilde{k}_{\max}^2 + \tilde{\omega}_{pe}{}^2\right)\tilde{\omega}^2 - \mu\tilde{\omega}_{pe}{}^2\tilde{k}_{\max}^2\right]}{1 + \tilde{k}_{\max}^2 + \tilde{\omega}_{pe}{}^2} \tag{3.42}$$

Hence, by replacing $\tilde{\omega}$ by

$$\delta_{\max} = \frac{e^{i\pi/4}}{2\tilde{\nu}^{1/2}} \left[\frac{\mu \tilde{\omega}_{pe}{}^6}{(1+\tilde{k}_{\max}^2)(1+\tilde{k}_{\max}^2+\tilde{\omega}_{pe}{}^2)^3} \right]^{1/4} , \tag{3.43}$$

and the growth rate (Eq. (3.31))

$$\boxed{\tilde{\xi} = \frac{\tilde{\nu}^{1/2}}{2^{3/2}} \left[\frac{\mu \tilde{\omega}_{pe}{}^6}{(1+\tilde{k}_{\max}^2)(1+\tilde{k}_{\max}^2+\tilde{\omega}_{pe}{}^2)^3} \right]^{1/4}} \tag{3.44}$$

is proportional to $\tilde{\nu}^{1/2}$ and not $\tilde{\nu}$ as for the other perturbed solutions.

The most unstable mode $\tilde{k}_{\max}$ that corresponds to $\tilde{\omega}_d = \tilde{\omega}_+$ is obtained from the root of a second order polynomial

$$\tilde{k}_{\max} = \frac{1}{\sqrt{2}} \left[-1 - \tilde{\omega}_{pe}{}^2 + \frac{\tilde{\omega}_{pe}{}^2 \mu}{\tilde{v}_d^2} + \left(\left[1 + \tilde{\omega}_{pe}{}^2 - \frac{\tilde{\omega}_{pe}{}^2 \mu}{\tilde{v}_d^2} \right]^2 + \frac{4\tilde{\omega}_{pe}{}^2 \mu}{\tilde{v}_d^2} \right)^{\frac{1}{2}} \right]^{\frac{1}{2}} \tag{3.45}$$

For large $\tilde{v}_d$ ($\tilde{v}_d^2/(\mu\tilde{\omega}_{pe}{}^2) \gg 1$), this expression is

$$\tilde{k}_{\max} \approx \frac{\tilde{\omega}_{pe}\mu^{1/2}}{\tilde{v}_d(1+\tilde{\omega}_{pe}{}^2)^{1/2}} . \tag{3.46}$$

which tends towards 0 for large $\tilde{v}_d$.

3.2.3 Dispersion Relation in an Inhomogeneous Plasma

The situation derived above corresponds to the ideal situation of a uniform plasma. When plasma inhomogeneities are to be taken into account, one cannot decouple the perturbed motion to the 0-th order drift motion.

It is now assumed that

$$\tilde{v}, d/d\tilde{t} = \mathcal{O}(\epsilon) \tag{3.47}$$

$$\tilde{\phi}, \tilde{n}, |\tilde{\nabla}| = \mathcal{O}(1) \tag{3.48}$$

where ϵ is a small parameter. We can expand $\tilde{\mathbf{v}}$ with respect to ϵ. To the 0-th order, Eq. (3.15) is

$$\tilde{\nabla}\tilde{\phi} - \tilde{\mathbf{v}} \times \mathbf{b} - \tilde{\nabla}\tilde{n}/\tilde{n} = 0 \tag{3.49}$$

which yields the $E \times B$ and diamagnetic drifts, respectively

$$\tilde{\mathbf{v}}_{E\times B} = \mathbf{b} \times \tilde{\nabla}\tilde{\phi} \quad \text{and} \quad \tilde{\mathbf{v}}_* = \frac{\tilde{\nabla}\tilde{n}}{\tilde{n}} \times \mathbf{b} , \tag{3.50}$$

such that to the 0-th order

$$\tilde{\mathbf{v}}^{(0)} = \tilde{\mathbf{v}}_{E\times B} + \tilde{\mathbf{v}}_* \,. \tag{3.51}$$

Eq. (3.15) is then to the first order

$$\frac{d}{d\tilde{t}}(\tilde{\mathbf{v}}_{E\times B} + \tilde{\mathbf{v}}_*) = -\tilde{\mathbf{v}}^{(1)} \times \mathbf{b} - \tilde{\nu}(\tilde{\mathbf{v}}_{E\times B} + \tilde{\mathbf{v}}_*) \tag{3.52}$$

where $\tilde{\mathbf{v}}^{(1)} = \tilde{\mathbf{v}} - \tilde{\mathbf{v}}_{E\times B} - \tilde{\mathbf{v}}_* + \mathcal{O}(\epsilon^2)$ is the first order term of the electron velocity. Hence,

$$\tilde{\mathbf{v}}^{(1)} = \tilde{\mathbf{v}}_p + \tilde{\mathbf{v}}_{dp} \tag{3.53}$$

where

$$\tilde{\mathbf{v}}_p = \left(\frac{d}{d\tilde{t}} + \tilde{\nu}\right)\tilde{\mathbf{v}}_{E\times B} \times \mathbf{b} = \left(\frac{d}{d\tilde{t}} + \tilde{\nu}\right)\tilde{\nabla}\tilde{\phi} \tag{3.54}$$

and

$$\tilde{\mathbf{v}}_{dp} = \left(\frac{d}{d\tilde{t}} + \tilde{\nu}\right)\tilde{\mathbf{v}}_* \times \mathbf{b} = -\left(\frac{d}{d\tilde{t}} + \tilde{\nu}\right)\frac{\tilde{\nabla}\tilde{n}}{\tilde{n}} \tag{3.55}$$

are the polarization drift terms due to the $E \times B$ and the diamagnetic drifts, respectively (including the friction force). It is useful to derive the divergence of the fluxes corresponding to each of the drift terms.

$$\tilde{\nabla} \cdot (\tilde{n}\tilde{\mathbf{v}}_{E\times B}) = (\mathbf{b} \times \tilde{\nabla}\tilde{\phi}) \cdot \tilde{\nabla}\tilde{n} + \tilde{n}\tilde{\nabla} \cdot (\mathbf{b} \times \tilde{\nabla}\tilde{\phi}) \tag{3.56}$$

The second term is zero since for any vectors $\mathbf{u}$ and $\mathbf{v}$

$$\nabla \cdot (\mathbf{u} \times \mathbf{v}) = -\mathbf{u} \cdot (\nabla \times \mathbf{v}) + \mathbf{v} \cdot (\nabla \times \mathbf{u}) \,. \tag{3.57}$$

Thus,

$$\tilde{\nabla} \cdot (\tilde{n}\tilde{\mathbf{v}}_{E\times B}) = (\mathbf{b} \times \tilde{\nabla}\tilde{\phi}) \cdot \tilde{\nabla}\tilde{n} \tag{3.58}$$

Using again Eq. (3.57),

$$\tilde{\nabla} \cdot (\tilde{n}\tilde{\mathbf{v}}_*) = 0. \tag{3.59}$$

Eq. (3.59) is sometimes known as the *gyroviscous cancellation*.

As previously, all the particle source and loss terms are neglected ($\tilde{\nu}_{iz} \ll \tilde{\omega}$), such that the electron continuity equation is

$$\partial_{\tilde{t}}\tilde{n} + \tilde{\nabla} \cdot (\tilde{n}\tilde{\mathbf{v}}) = 0. \tag{3.60}$$

So to the first order in ϵ,

$$\partial_{\tilde{t}}\tilde{n} + \tilde{\nabla} \cdot [\tilde{n}(\tilde{\mathbf{v}}_{E\times B} + \tilde{\mathbf{v}}_* + \tilde{\mathbf{v}}_p + \tilde{\mathbf{v}}_{dp})] = 0, \tag{3.61}$$

or

$$\partial_{\tilde{t}}\tilde{n} + (\mathbf{b} \times \tilde{\nabla}\tilde{\phi}) \cdot \tilde{\nabla}n + \tilde{\nabla} \cdot \left[\tilde{n}\left(\frac{d}{d\tilde{t}} + \tilde{\nu}\right)\left(\tilde{\nabla}\tilde{\phi} - \frac{\tilde{\nabla}\tilde{n}}{\tilde{n}}\right)\right] = 0 \tag{3.62}$$

The only term contributing to the motion of the electron guiding centers is the $E \times B$ drift [162]

$$\frac{d}{d\tilde{t}} = \partial_{\tilde{t}} + \tilde{\mathbf{v}}_{E\times B} \cdot \tilde{\nabla} \tag{3.63}$$

Using the property

$$\tilde{\nabla}\cdot[(\tilde{\mathbf{v}}_{E\times B}\cdot\tilde{\nabla})\tilde{\nabla}\tilde{\phi}] = (\tilde{\mathbf{v}}_{E\times B}\cdot\tilde{\nabla})\tilde{\nabla}^2\tilde{\phi}, \tag{3.64}$$

$$\begin{aligned}\tilde{\nabla}\cdot(\tilde{n}\tilde{\mathbf{v}}_p) = {}& \tilde{n}\left(\partial_{\tilde{t}} + \tilde{\mathbf{v}}_{E\times B}\cdot\tilde{\nabla} + \tilde{\nu}\right)\nabla^2\tilde{\phi} \\ & + \tilde{\nabla}\tilde{n}\cdot\left(\partial_{\tilde{t}} + \mathbf{v}_{E\times B}\cdot\tilde{\nabla} + \tilde{\nu}\right)\tilde{\nabla}\tilde{\phi}.\end{aligned} \tag{3.65}$$

For the density gradient polarization drift,

$$\begin{aligned}\tilde{\nabla}\cdot(\tilde{n}\tilde{\mathbf{v}}_{dp}) = {}& \tilde{\nabla}\cdot\left[\frac{\tilde{\nabla}\tilde{n}}{\tilde{n}}\left(\partial_{\tilde{t}} + \tilde{\mathbf{v}}_{E\times B}\cdot\tilde{\nabla}\right)\tilde{n}\right] \\ & - \left(\partial_{\tilde{t}} + \tilde{\nu}\right)\tilde{\nabla}^2\tilde{n} - \tilde{\nabla}\cdot[(\tilde{\mathbf{v}}_{E\times B}\cdot\tilde{\nabla})\tilde{\nabla}\tilde{n}].\end{aligned} \tag{3.66}$$

It is now assumed that

$$\tilde{n} = \tilde{n}_0(\tilde{x}) + \tilde{n}_1(\tilde{y},\tilde{t}) \quad ; \quad \tilde{\phi} = \tilde{\phi}_0(\tilde{x}) + \tilde{\phi}_1(\tilde{y},\tilde{t}) \tag{3.67}$$

with $n_1 \ll n_0$ and $\tilde{\phi}_1 \ll \tilde{\phi}_0$, and $\tilde{n}_1$ and $\tilde{\phi}_1$ proportional to $\exp(-i\tilde{\omega}\tilde{t} + i\tilde{k}\tilde{y})$. To the first order in $\tilde{\phi}_1$ and $\tilde{n}_1$:

$$\begin{aligned}\tilde{\nabla}\cdot(\tilde{n}\tilde{\mathbf{v}}_p) = {}& \tilde{n}_0\left[\partial_{\tilde{t}} + (\mathbf{b}\times\tilde{\nabla}\tilde{\phi}_0\cdot\tilde{\nabla}) + \tilde{\nu}\right]\tilde{\nabla}^2\tilde{\phi}_1 \\ & + \tilde{\nu}\tilde{n}_1\tilde{\nabla}^2\tilde{\phi}_0 + n_0(\mathbf{b}\times\tilde{\nabla}\tilde{\phi}_1\cdot\tilde{\nabla})\tilde{\nabla}^2\tilde{\phi}_0 \\ & + \tilde{\nabla}n_0\cdot(\mathbf{b}\times\tilde{\nabla}\tilde{\phi}_1\cdot\tilde{\nabla})\tilde{\nabla}\tilde{\phi}_0\end{aligned} \tag{3.68}$$

$$\begin{aligned}\tilde{\nabla}\cdot(\tilde{n}\tilde{\mathbf{v}}_p) = {}& i\tilde{n}_0\tilde{k}^2(\tilde{\omega} + \tilde{\omega}_0 + i\tilde{\nu})\tilde{\phi}_1 + \tilde{\nu}\tilde{n}_1\tilde{\phi}_0'' \\ & - i\tilde{k}\tilde{n}_0\tilde{\phi}_0'''\tilde{\phi}_1 + i\tilde{\omega}_*\tilde{n}_0\tilde{\phi}_0''\tilde{\phi}_1\end{aligned} \tag{3.69}$$

where $\tilde{\omega}_* = -\tilde{k}\tilde{n}_0'/n_0$ and $\tilde{\omega}_{E\times B} = -\tilde{k}\tilde{\phi}_0'$. Similarly,

$$\begin{aligned}\tilde{\nabla}\cdot(\tilde{n}\tilde{\mathbf{v}}_{dp}) = {}& \tilde{\nabla}\cdot\left\{\frac{\tilde{\nabla}\tilde{n}_0}{\tilde{n}_0}\left[\partial_{\tilde{t}} + (\mathbf{b}\times\tilde{\nabla}\tilde{\phi}_0\cdot\tilde{\nabla})\right]\tilde{n}_1\right\} \\ & + \tilde{\nabla}\cdot\left[\frac{\tilde{\nabla}\tilde{n}_0}{\tilde{n}_0}(\mathbf{b}\times\tilde{\nabla}\tilde{\phi}_1\cdot\tilde{\nabla})\tilde{n}_0\right] \\ & - \left(\partial_{\tilde{t}} + \tilde{\nu}\right)\tilde{\nabla}^2\tilde{n}_1 - \tilde{\nabla}\cdot\left[(\mathbf{b}\times\tilde{\nabla}\tilde{\phi}_0\cdot\tilde{\nabla})\tilde{\nabla}\tilde{n}_1\right] \\ & - \tilde{\nabla}\cdot\left[(\mathbf{b}\times\tilde{\nabla}\tilde{\phi}_1\cdot\tilde{\nabla})\tilde{\nabla}\tilde{n}_0\right]\end{aligned} \tag{3.70}$$

$$\begin{aligned}= {}& -i\tilde{n}_1(\tilde{\omega} + \tilde{\omega}_{E\times B})\left(\frac{\tilde{n}_0''}{\tilde{n}_0} - \frac{\tilde{\omega}_*^2}{\tilde{k}^2}\right) - i\tilde{n}_1\tilde{\omega}_*\tilde{\phi}_0'' \\ & + i\tilde{\omega}_*\tilde{n}_0\tilde{\phi}_1\left(2\frac{\tilde{n}_0''}{\tilde{n}_0} - \frac{\tilde{\omega}_*^2}{\tilde{k}^2}\right) \\ & - i\tilde{k}^2(\tilde{\omega} + \tilde{\omega}_{E\times B} + i\tilde{\nu})\tilde{n}_1 + i\tilde{k}\tilde{\phi}_1\tilde{n}_0'''.\end{aligned} \tag{3.71}$$

Finally, Eq. (3.58) yields

$$\tilde{\nabla}\cdot(\tilde{n}\tilde{\mathbf{v}}_{E\times B}) = -i\tilde{\omega}_{E\times B}\tilde{n}_1 + i\tilde{\omega}_*\tilde{n}_0\tilde{\phi}_1 \tag{3.72}$$

To the first order in $\tilde{\omega}_*$, and neglecting second and third order derivatives of $\tilde{n}_0$ and $\tilde{\phi}_0$ (no shear),

$$\tilde{\nabla} \cdot (\tilde{n}\tilde{\mathbf{v}}_p) = i\tilde{n}_0\tilde{k}^2(\tilde{\omega} + \tilde{\omega}_{E\times B} + i\tilde{\nu})\tilde{\phi}_1 \tag{3.73}$$

$$\tilde{\nabla} \cdot (\tilde{n}\tilde{\mathbf{v}}_{dp}) = -i\tilde{k}^2(\tilde{\omega} + \tilde{\omega}_{E\times B} + i\tilde{\nu})\tilde{n}_1 \tag{3.74}$$

Eq. (3.60) is therefore:

$$\begin{aligned} &- i\tilde{\omega}\tilde{n}_1 - i\tilde{\omega}_{E\times B}\tilde{n}_1 + i\tilde{\omega}_*\tilde{n}_0\tilde{\phi}_1 + i\tilde{n}_0\tilde{k}^2(\tilde{\omega} + \tilde{\omega}_{E\times B} + i\tilde{\nu})\tilde{\phi}_1 \\ &- i\tilde{k}^2(\tilde{\omega} + \tilde{\omega}_{E\times B} + i\tilde{\nu})\tilde{n}_1 = 0 \end{aligned} \tag{3.75}$$

Hence,

$$\frac{\tilde{n}_1}{\tilde{n}_0} = \frac{\tilde{\omega}_* + \tilde{k}^2(\tilde{\omega} + \tilde{\omega}_{E\times B} + i\tilde{\nu})}{\tilde{\omega} + \tilde{\omega}_{E\times B} + \tilde{k}^2(\tilde{\omega} + \tilde{\omega}_{E\times B} + i\tilde{\nu})}\tilde{\phi}_1 \,. \tag{3.76}$$

It follows then that the electron susceptibility is

$$\chi_e \equiv \frac{\tilde{\omega}_{pe}{}^2}{\tilde{k}^2}\frac{\tilde{n}_{e1}}{\tilde{\phi}_1} = \frac{\tilde{\omega}_{pe}{}^2}{\tilde{k}^2}\frac{\tilde{\omega}_* + \tilde{k}^2(\tilde{\omega} + \tilde{\omega}_{E\times B} + i\tilde{\nu})}{(\tilde{\omega} + \tilde{\omega}_{E\times B}) + \tilde{k}^2(\tilde{\omega} + \tilde{\omega}_{E\times B} + i\tilde{\nu})} \tag{3.77}$$

where

$$\tilde{\omega}_{E\times B} = -\tilde{k}\tilde{\phi}' \quad , \quad \tilde{\omega}_* = -\tilde{k}\tilde{n}'/\tilde{n} \,. \tag{3.78}$$

The formula for the electron susceptibility should be compared with Eq. (3.21). The $E \times B$ drift plays a role that is similar to the fluid drift velocity of the homogeneous plasma approach. However, the diamagnetic drift plays a role that is entirely different because of the contribution of the density gradient. Eq. (3.77) was also introduced by the gyroviscosity formalism in Smolyakov *et al.* [139].

Since the ions are not magnetized, the derivation of their susceptibility does not require special treatment and Eq. (3.14) is retained [9]. The assumption that $\tilde{\nu}_i \ll \tilde{\nu}$ is made again.

The first order Poisson's equation Eq. (3.8) provides a new dispersion relation. Introducing the polynomial

$$P_{0,I}(\tilde{\omega}) = (\tilde{\omega} + \tilde{\omega}_{E\times B})\left[(1 + \tilde{k}^2 + \tilde{\omega}_{pe}{}^2)\tilde{\omega}^2 - \mu\tilde{\omega}_{pe}{}^2(1 + \tilde{k}^2)\right] + \tilde{\omega}^2\tilde{\omega}_{pe}{}^2\tilde{\omega}_*/\tilde{k}^2 \tag{3.79}$$

the dispersion relation is

$$P_I(\tilde{\omega}) = P_{0,I}(\tilde{\omega}) + i\tilde{\nu}Q(\tilde{\omega}) = 0. \tag{3.80}$$

where the Q polynomial is the same as in Section 3.2.2 (Eq. (3.24)). Interestingly,

$$P_{0,I}(\tilde{\omega}) = P_0(\tilde{\omega}) + \tilde{\omega}^2\tilde{\omega}_{pe}{}^2\tilde{\omega}_*/\tilde{k}^2 \tag{3.81}$$

under the assumption that $\tilde{\omega}_{E\times B} = \tilde{\omega}_d$. Eq. (3.80)) is valid as long as the frequency of the instability is smaller than the electron cyclotron harmonics, where a kinetic description of the Bernstein modes is required [5, 133, 9, 92]. Inspecting the following table, $P_{0,I}$ has always two negative roots and one positive root:

$\tilde{\omega}$	$-\infty$	$-\tilde{\omega}_{E\times B}$	0	$+\infty$
$P_{0,I}(\tilde{\omega})$	<0	>0	<0	>0

Let $\tilde{\omega}_r$ be the positive root. Since $\tilde{\nu} \ll 1$, collisions can be treated as a perturbation term. Once again, the perturbed solution being $\tilde{\omega}_r + i\tilde{\nu}\delta$, to the first order in $\tilde{\nu}$,

$$P_I(\tilde{\omega}_r + i\tilde{\nu}\delta) = 0 \Leftrightarrow \delta = -Q(\tilde{\omega}_r)/P'_{0,I}(\tilde{\omega}_r) \tag{3.82}$$

The growth rate of the wave is hence

$$\boxed{\tilde{\xi} = -\frac{\tilde{\nu}Q(\tilde{\omega}_r)}{P'_{0,I}(\tilde{\omega}_r)}} \tag{3.83}$$

Since $P'_{0,I}(\tilde{\omega}_r) > 0$, the mode stability is determined by the sign of $Q(\tilde{\omega}_r)$. If $\tilde{\omega}_* = \tilde{\omega}_{E\times B} = 0$, the positive root is

$$\tilde{\omega}_r = \mu^{1/2}\left(\frac{1}{\tilde{\omega}_{pe}{}^2} + \frac{1}{1+\tilde{k}^2}\right)^{-1/2}, \tag{3.84}$$

a mode transiting from the lower hybrid frequency at low $\tilde{k}$'s to the ion plasma frequency at high $\tilde{k}$'s, and damped by collisions. If $\tilde{\omega}_{E\times B} = 0$, but $\tilde{\omega}_* \neq 0$, the solution is

$$\tilde{\omega}_r = \frac{\tilde{\omega}_*\tilde{\omega}_{pe}{}^2\left\{\left[1 + \frac{4\mu\tilde{k}^4(1+\tilde{k}^2)(1+\tilde{k}^2+\tilde{\omega}_{pe}{}^2)}{\tilde{\omega}_{pe}{}^2\tilde{\omega}_*^2}\right]^{\frac{1}{2}} - 1\right\}}{2\tilde{k}^2(1+\tilde{k}^2+\tilde{\omega}_{pe}{}^2)} \tag{3.85}$$

The general instability criterion is found by solving jointly $P_0(\tilde{\omega}) = 0$ (the mode exists) with $Q(\tilde{\omega}) = 0$ (the mode is at stability limit):

$$\boxed{\tilde{\omega}_* - \tilde{\omega}_{E\times B} = \tilde{\omega} = \frac{\mu^{1/2}\tilde{k}}{(1+\tilde{k}^2/\tilde{\omega}_{pe}{}^2)^{1/2}}.} \tag{3.86}$$

This criterion is exactly the same one as in the homogeneous fluid model (see Eq. (3.38)) when $\tilde{\omega}_d = \tilde{\omega}_* - \tilde{\omega}_{E\times B}$. This confirms that the plasma is unstable when the total fluid electron drift is higher than the ion sound speed. The numerical resolution of the two other roots of P_I shows that they are all stable in the regime of interest here.

The most unstable mode $\tilde{k}_{\max}$ can be solved numerically for all the plasma conditions. Under the assumption

$$\tilde{\omega}_{E\times B} = 0\,,\ \tilde{\omega}_{pe} \to \infty\,,\ \text{ and } \tilde{\nu} \to 0\,, \tag{3.87}$$

the following power law was found to be in very good agreement with the numerical determination of the most unstable mode

$$\boxed{\tilde{k}_{\max} = 0.709\left(\frac{\tilde{v}_*}{\mu^{1/2}}\right)^{0.362}.} \tag{3.88}$$

Moreover, the equilibrium electron momentum conservation equation (Eq. (2.10)) in normalized quantities is

$$-\tilde{\phi}' = -\frac{\tilde{n}'}{\tilde{n}} - \tilde{v}_x \left(\frac{1}{\tilde{\nu}} + \nu\right) . \tag{3.89}$$

Using Eqs. (3.78) and (3.89) for low wavenumbers, the plasma is unstable if:

$$\tilde{v}_x \left(1/\tilde{\nu} + \tilde{\nu}\right) > \mu^{1/2}. \tag{3.90}$$

At the sheath edge, $\tilde{v}_x = \mu^{1/2}$, and $1/\tilde{\nu} + \tilde{\nu}$ is greater than 1 for all $\tilde{\nu} > 0$. Therefore, the plasma is always unstable, at least at the sheath edge, as long as the electrons are magnetized ($\tilde{l} \gg 1$). The destabilization of similar modes by collisions was first found experimentally [15, 78] and explained theoretically by Chen [36] as a particular type of resistive drift mode [35].

3.2.4 Comparison of the Two Models

Figs. 3.7 and 3.8 show the solutions of the dispersion relations for $\tilde{\omega}_{pe} = 2$ and $\tilde{v}_{E\times B} = 0.2\mu^{1/2}$. The $E \times B$ drift $\tilde{v}_{E\times B}$ is here equal to $\tilde{\omega}_{E\times B}/\tilde{k}$, such that $\tilde{\mathbf{v}}_{E\times B} = -\tilde{v}_{E\times B}\mathbf{e}_y$. We remind that all the dispersion relations investigated here correspond to the high magnetic field approximation ($\tilde{\omega} \ll 1$). In every case, at high wavenumbers $\tilde{k}$, two modes represent the ion plasma oscillations $\tilde{\omega} = \pm\mu^{1/2}\tilde{\omega}_{pe}$ and the third mode represents the electron beam mode $\tilde{\omega} = \tilde{\omega}_d$. At low wavenumbers, the ion plasma oscillations become lower hybrid modes $\tilde{\omega} = \mu^{1/2}$. The collisionless case is illustrated in Fig. 3.8(b) in the case where $\tilde{v}_* = 1.3\mu^{1/2}$. In the collisionless case, only the inhomogeneous plasma theory can predict the anti-drift mode [139] at low wavenumber, where the frequency is proportional to $-\tilde{k}^{-1}$. In the present models, the growth rate is always zero without collisions, but we are aware that other mechanisms can cause instabilities to form in experimental plasmas, such as a non-zero component of the wavevector in the direction parallel to the magnetic field for example. The latter mechanism triggers the well-known *flute mode* [37].

Adding collisions to the models leads to non-zero imaginary parts of the solutions of the dispersion relations. In most cases, collisions result in a damping of plasma oscillations (negative imaginary part), but the plasma can also become unstable in some cases. We first notice that the homogeneous plasma model where the drift velocity is equal to the $E \times B$ drift predicts that the plasma is always stable for $E \times B$ drifts lower than the Bohm speed, while PIC simulations showed that the plasma's unstable behavior appeared even at relatively low electric fields. In the homogeneous plasma model, the instability can be interpreted as a wave mixing between the electron beam mode and the lower hybrid / ion plasma mode. In the frame of the inhomogeneous plasma theory, the potentially unstable mode is the only mode that propagates in the drift direction (positive real part).

Stability criteria were established in Sections 3.2.2 and 3.2.3 in the frameworks of homogeneous and inhomogeneous plasma theories. It was found that the homogeneous plasma theory yields the same stability criterion as the inhomogeneous

plasma theory, provided that the electron drift velocity is the sum of the $E \times B$ and the diamagnetic drift. However, in a homogeneous plasma, the diamagnetic drift should be zero, and the electron beam mode should be defined by $\tilde{\omega} = -\tilde{\omega}_{E\times B}$, which is in agreement with the predictions of the inhomogeneous plasma theory. The diamagnetic drift can be added to the electron drift of the homogeneous plasma theory, but this would completely neglect finite Larmor radius effects, which seem to play an essential role in our case. The models are compared to each other in Fig. 3.7. For a diamagnetic drift velocity equal to $1.1u_B$ ($\tilde{v}_*/\mu^{1/2} = 1.1$), the electron beam mode is correctly predicted by the homogeneous theory with $\tilde{v}_d = -\tilde{v}_{E\times B}$ but with no unstable mode. The instability criterion corresponds better to $\tilde{v}_d = \tilde{v}_* - \tilde{v}_{E\times B}$. Nevertheless, the growth rate is overestimated in the latter case.

Fig. 3.8(b) shows the harmonic solutions for the different dispersion relations in the collisionless case. Although the inhomogeneous plasma theory yields a growth rate proportional to $\tilde{\nu}$ for the resistive drift wave instability (Eq. (3.83)), the homogeneous plasma theory predicts a growth rate proportional to $\tilde{\nu}^{1/2}$ for the most unstable mode Eq. (3.44). As it is shown in Fig. 3.9(a), the homogeneous plasma theory tends to overestimate the growth rate of the instability. In the framework of homogeneous plasma theory, the discrepancy between the growth rate predicted by the mode intersection and the numerical solution of the dispersion relation comes from the approximation $\tilde{\nu}^{1/2} \ll \tilde{\omega}$ which is necessary in order to apply the perturbation theory on the solution of the homogeneous plasma dispersion relation, but can be difficult to satisfy. Fig. 3.9(b) shows the most unstable modes predicted by the various models as a function of the diamagnetic drift normalized to the Bohm speed. The homogeneous plasma theory predicts that the normalized wavenumber of the most unstable mode goes to zero for very high diamagnetic drifts, which is in disagreement with the inhomogeneous plasma theory that predicts that a minimum $\tilde{k}_{\max}$ should exist.

The predictions of the linear perturbation theory in the framework of homogeneous plasma and inhomogeneous plasma are summarized in Table 3.4.

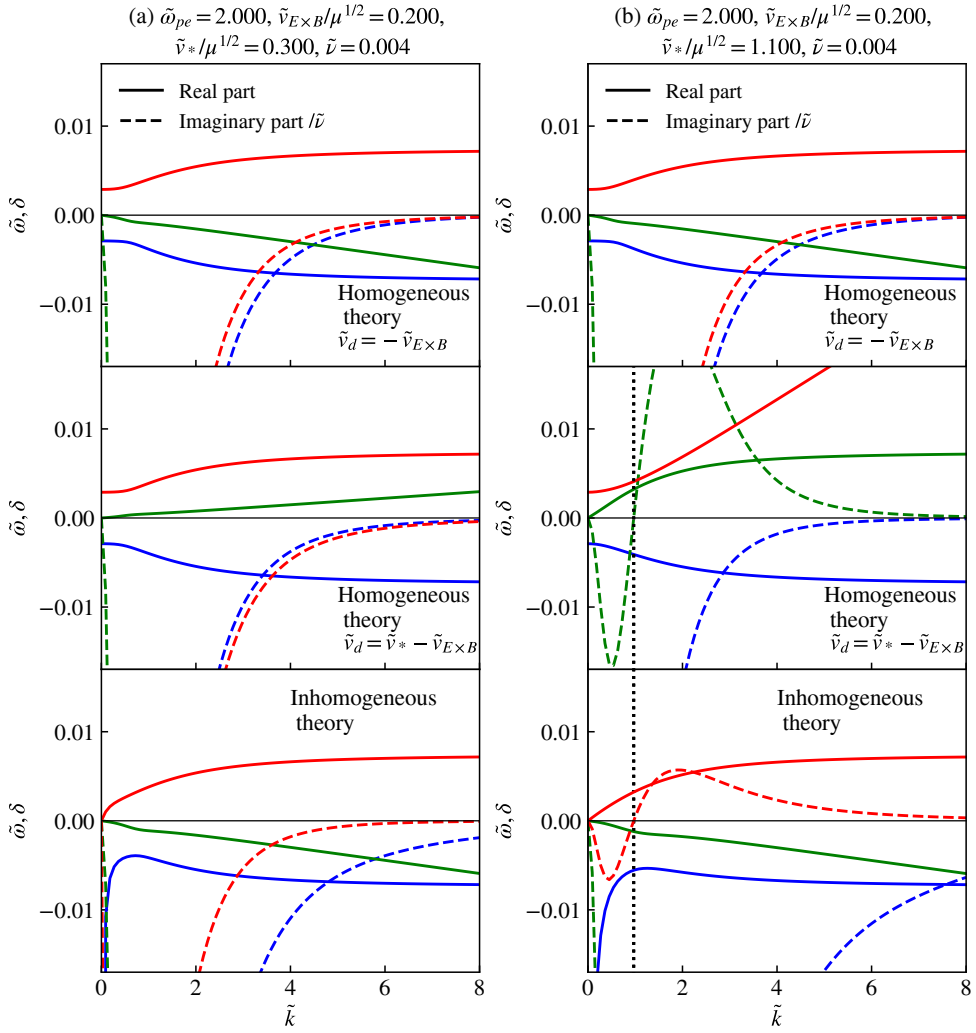

Figure 3.7: Phase diagrams for the three solutions (in blue, green, and red) of the polynomial dispersion relations $(\tilde{k},\tilde{\omega})$ in normalized units plotted using various theories. The real part is represented in solid line and the reduced growth rate $\delta=\tilde{\xi}/\tilde{\nu}$ in dashed line. The top diagrams correspond to the homogeneous plasma theory, where the $E\times B$ drift is taken as the drift velocity. The diagrams in the middle present the homogeneous plasma theory with a drift velocity equal to the sum between the $E\times B$ and the diamagnetic drifts. The diagrams in the bottom represent the more accurate inhomogeneous plasma theory. (a) Stable configuration $(\tilde{v}_*-\tilde{v}_{E\times B}<\mu^{1/2})$; (b) Transition to unstable plasma. The vertical dotted line represents the transition to unstable wavenumbers.

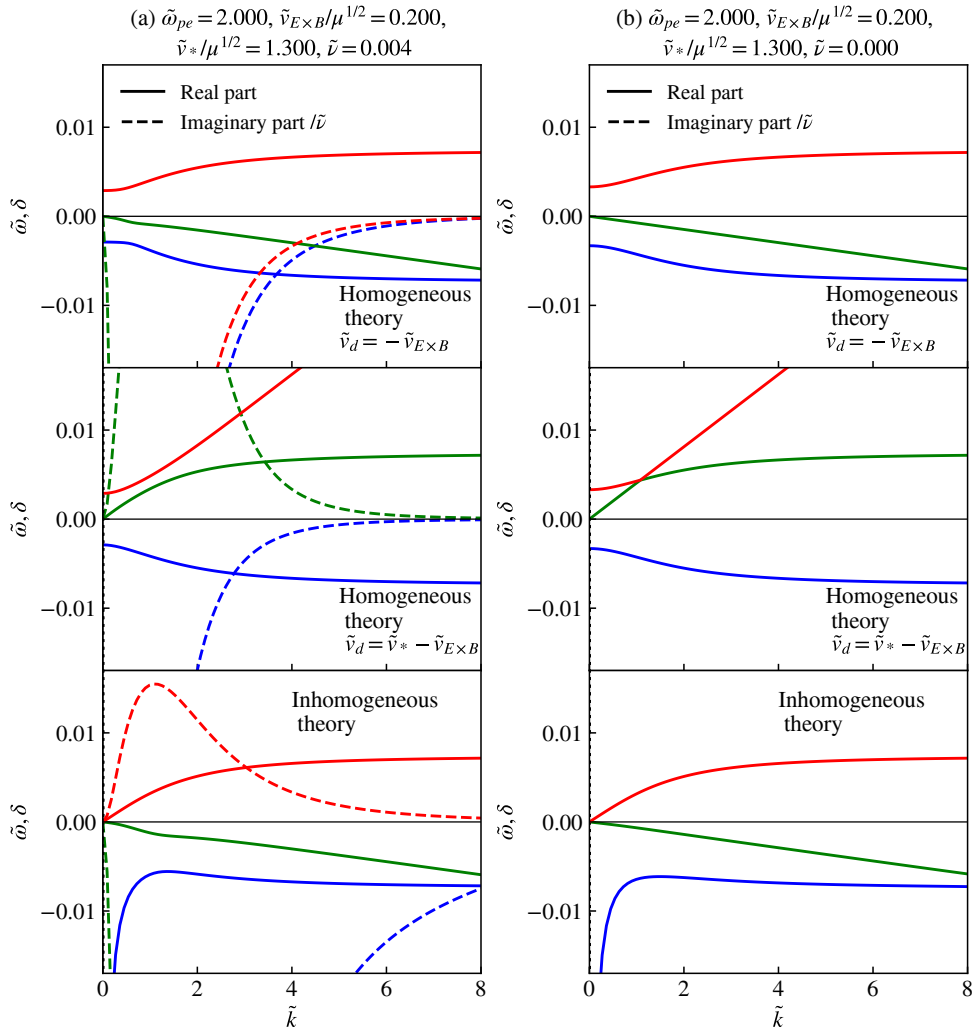

Figure 3.8: Phase diagrams for the three solutions (in blue, green, and red) of the polynomial dispersion relations $(\tilde{k},\tilde{\omega})$ in normalized units plotted using various theories. The real part is represented in solid line and the reduced growth rate $\delta = \tilde{\xi}/\tilde{\nu}$ in dashed line. The top diagrams correspond to the homogeneous plasma theory, where the $E\times B$ drift is taken as the drift velocity. The diagrams in the middle present the homogeneous plasma theory with a drift velocity equal to the sum between the $E\times B$ and the diamagnetic drifts. (a) Unstable configuration $(\tilde{v}_* - \tilde{v}_{E\times B} > \mu^{1/2})$. (b) Collisionless case (harmonic waves).

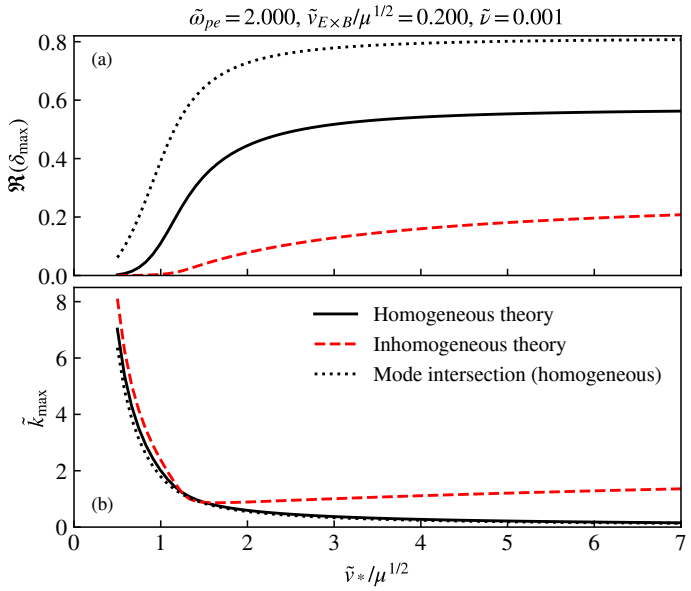

Figure 3.9: The most unstable modes are computed numerically using the homogeneous plasma theory where $\tilde{v}_d = \tilde{v}_* - \tilde{v}_{E\times B}$ (solid black lines) and the inhomogeneous plasma theory (red dashed lines). (a) Maximum growth rate divided by the collision frequency $\Re(\delta_{\max})$. (b) Corresponding wavenumber $\tilde{k}_{\max}$. The black dotted lines correspond to the intersection between the harmonic modes $\tilde{\omega} = \tilde{\omega}_d$ and $\tilde{\omega} = \tilde{\omega}_+$ in the homogeneous plasma case ("wave mixing").

	Homogeneous plasma	**Inhomogeneous plasma**
Frequency $\tilde{\omega}_r$	$\min\left\{\tilde{\omega}_*, \tilde{\omega}_{pe}\left[\frac{\mu(1+\tilde{k}^2)}{1+\tilde{k}^2+\tilde{\omega}_{pe}}\right]^{1/2}\right\}$	$\frac{\tilde{\omega}_*\tilde{\omega}_{pe}{}^2\left\{\left[1+\frac{4\mu\tilde{k}^4(1+\tilde{k}^2)(1+\tilde{k}^2+\tilde{\omega}_{pe}{}^2)}{\tilde{\omega}_{pe}{}^2\tilde{\omega}_*^2}\right]^{\frac{1}{2}}-1\right\}}{2\tilde{k}^2(1+\tilde{k}^2+\tilde{\omega}_{pe}{}^2)}$
Maximum growth rate $\tilde{\xi}_{\max}$	$\frac{\tilde{\nu}^{1/2}}{2^{3/2}}\left[\frac{\mu\tilde{\omega}_{pe}{}^6}{(1+\tilde{k}^2)(1+\tilde{k}^2+\tilde{\omega}_{pe}{}^2)^3}\right]^{1/4}$	$-\frac{\tilde{\nu}Q(\tilde{\omega}_r)}{P'_{0,I}(\tilde{\omega}_r)}$
Most unstable mode $\tilde{k}_{\max}$	$\approx \frac{\tilde{\omega}_{pe}\mu^{1/2}}{\tilde{v}_d}$	$0.709\left(\frac{\tilde{v}_*}{\mu^{1/2}}\right)^{0.362}$
Instability criterion	$\tilde{\omega}_d > \frac{\mu^{1/2}\tilde{k}}{(1+\tilde{k}^2/\tilde{\omega}_{pe}{}^2)^{1/2}}$	$\tilde{\omega}_* - \tilde{\omega}_{E\times B} > \frac{\mu^{1/2}\tilde{k}}{(1+\tilde{k}^2/\tilde{\omega}_{pe}{}^2)^{1/2}}$
Electron beam mode	$\tilde{v}_d$	$\tilde{v}_{E\times B}$
Anti-drift mode	No	Yes, in $-\tilde{k}^{-1}$

Table 3.4: Comparison between the analytical results of the homogeneous and the inhomogeneous plasma theories of linear perturbations for low collision frequencies. On the RHS column, the assumption $\tilde{v}_d \approx \tilde{v}_* \gg \tilde{v}_{E\times B}$ was made.

3.2.5 Comparison with the PIC Simulations

Until Section 3.3.4, the de-normalized physical quantities are used again.

On the shorter time-scale, the spectrum of the grid data extracted from the PIC simulation can be computed and compared with the simple 1D models described above. The variable that is selected is the azimuthal electric field

$$E_\theta = \cos\theta E_y - \sin\theta E_x \tag{3.91}$$

where the polar angle θ is defined from the center of the discharge

$$\tan\theta = \frac{y - \tilde{l}_y/2}{x - \tilde{l}_x/2} \tag{3.92}$$

The advantage of this variable is that it should be approximately 0 in a stable plasma, away from the corners, even if the electrons are drifting. Therefore, the measured signal is either noise or an instability pattern. The distance from the center

$$r = (x - \tilde{l}_x/2)^2 + (y - \tilde{l}_y/2)^2 \tag{3.93}$$

is also introduced. The azimuthal electric field $E(r, \theta, t)$ contains the temporal and spatial spectra in t and θ respectively, at a given radial position r. The analogy with the 1D model is performed by assuming that the direction called y in the previous section is now represented by the distance along a circle of radius r, namely $r\theta$. Fig. 3.10 shows the map of the azimuthal electric field at 3 Torr and 20 mT. Of course, the 1D pseudo-cylindrical model cannot apply near the corners where the equilibrium azimuthal electric field is not zero anymore. In particular, one can observe that the azimuthal electric field becomes very high in the sheaths. This is, of course, a feature of the plasma equilibrium and does not come from the instability. At the center of the discharge, the amplitude of the instability is significantly lower. Since we have seen that the drift velocity was much lower at the discharge center, this is in agreement with the fact that the instability can develop only when the drift velocity is high enough. At low magnetic field, the drift velocity is higher than the Bohm speed only near the sheath edge. When the magnetic field increases, the instability penetrates inside the discharge until a certain penetration length. However, since the instability pattern is not purely azimuthal, the waves tend to travel radially, such that measuring a penetration length of the instability is not so easy.

In Fig. 3.11, the 2D maps of the azimuthal electric field are represented for a discharge at 3 mTorr in the non-magnetized case (a), and with magnetic fields of 10 mT (b) and 20 mT (c). The color scale is saturated in Fig. 3.11(c) to allow qualitative comparison with the noise detected in the non-magnetized case.

For a given radial position equal to 9 mm, the signal E_θ is plotted as a function of θ and t in Fig. 3.12(a) when the discharge has reached a steady state (for $t > 35\,\mu s$ in this case). The instability pattern has a quite distinct structure with several modes that can be appreciated by eye. The angular phase velocity can here be estimated

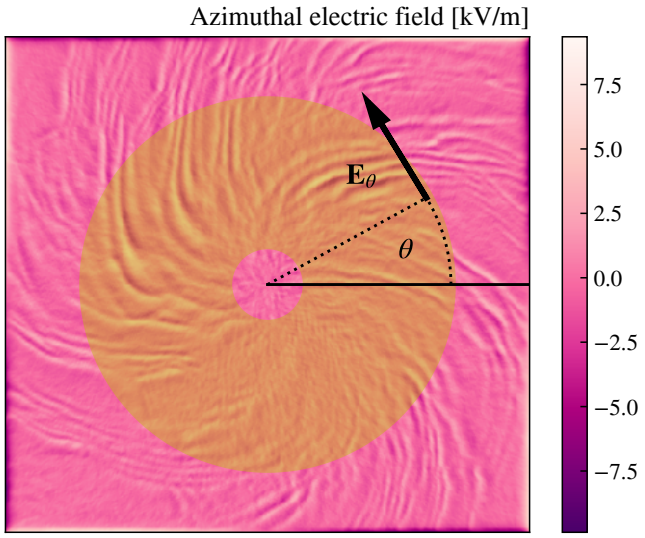

Figure 3.10: Map of the azimuthal electric field for a run at 3 mTorr and 20 mT. The Fourier transforms are performed in the azimuthal direction using $E_\theta(\theta)$.

to about 4.7×10^5 rad/s which corresponds to 4.2 km/s at a distance of 9 mm from the center. This is significantly higher than the Bohm speed (typically 2.7 km/s at $T_e = 3$ eV).

In order to be more accurate and to capture the different modes that develop in the plasma, Fourier transforms of E_θ for a given value of r can be performed, using the `scipy` fast Fourier transform algorithm. The 2D Fourier transform (FT) of $E_\theta(r\theta, t)$ for the typical run at 3 mTorr and 20 mT is plotted in Fig. 3.12(b). The original data were extracted with a rate of 30 ns to achieve the 2D FT but the result remains quite noisy. To allow for comparisons with the theoretical spectra, a 2D Gaussian filter was applied to the signal with a standard deviation $\sigma = 12.5$ (in both directions). The time-averaged and θ-averaged steady state plasma properties a $r = 9$ mm are summarized in Table 3.5. These numerical values can be inserted into the dispersion relation found with the inhomogeneous plasma theory (Eq. (3.80)) to provide a theoretical spectrum. This theoretical spectrum is plotted in solid cyan line in Fig. 3.12(b) and matches well the transformed PIC data. The approximate formulae of Eqs. (3.80) and (3.84) show good agreements with the simulated spectrum as well. Although it is not shown directly here, the solution of the dispersion relation coming from the homogeneous plasma theory with a drift velocity $\tilde{v}_d = \tilde{v}_* - \tilde{v}_{E\times B}$ also shows a good agreement at least for the real part. The transition from the lower hybrid mode to the ion plasma mode is also clearly visible in the transformed PIC data.

The 1D Fourier transforms are also presented in Fig. 3.13 in time (a) and space (b) for magnetic fields of 5, 10, 20 and 40 mT. Both series of curves feature clear maxima at the typical frequency and wavenumber of the instability. Once the in-

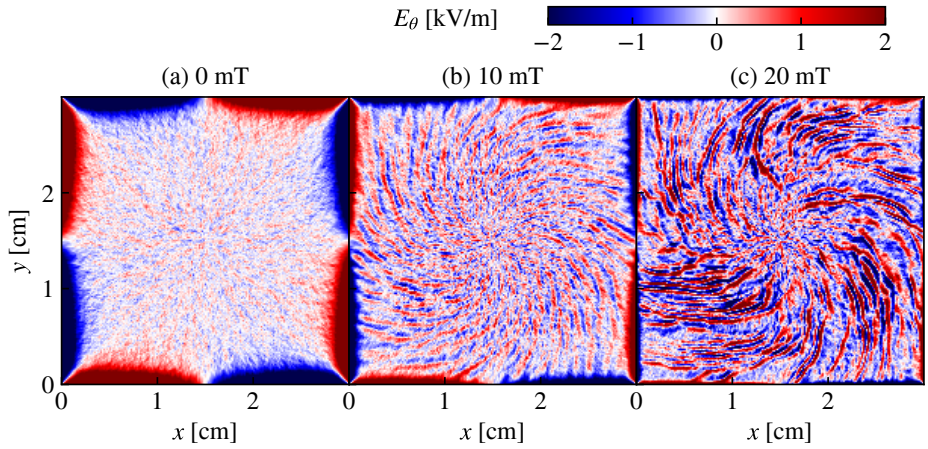

Figure 3.11: Snapshots of the azimuthal electric field in polar. Simulations were run at 3 mTorr of gas pressure, for magnetic fields of 0, 10, and 20 mT.

stability is triggered, the typical frequency and the wavenumber remain of the same order of magnitude. The temporal Fourier transform is averaged in θ and the spatial Fourier transform is averaged in time, such that the original curves are not so noisy even for sampling rates up to 100 ns. Gaussian filters (with $\sigma = 2$ and 3) were still employed to yield better estimates of the maxima of the curves.

The advantage of the inhomogeneous plasma theory compared to the homogeneous plasma approximation is revealed when looking at the growth rates of the various modes. As explained above (see, for example, Fig. 3.9), the growth rates and the most unstable wavenumbers predicted by both approaches are very different. The instability growth rate was also estimated in the PIC simulation. This requires particular care because the plasma equilibrium builds up at the same time as the instability develops. At every sampling time, the spatial Fourier transform was computed for a given mode whose amplitude can hence be tracked over time. The result is shown in Fig. 3.14 for wavenumbers corresponding to ρ_{Le}, $\rho_{Le}/2$, and $3\rho_{Le}/4$. The data was initially very noisy and had to be smoothed with a quite broad Gaussian filter ($\sigma = 30$). The mode amplitude is very small during the first few microseconds of the simulation. This onset time, which corresponds to the time needed for the discharge to build up, from the initial uniform situation was fitted manually and estimated to be about 4.2 µs. The mode amplitudes then seem to saturate. The exponential growths predicted by the linear perturbation theory are plotted in dotted lines in Fig. 3.14 (the y axis is in log scale so the exponential growth appears as a straight line). The growth rates are reasonably well predicted by the linear theories when the instability develops. Of course, the linear theory cannot capture the saturation of the instability. We are aware that the latter data analysis is at the limit of what can be extracted from the PIC simulations performed here. A more detailed investigation of the instability growth could be performed for example by starting a simulation with specially prepared initial electron and ion distributions that would

Magnetic field	20	mT
Pressure	3	mTorr
Plasma density	1.8×10^{16}	m^{-3}
Electron temperature	3.84	eV
Diamagnetic drift	17.3	km/s
$E \times B$ drift	-4.3	km/s

Table 3.5: Numerical quantities of the simulation used to solve the dispersion relation in Fig. 3.12. The plasma density and the diamagnetic drift are measured at steady state for the run at 20 mT and 3 mTorr, at $r = 9$ mm from the discharge center, and averaged over time and over θ.

correspond to a time-averaged plasma equilibrium under the same conditions. The number of particles should also be increased to reduce the noise level. Finally, a purely cylindrical simulation code could be used to remove the effects of the corners.

Using a series of data generated in the same way as for Fig. 3.13(b) we could identify the dominant mode in the PIC data and compare it with the most unstable mode predicted by the fluid theory for a wide range of conditions of pressure and magnetic field. The comparison is presented in Fig. 3.15, which is analogous to Fig. 3.9 but with assumptions (3.87). These assumptions of weak $E \times B$ drift and low collision frequency are only approximately valid in the PIC simulations but they do not have a major contribution to the solution and allow to plot all the data on the same graph. The drift velocity is measured directly from the simulation at a distance of 9 mm from the discharge center. The drift velocity decreases with the magnetic field, so the runs at higher magnetic field are on the LHS of the curve. Considering the data quality and the methods employed to treat it, a typical error of 15 to 20% should be assumed on the estimates of the dominant modes. At high magnetic field, the agreement between the dominant mode in the simulation and the most unstable mode predicted by the inhomogeneous plasma theory of linear perturbations is satisfactory. In our LTP conditions, when the ratio between the diamagnetic drift and the Bohm speed is larger than about 10, the instability is not seen in the simulation, and the dominant mode departs from the prediction of the linear perturbation theory. The homogeneous plasma theory predicts that the wavenumber of the most unstable mode should decrease with the diamagnetic drift, which does not seem to match the simulation data.

As will be seen in the next Section, the $E \times B$ drift becomes negligible at high magnetic fields, such that the part of the graph that corresponds to $\tilde{v}_*/\mu^{1/2} < 1$ would correspond to a stable configuration. This could define a condition of marginal stability that may be of interest to describe the plasma for magnetic fields higher than those investigated in the present work. This condition will be partially discussed in Section 3.3.4.

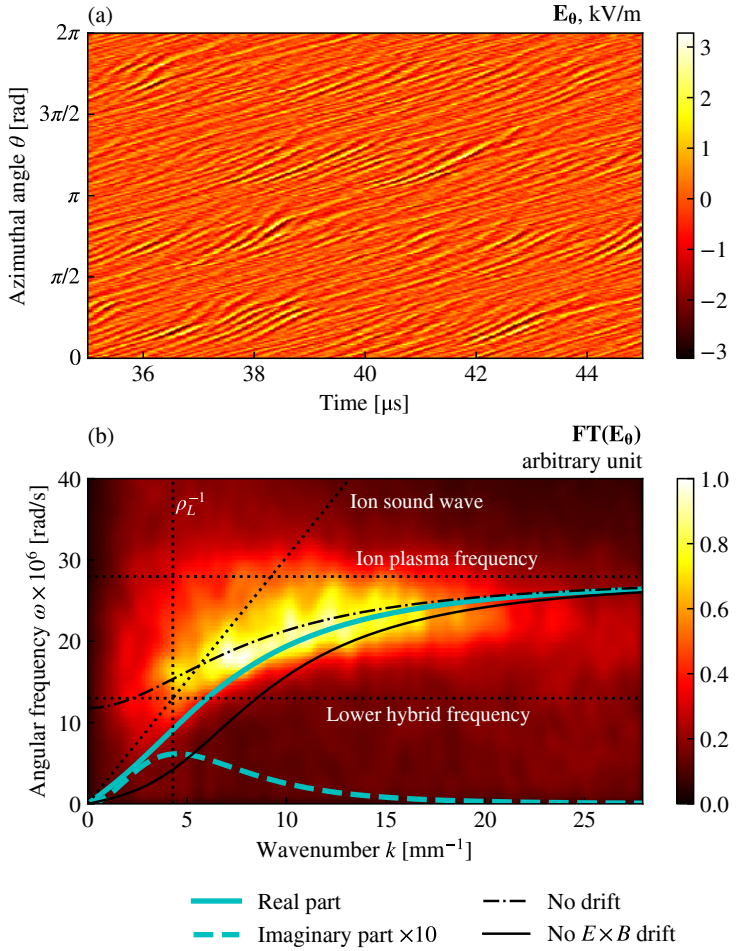

Figure 3.12: (a) The azimuthal electric field obtained at 3 mTorr, and 20 mT, at a distance of 9 mm from the center of the simulation domain. (b) The corresponding spatio-temporal FT (color plot) with a numerical solution of Eq. (3.80) in cyan, approximate solutions in dashed (Eq. (3.84)) and solid black lines (Eq. (3.85)), with the parameters of Table 3.5. All the theoretical curves come from the inhomogeneous plasma theory.

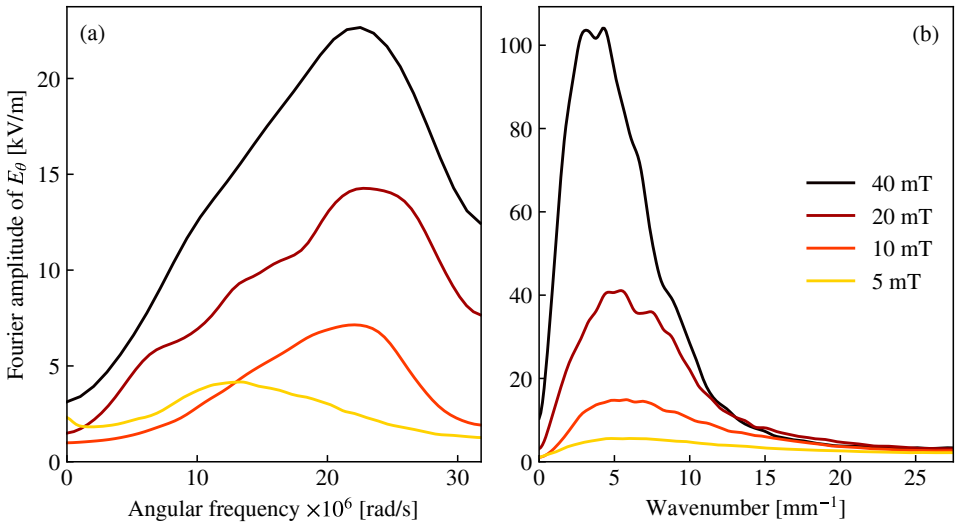

Figure 3.13: Fourier spectra of the azimuthal electric field $E_\theta(\theta, t)$ at a distance $r = 9$ mm from the discharge center for several values of the magnetic field, at 3 mTorr of gas pressure. (a) Temporal Fourier transform averaged in θ with a Gaussian filter ($\sigma = 2$). (b) Spatial Fourier transform averaged in time with a Gaussian filter ($\sigma = 3$). The spatial coordinate is $r\theta$.

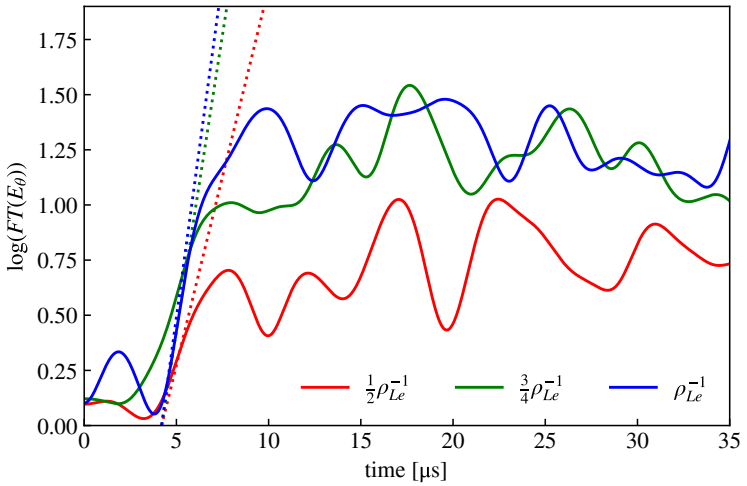

Figure 3.14: Instability growth rates at 3 mTorr and 20 mT, at a distance $r = 9$ mm from the discharge center for various wavenumbers. The data extracted from the PIC simulation (solid lines) is compared with the predictions of the inhomogeneous plasma theory (dotted lines).

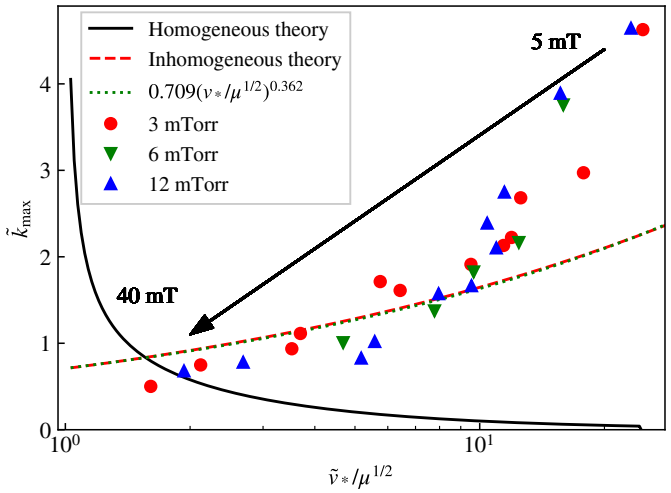

Figure 3.15: Comparison between the most unstable mode $\tilde{k}_{\max} = k_{\max}\rho_{Le}$ predicted by the inhomogeneous (red dashed line) and homogeneous (solid black line) linear fluid theories with simplifying assumptions of Eq. (3.87), and the Fourier spectrum of the PIC simulation data (solid markers) at a distance $r = 9\,\text{mm}$ from the discharge center. The x axis is the diamagnetic drift normalized to the Bohm speed. The magnetic field of the PIC simulation is varied from 5 to 40 mT. The fit (green dotted line) is given by Eq. (3.88)

3.3 Transport Theory at High Magnetic Fields

The general 1D model of the plasma transport described in Chapter 2 was based on the ambipolar assumption in the transport direction. While this assumption is perfectly justified in 1D, it cannot be made in 2D. The non-magnetized 2D case could be treated by assuming Boltzmann electrons in Section 2.3, but this assumption does not hold either at high magnetic fields. The general two-fluid magnetohydrodynamics (MHD) equations do not seem to have analytical solutions, even in a quasineutral isothermal plasma. In this section, we will show that the electric field becomes weak at high magnetic fields and that, under these conditions, the properties of the plasma equilibrium can be estimated with very simple formulae.

3.3.1 Two-dimensional Isothermal Model

The Weak Electric Field Assumption

The approximation where the electric field is neglected was already used by Sternberg *et al.* [146] to model the radial profile of a magnetized plasma column. The behavior of the electric field can be explained by observing that the electric field always accelerates the ions to the walls, and does not change sign at high magnetic field. Then, looking at the steady state electron momentum balance equation along x as it was done to obtain Eq. (2.10)

$$-k_B T_e \frac{n'}{n} - eE - m_e \nu_e (1+{\eta_e}^2) v = 0$$

where x is here defined from the discharge center, and v is the ambipolar plasma velocity along the x axis. We found in the simulations that $E > 0$, $n'/n < 0$ and $v > 0$ in the region $x \in [0, l_x/2]$. We also observed that the density profiles keep a familiar shape (approximately a cosine shape) such that

$$n'/n = 1/L \tag{3.94}$$

where L is a gradient length that remains of the order of the system size (except near the center). As the Hall parameter increases with the magnetic field, the electric field term does no have the right sign to balance the velocity term. Only the pressure term can balance the increase of the velocity term. Since the electron temperature and the gradient length remain bounded, the velocity also has to go to zero.

The ratio between the electric field term and the velocity term in the electron momentum conservation equation can be calculated by replacing n'/n with Eq. (2.30) in Eq. (2.10). This yields to the first order in T_i/T_e

$$\frac{eE}{m_e \nu_e v (1+{\eta_e}^2)} = \frac{m_i}{m_e \nu_e (1+{\eta_e}^2)} \left[\frac{\nu_{iz} + \frac{v^2}{D_a} - \frac{T_i}{T_e}\left(\frac{{u_B}^2}{D_a} + \nu_{iz}\right)}{1 - v^2/{u_B}^2} + \nu_{i,tot}(1+{\eta_i}^2) \right] \tag{3.95}$$

At high magnetic field, the ionization frequency can be estimated by Eq. (2.67) such that ν_{iz} goes to zero. Moreover, the ratio $\frac{m_i \nu_{i,tot}(1+{\eta_i}^2)}{m_e \nu_e (1+{\eta_e}^2)}$ is equal to $(m_e \nu_e)/(m_i \nu_{i,tot})$ at high magnetic field, which is very small. Finally,

$$D_a \approx \frac{m_i {u_B}^2}{m_e \nu_e (1+{\eta_e}^2)} \tag{3.96}$$

at high magnetic field. Therefore,

$$\frac{eE}{m_e \nu_e v (1+{\eta_e}^2)} = \frac{\left(\frac{v}{u_B}\right)^2 - \frac{T_i}{T_e}}{1 - \left(\frac{v}{u_B}\right)^2} \tag{3.97}$$

We can see here that the electric field might reverse because of the ion temperature. This was however not observed in the simulations. At high magnetic fields, the tangent velocity profile found in Chapter 2 is retained and the velocity is much lower than the Bohm speed everywhere except at the sheath edge. Everywhere in the plasma bulk, the ratio between the electric field term and the velocity term is hence of the order of $-T_i/T_e$ whose absolute value is much smaller than 1 in LTP conditions. The electric field term can thus be neglected in the transport equations of magnetized LTP, when the electron mobility becomes lower than the ion mobility (equivalent to Eq. (3.96)).

The model above is 1D and the assumption of low electric fields has to be validated in 2D. This can be done using the PIC simulation data. Fig. 3.16 shows the ratio between the electric field term and the electron pressure term in many simulated conditions, for $y = l_y/2$. When there is no magnetic field, the ratio is approximately 1 (or -1) everywhere in the plasma bulk , which corresponds to the Boltzmann equilibrium. When the magnetic field increases, both terms tend to decrease but the electric field term decreases much faster than the pressure term. For gas pressures of 3 and 6 mTorr, the electric field term is less than 15% of the pressure term when the magnetic field is higher than 15 mT. The effect is less visible at 12 mTorr as a higher magnetic field is required to reach the strongly magnetized regime.

Although 2D effects and the instability onset make the interpretation of the PIC data more complicated than with the simple 1D model described above, the low electric field assumption seems legitimate to describe the high magnetic field regime of the plasma column studied here.

Introduction of the Effective Collision Frequency

The effect of the instability on the time-averaged transport is difficult to predict. However, the momentum conservation equations can be written at a shorter timescale and then averaged in time to evidence the formal contribution of the instability. This was done, for example, by T. Lafleur for the study of the electron drift instability in Hall thrusters [91]. The electric field, the electron density and the electron

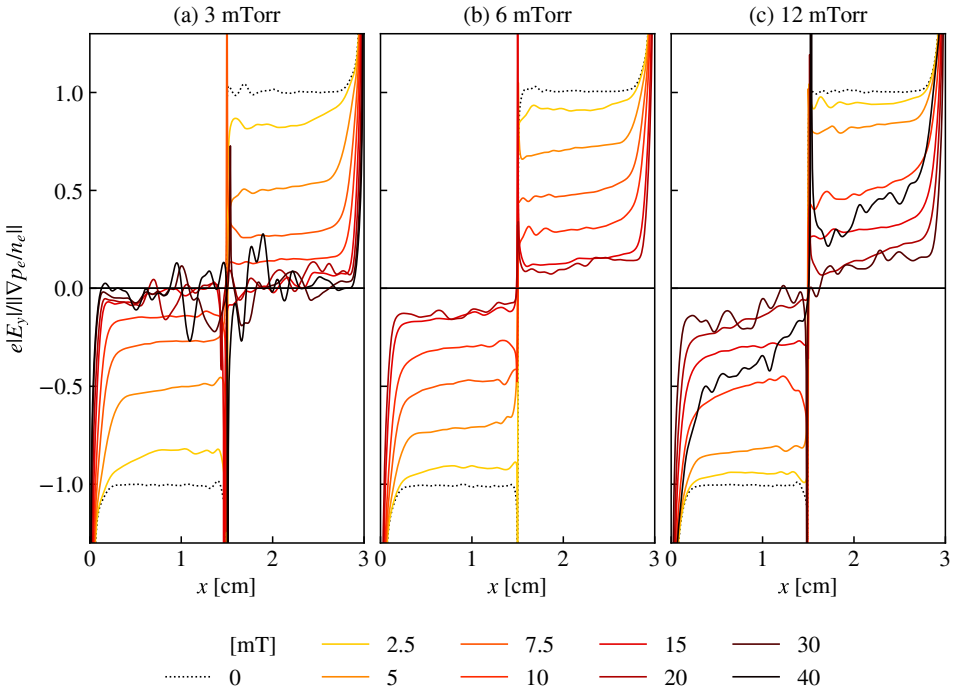

Figure 3.16: Ratio between the electric field term and the pressure term in the electron momentum conservation equation as a function of x, for $y = l_y/2$. The magnetic field is varied from 0 to 40 mT, for $p = 3$ mTorr (a), 6 mTorr (b) and 12 mTorr (c).

velocity can be split into a time-averaged ($\langle\cdot\rangle$) term and a fluctuating term:

$$n_e = \langle n_e\rangle + n_{e1}\ ;\ \mathbf{v}_e = \langle \mathbf{v}_e\rangle + \mathbf{v}_{e1}\ ;\ \mathbf{E} = \langle \mathbf{E}\rangle + \mathbf{E}_1 \tag{3.98}$$

By neglecting the electron inertia, the electron momentum conservation equation is

$$\begin{aligned} & m_e\left(\langle n_e\rangle\partial_t\mathbf{v}_{e1} + n_{e1}\partial_t\mathbf{v}_{e1}\right) \\ & + k_B T_e\left(\nabla\langle n_e\rangle + \nabla n_{e1}\right) + e\left(\langle n_e\rangle\langle\mathbf{E}\rangle + \langle n_e\rangle\mathbf{E}_1 + n_{e1}\langle\mathbf{E}\rangle + n_{e1}\mathbf{E}_1\right) \\ & + e\left[\left(\langle n_e\rangle\langle\mathbf{v}_e\rangle + \langle n_e\rangle\mathbf{v}_{e1} + n_{e1}\langle\mathbf{v}_e\rangle + n_{e1}\mathbf{v}_{e1}\right)\times\mathbf{B}\right] \\ & + m_e\nu_e\left(\langle n_e\rangle\langle\mathbf{v}_e\rangle + n_{e1}\langle\mathbf{v}_e\rangle + \langle n_e\rangle\mathbf{v}_{e1} + n_{e1}\mathbf{v}_{e1}\right) = 0\,. \end{aligned} \tag{3.99}$$

Since the time average of the fluctuating quantities is 0, the average of the equation above yields

$$\begin{aligned} & k_B T_e\nabla\langle n_e\rangle + e\left(\langle n_e\rangle\langle\mathbf{E}\rangle + \langle n_e\rangle\langle\mathbf{v}_e\rangle\times\mathbf{B}\right) + m_e\nu_e\langle n_e\rangle\langle\mathbf{v}_e\rangle \\ & + m_e\langle n_{e1}\partial_t\mathbf{v}_{e1}\rangle + e\langle n_{e1}\mathbf{E}_1\rangle + e\langle n_{e1}\mathbf{v}_{e1}\rangle\times\mathbf{B} + m_e\nu_e\langle n_{e1}\mathbf{v}_{e1}\rangle = 0\,. \end{aligned} \tag{3.100}$$

The four last terms of Eq. (3.100) are of second order with respect to the perturbation and account for the effects of the instability on the time-averaged plasma transport.

The same process can be applied to the electron continuity equation

$$\partial_t n_{e1} + \nabla\cdot\left(\langle n_e\rangle\langle\mathbf{v}_e\rangle + n_{e1}\langle\mathbf{v}_e\rangle + \langle n_e\rangle\mathbf{v}_{e1} + n_{e1}\mathbf{v}_{e1}\right) = \left(\langle n_e\rangle + n_{e1}\right)\nu_{iz} \tag{3.101}$$

The average yields

$$\nabla\cdot\left(\langle n_e\rangle\langle\mathbf{v}_e\rangle + \langle n_{e1}\mathbf{v}_{e1}\rangle\right) = \langle n_e\rangle\nu_{iz} \tag{3.102}$$

For wave perturbations along y

$$n_{e1} = n_{e10}\cos(\omega t - ky) \quad\text{and}\quad \mathbf{v}_{e10} = v_{e10}\cos(\omega t - ky - \varphi)\,\mathbf{e}_y \tag{3.103}$$

where φ is the phase angle between the density and velocity perturbations, and for an equilibrium profile that depends only on x,

$$\partial_x\left(\langle n_e\rangle\langle\mathbf{v}_{ex}\rangle\right) + \frac{\mathbf{v}_{e10}n_{e10}}{2}\partial_y\cos\varphi = \langle n_e\rangle\nu_{iz} \tag{3.104}$$

Hence

$$\partial_x\left(\langle n_e\rangle\langle\mathbf{v}_{ex}\rangle\right) = \langle n_e\rangle\nu_{iz} \tag{3.105}$$

Thus, the fluctuations do not affect the equilibrium electron continuity equation. In the work of T. Lafleur on Hall thrusters [91, 92], it is claimed that the main perturbation term in the electron momentum balance equation is the correlation term between the density and the electric field, and it is shown that the saturation comes from ion trapping, such that an estimate of the term $\langle n_{e1}\mathbf{E}_1\rangle$ is provided. Here, we assume that the main equilibrium perturbation also comes from the $\langle n_{e1}\mathbf{E}_1\rangle$ quantity and the only term with fluctuations that remains in Eq. (3.100) is $\langle n_{e1}\mathbf{E}_1\rangle$.

According to Eq. (3.77), the phase shift between the fluctuations of density and electric field is $\pi/2$ without collisions, in which case $\langle n_{e1}\mathbf{E}_1\rangle = 0$. So only collisions can introduce a term coming from fluctuating quantities in the equilibrium momentum conservation equation. The equilibrium continuity and momentum conservation equations are therefore

$$\nabla \cdot \left(\langle n_e\rangle\langle \mathbf{v}_e\rangle\right) = \langle n_e\rangle \nu_{iz} \tag{3.106}$$

and

$$0 = -k_B T_e \nabla\langle n_e\rangle - e\left(\langle n_e\rangle\langle \mathbf{E}\rangle + \langle n_e\rangle\langle \mathbf{v}_e\rangle \times \mathbf{B}\right) - m_e\nu_e\langle n_e\rangle\langle \mathbf{v}_e\rangle - e\langle n_{e1}\mathbf{E}_1\rangle \tag{3.107}$$

The last term of Eq. (3.107) cannot be estimated without investigating the saturation mechanism of the instability. A slightly different approach is proposed here compared to T. Lafleur *et al.* [91]. It is assumed that the two last terms of the RHS of Eq. (3.107) can be represented in the form of a collision term, with different effective collision frequencies in each direction. In the following, we get rid of the brackets $\langle\cdot\rangle$ for the time averaged quantities, and write

$$m_e\nu_e n_e \mathbf{v}_e + e\langle n_{e1}\mathbf{E}_1\rangle = m_e n_e \underline{\nu_{\text{eff}}}\,\mathbf{v}_e \tag{3.108}$$

where

$$\underline{\nu_{\text{eff}}} = \nu_x \mathbf{e}_x \otimes \mathbf{e}_x + \nu_y \mathbf{e}_y \otimes \mathbf{e}_y + \nu_z \mathbf{e}_z \otimes \mathbf{e}_z \tag{3.109}$$

is a diagonal effective collision tensor. It accounts both for the collisional processes and for the effects of temporal fluctuations on the mean plasma transport.

The Solution of the Model

At high magnetic fields, the equilibrium electric field is neglected, such that the stationary momentum conservation equation is

$$0 = -k_B T_e \nabla n_e - e n_e \mathbf{v}_e \times B - m_e n_e \underline{\nu_{\text{eff}}}\,\mathbf{v}_e \tag{3.110}$$

It is assumed that the plasma is quasineutral, hence $n_e = n_i = n$. The projections in the plane perpendicular to the magnetic field are therefore

$$-\omega_{ce}\Gamma_{ey} - {v_{Te}}^2 \partial_x n - \nu_x \Gamma_{ex} = 0 \tag{3.111}$$

$$\omega_{ce}\Gamma_{ex} - {v_{Te}}^2 \partial_y n - \nu_y \Gamma_{ey} = 0 \tag{3.112}$$

where Γ_{ex} and Γ_{ey} are the components of the equilibrium electron flux $\mathbf{\Gamma}_e = n\mathbf{v}_e$. The electron flux is then

$$\Gamma_{ex} = -\frac{{v_{Te}}^2}{{\omega_{ce}}^2 + \nu_x\nu_y}(\nu_y \partial_x n - \omega_{ce}\partial_y n) \tag{3.113}$$

$$\Gamma_{ey} = -\frac{{v_{Te}}^2}{{\omega_{ce}}^2 + \nu_x\nu_y}(\nu_x \partial_y n + \omega_{ce}\partial_x n) \tag{3.114}$$

We now assume that ν_x and ν_y are independent of space. Although this is not strictly true, but it allows to solve the set of equations and will later be justified by the PIC simulations. Injecting these expressions in the steady state continuity equation,

$$\nu_y \partial_x^2 n + \nu_x \partial_y^2 n = -\left({\omega_{ce}}^2 + \nu_x \nu_y\right) \frac{\nu_{iz}}{{v_{Te}}^2} n \,. \tag{3.115}$$

Eq. (3.115) is a generalized Helmholtz equation that has solutions under the form

$$\begin{aligned} n = n_0 \cos \left[\left({\omega_{ce}}^2 + \nu_x \nu_y\right)^{\frac{1}{2}} \left(\frac{\nu_{iz}}{\nu_y}\right)^{\frac{1}{2}} \frac{x}{v_{Te}} + \varphi_x \right] \\ \times \cos \left[\left({\omega_{ce}}^2 + \nu_x \nu_y\right)^{\frac{1}{2}} \left(\frac{\nu_{iz}}{\nu_x}\right)^{\frac{1}{2}} \frac{y}{v_{Te}} + \varphi_y \right] \end{aligned} \tag{3.116}$$

where n_0 is the maximum density, and φ_x and φ_y are integration constants that depend on the initial conditions. Since the maximum density is reached at the center of the domain, $\varphi_x = \varphi_x = 0$. We have already seen in Section 2.2.4 that the Bohm criterion at high magnetic fields is equivalent to Schottky's boundary conditions: $n = 0$ at the walls. Using the latter condition:

$$n = n_0 \cos\left(\frac{\pi x}{l_x}\right) \cos\left(\frac{\pi y}{l_y}\right) \tag{3.117}$$

where

$$\pi^2 {v_{Te}}^2 \left(\frac{\nu_y}{l_x^2} + \frac{\nu_x}{l_y^2}\right) = \nu_{iz}({\omega_{ce}}^2 + \nu_x \nu_y). \tag{3.118}$$

is the electron temperature equation.

When the electric field is neglected, the electron and ion equations are entirely decoupled, such that the plasma density is found using only the fluid equations for the electrons: the transport is limited by electron magnetic confinement. At the walls, the electron flux is

$$\Gamma_{ex}\left(x = \pm\frac{l_x}{2}, y\right) = \frac{\pi n_0 {v_{Te}}^2 \nu_y}{({\omega_{ce}}^2 + \nu_x \nu_y) l_x} \cos\left(\frac{\pi y}{l_y}\right) \tag{3.119}$$

$$\Gamma_{ey}\left(x, y = \pm\frac{l_y}{2}\right) = \frac{\pi n_0 {v_{Te}}^2 \nu_x}{({\omega_{ce}}^2 + \nu_x \nu_y) l_y} \cos\left(\frac{\pi x}{l_x}\right). \tag{3.120}$$

It is not clear which collision frequency should be taken for each direction, since the instability is rotating, with a wavevector that is mainly azimuthal but with a significant radial contribution as well. However, we have seen that the instability develops mainly in the azimuthal direction, and the local electric field fluctuations are expected to push the electrons in the $E \times B$ direction [46]. To estimate ν_x and ν_y, the simulation domain is split into 4 regions as illustrated in Fig. 3.17. For

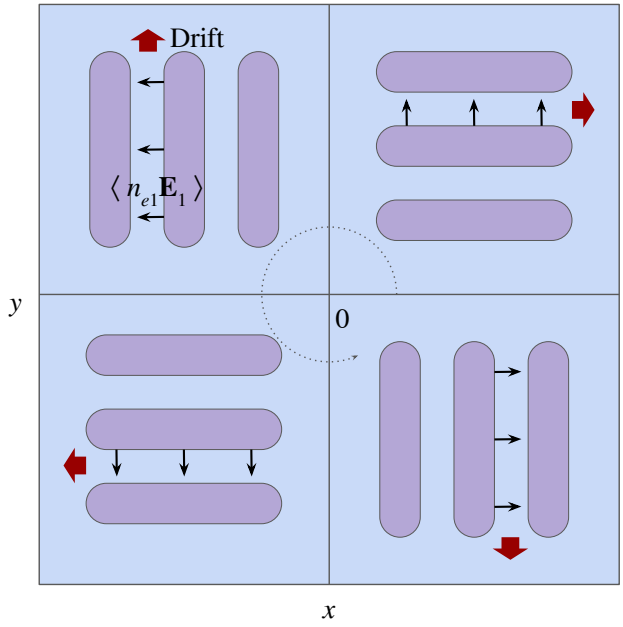

Figure 3.17: Sketch of the model where the domain is split into 4 sub-domains. The instability is always either parallel to the wall, or perpendicular to it.

each section of the wall, the anisotropic collision frequency is either ν_e when the instability is perpendicular to the wall, or equal to a scalar ν_{eff} when it is parallel to it. Since at steady state, the total current leaving the plasma is zero ($\oiint_S \mathbf{\Gamma}_i \cdot \mathbf{dS} = \oiint_S \mathbf{\Gamma}_e \cdot \mathbf{dS}$), the h factor of the discharge defined by Eq. (1.96) can directly be estimated through the electron flux

$$\boxed{h_B = \frac{(m_i/m_e)^{1/2} v_{Te}(\nu_e + \nu_{\text{eff}})}{({\omega_{ce}}^2 + \nu_e \nu_{\text{eff}})(l_x + l_y)} \left(\frac{l_y}{l_x} + \frac{l_y}{l_x} \right)} \tag{3.121}$$

which reduces to

$$h_B = \frac{v_{Te}(\nu_e + \nu_{\text{eff}})}{({\omega_{ce}}^2 + \nu_e \nu_{\text{eff}}) l} \left(\frac{m_i}{m_e} \right)^{1/2} \tag{3.122}$$

for a square ($l_x = l_y = l$). Index $_B$ indicates that this equation is valid at high magnetic field only, otherwise the assumption of low electric field cannot be made.

If the instability does not affect the transport, then $\nu_{\text{eff}} = \nu_e$ and the h factor decreases as B^{-2} with the magnetic field, which corresponds to the classical regime found by Sternberg *et al.* [146]. However, as will be shown in the next paragraph, the Hall parameter cannot be arbitrarily large, which sets boundaries for the possible values of h and ν_{eff}.

3.3.2 Saturation of the Magnetic Confinement

Upper bound for the Hall parameter

At $y = 0$, $\partial_y n = 0$, such that Eq. (3.112) becomes

$$\Gamma_{ey} = \frac{\omega_{ce}}{\nu_y}\Gamma_{ex} \tag{3.123}$$

If the instability propagates approximately in the y direction, then $\nu_y = \nu_{\text{eff}}$ such that the Hall parameter for the electrons is

$$\eta_e = \frac{\Gamma_y}{\Gamma_x} \approx \frac{\omega_{ce}}{\nu_{\text{eff}}} \tag{3.124}$$

which also writes

$$v_{ey} = \eta_e v_{ex} \tag{3.125}$$

Fig. 3.18 shows the profiles of v_y/v_{Te} at $y = 0$, where v_{Te} is computed from the volume-averaged electron energy at 3 mTorr and 12 mTorr, for several values of the magnetic field. Of course, these profiles are averaged over the larger time-scale. The electron drift velocity v_y always remains lower than the electron thermal velocity, and becomes very close to it at the wall (which is consistent with the thermal electron flux at the wall) at high magnetic field. In the plasma bulk, v_y is always only a fraction of the thermal velocity. This seems consistent with the fact that the electron drift velocity is dominated by the diamagnetic drift at high magnetic fields. The diamagnetic drift is purely a fluid drift, it is not related to the motion of the electron guiding centers,[1] and should in principle remain lower than the electron thermal velocity.

$$\boxed{v_* < v_{Te}} \tag{3.126}$$

The paragraph below is an attempt to provide a qualitative interpretation of this observation.

In Fig. 3.19, the electron density gradient is in the vertical direction. The electron density decreases from the top to the bottom. We assume that all the electrons have a gyration velocity of $\pi v_0/2$ such that the mean velocity over half a gyration is v_0. The Larmor radius is

$$\rho_{Le} = \frac{\pi v_0 m_e}{2eB} \tag{3.127}$$

Let us consider a slice of thickness $2\rho_{Le}$.

[1] A diamagnetic drift higher than the thermal velocity would not necessarily break the PIC CFL conditions since it comes from a strong density gradient and not necessarily from a high gyration velocity or a high guiding center velocity. However, we must ensure that the Larmor radius is well resolved by the grid.

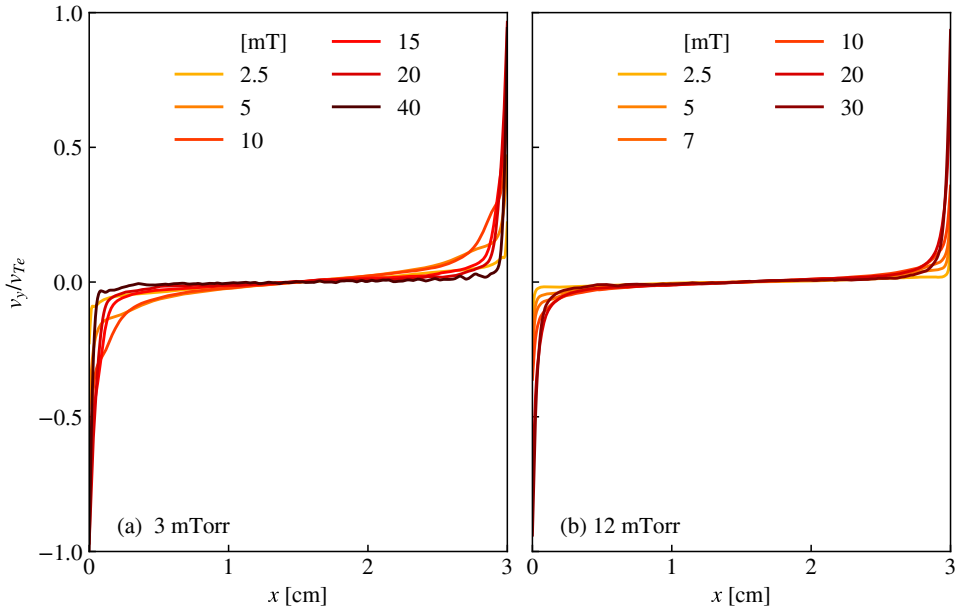

Figure 3.18: Profiles of electron fluid velocity along y as a function of x, measured at $y = l_y/2$, and normalized to the electron thermal velocity for various values of the magnetic field at 3 mTorr (a) and 12 mTorr (b).

- If the density gradient is 0, there are as many electrons whose velocity contribution along x is v_0 as electrons whose velocity contribution along x is $-v_0$. The diamagnetic drift is therefore 0, which is in agreement with Eq. (3.3) when there is no pressure gradient.

- If the density gradient is $n/(4\rho_{Le})$, there are half fewer electrons after a distance of $2\rho_{Le}$. In Fig. 3.19, the resulting fluid velocity is $\frac{4v_0-2v_0}{6} = \frac{v_0}{3}$.

- If the density gradient is greater than $n/(2\rho_{Le})$, it means that all the electrons have disappeared after a distance of $2\rho_{Le}$. The mean velocity is therefore v_0.

This means that the diamagnetic drift velocity should be limited by the electron gyration velocity, that is of the order of v_{Te} in an isotropic plasma. More precisely, since for an isotropic Maxwellian electron distribution function the mean absolute velocity is

$$\langle \|\mathbf{v}_e\| \rangle = \left(\frac{8}{\pi}\right)^{1/2} v_{Te} \tag{3.128}$$

where $v_{Te} = (k_B T_e/m_e)^{1/2}$. The mean v_0 is

$$\langle v_0 \rangle = \frac{2}{\pi}\langle \|\mathbf{v}\| \rangle \approx 1.016\, v_{Te} \tag{3.129}$$

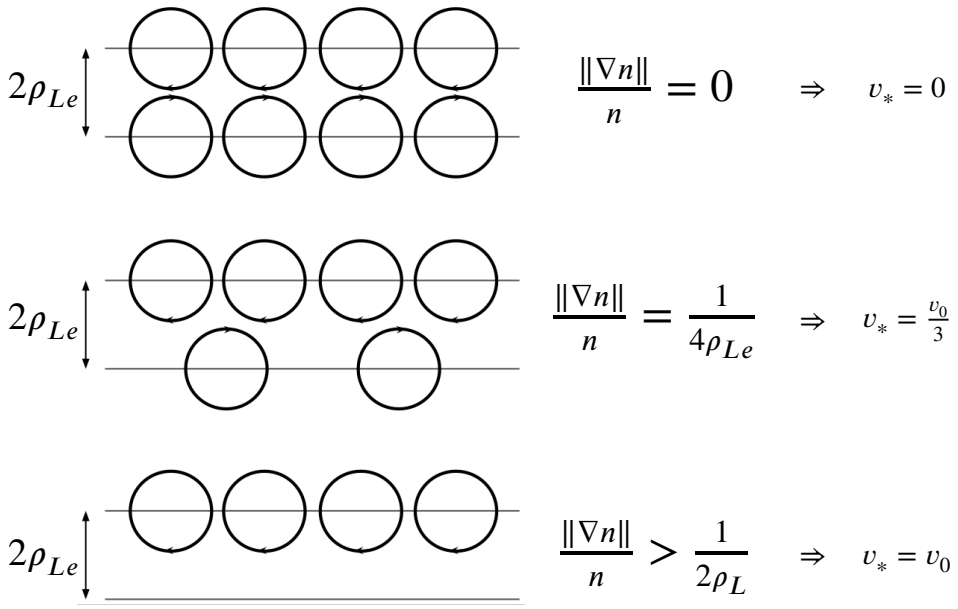

Figure 3.19: Sketch of the electron gyration motion for several values of the density gradient.

The diamagnetic drift velocity should typically be lower than $1.016\, v_{Te}$. However, the single particle approach should be generalized to a population of electrons using the kinetic theory, which could be the focus of a future study.

It is assumed in the following that the drift velocity is limited by the electron thermal velocity, such that

$$v_x \eta_e < v_{Te} \tag{3.130}$$

In the sheath, the ion flux remains equal to the electron flux on average (global ambipolarity condition), and the electron density drops more rapidly than the ion density. The electron fluid velocity is therefore typically higher than the ion velocity in the sheath.

$$v_{ix} < v_{ex} \tag{3.131}$$

Hence,

$$\eta_e < \frac{v_{Te}}{v_{ix}} \tag{3.132}$$

For reasonable magnetic fields, the density gradient and the space charge electric field terms are so strong in the sheath that electrons can be described with a Boltzmann factor. Using an isothermal sheath model, the ions are accelerated by the sheath potential ϕ_s defined by Eq. (1.93). Provided that they enter the sheath at the Bohm speed, their velocity at the wall is

$$v_{ix,w} = u_B \left[1 + \ln\left(\frac{m_i}{2\pi m_e}\right)\right]^{1/2} \tag{3.133}$$

This yields an upper bound for the Hall parameter

$$\eta_e < \eta_{c1} = \left\{ \frac{m_i}{m_e \left[1 + \ln\left(\frac{m_i}{2\pi m_e} \right) \right]} \right\}^{1/2} . \tag{3.134}$$

For argon,

$$\eta_{c1} \approx 84 \tag{3.135}$$

On the $y = l_y/2$ axis, the Hall parameter can be measured from the PIC simulation data using

$$\eta_e = \frac{\Gamma_{ey}}{\Gamma_{ex}} . \tag{3.136}$$

In order to reduce the noise level, an azimuthal average is performed, such that

$$\eta_e = \frac{\langle \Gamma_{e\theta} \rangle}{\langle \Gamma_{er} \rangle} \tag{3.137}$$

where $\Gamma_{e\theta}$ and Γ_{er} are respectively the azimuthal and radial components of the electron flux, and $\langle \cdot \rangle$ denotes the average in time and along the θ coordinate.

Consequently, Eq. (3.134) can be validated against the PIC simulation data. Fig. 3.20 shows the Hall parameter measured in polar coordinates in the PIC simulations at 3 and 12 mTorr for various magnetic field strengths. The error bars correspond to the minimum and maximum values found when varying the radial position where the fluxes are estimated from 3 mm to 12 mm. Given the relatively small size of the error bars, the approximation of a uniform Hall parameter seems reasonable. The Hall parameter reaches a maximum η_c of approximately $0.72\,\eta_{c1}$ in the 3 mTorr case and $0.37\,\eta_{c1}$ in the 12 mTorr case and decreases at high magnetic fields. The x axis is the electron drift velocity at the wall divided by the electron thermal velocity. In order to determine η_{c1}, it was assumed that the drift velocity was equal to v_{Te} at the wall. If this rough estimate is corrected by using the value found in the PIC simulation, the predicted Hall parameter would be the one given by the black dashed line in Fig. 3.20.

A minimum h factor?

Let us introduce an *instability-enhanced* collision frequency ν_B such that

$$\nu_B^2 = \nu_{\text{eff}}^2 - {\nu_e}^2 \tag{3.138}$$

Since $\eta_e = \omega_{ce}/\nu_{\text{eff}}$ decreases at high magnetic fields, it means that ν_B and ν_{eff} increase with the magnetic field and $\nu_B \approx \nu_{\text{eff}}$ at high magnetic field. Furthermore, we can reasonably assume that ${\omega_{ce}}^2 \gg \nu_e \nu_{\text{eff}}$ at high magnetic fields. Using Eq. (3.122), the h factor of the discharge is in the high magnetic field limit

$$h_m = \frac{v_{Te}\nu_B}{{\omega_{ce}}^2 l} \left(\frac{m_i}{m_e} \right)^{1/2} \tag{3.139}$$

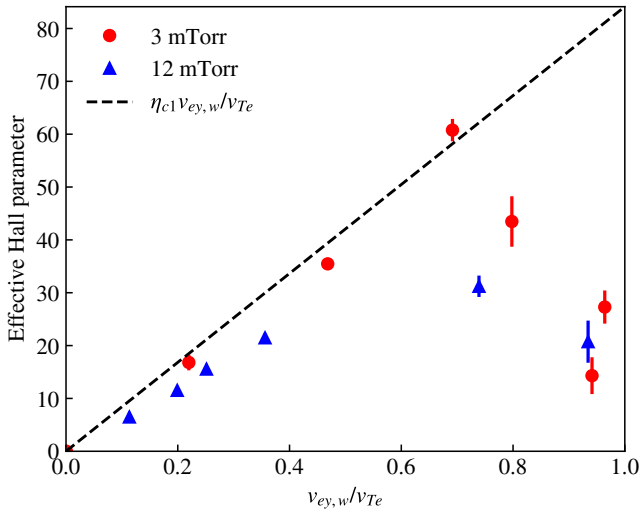

Figure 3.20: Effective Hall parameters plotted as a function of v_{ey}/v_{Te} for simulation runs at 3 and 12 mTorr, measured with Eq. (3.137). The error bars represent values extracted between 3 and 12 mm from the discharge center.

Hence, the h factor has a lower bound if and only if $\nu_B \underset{B\to\infty}{\sim} {\omega_{ce}}^2$. If this is the case, then h_m is strictly positive. Otherwise, since the h factor cannot be higher than 1, $h_m = 0$.

Classical Ion-Electron Transport Transition at $h_0 = h_B$

We now investigate the transition between the low magnetic field regime where the ions dominate the transport, and the high magnetic field regime where the model described above applies.

At high magnetic fields, the density profiles have cosine shapes and the global particle balance equation is

$$\tilde{n}\nu_{iz} = 4h_B u_B/l \tag{3.140}$$

where $\tilde{n} = (2/\pi)^2$ is the 2D mean normalized electron density. Replacing ν_{iz} in the electron temperature equation (3.118)

$$l{\omega_{ce}}^2 h_B \left(\frac{m_e}{m_i}\right)^{1/2} = v_{Te}(\nu_e + \nu_{\text{eff}}) > 2v_{Te}\nu_e \tag{3.141}$$

Hence;

$${\omega_{ce}}^2 > \frac{2\nu_e v_{Te}}{lh_0}\left(\frac{m_i}{m_e}\right)^{1/2} \tag{3.142}$$

where h_0 is the non-magnetized h factor given for instance by Eq. (2.130), and where it has been assumed that $h_0 > h_B$ (the magnetic field does not enhance the transport in any case). Inequality (3.142) represents the transition between the low

magnetic field regime where the transport is limited by the ion drift-diffusion, and the high magnetic field regime where the electrons drive the transport, whatever the role of the instability. Inequality (3.142) does not depend on any quantity related to the plasma unstable behavior, such as ν_B or h_m, for example. Hence, it does not depend on any instability-enhanced transport model. In terms of Larmor radius, this transition defined by inequality (3.142) translates into

$$\rho_{Le,\text{ion/elec}}^{\ 2} = \frac{h_0 l \lambda_e}{2} \left(\frac{m_e}{m_i} \right)^{1/2} \tag{3.143}$$

where λ_e is the electron mean free path.

Classical / Instability-Enhanced Transport Transition at $\nu_e = \nu_B$.

In this small paragraph, the Larmor radius that corresponds to the transition to the regime where the instability dominates the plasma transport is established. We assume that this transition occurs when the maximum of the Hall parameter is reached.

The effective Hall parameter η_e satisfies

$$\frac{1}{{\eta_e}^2} = \frac{{\nu_e}^2}{{\omega_{ce}}^2} + \frac{\nu_B^2}{{\omega_{ce}}^2} \tag{3.144}$$

Using Eq. (3.139),

$$\frac{1}{{\eta_e}^2} = \frac{{\nu_e}^2}{{\omega_{ce}}^2} + \frac{h_m^2 l^2 m_e {\omega_{ce}}^2}{m_i {v_{Te}}^2} \tag{3.145}$$

We have seen in the simulation that the electron temperature does not vary much with the magnetic field, especially when the transport is dominated by the instability. Since $1/\eta_e$ has a lower bound that is strictly positive, h_m cannot be zero. Consequently, the derivative of Eq. (3.144) with respect to the cyclotron frequency, with constant v_{Te} and ν_e is

$$\frac{d}{d\omega_{ce}} \left(\frac{1}{{\eta_e}^2} \right) = -\frac{2{\nu_e}^2}{{\omega_{ce}}^3} + \frac{2h_m^2 l^2 m_e \omega_{ce}}{m_i {v_{Te}}^2} \tag{3.146}$$

The maximum Hall parameter is hence reached for a magnetic field corresponding to

$$\omega_{ce0}^{\ 2} = \frac{\nu_e v_{Te}}{h_m l} \left(\frac{m_i}{m_e} \right)^{1/2} \tag{3.147}$$

which yields a critical Larmor radius

$$\rho_{Le,\text{stable/unstable}}^{\ 2} = h_m l \lambda_e \left(\frac{m_e}{m_i} \right)^{1/2} \tag{3.148}$$

and corresponds to the transition between the classical regime and the instability-enhanced regime for the electrons. A heuristic branching under the form

$$\nu_{\text{eff}} = ({\nu_e}^2 + \nu_B^2)^{1/2} \tag{3.149}$$

w was chosen to manage the transition between the classical regime and the instability-enhanced regime. As the critical magnetic field corresponds to evaluating $\nu_B = \nu_e$, we can be confident that the transition criterion does not depend on the type of heuristic branching[2].

3.3.3 Instability-Enhanced Transport

The previous paragraph has shown that the Hall parameter was uniform in space as a first approximation and that it had an upper bound that was lower than 84 for argon. This upper bound leads to the existence of a minimum h factor $h_m > 0$, whatever the value of the magnetic field, and an instability-enhanced collision frequency proportional to ${\omega_{ce}}^2$. Since

$$\eta_c = \frac{\omega_{ce0}}{\nu_e} < \eta_{c1} \tag{3.150}$$

Eq. (3.134) yields

$$h_m > \frac{\lambda_e}{l}\left(\frac{m_e}{m_i}\right)^{1/2}\left[1 + \ln\left(\frac{m_i}{2\pi m_e}\right)\right] \tag{3.151}$$

At low magnetic fields, we have seen that a significant fraction of the plasma can be unstable near the sheath, but the transport is still driven by the ions. The existence of a lower bound for h is fundamental: it means that the magnetic confinement of the electrons completely saturates due to the instability at high magnetic fields.

Increasing the magnetic field strength, soon after the electrons start driving the transport, the unstable nature of the plasma becomes important, and the Hall parameter starts decreasing. Conversely, the instability affects mainly the electron motion, so the transport cannot be instability-driven without being electron-driven. Hence

$${\rho_{Le,\text{stable/unstable}}}^2 < {\rho_{Le,\text{ion/elec}}}^2 \tag{3.152}$$

which implies that

$$h_m < h_0/2 \tag{3.153}$$

In summary, it was demonstrated that

$$\boxed{\frac{\lambda_e}{l h_0}\left(\frac{m_e}{m_i}\right)^{1/2}\left[1 + \ln\left(\frac{m_i}{2\pi m_e}\right)\right] < \frac{h_m}{h_0} < \frac{1}{2}} \tag{3.154}$$

[2]The critical Larmor radius would be the same for any heuristic formula under the form $\nu_{\text{eff}} = ({\nu_e}^\alpha + \nu_B^\alpha)^{1/\alpha}$ for $\alpha > 1$

It was found in the PIC simulations that

$$0.32 < \frac{h_m}{h_0} < 0.42 \tag{3.155}$$

for the range of pressure investigated, from 3 to 12 mTorr, such that the predictions from the theory are always satisfied. Moreover, the ratio h_m/h_0 is quite close to 0.5 and depends weakly on the pressure, which indicates that the instability starts playing an important role soon after the electrons start driving the transport. However, as shown in Appendix B, the simulation results are subject to numerical noise, such that the value of 0.32 and 0.42 may be overestimated. In the following, it will be assumed that instability-dominated transport leads to a minimum h factor $h_m \approx 0.32 h_0$. According to Eq. (3.139),

$$\nu_B = \frac{l h_m {\omega_{ce}}^2}{v_{Te}} \left(\frac{m_e}{m_i}\right)^{1/2} . \tag{3.156}$$

The instability criterion that comes from the linear theory of perturbations has shown that the plasma was unstable as soon as the total fluid electron drift is larger than the Bohm speed. This is always true at the sheath edge such that any plasma where the electrons are magnetized is subject to the resistive drift instability, in a region that is close to the sheath edge. However, the instability starts playing a significant role in the global plasma transport only when $\rho_{Le} < \rho^2_{Le,\text{stable/unstable}}$. The transition magnetic field depends on the pressure, the system size, the type of gas, and the electron temperature, as expressed by Eq. (3.148). The curve of the magnetic field that sets the transition from globally stable to globally unstable plasma transport in the conditions of the PIC simulations, and with a typical electron temperature of 4 eV, is shown in Fig. 3.21 as a function of the pressure.

Fig. 3.22 shows the effective collision frequency measured from the PIC simulation

$$\nu_{\text{eff}} = \frac{\langle \Gamma_{er} \rangle}{\langle \Gamma_{e\theta} \rangle} \omega_{ce} . \tag{3.157}$$

The ν_B asymptote is verified and the heuristic formula of Eq. (3.149) shows a satisfactory agreement with the PIC data. Eq. (3.149) is equivalent to

$$\boxed{\nu_{\text{eff}} = \nu_e \left[1 + 0.1 \left(\frac{h_0 l}{\nu_e v_{Te}}\right)^2 \frac{m_e}{m_i} {\omega_{ce}}^4\right]^{1/2}} \tag{3.158}$$

This equation can be used for electron transport in the direction mutually perpendicular to the magnetic field and the instability. The "0.1" factor in Eq. (3.158) comes from 0.32^2, so it may depend on the pressure and the discharge geometry as well.

As it was done for the effective electron collision frequency, the regime where the electrons are strongly magnetized can be bridged heuristically to the non-magnetized case where the ions dominate the transport by writing

$$\boxed{h = h_0 \left(1 + G + G^2\right)^{-1/2}} \tag{3.159}$$

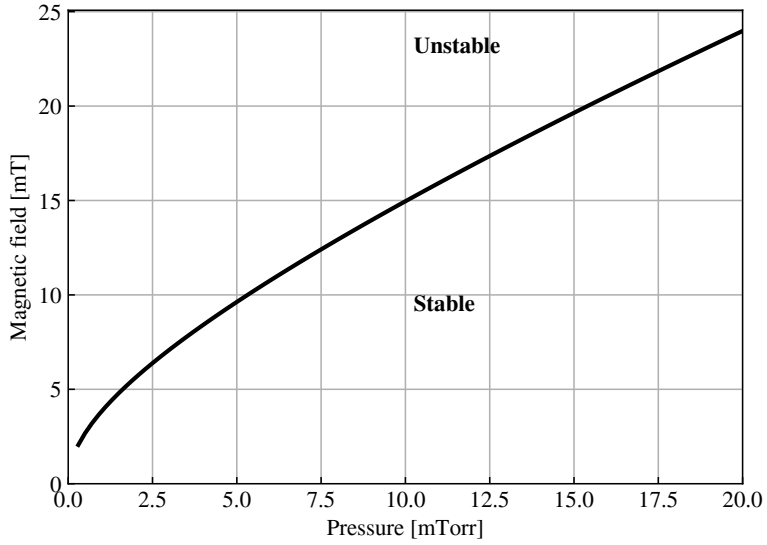

Figure 3.21: Transition from stable to unstable transport for a square argon discharge of 3 cm, with a typical electron temperature of 3 eV.

where

$$G = h_0/h_B \tag{3.160}$$

This heuristic formula was first proposed by Sternberg *et al.* [146] as a fit to 1D fluid simulation results. This formulation is compared to the 2D PIC simulation data in Fig. 3.23. As simulations were performed both with and without electron subcycling, with some influence on the results (see Appendix B), both data series were presented together: the runs with no electron subcycling are displayed with solid markers, and the runs were an electron subcycling of 10 was used are displayed with empty markers. The classical theory where $\nu_{\mathrm{eff}} = \nu_e$ is depicted in Fig. 3.23(a). In the classical approximation, Eq. (3.159) correctly predicts the plasma transport properties up to the regime where the instability strongly develops. In Fig. 3.23(b), the effective collision frequency includes the effects of the instability, and the h factor is correctly predicted by Eq. (3.159) for all ranges of pressure and magnetic field.

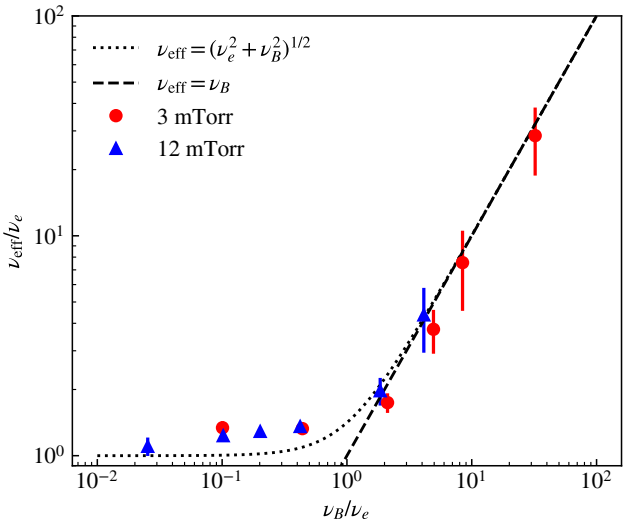

Figure 3.22: Effective collision frequency as a function of the instability-enhanced collision frequency with $h_m = 0.32h_0$, normalized by the classical collision frequency ν_e . Error bars correspond to data extracted at distances between 3 and 12 mm from the discharge center.

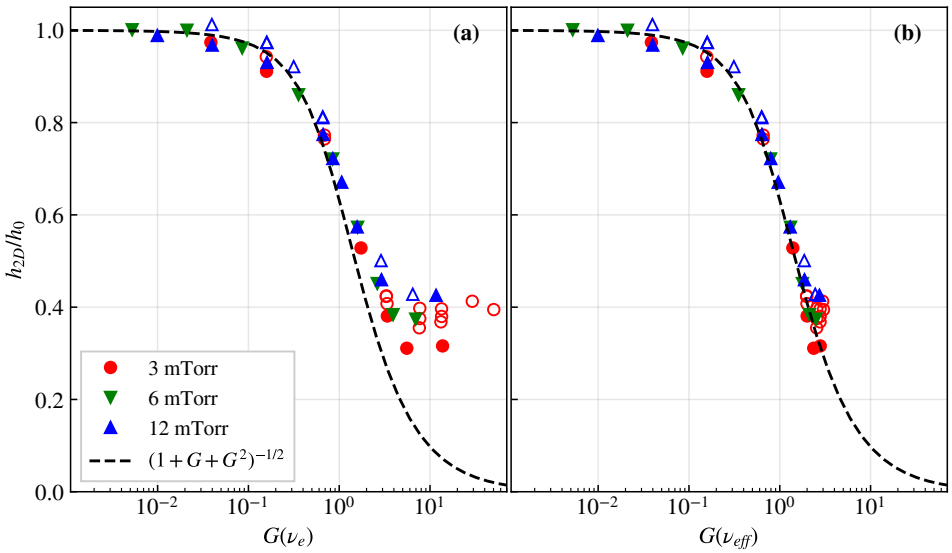

Figure 3.23: Edge-to-center plasma density ratio (h factor) plotted against the parameter $G = h_0/h_B$. In (a), only the classical collision frequency is taken into account in the computation of h_B . In (b), the effective collision frequency is computed with $h_m = 0.32h_0$. The solid markers represent simulation runs with no electron subcycling, and the empty markers correspond to an electron subcycling equal to 10.

3.3.4 Discussion on the Marginal Stability

Marginal stability is satisfied when the plasma properties are such that it is at stability limit, which means that it is unstable but with a growth rate equal to zero. This is the case, for example, when Eq. (3.90) becomes an equality. The fundamental assumption made in this paragraph is that when the instability develops and saturates, it affects the time-averaged plasma properties in such a way that the plasma tends towards marginal stability. If this is not the case, the system should always tend to develop structures at lower frequencies, which is not the case since an oscillatory steady state is reached. In other words, the instability should have negative feedback on its cause.

A model using a local marginal stability condition can be developed the same way as for the classical model described in Section 2.2. The model has one more equation corresponding to the marginal stability (equality form of Eq. (3.90)), and one more variable being the effective electron collision frequency, which is not a parameter anymore. According to Eq. (3.90), at marginal stability, the total electron drift should be equal to the Bohm speed. This idea was suggested in an article by Lakhin *et al.* [96], but the derivation is entirely new.

In this section, as the regime of interest is at high magnetic fields, the normalized quantities defined in Section 3.2.1 are used again.

The behavior of the drift velocity in the PIC simulations is summarized in Fig. 3.24. In this graph, the colored dashed lines were plotted using a simplified formula for the electron drift velocity

$$\tilde{v}_\theta = \tilde{v}_r / \tilde{\nu}_e \tag{3.161}$$

$\tilde{v}_r$ being the radial velocity predicted by a simple 1D, non-magnetized model:

$$\tilde{v}_r = \mu^{1/2} h \tan\left(\frac{\pi \tilde{x}}{\tilde{l}}\right) \tag{3.162}$$

At high magnetic fields, the solid black line represents a diamagnetic drift estimated by

$$\tilde{v}_\theta \approx \tilde{v}_* = \frac{\pi}{\tilde{l}} \tan\left(\frac{\pi \tilde{r}}{\tilde{l}}\right) \tag{3.163}$$

where $\tilde{r}$ is the normalized distance from the discharge center.

We observe in Fig. 3.24 that the electron drift first becomes much higher than the Bohm speed at intermediate magnetic fields, and then decreases to some value that becomes close to the Bohm speed. At very high magnetic fields, the intuition is that the time-averaged drift velocity should become equal to the Bohm speed and that the electric field cannot be neglected anymore.

The transition to this "very high magnetic field regime" occurs when the diamagnetic drift velocity is equal to the Bohm speed. If L is the pressure gradient length,

$$\frac{1}{\tilde{L}} = \mu^{1/2} \tag{3.164}$$

It is hard to reach this regime by 2D PIC simulations because if we make the approximation $L \approx \tilde{l}/\pi$ which is valid near the sheath edge, the number of cells in one direction needed to resolve the Larmor radius in one direction is at least $\pi/\mu^{1/2}$, which is equal to 850 for argon. The modeling of this regime is, therefore, slightly beyond the range of parameters investigated with our simulations. For example, for an argon discharge at 3 eV, with $\tilde{L} = \tilde{l}/\pi \approx 0.96$ cm, the transition magnetic field is 117 mT. At this regime, the stability criterion of Eq. (3.90) might not hold because the plasma response to electrostatic perturbations may not be isothermal anymore. Interestingly, this transition is almost equivalent to the magnetic field where the ions that travel with the Bohm velocity become magnetized. Although ion magnetization does not have a large influence in the equilibrium transport equations, it may modify the stability criterion.

The 1D differential equation of the transport is still given by Eq. (2.17). At high magnetic fields, the ambipolar diffusion is driven by the electron confinement, such that in normalized units

$$\left(1 - \frac{\tilde{v}^2}{\mu}\right) v' = \tilde{\nu}_{iz} + \left(\tilde{\nu} + \frac{1}{\tilde{\nu}}\right) \tilde{v}^2 \tag{3.165}$$

where $\tilde{\nu}$ is the effective electron collision frequency, $\tilde{v}$ is the velocity along the x axis, and $\tilde{x}$ varies from 0 to $\tilde{l}/2$. Using Eq. (3.161),

$$\tilde{v} = \frac{\mu^{1/2}}{\tilde{\nu} + 1/\tilde{\nu}} < \frac{\mu^{1/2}}{2} \tag{3.166}$$

which gives a corrected Bohm sheath criterion applicable to our model. Now that the variable $\tilde{\nu}$ can be eliminated, the differential equation of the transport is

$$\left(1 - \frac{\tilde{v}^2}{\mu}\right) \tilde{v}' = \tilde{\nu}_{iz} + \mu^{1/2} \tilde{v} \tag{3.167}$$

which integrates into

$$\tilde{x} = -\frac{\tilde{v}^2}{2\mu^{3/2}} + \frac{\tilde{\nu}_{iz}\tilde{v}}{\mu^2} + \frac{1 - \left(\tilde{\nu}_{iz}/\mu\right)^2}{\mu^{1/2}} \ln\left(1 + \frac{\mu^{1/2}\tilde{v}}{\tilde{\nu}_{iz}}\right) \tag{3.168}$$

Using the boundary condition $\tilde{v} = \mu^{1/2}/2$ at $\tilde{x} = \tilde{l}/2$, the electron temperature equation is

$$\frac{\tilde{l}\mu^{1/2}}{2} = \mathcal{F}\left(\frac{\tilde{\nu}_{iz}}{\mu}\right) \tag{3.169}$$

where the $\mathcal{F}$ function is defined by

$$\mathcal{F}(x) = -\frac{1}{8} + \frac{x}{2} + \left(1 - x^2\right) \ln\left(1 + \frac{1}{2x}\right) \tag{3.170}$$

The curve corresponding to Eq. (3.169) is provided in Fig. 3.25(a).

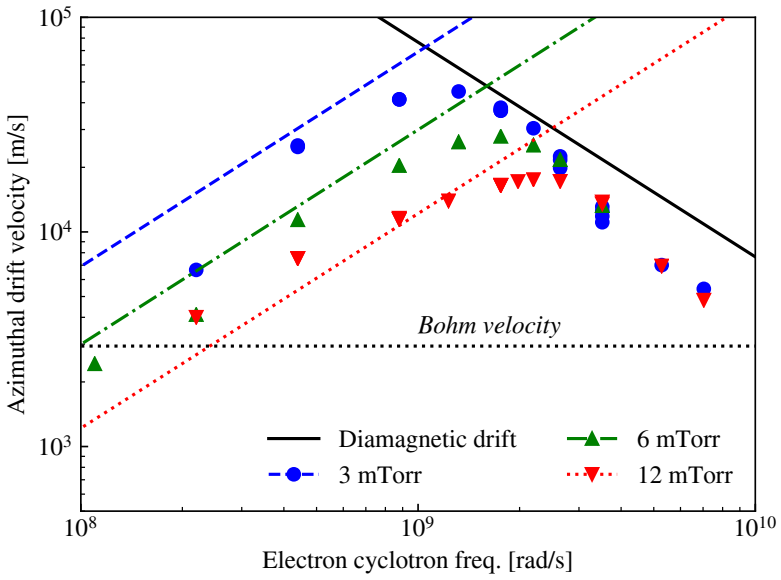

Figure 3.24: Azimuthal drift velocities measured for various values of the pressure and magnetic field, measured at $r = 9\,\text{mm}$ from the discharge center. The various dashed lines correspond to the classical regime (Eq. (3.161)), and the solid black line corresponds to the instability dominated regime described by Eq. (3.163).

We can study the case where the magnetic field is not too high, $\tilde{\nu}_{iz} \gg \mu$, for which a third order Taylor expansion gives

$$\tilde{\nu}_{iz} = \frac{11}{12}\mu^{1/2}/\tilde{l} \tag{3.171}$$

which is to be compared with the temperature equation in the low pressure, non-magnetized case of Eq. (2.61). The confinement has the same properties as in the low-pressure regime, but with a factor $11/12$ instead of $\pi - 2$, which indicates slightly better confinement. The very high magnetic field limit yields

$$\tilde{\nu}_{iz} = \frac{\mu}{2}\exp\left(-\frac{\tilde{l}\mu^{1/2}}{2}\right) \tag{3.172}$$

The density profile can also be derived analytically

$$\tilde{n} = \tilde{n}_0\left(1 + \frac{\mu^{1/2}\tilde{v}}{\tilde{\nu}_{iz}}\right)^{-1+(\tilde{\nu}_{iz}/\mu)^2}\exp\left(-\frac{\tilde{\nu}_{iz}\tilde{v}}{\mu^{3/2}}\right) \tag{3.173}$$

To be consistent with the general definition of Eq. (1.96), the h factor is here

$$h = \frac{\tilde{n}|_{\tilde{v}=\mu^{1/2}/2}}{2\tilde{n}_0} \tag{3.174}$$

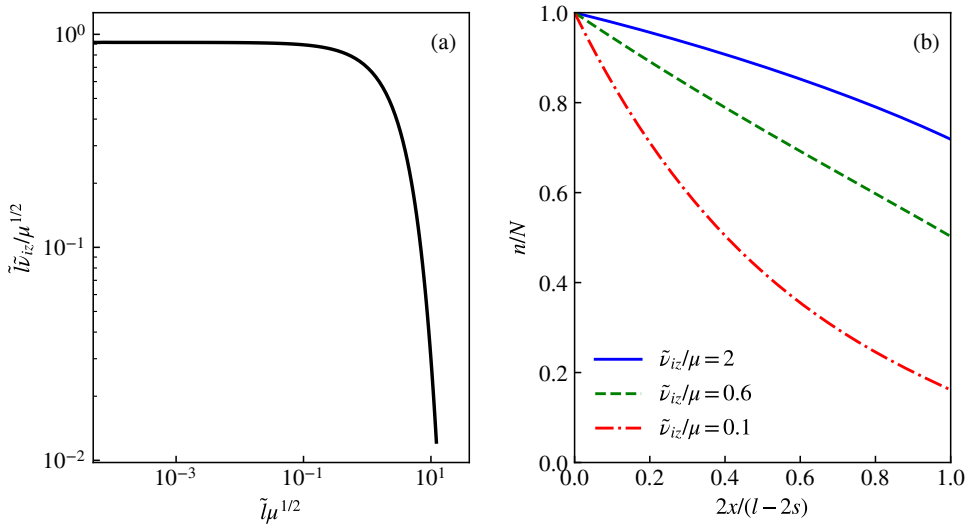

Figure 3.25: (a) Graph of the electron temperature equation defined by Eq. (3.169). (b) Normalized plasma density profiles for various values of the normalized ionization frequency $\tilde{\nu}_{iz}$.

which yields

$$h = \frac{1}{2}\left(1 + \frac{\mu}{2\tilde{\nu}_{iz}}\right)^{-1+(\tilde{\nu}_{iz}/\mu)^2} \exp\left(-\frac{\tilde{\nu}_{iz}}{2\mu}\right) \tag{3.175}$$

The h factor depends only on the ratio $\tilde{\nu}_{iz}/\mu$.

- If $\tilde{\nu}_{iz} \gg \mu$, $h = \frac{e^{-1/8}}{2} \approx 0.44$;
- If $\tilde{\nu}_{iz} \ll \mu$, $h = \tilde{\nu}_{iz}/\mu$.

For $\tilde{\nu}_{iz} \ll \mu$, the density profile becomes convex and peaks in the center. Moreover, the mean normalized density starts decreasing significantly. Normalized plasma density profiles are given in Fig. 3.25(b) for various values of the normalized ionization frequency $\tilde{\nu}_{iz}$ (the lower $\tilde{\nu}_{iz}$ the higher the magnetic field).

If the density profile had remained approximately the same, the exponential decrease found in Eq. (3.172) would have been particularly surprising as it would have meant that the confinement is better than in the classical model where it is proportional to $1/B^2$. The distortion of the plasma density profile with the magnetic field is in contrast with the uniform effective collision frequency model that predicts a cosine shape.

This model is not difficult to derive and yields some reasonable estimates of the plasma properties. However:

- We are not sure that local marginal stability is a reasonable assumption since very few studies were found on the subject for low-temperature plasmas;

- The non-isothermal response of the plasma and ion magnetization will change the dispersion relation and affect the stability criterion in a way that we do not know.

The validity of the results is therefore arguable, but the method has some interest and may give rise to more simulations and experiments.

Summary

Many 2D PIC simulations of a magnetized plasma column were performed for several values of the pressure and a wide range of magnetic field strengths. Although the size of the system is rather small (3×3 cm), the discharge parameters are typical for magnetized plasma processing reactors. A resistive drift wave instability rotating in the azimuthal direction was observed and characterized. The instability propagates in the electron fluid drift direction, which is dominated by the diamagnetic drift.

Linear fluid theories of perturbations were investigated both in the homogeneous plasma approximation, and in an inhomogeneous plasma framework. Dispersion relations were derived and solved in both cases. The spatio-temporal FT of the azimuthal electric field found in the PIC simulations is compared with the predictions of the linear theories. In a collisionless plasma, the solutions of the dispersion relations are purely real (no instability nor damping), and one of the modes matches the (k, ω) spectrum found in the PIC simulations at saturated state. When collisions are added, the linear theories show that this mode becomes unstable if the total electron fluid drift is larger than the Bohm speed. The most unstable wavenumber and the instability growth rate are well predicted by the inhomogeneous plasma theory, while this is not the case when the plasma is assumed homogeneous.

When the electron mobility becomes lower than the ion mobility due to magnetic confinement, the instability starts playing an important role in plasma transport. At high magnetic fields (from typically 10 mT) and at a given pressure, the plasma magnetic confinement is completely destroyed by the instability. This de-confinement can be justified by the fact that the electron drift velocity should remain lower than the electron thermal velocity. This effect is well captured by an effective electron collision frequency that scales as $\boldsymbol{B}^2$, and a constant h factor. We found that the minimum h factor at high magnetic fields is about 32 % of the discharge h factor with no magnetic field. Another more self-consistent approach consists in using a local marginal stability condition. This condition has been implemented in a 1D isothermal model that is solved analytically and yields reasonable predictions of the equilibrium plasma properties.

Studying the instability-enhanced transport in a magnetized plasma column, as we did, is a prerequisite for understanding the more complicated situation of a magnetic filter such as PEGASES, where the heating is localized, and where magnetic field and electron temperature gradients become important.

Chapter 4

MAGNETIC FILTER THEORY AND MODELING

Contents

The simulation of the magnetized column is generalized to a magnetic filter configuration where the heating electric field is localized in the upstream region, while the magnetic strength has a Gaussian shape with a maximum at the vicinity of $x = l_x/2$. As can be expected from the results on the magnetized

plasma column, instabilities develop in the high magnetic field region. The sensitivity to many simulation parameters is investigated, such as the pressure, the magnetic field strength and the wall properties, among others. The simulation results are also compared with former experimental measurements performed on the PEGASES thruster. A new 1D Euler fluid model is presented and first results are presented. The agreement with the PIC simulations becomes satisfactory when the instability-enhanced transport parameters found in Chapter 3 are implemented.

4.1 Why studying magnetic filters?

Magnetic filters feature an *upstream* region and a *downstream* region separated by an area where the magnetic field increases considerably, such that the thermal electron Larmor radius becomes much smaller than the system size. The plasma is usually generated or injected in the upstream region and then flows through the magnetic filter towards the downstream region. When the kinetic energy of an electron that reaches the high magnetic field region is such that the Larmor radius is larger than the width of the high magnetic field region, it can typically pass through the magnetic filter. On the contrary, when the electron kinetic energy is too low and its Larmor radius is smaller than the width of the magnetic filter, it may remain trapped in the high magnetic field region, until collisions or instabilities transport it elsewhere, for example to the walls. Due, to their large mass, the ion Larmor radius is generally larger than the size of the magnetic filter, such that the ions can pass through it.

The first simulations performed by the author irein the magnetic filter configuration revealed strong instability in the frequency range of a few MHz. These instabilities look quite similar to the ones that form in the magnetized plasma column simulated in Chapter 3. Fluid models are not able to capture the influence of the instability on the transport correctly, and only PIC simulation can give some insight. In this chapter, we will mainly discuss the properties of the classical equilibrium transport, but also the characteristics of the instability and its possible influence on the magnetic filter properties.

The electrons that remain in the high magnetic field region are those with lower kinetic energy, thus a decreasing electron temperature through the filter. Downstream, only the high energy electrons with a velocity directed along the main direction (x) may be able to go through the filter. Collectively, this could translate into higher kinetic energy of the electron flow but not higher thermal energy. This mechanism could possibly explain the operating principle of a magnetic filter, which would in this case filter out low energy electrons. This assumptions can be challenged with the results presented below, but it is not the main focus of the present work.

Former experimental results on the PEGASES device will be summarized in Section 4.1.3, but we first describe some applications of magnetic filters.

4.1.1 Applications

Neutral beam Injectors

The operation of efficient neutral beam injector (NBI)s remains one of the main challenges of the International Thermonuclear Experimental Reactor (ITER) experimental fusion reactor [23]. The aim of NBIs is to inject power in the discharge but also to yield better control over plasma instabilities. The requirement for the two ITER NBIs is to deliver a 40 A current of high energy deuterium negative ions (1 MeV) [135]. The total power for these subsystems can be up to 50 MW, so design optimization with respect to power efficiency is crucial. A variety of reduced scale experimental negative ion sources were developed as a joint effort among partners of the ITER project.

Several test-beds were developed at the Max-Planck Institute for Plasma Physics in Garching, Germany, where the Axially Symmetric Divertor Experiment (ASDEX) is also operated, for example the former RADIal injector of Wendelstein 7 Advanced Stellarator (RADI), Bavarian Test Machine for Negative Ions (BATMAN) and Multi Ampere Negative Ion Test Unit (MANITU) ion sources [140, 55]. The same group also designed the source test facility Extraction from a Large Ion Source Experiment (ELISE) which is about half the size of the ITER configuration and whose operation has started since early 2010's [77]. In Padua, Italy, an upgraded test-bed facility Source for the Production of Ions of Deuterium Extracted from a Radio-frequency plasma (SPIDER) has recently been assembled, and the construction of a real-size ITER NBI called Megavolt ITER Injector and Concept Advancement (MITICA) has just started as of mid-2019 [135, 154].

In the NBI technology, the magnetic filter is used to enhance plasma electronegativity

$$\alpha = n_-/n_e \tag{4.1}$$

where n_- is the negative ion density, and a high flux ratio between negative ions and electrons. Negative ion production mainly relies on surface production by positive ion impact on the inner grid surface that is activated with cesium [112, 49]. The beam of negative ions then has to be recombined with positive ions to form a neutral beam that is not perturbed by the strong magnetic field inside the tokamak. As electron-ion recombination CSs are very low, achieving high electronegativity is essential for efficient operation.

Electric propulsion concepts and applications

Electric propulsion with negative and positive ions is the initial goal of the PEGASES concept described in the introduction. The original 3D computer aided design (CAD) model of the PEGASES thruster prototype is shown in Fig. 4.1. The gas is injected on the side walls near the RF antenna. The permanent magnets are localized near the center of the plasma chamber. The thrust is generated by both positive and negative ion extraction. Ideally, negative ions should recombine with positive ions in the

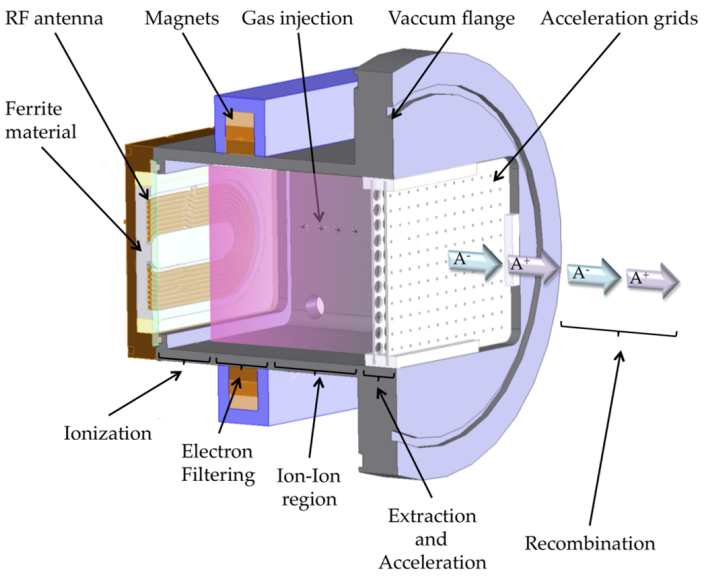

Figure 4.1: The PEGASES thruster prototype designed and assembled at LPP [119].

plume region, downstream from the thruster outlet. In operating conditions, high electronegativity is required for the PEGASES thruster, which is possible only if the electron temperature decreases in the filter. Studies were first performed in argon to focus on the cooling mechanism, with no negative ion production. No flight model of PEGASES is currently being investigated at LPP but the concept gave birth to another type of plasma thruster called Neptune, that does not rely on negative ion generation, but also involves alternate extraction of positive and negative charge carriers (electrons) through the grid. This technology is at the origin of the flagship product of the ThrustMe company that designs and manufactures electric propulsion systems for small satellites [121].

In a sense, HT also feature a magnetic filter, whose role is also to slow down the electrons, but with the main difference with the PEGASES concept is that the high magnetic field region overlaps with the ionization and the acceleration stages. Moreover, the electron drift is closed in the annular channel of a HT whereas it hits the wall sheath in the Cartesian geometry of PEGASES. The concept of double stage Hall thruster (DSHT) is a magnetic barrier configuration as this prospective thruster design relies on the de-coupling between the ionization stage and the acceleration stage. In particular, the ID-HALL DSHT developed at Laplace in Toulouse is based on an RF ICP generation, which makes it quite similar to the PEGASES configuration [50]. Again the annular geometry of DSHT design involves a closed electron drift in the azimuthal direction, as opposed to the Cartesian geometry, and the electrons are still mainly produced downstream by an external cathode system.

4.1.2 Literature Review on Magnetic Filter Studies

Experimental studies on magnetic filters were of course supported by theoretical and numerical studies. Kolev *et al.* [87] developed 1D, 2D, and 3D Cartesian fluid codes for the simulation of magnetic filters in hydrogen plasmas. These models rely on the drift-diffusion approximation that is not valid for gas pressures of 1 mTorr, which is the range of pressure contemplated for the operation of experimental NBI. The effects of the magnetic field strength and multidimensional geometry were assessed. Positive ion inertia was added by Hagelaar *et al.* [72] in a 2D fluid code that could allow for a more realistic description of the geometry of an experimental NBI for the ITER fusion reactor. The value of the magnetic field in this article is limited to 0.5 mT which is about 20 times less than the real magnetic field contemplated for the real device. The 2D plasma was found stable, which appears not to be the case at higher magnetic field, as shown in Chapter 3. In 2012, Kolev revisited the Physics of the magnetic barrier in low-temperature plasmas by 2D PIC simulations [86]. The general behavior of the plasma was correctly predicted, though with two main limitations:

1. The plasma density was scaled down to a few 1×10^{13} m^{-3}, which reverts the ratio ω_{pe}/ω_{ce} with respect to the real system and artificially reduces the ion plasma frequency. As described in Chapter 3, this is expected to influence the observed instabilities;

2. The electrons are produced by an artificial source term, which means that the electron temperature is not consistent with the particle balance.

A more detailed analysis of 2D PIC simulation results was also performed by J.-P. Boeuf *et al.*, [17]. In particular, it was identified in this work that electron transport is very much driven by the large $E \times B$ drift in the near sheath region.

Full size "2.5D" PIC simulation of the entire BATMAN source was performed by Taccogna and Minelli [148]. A transition from stable to unstable plasma behavior was identified by observing the electron current streamlines. However, the vacuum permittivity ϵ_0 was scaled by a factor 25 ($\epsilon_0' = 25\epsilon_0$) to allow for larger cell size and time step. This of course affects the sheath dimension, but also the onset of instabilities. G. Fubiani was probably the first author to propose a full 3D PIC modeling of ITER NBI [60, 61]. At high dimensionality, the scaling factor for permittivity needs to be used. In 3D PIC simulations, multiplying the vacuum permittivity artificially by a factor 2 allows for 2^3 times fewer cells to resolve and a twice bigger time step. The simulation time is hence, generally reduced by a factor 16. However, the plasma instabilities may not be captured correctly when such scaling is used.

More than ten years of research were dedicated to the simulation of NBI in several research groups across Europe, mostly on hydrogen and hydrogen/deuterium plasmas. The aim of the present work is not to compete with the level of refinement, but rather to assess how the plasma characteristics depend on the various parameters, e.g.

- gas pressure
- magnetic field strength
- width of the magnetic filter
- power deposition
- dielectric coating

The corresponding simulation results will be presented in Section 4.3. The general aim is to assess fundamental plasma characteristics, in argon first, and ultimately iodine in Chapter 5.

4.1.3 The PEGASES Experiment

The PEGASES ion source has not been used as a real prototype of plasma thruster or NBI but rather like a model system that can help the community understanding the physics of magnetic filters.

The PEGASES experiment was first used with argon gas and allowed for some detailed analysis of the fundamental plasma properties. For example, Bredin *et al.* [21, 20] measured electron distribution functions at various locations of the plasma chamber, and found that the EEDF was Maxwellian, as opposed to the case where no magnetic field is applied. It was also confirmed experimentally by Thomas *et al.* [153] that a significant part of the electron transport across a magnetic filter was made by $E \times B$ drift in the sheath. Optical measurement techniques that are not necessarily possible in larger test beds could also perfomed in PEGASES to yield for example measured profiles of negative ion density [127, 126].

Experimental results obtained previously with and without the permanent magnets are presented in Fig. 4.2. In the experimental device, $l_x = 12\,\text{cm}$, $l_y = 10\,\text{cm}$, and $l_z = 8\,\text{cm}$, and the magnetic field is in the z direction. The magnetic field profile was measured and is shown in solid line in Fig. 4.2(a) and (b). The magnetic field maximum is at 24.5 mT. The measurements were performed in a 10 mTorr argon discharge with a coil RF power of 130 W. The plasma density in the upstream region becomes higher when permanent magnets are added, and drops more sharply in the downstream region of the filter. The electron temperature decreases from 4 to 3 eV when no magnets are present, but the downstream electron temperature drops to less than 1 eV in the downstream region under the influence of the magnetic field. The upstream electron temperature remains unchanged, at 4 eV approximately.

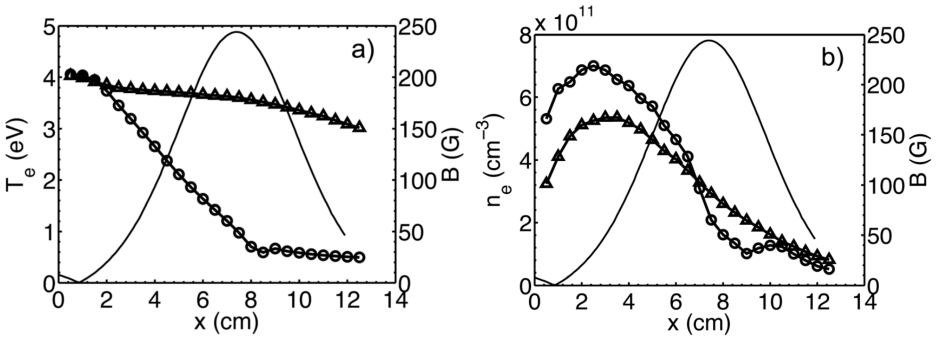

Figure 4.2: Experimental measurements obtained in PEGASES operated with argon at 10 mTorr by A. Aanesland *et al.* in 2012 [1]. "*The electron temperature (a) and the plasma density (b) along the x direction. Triangles and circles are obtained without and with the magnetic filter, respectively. The solid line is the calculated magnetic field strength on axis.*"

4.2 Two-dimensional PIC Simulations of a Magnetic Filter with Argon

4.2.1 Simulation in Real Conditions

In this subsection, an attempt to simulate the entire PEGASES thruster with a 2D PIC simulation is presented. The simulation parameters are adjusted to match the experimental conditions described above. The simulation domain corresponds to the plane perpendicular to the magnetic field lines with $l_x = 12\,\text{cm}$ and $l_y = 10\,\text{cm}$, and we focus on the cross-field transport phenomena. No permittivity scaling is used. The PEGASES thruster is typically 20 times smaller than an industrial NBI in each direction, which may allow for direct experimental validation. However, direct PIC simulation remains quite challenging.

Simulation Parameters

The simulation parameters are close to the experimental conditions described in a study on the properties of the EEDF in the PEGASES device operated with argon [1]. The gas pressure is 10 mTorr, and the absorbed power density is $124\,\text{kW/m}^3$ such that the plasma density reaches almost $4 \times 10^{17}\,\text{m}^{-3}$ in the upstream region. The mesh is made of a uniform grid of $6\,000 \times 5\,000$ cells and the time step is 4.24 ps. Due to to the very large grid size the simulation is expected to scale much better than the case with a reduced geometry. The run was performed on 3 800 CPU on the CINES OCCIGEN computational facility. Each node has 64 GB of memory and when less than typically 3 000 CPU are used, memory issues arise rapidly. The run lasts for 3 days to simulate 3.1 µs of physical time. A steady state is not reached

within this time, which corresponds to a fraction of the ion transit time. By the time of the simulation, the sheaths are formed and the discharge general aspect is recovered. There are 2.1×10^8 super-particles (both electron and ion) and this number rises to about 4×10^8 super-particles in about 3 µs, because of ionization reactions. All the walls are conducting and grounded to a 0 V potential, so no bias voltage at the grid location is considered. The sampling rate is 10 000 time-steps, or 42.4 ns which is good enough to resolve the unstable phenomena described in the previous chapter. The wall model used here is straightforward as no SEE is taken into account either from electron or ion bombardment, and all the charged particles are simply absorbed when they hit the walls. The heating electric field profile features a linear decrease from 0 to l_x, as shown in Fig. 1.6(e). Moreover, an ion subcycling of 10 is used, which means that the ions are moved only every 10 time steps, to decrease computation time. The shape of the magnetic filter is also taken from the published experimental data [1], and the maximum magnetic field is 24.5 mT located at $x = 7.5$ cm. As in previous simulation cases, the gas is treated as a steady homogeneous background at a constant temperature of 300 K.

Most of the physical and numerical parameters used for this (not-converged) simulation are summarized in Section 4.2.1.

Simulation Results

The maps of the main plasma properties at the end of the simulation are shown in Fig. 4.3. The plasma features a clear asymmetry such that the 2D description seems essential. The peak of electron current visible at the left bottom corner of Fig. 4.3(c) validates the former observations made by other authors with reduced geometry and enhanced permittivity [86, 148, 17]. The maps of electron and ion currents presented in Fig. 4.3(c,d) were made with data averaged over 1.3 µs of physical simulation time, which enables to draw distinct current lines. The currents are fluid currents, which means that they account for the diamagnetic drift, that dominates in the plasma bulk in the high magnetic field region. Although a steady state is not reached, one can still observe that the electron and ion currents are not equal, which shows that the plasma is not ambipolar, as it was already observed experimentally [89]. The electron temperature also features some asymmetry with gradients that are significantly different from the uniform magnetic field situations in both directions (see Fig. 4.3(e)). The ion temperature given by the simulation is displayed in Fig. 4.3(f) but the validity of these predictions is questionable since no power conservation balance for the gas is taken into account. In the simulations, ion heating comes from the electric field acceleration combined with ion-neutral collisions that transfer directional kinetic energy to thermal energy. When an ion-neutral backscattering collision occurs, some ion energy is lost. This energy should then be transferred to the gas such that the ion temperature and the gas temperature become coupled. The simulation hence tends to underestimate the ion temperature and the gas temperature.

	Physical parameters		
Gas type		Ar	
Discharge size in x direction	l_x	120	mm
Discharge size in y direction	l_y	100	mm
Neutral pressure	p	10	mTorr
Transverse magnetic field	B	24.5	mT
Neutral density	n_g	3.20×10^{20}	m^{-3}
Neutral temperature	T_g	0.026	eV
Frequency	f_{RF}	13.56	MHz
Power density	w	208	kW/m^3
Absorbed power	$\mathcal{W}_{abs} = w l_x l_y 2\Delta x$	0.1	W
Physical time of the simulation	$t_{\text{simulation}}$	3.01	µs
Averaging time	t_{average}	0.042	µs
Particle source		Ionization	
Heating profile		Linear, Fig. 1.6(e)	
Walls		Conducting (0 V), absorbing	
SEE model		No SEE	
	Initial conditions		
Plasma density	$n_e = n_i$	1×10^{15}	m^{-3}
Electron temperature	T_e [eV]	4.0	eV
Ion temperature	T_i [eV]	0.026	eV
Particles per cell	$N_{\text{part./cell}}$	7 – 50	
Heating electric field amplitude	E_0	1.0	kV/m
	Numerical parameters		
Cell size	Δx	20	µm
Time step	Δt	4.24×10^{-12}	s
CFL factor	$\Delta x / \Delta t$	4.72×10^6	[m/s]
Number of gridpoints along y	y_{max}	5 000	
Number of gridpoints along x	x_{max}	6 000	
Executed time steps	$N_{simulation}$	710 000	
Steps to average	N_{average}	10 000	
Weighting factor	q_f	5 714 290	m^{-1}
Initial number of super-particles	$N_{part,0}$	210 000 000	
Final # of elec. super-particles	$N_{elec,end}$	369 159 794	
Final # of ion super-particles	$N_{ion,end}$	369 519 201	
Number of CPU	N_{CPU}	3 800	
Run data volume	$V_{storage}$	259.1	GB
Data volume per grid snapshot	$V_{grid,snap}$	2.9	GB
Total runtime		72	h
Computing resource		273 000	CPU.h
Computing facility		OCCIGEN	

Table 4.1: *LPPic* simulation characteristics for the full scale 2D PIC simulation of the PEGASES thruster.

The electron density and electron temperature profiles are given in Fig. 4.5 as a function of x and for various values of y. As the electron and ion densities are statistically equal everywhere and considering the small size of the sheath, a 1D quasineutral description seems correct except close to the lower wall $y = 0$. The electron temperature decreases almost linearly from the upstream to the downstream region of the magnetic filter. The electron temperature profiles are much faster to converge in PIC simulations, and this profile is expected to be close to the converged solution. It is not in qualitative agreement with experimental results [20]. We believe that this discrepancy is due to the heating localization that can play an important role in magnetized plasmas. The choice was made for this simulation to use an electric field amplitude that decreases linearly from 0 to l_x with no y dependency. Due to the relatively high plasma density, the skin depth does not exceed 1 cm, so the heating is much more localized. Better modeling would involve very high heating electric fields in the transient that would make the simulation quite challenging to run. Without experimental data about the local power deposition or self-consistent solution of Maxwell's equation, the heating source term remains artificial. Furthermore, some distinct instability patterns that resemble the ones described in Chapter 3 are visible in Fig. 4.3(a). The understanding of the instabilities in a magnetic filter requires more fundamental investigations. Instead of pursuing the most accurate PIC model of PEGASES, we focus on a simulation case with a reduced geometry that allowed for some testing of the main driving parameters.

Comparison with Experiments

As said previously, the steady state experimental conditions are difficult to reach with (realistic) PIC simulation, and the heating profile remains arbitrary in an electrostatic code. Every code described in the literature makes assumptions that make simulations easier to run. No benchmark case currently exists for these simulations and it might be of interest to develop one. However, code benchmarking is a difficult task that requires many resources in the various teams inclined to join the benchmark. It can sometimes distract from physical understanding and experimental validation. The *LPPic* code was validated with the 1D CCP benchmark developed by Turner *et al.* [157] and a large effort was sustained by T. Charoy at LPP to develop an international benchmark case for the simulation of a HT model in the $z-\theta$ plane.

We propose in the following paragraph qualitative comparisons with historical experimental data. Qualitative comparison with previous 2D fluid simulations will also be shown in Section 4.2.3.

In non-magnetized ICP discharges, the EEDF is usually not Maxwellian, as was shown, for example, in Fig. 1.8(c) where two distinct slopes are visible in the EEPF. However, Langmuir probe measurements have shown that the Maxwellian character of the electrons was recovered in the magnetic filter configuration, everywhere along the thrust axis [1]. In Fig. 4.4, we have plotted the EEPF at various positions along the x axis of the realistic simulation. In order to generate this graph, the list of all the super-particles at the end of the simulation is parsed and all the particles whose

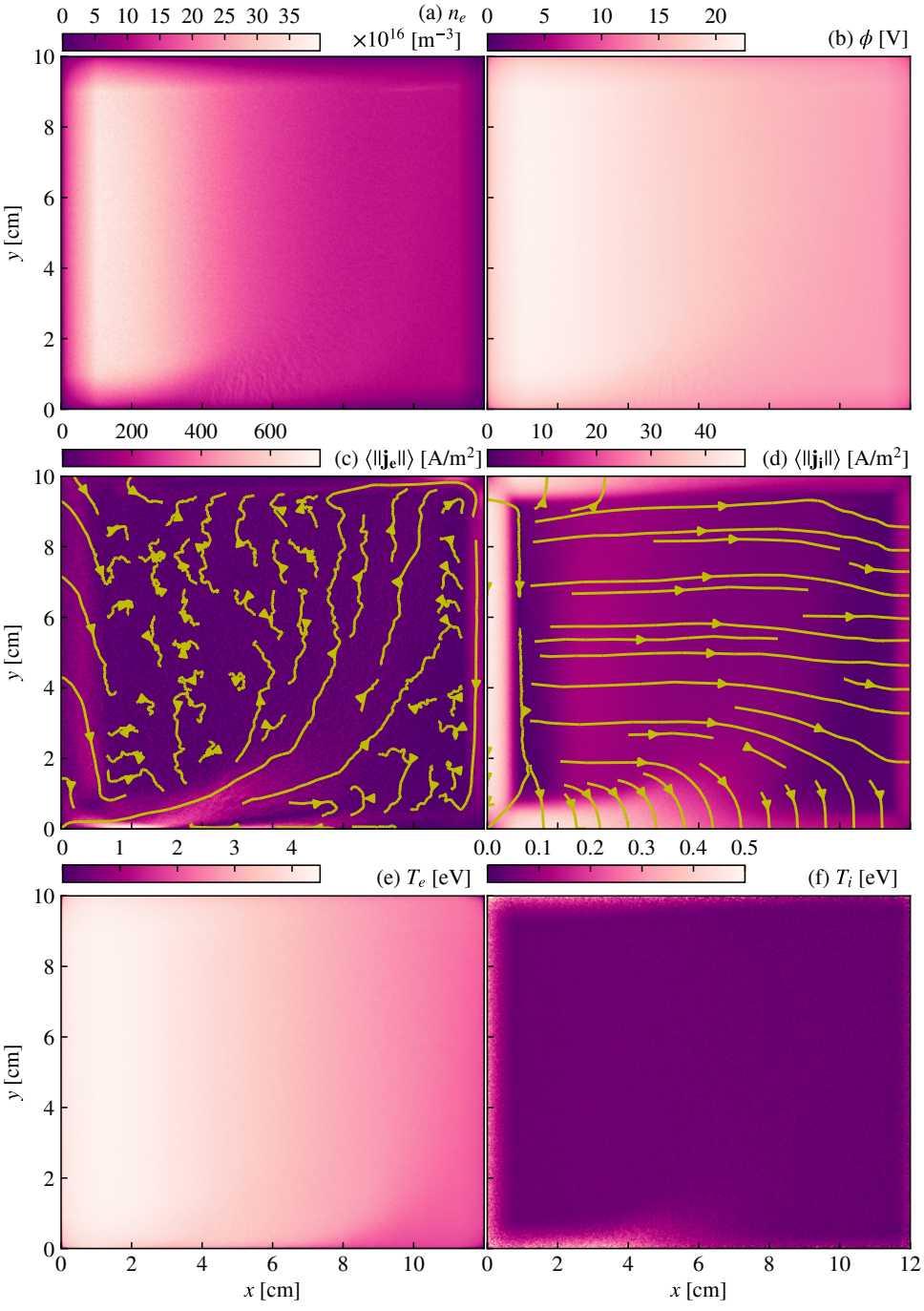

Figure 4.3: Properties of the discharge with magnetic filter after 3.1 µs of simulation. The electron and ion currents are averaged over the last 1.3µs of the simulation.

position is $x \pm 3$ mm, whatever their position in y, are selected to generate the velocity histogram that can easily be converted into a numerical EEPF, taking the weight factor of the particles into account. The procedure was repeated for $x = 1, 4, 6, 7.5$ and 11.5 cm to generate the plots of Fig. 4.4(a) that could be compared with the experimental data in Fig. 4.4(b) [1]. One of the main results of the experiments performed on the PEGASES ion source operated with argon could was retrieved with the 2D PIC simulation: the electrons remain Maxwellian from the upstream region to the downstream region, with a decreasing temperature through the filter.

Comparison between Fig. 4.5 and Fig. 4.2 shows that the orders of magnitude of electron density and electron temperature found in the simulation agree with the experimental results. The maximum plasma density found in the experiment is twice larger as in the PIC simulation, which could be due to the fact that the simulation is not converged in the realistic simulation case. However, the order of magnitude of the EEPF density (nf_P) for low energy electrons and the integrals of the curves are of the same order of magnitude. The electron temperature converges faster than the plasma density in the PIC simulation, so the electron profile found in Fig. 4.5(b) is likely to be close to the converged solution. Nevertheless, the downstream electron temperature found in the simulation is higher than the experimental values. Moreover, Fig. 4.5(b) does not feature the same plateau in the downstream region as Fig. 4.2(b), for the electron temperature. These discrepancies could be related to the heating power deposition, which is not self-consistently modeled.

As explained above, this simulation is very computationally expensive and does not account self-consistently for the local power deposition. Since the experimental power deposition profile is not known, the choice was made to investigate the role of many control parameters of the simulation rather than seeking a perfect agreement with the experimental data with a real size converged simulation. In order to be able to investigate this multi-parameter problem, the geometry and the plasma density were downscaled. The reduced simulation setup is described in the next section.

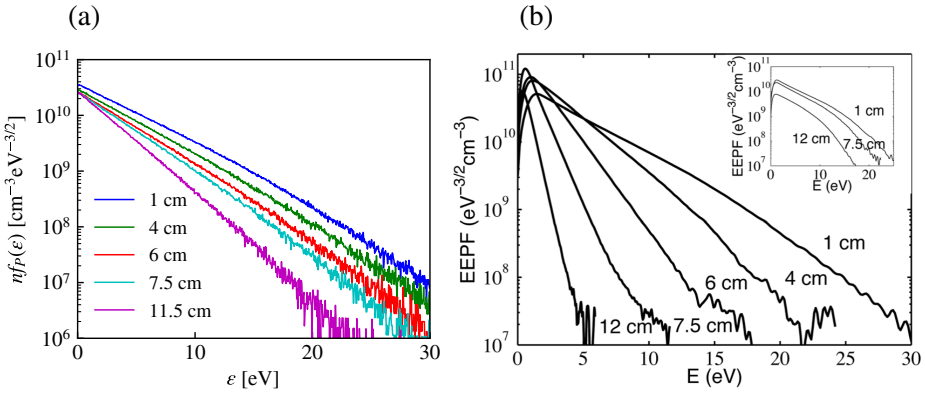

Figure 4.4: (a) EEPF measured from the PIC simulation. The distribution function is estimated by including the electrons at the given x position ± 3 mm. (b) Experimental data collected by A. Aanesland and J. Bredin in 2012 [1].

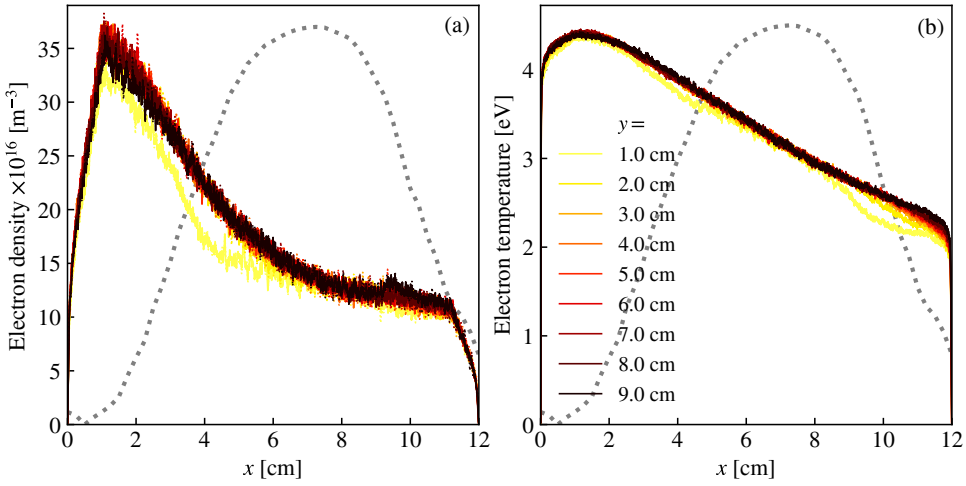

Figure 4.5: (a) Electron density and (b) electron temperature profiles along the x axis for different values of y. In (a), the dotted lines represent the ion density, and the solid lines represent the electron density. The ion density profiles were smoothed with a Gaussian filter ($\sigma = 4$). The gray dotted line is the experimental magnetic field [1] profile used in the simulation. The maximum of the magnetic field is 24.5 mT. The ion density profiles overlap the electron density profiles within the noise, and the sheaths are extremely small.

4.2.2 Simulation with Reduced Size and Plasma Density

General Parameters

For most of the simulations presented in this chapter, the general parameters are those of Table 3.1 that were used for the simulation of the magnetized plasma column. The simulation domain is a 3×3 cm square domain with a cell size of 75 µm and a time step of 33 ps. Pressures of 3, 6 and 12 mTorr and magnetic field strengths of 20, 40 and 80 mT are investigated. The location of the maximum magnetic field is always kept at the discharge center and ion magnetization is neglected. The heating power density is also varied between 9.6 and 38.2 kW/m^3. The influence of the heating electric field profile and the shape of the magnetic filter, and the role of dielectric boundaries on the lower and upper ends of the discharge are also investigated. All the varied parameters will be specified in each paragraph and figure. The simulation converges to steady state in about 15 to 30 µs depending on the simulation condition (mainly the pressure and the magnetic field). Three different values for the standard deviation ς of the Gaussian magnetic filter are tested: $0.2l_x$, $0.23l_x$, and $0.5l_x$, while l_x is always equal to 3 cm. Unless otherwise stated, the standard deviation for the "reduced simulations" is $0.2l_x$. The analytical expression of the imposed magnetic field is

$$B_z = B_0 \exp\left[\frac{1}{2}\left(\frac{x - l_x/2}{\varsigma}\right)^2\right] . \tag{4.2}$$

First Simulation Results in Reduced Geometry

In Fig. 4.6, the maps of electron density and temperature are presented for a simulation case at 3 mTorr and a peak magnetic field of 20 mT. All the walls are conducting, and the heating electric field is localized in the first third of the discharge, near the antenna, as depicted in Fig. 1.6(f). In Fig. 4.6, the maximum of plasma density is shifted towards the top left corner of the simulation domain and instabilities arise in the high magnetic field region. The electron temperature map presented in Fig. 4.6 shows a 2D dependency of the electron temperature. The electron temperature is higher at the top left corner of the simulation domain where it reaches almost 7 eV and tends to decrease as x increases or y decreases, down to less than 4 eV.

Many parameters were varied at the same time when shifting from the realistic simulation to the reduced simulation case, such that quantitative comparison is not relevant. A few comments can, however, be made:

- The 2D effects are more visible in the (converged) reduced simulation compared with the realistic one. Measurements performed at LPP [20] showed that the electron temperature mainly depends on the main x coordinate, while most of the former theoretical and computational works have shown a significant electron temperature gradient in the y direction. The two simulation cases investigated in this work, in real conditions and reduced conditions were able

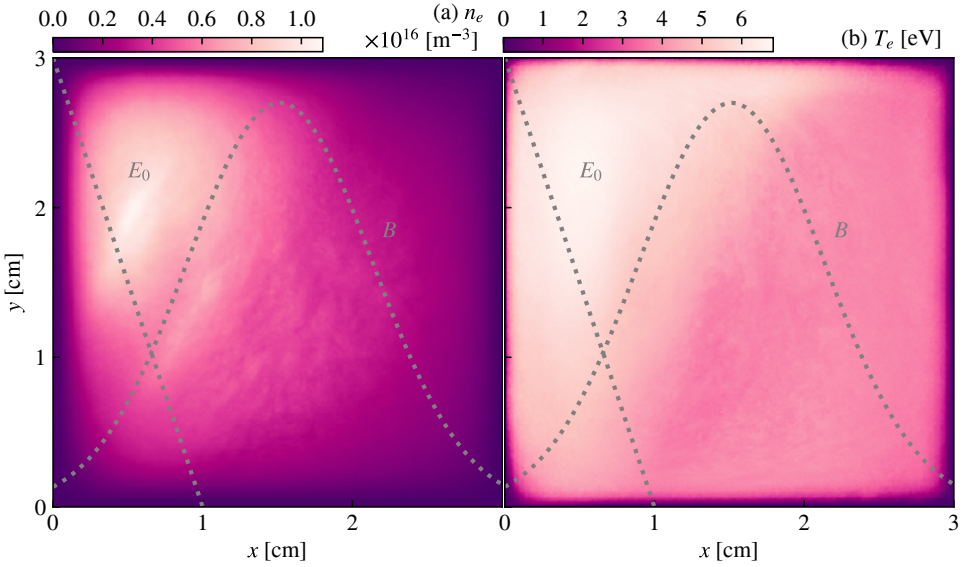

Figure 4.6: (a) Plasma density and (b) electron temperature maps at 3 mTorr along the x axis for different values of y. The gray dotted line is the Gaussian magnetic field profile used in the simulation. The maximum magnetic field is 20 mT here, the mean heating power density is 9.6 kW/m^3, and the heating electric field is localized in the first third of the discharge.

to capture both trends. The difference may come from the different Knudsen numbers, as will be shown later.

- The profile of plasma density is more peaked on the LHS of the discharge in the real case.
- The electron temperature features a plateau in the downstream region in reduced conditions while it seems to decrease linearly with x in the more realistic simulation conditions.

4.2.3 Comparison with Previous Fluid Simulations

We propose here some qualitative comparison with a 2D quasineutral fluid code developed by R. Futtersack at LAPLACE and published in his thesis [62]. The injected power used in the fluid simulation is 217 kW/m^3, and the gas pressure is 1 mTorr. This simulation parameters are quite close to the realistic simulation case presented above but with a gas pressure that is 10 times lower. The maximum plasma density is about 10^{17} m^{-3} in the fluid simulation. The results obtained with the *LPPic* code in the reduced simulation case and with the fluid simulation are shown in Fig. 4.7(a) and (b). On a short time-scale, the electron current streamlines are very much impacted by the growth of instabilities as will be shown in Section 4.2.4. Thus,

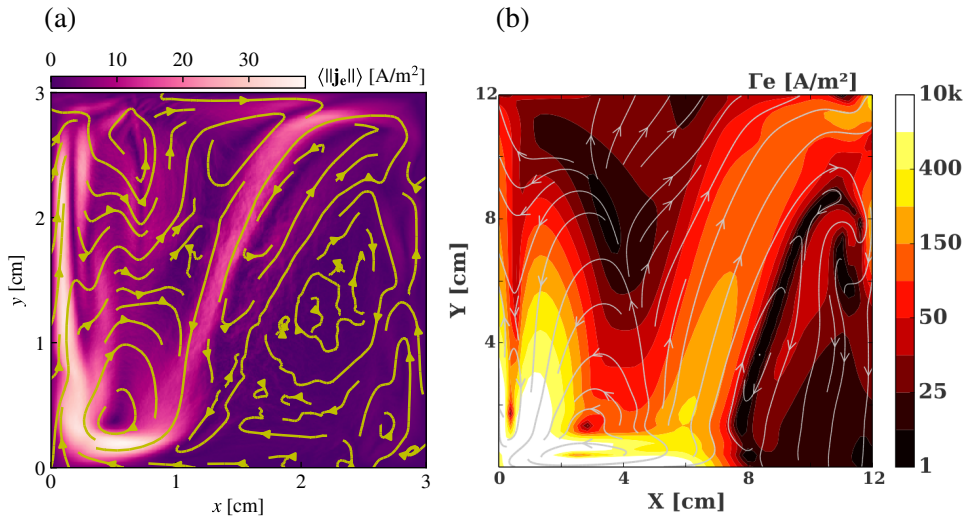

Figure 4.7: (a) Electron current measured in the PIC simulation with a maximum magnetic field of 20 mT at 3 mTorr. (b) 2D fluid simulation results by R. Futtersack [62].

the electron current densities shown in Fig. 4.7 are averaged over 4 µs. The current streamlines found by other authors for hydrogen negative ion source modeling were found again with argon. [1]

The characteristic of these time-averaged current maps is a very distinct electron fluid stream that flows from the top left corner of the discharge to the bottom left corner and then upwards through the high magnetic field region. In Fig. 4.7(b), the high current region in the LHS of the discharge is not as well resolved as in the PIC simulation probably because the fluid model [62] is limited to the quasineutral region. The characteristic "v" shape that can be seen in Fig. 4.7 produces closed streamlines. A symmetric picture was observed when inverting the sign of the magnetic field. On a shorter time scale, many small scale structures appear that reveal the unstable discharge behavior.

[1] The color scale is not very clear in Fig. 4.7(b) [62] and indicates that the electron current reaches 10^4 A/m^2 at the bottom left corner of the simulation domain. The plasma density in this region is lower than 10^{17} m^3, which suggests that the electron fluid velocity is about half of the thermal velocity, which might be overestimated.

4.2.4 Instabilities in a Magnetic Filter

In the high magnetic field region of a magnetic filter, the density gradients may produce a resistive drift instability in the same way as in the magnetized plasma column. In the 2D simulation, the magnetic field has no gradient along the field lines, and the field lines are not curved either. Therefore, the classical ∇B and curvature drifts [9] do not need to be taken into account. The derivation of the unstable modes with a non-uniform magnetic field in the inhomogeneous plasma framework is not provided here. The derivation made in the Padé approximation in Section 3.2.3 should be done again with temperature gradients and a variation of B_z along x. The same normalization cannot be used anymore as ω_{ce} and v_{Te} vary and the dispersion relation is expected to be significantly different. Furthermore, capturing the electron temperature response to the perturbed electric field requires to account for the electron energy equation. A similar derivation was made in an article by Frias *et al.* (2012) [58] on Hall thrusters. The instabilities considered in this work do not require collisions to grow. A more general derivation relevant to the problem of the PEGASES thruster would include collisions.

In this paragraph, we provide some qualitative descriptions of the instabilities observed in the reduced simulation case. We chose to focus here on the 12 mTorr case at 9.6 kW/m^3 of mean absorbed power density. The amplitude of the heating electric field decays linearly in the first third of the discharge.

As opposed to the mean quantities shown in the previous paragraph, Fig. 4.8 displays snapshots (averaged quantities over only 132 ns) of the electron density and the electron current. Instabilities of several different lengths are visible both in the density and the current snapshots. The geometrical distribution of these instabilities, their wavelengths and their propagation direction vary strongly when the magnetic field is changed. In the high-density region, a quite well-resolved wave with a 2-3 mm wavelength propagates in the x direction from the downstream region towards the upstream region. The wavelength seems to slightly decrease with the magnetic field. The phase velocity is of the same order of magnitude as the Bohm speed and seems to slightly decrease with the magnetic field. These waves are best resolved at 40 mT, in which case the frequency is estimated to be 1.34 MHz, and the wavelength 2.34 mm, which yields a phase velocity of 3.14 km/s. In order to better visualize these waves, the x profiles of the electron density near the maximum $y = 1.75$ cm are given in Fig. 4.9 at various times. The profiles are given in the form of a color plot that allows to quickly estimate the phase velocity and the direction of the wave propagation ($-\mathbf{e}_x$). The phase velocity is of the order of the ion acoustic speed. This axial backward propagating mode also affects the electron current maps.

At higher magnetic fields, the electron current that flows near the sheath in the upstream region becomes much higher, and a larger fraction of the electron fluid stream circulates inside the upstream region without crossing the filter. This may not be in favor of better confinement as the maximum electron density found in the upstream region at 80 mT is only about 10% higher than at 20 mT. This can partially be interpreted by the de-confining effect of the instability and also by the structure of

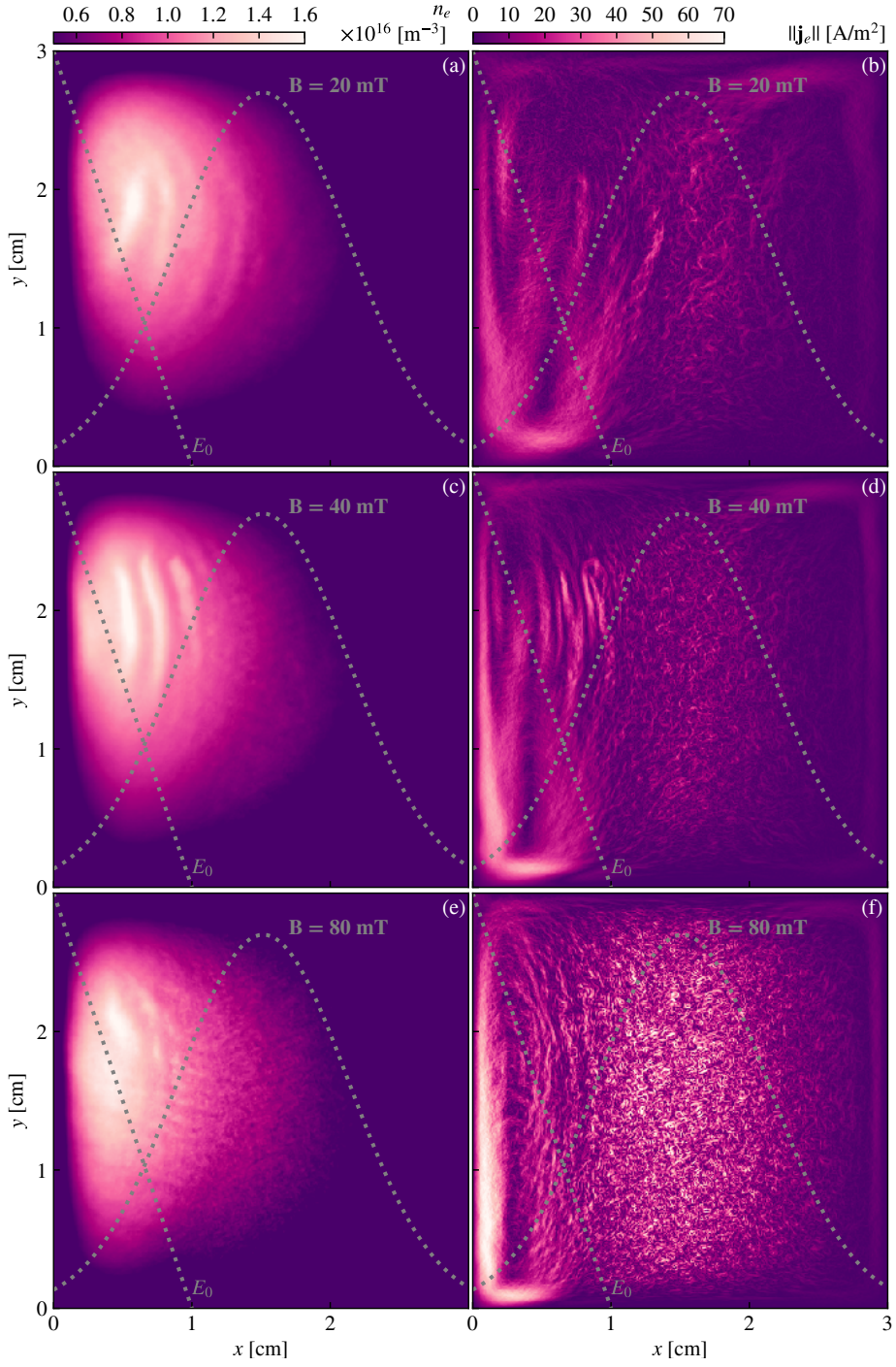

Figure 4.8: (a,c,e) Plasma density and (b,d,f) electron current maps at the end of the simulation ($t > 16\,\mu s$) for an argon discharge at 12 mTorr, and for multiple values of the magnetic field: 1st row 20 mT, 2nd row 40 mT, 3rd row 80 mT. The gray dotted lines represent the Gaussian magnetic field and the heating electric field profiles used in the simulation. The mean absorbed power density is set to 9.6 kW/m^3. In the electron density maps (a,c,e), the color scale is saturated between 5×10^{15} and 1.6×10^{16} m^{-3}.

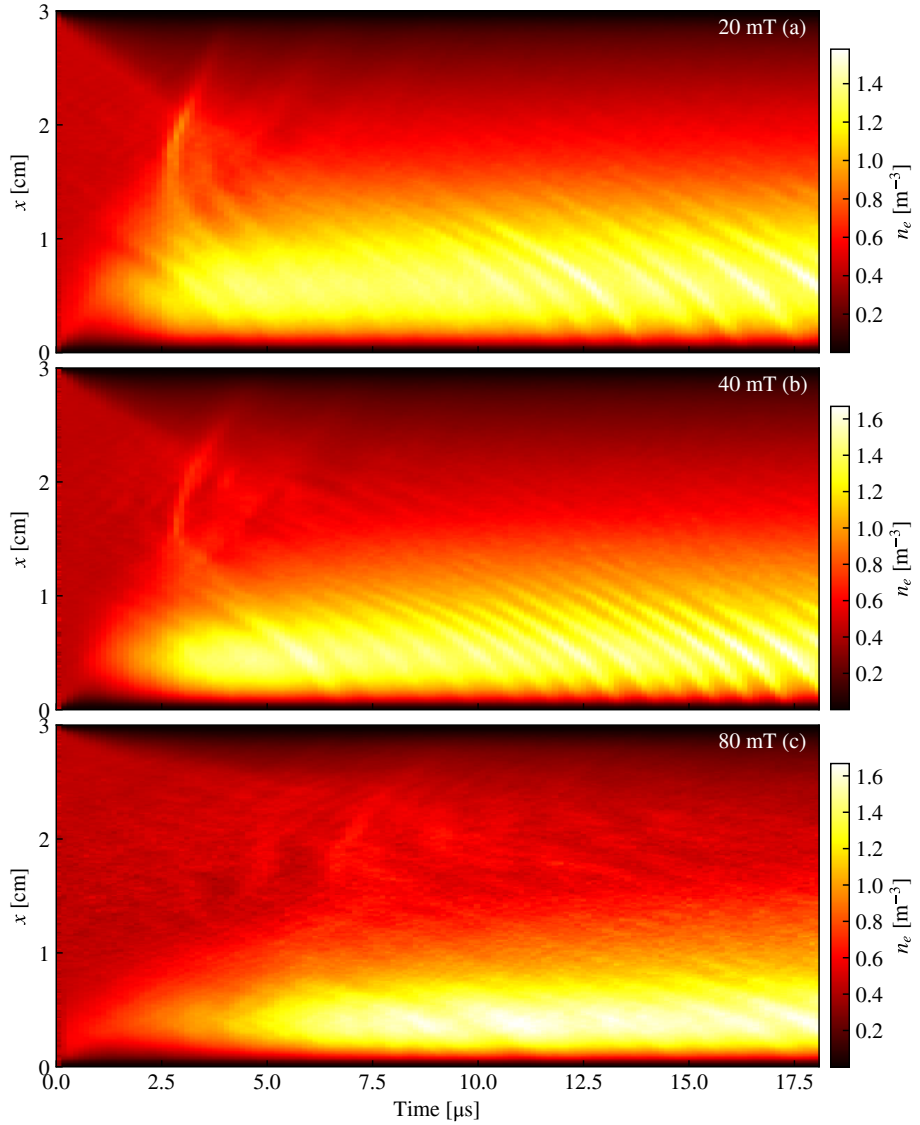

Figure 4.9: Temporal maps of the electron density at 20 mT (a), 40 mT (b) and 80 mT (c) for a gas pressure of 12 mTorr. The density is evaluated at different times and locations x for $y = 1.75$ cm (corresponding approximately to the density maximum along y). The mean absorbed power density is set to 9.6 kW/m^3 and the magnetic field and electric field amplitude profiles are the same as in Fig. 4.8.

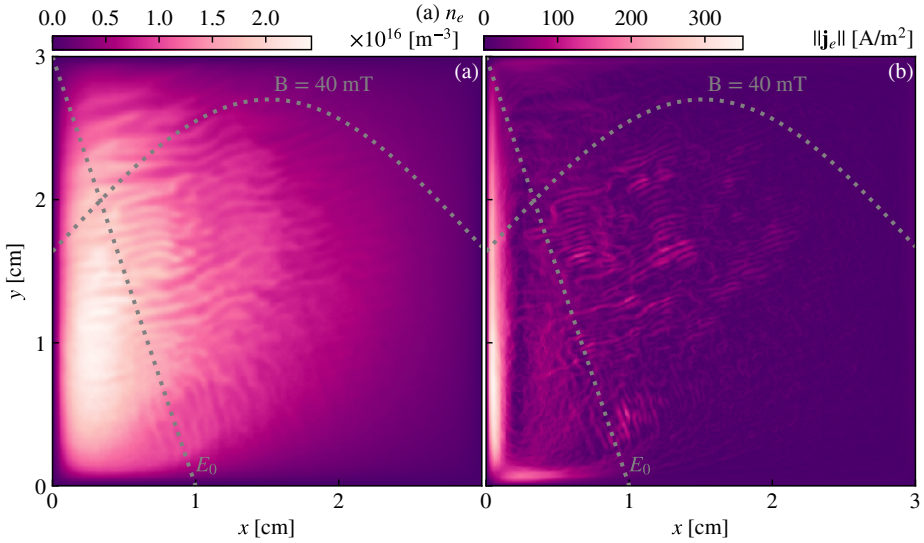

Figure 4.10: (a) Plasma density and (b) electron current maps at 12 mTorr for a maximum magnetic field of 40 mT. The gray dotted line is the Gaussian magnetic field profile used in the simulation; the standard deviation of the magnetic filter is $\varsigma = 0.5l_x$. The mean absorbed power density is 9.6 kW/m^3, and the heating electric field is localized in the first third of the discharge. Comparison with Fig. 4.8(c) and (d) is useful.

the electron stream lines. At 80 mT, the electron current in the downstream region features quite chaotic structures. An analysis of the turbulence may be of interest but is far beyond the scope of the present work. At higher magnetic fields, another distinct mode appears that propagates in the $-\mathbf{e}_y$ direction. This mode is visible in Fig. 4.8(e) and has a wavelength of the order of 1 mm and about the same velocity as the other mode.

The maps of electron density and electron currents are also provided in Fig. 4.10 in the case of a broader magnetic filter, with a standard deviation of $0.5l_x$, instead of $0.2l_x$ as was the case for the simulations presented in Figs. 4.8 and 4.9. All the other parameters remain the same as in Fig. 4.8 ($B = 40$ mT). The drift wave that propagates along $-\mathbf{e}_x$ has completely disappeared and instead, an instability pattern that looks very similar to the resistive drift instability found in the simulations of the magnetized plasma column (Chapter 3) grows. This instability propagates mainly in the $+\mathbf{e}_y$ direction but also seems to feature a rotational motion that is discontinued by the sheath. Therefore, the spatial variation of the magnetic field seems to play a major role in the types of instabilities that develop in a magnetic filter, and hence on the transport characteristics.

4.3 Identifying the Main Drivers of a Magnetic Filter

4.3.1 Intensity and Localization of the Heating Source

Heating Localization without Magnetic Fields

Before investigating the role of localized heating in a proper magnetic filter, it is important to sense these effects in the non-magnetized case. We have plotted the PIC simulation results for a square discharge of 3 cm with various configurations for the heating electric field in Fig. 4.11. In every case, the mean heating power density is 9.6 kW/m^3. In other words, the integrated power absorbed by the plasma remains the same. Configuration (A) corresponds to the case of a uniform heating electric field, as illustrated by Fig. 1.6(a). The electron density and temperature profiles are perfectly symmetrical in this case, at pressures of 3, 6 and 12 mTorr. The case where the amplitude of the heating electric field decreases linearly from $x = 0$ to $x = l_x$ is represented by the label (B) and corresponds to Fig. 1.6(b). In this case, the density profile is slightly shifted to the left and the electron temperature increases by about 10% inside the discharge. In case (C) (Fig. 1.6(c)), the heating is localized in the first third of the discharge. The plasma density profile is again more shifted to the left and the electron temperature increases from the center to the wall, before decreasing again in the sheath. The maxima of the electron temperature in the pre-sheath region, at $x \approx 0.5$ and 2.5 cm here, is more visible at lower gas pressure.

The heating geometry has a significant influence on the mean electron energy, both locally and in average, and the coil configuration can induce discrepancies of about 10% for the same total power absorbed by the plasma. However, the plasma density profile remains quite robust. The maximum plasma density has relative variations of only about 3%. At 12 mTorr, the profile leans towards the side where the heating is higher. At 6 mTorr and 12 mTorr, the profile is also distorted but the trend is not so clear.

These observations consolidate the results of Chapter 2 as we confirmed that the power deposition process and localization do not play a major role in a non-magnetized plasma at low pressure.

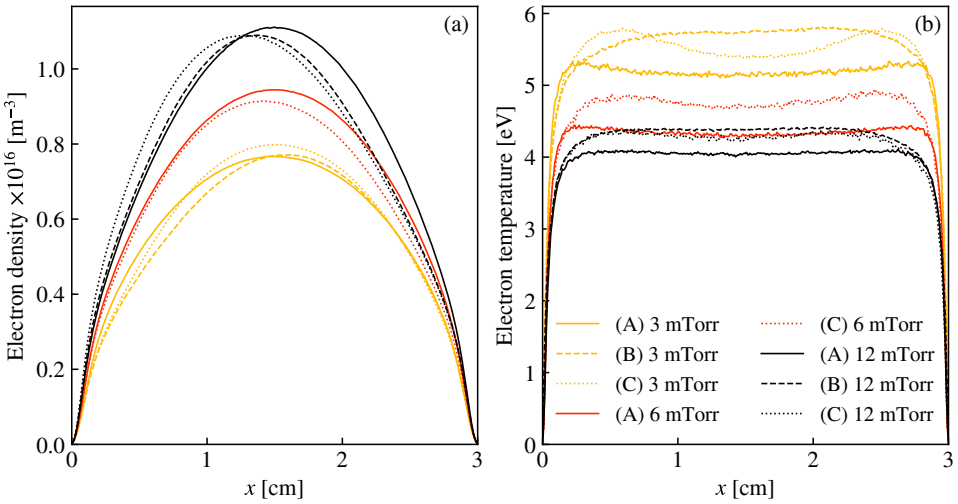

Figure 4.11: Mean electron density (a) and temperature (b) profiles at $y = l_y/2$ for non-magnetized argon discharges for 3, 6 and 12 mTorr of gas pressure. Three different heating configurations are tested: (A) Uniform heating electric field (Fig. 1.6(a)). (B) corresponds to a linearly decreasing heating electric field with $\alpha = 1$ (Fig. 1.6(b)), and (C) corresponds to heating localized only in the first third of the discharge (Fig. 1.6(c)).

Heating Localization with Magnetic Fields

The picture becomes quite different when a magnetic filter is added. Two runs at 3 mTorr of gas pressure and with a Gaussian magnetic field profile reaching 20 mT at the discharge center ($x = l_x/2$) were performed. In the first simulation, the heating electric field decreases in a linear fashion with x from 0 to l_x (case (B), Fig. 1.6(e)), and in the second one, it is localized in the first third of the discharge (case C, Fig. 1.6(f)). Fig. 4.12 shows the electron and ion density profiles (a), and the electron temperature (b), as a function of x evaluated at the discharge center ($y = l_y/2$). The mean power density remains equal to 9.6 kW/m^3 in both cases.

When the heating electric field is more localized (in green in Fig. 4.12), the maximum of the plasma density is shifted towards the left with a lower maximum plasma density. This gives a hint that the losses are larger when the heating is more localized close to the heating RF coil, which can be interpreted by the fact that more electrons are produced (by electron impact ionization) closer to the wall. The electron temperature features a sharper maximum close to $x = 0$ when the heating is localized. Indeed, the electron temperature needs to rise to balance wall losses by ionization. When the heating is more localized, the electron temperature reaches a minimum at the location corresponding to the maximum of the magnetic field and then remains approximately constant in the downstream region. When the heating electric field is spread over the whole discharge, the electron temperature decreases less in the upstream region but then keeps decreasing in the downstream of the magnetic fil-

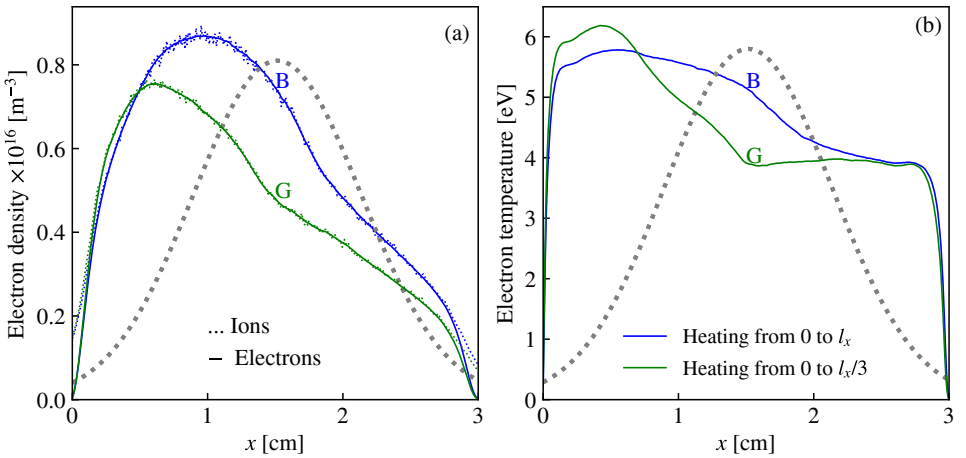

Figure 4.12: Electron density (a) and electron temperature (b) profiles at $y = l_y/2$ for magnetic filter configurations at 3 mTorr of gas pressure. Two different heating configurations are tested: linear decrease of the heating electric field from 0 to l_x (in blue (B), see Fig. 1.6(b)), and linear decrease localized between $x = 0$ and $x = l_x/3$ (in green (G), see Fig. 1.6(c)). The Gaussian magnetic field profile is indicated with the gray dotted lines with a maximum of 20 mT. The mean absorbed power density is 9.6 kW/m^3.

ter. The localized heating configuration corresponds well to the observations made by J. Bredin in his experimental works [20]. The way the heating region overlaps with the magnetic filter itself can have a large influence over the plasma properties. However, in a simple model where the heating region is mainly decoupled from the magnetic filter region, the qualitative agreement with the experimental results seems reasonable. Interestingly, the electron temperature in the downstream region does not seem to depend on the heating power deposition, as shown by the very good similarity of the electron temperature profiles in both situations when $y > 2.5$ cm.

Influence of the Mean Absorbed Power Density

In general, in LTP, the power absorbed drives the plasma density. According to global models, when the following two conditions are fulfilled, the absorbed power should not affect the electron temperature:

1. The plasma is weakly ionized such that the effect of ionization processes on the population of neutrals can be neglected;

2. The plasma density (and hence the power) is high enough such that the sheath size is much smaller than the system size;

3. No non-linear processes, such as recombination, occur.

Both conditions are satisfied in the PIC simulation.[2] We could verify that this general picture is valid for the magnetic filter configuration.

In Fig. 4.13, the plasma density and the electron temperature are represented for a magnetic filter configuration where the heating electric field decays from 0 to l_x (Fig. 1.6(e)) with a slightly broader magnetic field compared to the previous configuration. The standard deviation for the magnetic filter is here $\varsigma = 0.23 l_x$. The electron temperature curves at 19.1 and 38.2 kW/m^3 of mean absorbed power density displayed in Fig. 4.13(b) almost overlap. In Fig. 4.13(a), both electron and ion densities are represented, in solid and dotted line respectively. As observed previously, the quasineutral approximation seems reasonable for both values of the absorbed power, such that the assumption of small plasma sheath is satisfied even at relatively low power density. The curve of the high power electron density profile divided by $38.2/19.1 = 2$ (thick light blue line) almost overlaps the density profile found at low power. Therefore, the local plasma density scales linearly with the heating power. The observations that the electron temperature is not affected by the power and that the plasma density scales linearly with the absorbed power is in agreement with typical weakly ionized LTP models [100].

The injected power increases ionization and hence, the plasma density. In turn, the plasma density should affect the characteristics of the instability and thus the instability-enhanced transport. This could affect the shape of the plasma density profile. However, we have seen here that the power absorbed does not affect the density profile (it is just scaled with the mean power). Therefore, the mean injected power has only a minor influence on the quasineutral plasma transport. The main drivers for the instability onset are rather the magnetic field, the gas pressure, and the power localization.

[2] Condition 1 is always an assumption of the PIC model where neutral depletion is neglected.

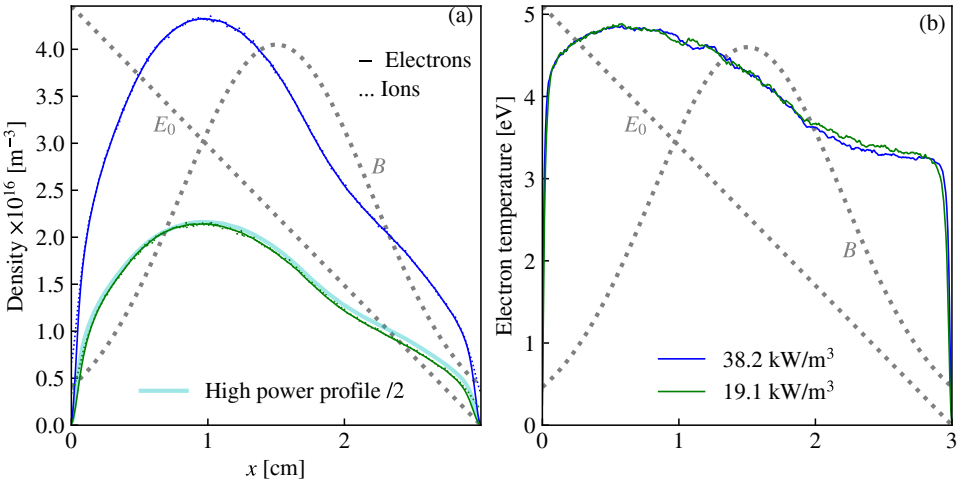

Figure 4.13: (a) Plasma density and (b) electron temperature profiles at $y = l_y/2 = 1.5\,\text{cm}$. The two runs are performed at 6 mTorr and 19.1 kW/m^3 (blue) and 38.2 kW/m^3 (green). The Gaussian magnetic field profile is indicated in gray dotted lines, and the maximum value is 20 mT. In (a), the dotted lines represent the ion density, and the solid lines represent the electron density, and the thick cyan line is the high power electron density curve divided by 2. The heating electric field decreases linearly with x from 0 to l_x. The plasma density data are averaged over more than 5 µs at steady state.

4.3.2 Influence of Dielectric Boundaries

The modeling of a dielectric boundary was made possible by the work of A. Tavant at LPP in 2016 and 2017. The method has been partially explained in V. Croes' PhD thesis [41] and has been used for a journal article of the group on alternative propellants in HT [44]. The algorithm will be described in more details in A. Tavant's PhD thesis which will be released in early 2020. The algorithm will not be explained here and only the physical principle will be given.

This model aims to represent a dielectric layer with a finite relative permittivity, which allows for a more realistic physical modeling than infinite permittivity models that impose Neumann boundary conditions instead of Dirichlet boundary conditions at the wall. When electrons and ions are collected at a plasma wall boundary, they build up a surface charge that can be spread in one cell to yield an equivalent volume charge density. This charge density is added into the RHS of Poisson's equation. The domain for the Poisson's equation is then composed of the discharge volume and the physical dielectric layer that is 1 mm thick. At the end of the dielectric layer, we assume that a grounded metallic surface is present such that the boundary conditions are simple Dirichlet boundary conditions with a 0 V boundary potential. The charge density is composed of the plasma space charge in the discharge volume, and the wall charge at the plasma dielectric interface. The relative permittivity of the dielectric material is set to $\epsilon_r = 5$. The Poisson's equation is then solved for the whole domain at each time step. Fig. 4.14 illustrates the simulation setup.

The general aspect of the plasma at the discharge center $y = l_y/2$ is visible in Fig. 4.15. The plasma density and the electron temperature in the bulk are generally not affected by the dielectric, as stressed out in Fig. 4.15(a) and (b). The plasma potential is however shifted by 2.8 V everywhere in the plasma bulk Fig. 4.15(c). Similar features were observed experimentally on PEGASES [89]. The difference between the plasma potential with and without a dielectric can be interpreted by a difference in collected currents on the RHS electrode. The collected currents on all the discharge boundaries for the two cases are presented in Fig. 4.16. The ion current

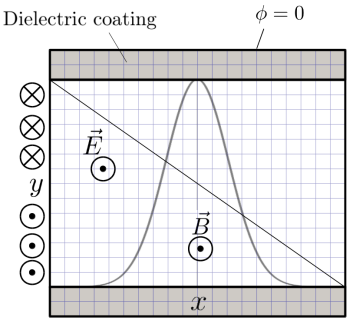

Figure 4.14: Sketch of the simulation setup with dielectric coatings at $y = 0$ and $y = l_y$. The gray area represents the dielectric region.

always follows approximately the shape of the plasma density at the center of the discharge and is not affected by the dielectric. On the dielectric surface, the electron flux is locally equal to the ion flux, which means that the current is ambipolar in the direction perpendicular to the wall. With conducting walls everywhere, the electron current at the top and bottom surfaces ($y = 0$ and $y = l_y$) are slightly lower than the ion current on average. When a dielectric layer is added, the electron current increases at the top and bottom surfaces because of the ambipolar condition, such that the electron current decreases on the left and right surfaces. The decrease of electron current in these poorly magnetized regions where the electrons are almost Boltzmann is related to an increase of the sheath potential, and thus the plasma potential as a whole. The potential difference between both cases (≈ 2.8 eV) is almost equal to the downstream electron temperature. In the following paragraphs, we will compare a simulation case with dielectric layers on surfaces at $y = 0$ and $y = l_y$ and metallic walls on the other electrodes, with a case where all the walls are metallic.

In Fig. 4.17(a), the wall potential is plotted as a function of x at the top and bottom boundaries of the simulation domain. When comparing these curves with the collected currents shown in Fig. 4.16, it appears that the local wall potential adjusts to balance the difference between electron and ion currents found when the walls are conducting. However, the electrons do not follow a Boltzmann relation in the filter, and the local electron flux cannot be predicted from the wall potential and the plasma potential only.

Moreover, the presence of dielectric boundaries does affect the sheath properties, and in particular, the electron $E \times B$ drift in the sheath that was observed and described by several authors [17, 86]. These currents do not seem to play a very large role in the electron transport across the filter. Otherwise the electron temperature and plasma density profiles would have changed significantly in Fig. 4.15(a) and (b).

In summary, (i) we could confirm that local ambipolarity was retrieved in the case of dielectric walls ; (ii) we found that the ion current was not affected by the conductive nature of the boundary ; and (iii) that while the electron density and temperature remain almost unchanged, the plasma potential rises by about the downstream electron temperature when a dielectric is added. The latter observation is important for ion acceleration through the grid of a GIT, as higher kinetic energy can be reached without changing the grid polarization.

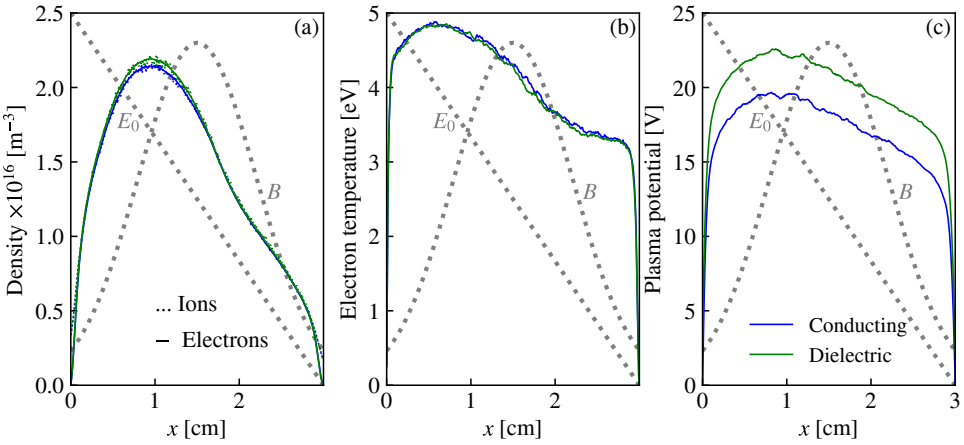

Figure 4.15: Properties along the x axis of a magnetic filter with conducting walls everywhere (blue lines), and with dielectric boundaries at the walls located at $y = 0$ and $y = l_y$ (green lines). The runs are performed at 6 mTorr of gas pressure, with a peak magnetic field of 20 mT. The Gaussian magnetic field profile is indicated with the gray dotted lines. (a) Electron and ion densities. (b) Electron temperature. (c) Plasma potential. All the quantities are averaged over 5 µs.

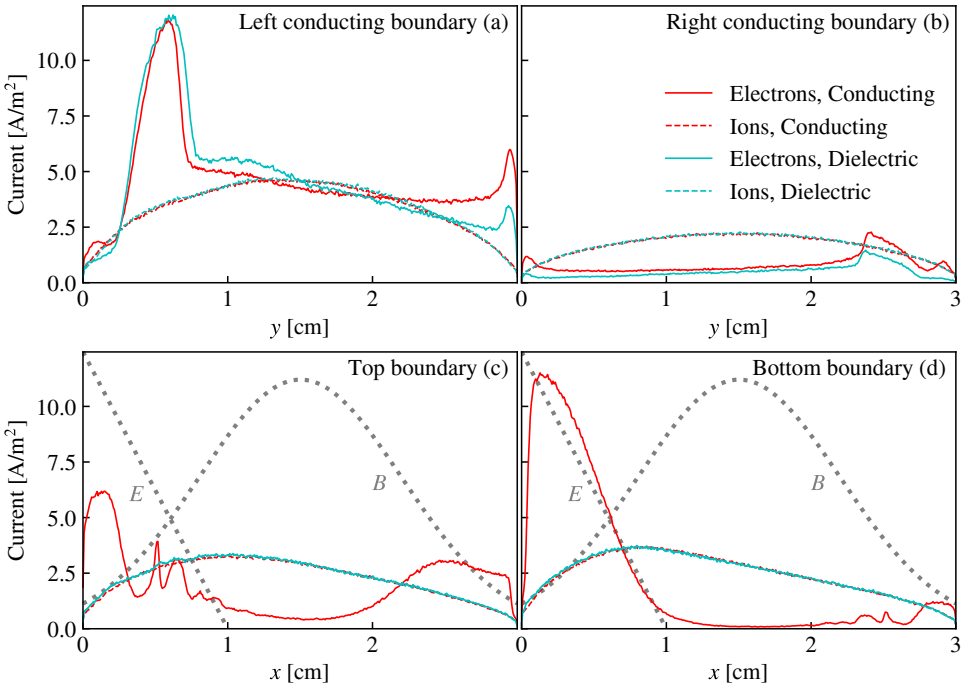

Figure 4.16: Electron and ion currents (absolute values) collected at the walls of the simulation domain at (a) $x = 0$, (b) $x = l_x$, (c)$y = l_y$, and (d) $y = 0$. The run characteristics are analogous to Fig. 4.15 with dielectric walls at $y = 0$ and $y = l_y$ (cyan), and with conducting walls everywhere (in red). The currents are averaged over 5 µs.

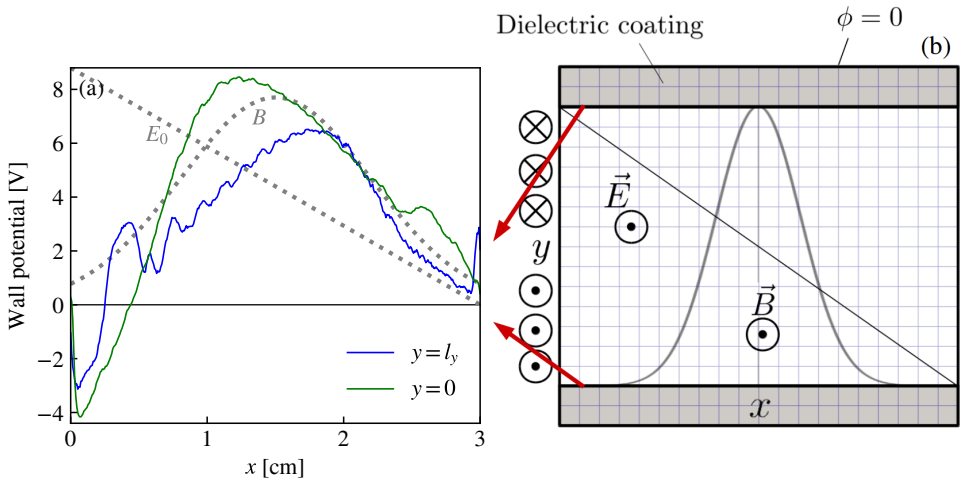

Figure 4.17: (a) Plasma potential averaged over the last 5 µs of the simulation at the inner walls of the discharge at $y = 0$ (green) and $y = l_y$ (blue). (b) Sketch of the simulation setup, including the dielectric layer.

4.3.3 Effects of the Gas Pressure

As already shown experimentally [20], the electron temperature decreases significantly with pressure, both upstream and downstream. The simulation presented here were run with a heating electric field localized in the first third of the discharge only. In this case, we found a minimum of the electron temperature close to the position of the maximum of the magnetic field, close to $x = l_x/2$. Among the various heating conditions investigated, this heating configuration seems to better match experimental results. Only conducting walls are studied in this paragraph.

As shown in Fig. 4.18(a), the plasma density increases when the gas pressure increases everywhere in the discharge, the location of the density maximum remains almost unchanged. In Fig. 4.18(c), we could observe that the upstream electron temperature decreases with the pressure, similarly to the non magnetized ICP discharge. The electron temperature decreases down to about 4 eV until the location of the maximum of the magnetic field. The electron temperature at low pressure remains higher, but the discrepancy has been reduced with respect to the upstream region. Fig. 4.18(b) and (d) show the plasma density and electron temperature profiles in the y direction and emphasize the plasma asymmetry. The plasma density profiles are approximately self-similar such that no real conclusion can be drawn from Fig. 4.18(b). On the contrary, Fig. 4.18(d) shows that the electron temperature has a much stronger asymmetry at low pressure. This result may explain why some theoretical and numerical studies found very strong plasma asymmetry [62, 86], while experimental studies showed that the plasma was essentially 1D [89].

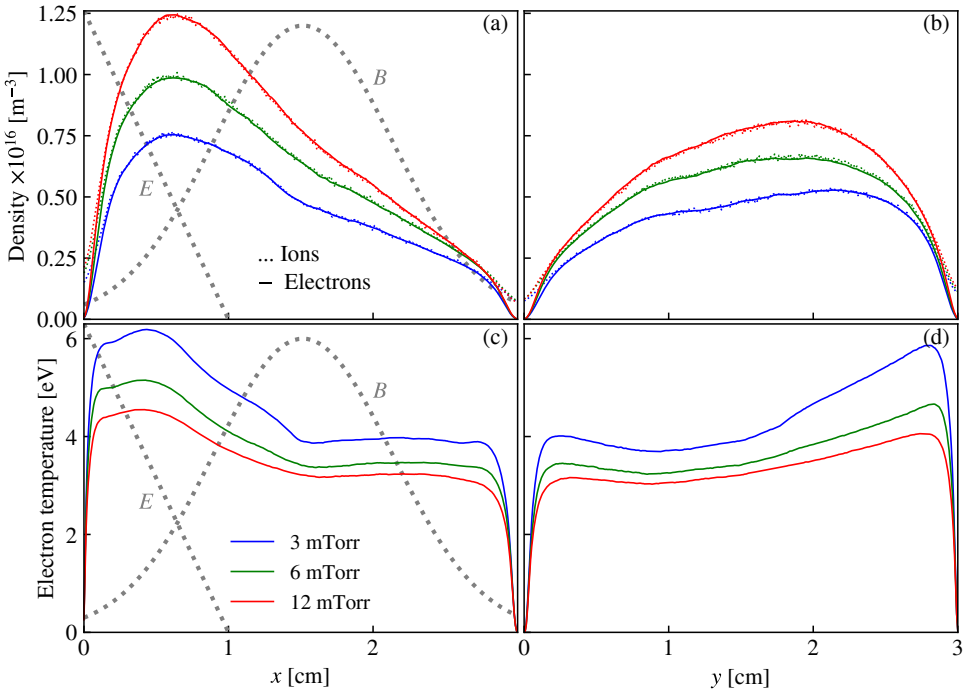

Figure 4.18: (a,b) Plasma density and (c,d) electron temperature profiles at $y = l_y/2 = 1.5$ (LHS column) and $x = l_x/2 = 1.5\,\text{cm}$ (RHS column) for a magnetic filter at 3 mTorr (blue), 6 mTorr (green), and 12 mTorr (red) of gas pressure. The heating power is $9.6\,\text{kW/m}^3$ and the heating electric field decreases linearly with x from 0 to $l_x/3$. The Gaussian magnetic field profile is indicated in gray dotted lines and the maximum value is 20 mT. In (a), the dotted lines represent the ion density and the solid lines represent the electron density. Both the density and the temperature data are averaged over more than 4 µs.

4.3.4 Magnetic Field Characteristics

Effects of the Magnetic Field Strength

The value of the maximum magnetic field affects mainly the downstream electron temperature but almost does not change the upstream electron temperature. In the simulations presented in this section, the magnetic field at the coil location ($x = 0$) is 5 % of the peak magnetic field. At 80 mT in the center, the magnetic field is 4 mT near the coil, which already has a significant influence on plasma transport. In Fig. 4.19 we can see that the value of the peak magnetic field has a minor influence on the upstream plasma properties. The value of the magnetic field seems to drive the slope of the decreasing electron temperature, such that the higher the magnetic field, the lower the downstream electron temperature. The saturation of the electron temperature at a minimum value near the location of the maximum magnetic field is generally observed. However, at 80 mT, the shape of the electron temperature profile is slightly more complicated. The plasma is very unstable in this case, which may explain why the magnetic confinement is destroyed and why the electron temperature does not decrease as much as could be expected from the analysis of the electron temperature profiles at 20 and 40 mT.

In Fig. 4.19(a), the plasma density is not much enhanced by an increase of the magnetic field because the ionization mainly occurs in the upstream region where the magnetic field is very weak anyway. The peak of the electron density slightly increases and is shifted closer to the RF coil (to the LHS) when the magnetic field increases.

Width of the Magnetic Filter

When the magnetic filter region is broader, it may overlap more with the ionization region. In this case, we have already seen in Section 4.3.1 that was more focused on the heating localization, that the minimum of the electron temperature is not precisely reached at the position of the maximum magnetic field. Two different runs are investigated in this paragraph for a power absorbed by the plasma of 9.6 kW/m^3 and 12 mTorr of gas pressure. The magnetic field peaks at 40 mT when $x = l_x/2$. The "narrow" magnetic filter simulation is the same as the one presented in the previous paragraph at 40 mT. In that case, the standard deviation of the Gaussian magnetic filter is $0.2l_x$. In the "broad" magnetic filter configuration, all the parameters remain unchanged except the standard deviation of the Gaussian magnetic filter that is increased to $0.5l_x$. The plasma density and electron temperature profiles are displayed in Fig. 4.20. The confinement is much better in the upstream region, such that the maximum plasma density in the upstream region is enhanced by about 60 %. The location of the maximum plasma density is also shifted towards left and becomes closer to the planar coil. The upstream temperature does not change much, which confirms the fact that the upstream electron temperature is mainly driven by the gas pressure. However, the filtering effect seems significantly more efficient when

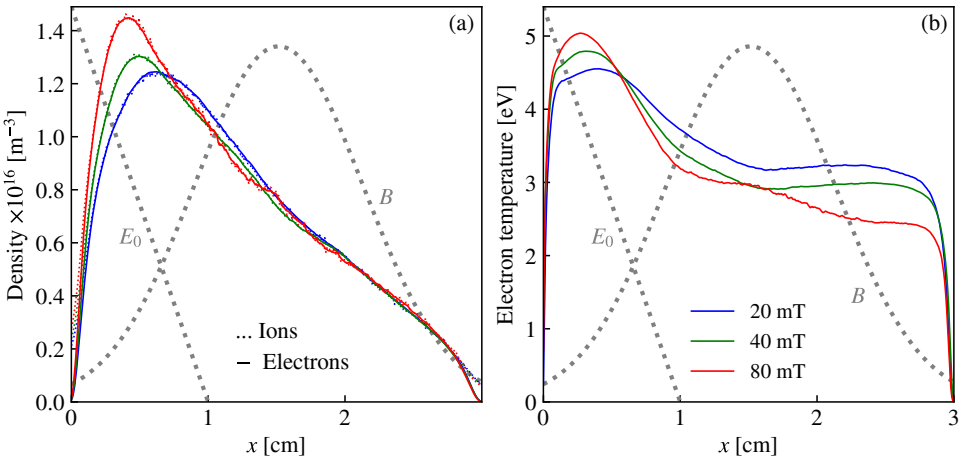

Figure 4.19: (a) Plasma density and (b) electron temperature profiles at $y = l_y/2 = 1.5\,\text{cm}$ for a magnetic filter at 12 mTorr. The heating power is $9.6\,\text{kW/m}^3$, and the heating electric field decreases linearly with x from 0 to $l_x/3$. The Gaussian magnetic field profile is indicated in gray dotted lines, and the maximum value varies between 20 and 80 mT. In (a), the dotted lines represent the ion density, and the solid lines represent the electron density. Both the density and the temperature data are averaged over more than 4 µs.

the width of the magnetic filter is increased. The downstream electron temperature drops from 2.9 eV with a narrow magnetic filter, down to 2.37 eV with a broad magnetic filter. This observation may partially explain why the downstream electron temperatures found in the simulations were always higher than the experimental values that can be as low as 1 eV [20].

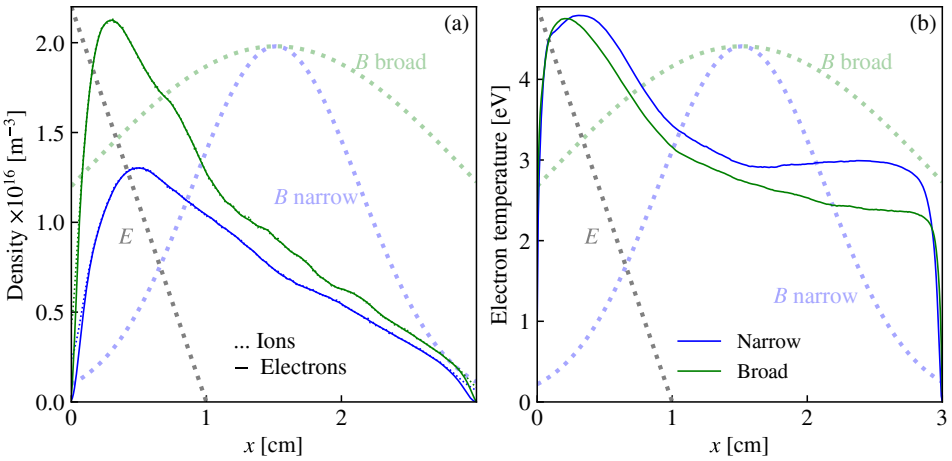

Figure 4.20: (a) Plasma density and (b) electron temperature profiles at $y = l_y/2 = 1.5$ cm for a magnetic filter at 12 mTorr. The heating power is 9.6 kW/m^3, and the heating electric field decreases linearly with x from 0 to $l_x/3$. The magnetic filters are modeled by Gaussian functions with a standard deviation of $0.2l_x$ (blue) and $0.5l_x$ (green), and the maximum magnetic field is 40 mT in both cases. In (a), the dotted lines represent the ion density, and the solid lines represent the electron density. Both the density and the temperature data are averaged over 7 µs.

4.4 One-dimensional Fluid Model of a Magnetic Filter

Previous fluid models of a magnetic filter [87, 73, 62] were quite successful in describing the main trends of a magnetic filter. However, there are still strong incentives to develop new fluid models of a magnetic filter

1. No systematic experimental validation was performed.

2. The instability-enhanced transport was not modeled correctly in previous fluid simulations.

Here, we propose a 1D model of a magnetic filter that is compared with PIC simulation and the ultimate aim of this code, which is slightly beyond the scope of the present work, is to bridge the PIC simulation data with experiments using a relatively simple fluid simulation tool. Similarly to global models in the case of non-magnetized discharges, this fluid model could help quick surveys and experimental design of magnetic filters.

4.4.1 Model Assumptions

The model is inspired both from global models of GIT using an ICP source, such as in the work of Chabert *et al.* [30], and 1D fluid models used for HT modeling, such as in Martorelli *et al.* [110]. The simulated direction is x and the magnetic field is along z. Energy and particle losses in the directions that are not simulated are represented with an h factor $h(x)$ that may depend on the local temperature and magnetic field. We consider an argon plasma with a power density source term w that is given as model input. The model assumptions are generally the same as in the isothermal models derived in Chapter 2:

- The plasma has only one, singly charged ion species, typically Ar^+.
- The neutral gas has uniform density and temperature. Gas heating and neutral depletion are neglected, such that the model applies for weakly ionized plasmas. The gas temperature is 300 K.
- The ionization frequency is smaller than the electron-neutral and the ion-neutral elastic collision frequencies.
- The ions are in thermal equilibrium with the gas, so their temperature is also fixed to 300 K.
- The plasma is quasineutral $n_i = n_e = n$.
- No current is drawn through the discharge such that the continuity equation implies that $v_{ix} = v_{ex} = v$.
- The parameters of the model are the local plasma density $n(x)$, the local plasma velocity $v(x)$ and the local electron temperature $T_e(x)$.
- Electron heat flux is neglected in the electron energy conservation equation.
- The ions are not magnetized but the electrons are.
- The plasma velocity in the quasineutral domain should remain lower than the Bohm speed, which is much smaller than the electron thermal velocity. Electron inertia and gyroviscosity are hence neglected.

4.4.2 Model Equations

For each value of x, the fluid equations are integrated in the (yz) plane. The particle losses perpendicularly to the x axis are accounted for using a 2D h factor.

The particle balance equation derived from Eq. (1.53) is

$$\partial_t n + \partial_x(nv) = n\nu_{iz} - \frac{hu_B nC}{S} \tag{4.3}$$

where C is the contour of the CS at $x = cst$ and S is the CS surface area. The projections of the momentum conservation equations along the x axis are

$$0 = -\frac{k_B\partial_x(nT_e)}{n} + e\partial_x\phi - m_e v\left(\frac{{\omega_{ce}}^2}{\nu_e} + \nu_e\right) \tag{4.4}$$

for the electrons and

$$m_i\partial_t v + m_i v\partial_x v = -\frac{k_B\partial_x(nT_i)}{n} - e\partial_x\phi - m_i\nu_i v \tag{4.5}$$

for the ions, where the ion temperature is assumed constant in time and space, and the electron inertia is neglected. Summing up Eqs. (4.4) and (4.5),

$$m_i\partial_t v + m_i v\partial_x v = -\frac{k_B\partial_x[n(T_e + T_i)]}{n} - \left[m_i\nu_i + m_e\left(\frac{{\omega_{ce}}^2}{\nu_e} + \nu_e\right)\right] v \tag{4.6}$$

As electron temperature gradients are inherent to the functioning of a magnetic filter, the electron energy equation has now to be taken into account. Neglecting the electron heat flux, the electron internal energy equation is [110, 9]:

$$\frac{3}{2}\partial_t(nk_BT_e)+\frac{3}{2}\nabla\cdot(nT_e\mathbf{v}_e)+nk_BT_e\nabla\cdot\mathbf{v}_e = m_e n\nu_e{\mathbf{v}_e}^2-n\nu_{iz}e\mathcal{E}_{iz}\gamma_i-3\mu k_B(T_e-T_g)n\nu_e \tag{4.7}$$

where

$$\mathcal{E}_{iz}\gamma_i = \mathcal{E}_{iz} + \sum K_{ex}\mathcal{E}_{ex}/K_{iz} \tag{4.8}$$

is the mean energy lost per electron created. The summation is performed over all the excitation levels included in the model. The previous expressions for the volume energy losses come from global models of gas discharges [100, 31] and can be retrieved from kinetic theory. Eq. (4.7) becomes in 1D

$$\begin{aligned}\frac{3}{2}\partial_t(nk_BT_e) + \frac{3}{2}\partial_x(nk_BT_e v) + nk_BT_e\partial_x v = w + nm_e\left(\nu_e + \frac{{\omega_{ce}}^2}{\nu_e}\right)v^2 - n\nu_{iz}e\mathcal{E}_{iz}\gamma_i \\ - 3\mu k_B(T_e - T_g)n\nu_e - \frac{hu_B ne\mathcal{E}_w C}{S}\end{aligned} \tag{4.9}$$

where w is the volume density of power absorbed by the plasma. The heating source comes from an RF induced electric field in the y and z directions and writes

$$w = \frac{ne^2E_{\max}^2}{2m_e\nu_e}. \tag{4.10}$$

where $E_{\max}$ is the amplitude of the heating electric field. In Eq. (4.9), $\mathcal{E}_w$ is the mean energy carried by each electron lost at the wall. Typically, $\mathcal{E}_w$ is proportional to the electron temperature.

$$e\mathcal{E}_w = \alpha k_B T_e \tag{4.11}$$

The total power absorbed by the plasma is

$$\mathcal{W} = S \int_0^{l_x} w \, dx \tag{4.12}$$

We introduce the normalized quantities

$$\begin{aligned} N &= n/n_{\mathcal{E}\,\mathrm{ref}} \\ T &= T_e/T_{\mathcal{E}\,\mathrm{ref}} \\ V &= v/v_{\mathcal{E}\,\mathrm{ref}} \\ \nu &= \nu_e/\nu_{\mathcal{E}\,\mathrm{ref}} \\ \nu_I &= \nu_i/\nu_{\mathcal{E}\,\mathrm{ref}} \\ \nu_{IZ} &= \nu_{iz}/\nu_{\mathcal{E}\,\mathrm{ref}} \\ \omega_{CE} &= \omega_{ce}/\nu_{\mathcal{E}\,\mathrm{ref}} \\ W &= w/w_{\mathcal{E}\,\mathrm{ref}} \\ X &= x/l_{\mathcal{E}\,\mathrm{ref}} \\ \tau &= t\nu_{\mathcal{E}\,\mathrm{ref}} \\ L_X &= l_x/l_{\mathcal{E}\,\mathrm{ref}} \end{aligned} \tag{4.13}$$

where the reference quantities are

$$\begin{aligned} l_{\mathcal{E}\,\mathrm{ref}} &= S/C \\ w_{\mathcal{E}\,\mathrm{ref}} &= \nu_e e\mathcal{E}_{iz} \left(\frac{C}{S}\right)^3 \\ n_{\mathcal{E}\,\mathrm{ref}} &= \frac{\mathcal{W}S}{Cv_{\mathcal{E}\,\mathrm{ref}} e\mathcal{E}_{iz}} \\ T_{\mathcal{E}\,\mathrm{ref}} &= e\mathcal{E}_{iz}/k_B \\ v_{\mathcal{E}\,\mathrm{ref}} &= \left(\frac{e\mathcal{E}_{iz}}{m_i}\right)^{1/2} \\ \nu_{\mathcal{E}\,\mathrm{ref}} &= \frac{C}{S}\left(\frac{e\mathcal{E}_{iz}}{m_i}\right)^{1/2} \end{aligned} \tag{4.14}$$

The set of normalized equations to be solved is (Eqs. (4.3), (4.6) and (4.9))

$$\partial_\tau N + \partial_X(NV) = N\nu_{IZ} - hNT^{1/2} \tag{4.15}$$

$$\partial_\tau V + V\partial_X V = -\partial_X T - (T+T_I)\frac{\partial_X N}{N} - \left[\nu_I + \mu\left(\frac{{\omega_{CE}}^2}{\nu} + \nu\right)\right] V \tag{4.16}$$

$$\begin{aligned}\frac{3}{2}\partial_\tau(NT) + \frac{3}{2}\partial_X(NVT) + NT\partial_X V = W + \mu N\left(\nu + \frac{{\omega_{CE}}^2}{\nu}\right)v^2 \\ - N\nu_{IZ}\gamma_i - 3\mu(T-T_g)\nu N - hT^{3/2}N\alpha\end{aligned} \tag{4.17}$$

The unknown variable vector of this system of equations is

$$U = \begin{pmatrix} N \\ V \\ T \end{pmatrix} \tag{4.18}$$

and the system takes the matrix form

$$\boxed{\partial_\tau U + A\partial_X U = B} \tag{4.19}$$

where

$$A = \begin{pmatrix} V & N & 0 \\ \frac{T+T_I}{N} & V & 1 \\ 0 & \frac{2}{3}T & V \end{pmatrix} \tag{4.20}$$

and

$$B = \begin{pmatrix} N\nu_{IZ} - hNT^{1/2} \\ -\nu_I V - \mu\left(\frac{{\omega_{CE}}^2}{\nu} + \nu\right)V \\ \frac{2W}{3N} + \left(1 - \frac{2\alpha}{3}\right)hT^{3/2} - \nu_{IZ}\left(T + \frac{2}{3}\gamma_i\right) + \frac{2\mu V^2}{3}\left(\nu + \frac{{\omega_{CE}}^2}{\nu}\right) - 2\mu(T-T_g)\nu \end{pmatrix} \tag{4.21}$$

4.4.3 Numerical Solution

Numerical Scheme

Eq. (4.19) is a Euler equation for our system. It has a steady state non-trivial solution if and only if

$$\det A \neq 0\,. \tag{4.22}$$

$$\det A = V\left[V^2 - \left(\frac{5}{3}T + T_I\right)\right] \tag{4.23}$$

If $V = 0$, any (N, T) can be a solution, but this is not compatible with the Bohm criterion

$$V = T^{1/2} \tag{4.24}$$

at the sheath edge. If we assume that the velocity is much smaller than the Bohm speed in the discharge center, Eq. (4.22) becomes

$$\boxed{|V| < \left(\frac{5}{3}T + T_I\right)^{1/2} = V_c} \tag{4.25}$$

which is an alternative to the usual Bohm criterion that resembles the sheath criterion found for polytropic electrons and with a correction coming from the ion temperature. The polytropic coefficient would be here $5/3$, which is consistent with the adiabatic hypothesis (no heat flux).

The system is solved using the Steger-warming scheme [98] that requires to compute the eigen-values and the eigen-vectors of the A matrix. The eigen-values are

$$V \ , \quad V - V_c < 0 \ , \quad \text{and} \quad V + V_c > 0 \ , \tag{4.26}$$

and the corresponding eigen-vectors are the columns of the matrix

$$R = \begin{pmatrix} -\frac{N}{T+T_I} & \frac{3}{2}\frac{N}{T} & \frac{3}{2}\frac{N}{T} \\ 0 & -\frac{3}{2}\frac{V_c}{T} & \frac{3}{2}\frac{V_c}{T} \\ 1 & 1 & 1 \end{pmatrix} \tag{4.27}$$

such that

$$R^{-1}AR = \begin{pmatrix} V & 0 & 0 \\ 0 & V - V_c & 0 \\ 0 & 0 & V + V_c \end{pmatrix} \tag{4.28}$$

Let

$$\Lambda^+ = \begin{pmatrix} \mathcal{H}(V)V & 0 & 0 \\ 0 & 0 & 0 \\ 0 & 0 & V + V_c \end{pmatrix} \text{ and } \Lambda^- = \begin{pmatrix} \mathcal{H}(-V)V & 0 & 0 \\ 0 & V - V_c & 0 \\ 0 & 0 & 0 \end{pmatrix} \tag{4.29}$$

be the diagonal matrices containing the positive and negative eigen-values of A, respectively, where $\mathcal{H}$ is the Heaviside function.

$$A = A^+ + A^- \tag{4.30}$$

where

$$A^+ = R\Lambda^+R^{-1} \text{ and } A^- = R\Lambda^-R^{-1} \tag{4.31}$$

Splitting the A matrix between A^+ and A^-

$$\boxed{\Delta x A \partial_X U \approx A^+_{i-1/2}(U_i - U_{i-1}) + A^-_{i+1/2}(U_{i+1} - U_i)} \tag{4.32}$$

allows using upwind numerical schemes for both terms. The temporal Eq. (4.19) can be integrated explicitly using the 4^{th} order Runge-Kutta solver `odeint` of the `scipy` Python package. In Eq. (4.32), $A^+_{i-1/2} = (A^+_{i-1} + A^+_i)/2$ and $A^-_{i+1/2} = (A^-_{i+1} + A^-_i)/2$, where i is the cell index.

The numerical scheme is of the first order in Δx. The vector splitting method ensures that the numerical scheme is conservative and stable.

Source Terms B

All the source and loss terms are contained in the $\boldsymbol{B}$ vector. The reaction rates for electron-neutral reactions were computed using the fits given in Fig. 1.4(a) [100]. Only one effective excitation reaction is taken into account. The rates allow in particular to compute the γ_i factor. For simplicity, an h factor corresponding a non-magnetized plasma was used. If the three directions are taken into account, then the losses are expected to be mainly in the z direction, which is the direction of the magnetic field, and a non-magnetized h factor can be used in this direction, for example Eq. (2.130). In order, to allow for comparison with the PIC simulation, the z direction has to be infinite, such that the particles are lost along the y direction only. Since the y direction is perpendicular to the magnetic field, a magnetized h factor has to be used. In the fluid simulation results presented below, Eq. (3.159) is employed, either with a classical electron collision frequency, or with an effective collision frequency that accounts for the role of the instability using Eq. (3.158). Ion collisions are computed using a constant and single momentum transfer collision frequency $\sigma_I = 1.0 \times 10^{-18}\,\mathrm{m}^2$ and the mean ion velocity is computed using Eq. (2.25). It is often assumed that the mean energy lost per ion collected at the wall is such that [100]

$$\alpha = 2 + \frac{1}{2}\ln\left(\frac{1}{2\pi\mu}\right) \approx 6.68 \quad \text{for argon.} \tag{4.33}$$

This expression comes from the integration of the heat flux over a Maxwellian distribution function for particles whose kinetic energy towards the wall in volts is higher than the plasma potential. Since the heat flux is neglected in the model, assuming $\alpha = 0$ seems reasonable. A much better agreement with the PIC simulation was found when taking $\alpha = 0$. When α is taken equal to 6.68, the electron temperature drops to almost 0 in the downstream region.

The source term W controls the power density injected in the plasma. To enable comparison with PIC simulation, it is assumed that the amplitude of the heating electric field decreases linearly with x from 0 to $l_x/3$ in Eq. (4.10).

Boundary Conditions and Initial Conditions

The only boundary condition that is used here is a Bohm criterion. We used a very simple form of the Bohm sheath criterion $|V| = T^{1/2}$ instead of the equality form of Eq. (4.25) to avoid singularities near the edge of the domain. Of course, when $|V| < T^{1/2}$, inequality (4.25) is always fulfilled. Numerically, the boundary condition is applied to the gradient of the velocity at the last cell and the first cell, such that the Bohm equality is strictly valid at two ghost cells:

$$V_{-1} = -T^{3/2} \quad \text{and} \quad V_N = T^{3/2} \tag{4.34}$$

where N is here the number of cells, indexed from 0 to $N-1$.

The simulation is started with a uniform normalized density equal to 0.1, a normalized velocity increasing linearly from $-1/2$ to $1/2$, and a uniform normalized electron temperature equal to 0.63.

4.4.4 First Results

With $N = 180$ and a normalized time step equal to 0.02, the simulation converges in about 25 000 iterations. The first results are shown in Fig. 4.21 for the density (a) and the electron temperature (b) and compared with the PIC simulation results. The total length of the magnetic filter is $l_x = 3$ cm and the transverse direction is also 3 cm long. The direction of the magnetic field z is infinite. The Gaussian magnetic filter is centered at $x = l_x/2$ with a maximum of 20 mT and a standard deviation of $0.2l_x$. The gas pressure is set to 12 mTorr.

In Fig. 4.21, the results are presented for two different models. The classical model assumes a classical electron-neutral collision frequency while the instability-enhanced model accounts for the effect of the instability on global transport with an effective collision frequency given by Eqs. (3.149) and (3.156). The fluid model is able to capture the drop in the electron temperature through the magnetic filter and predicts an approximately constant electron temperature in the downstream region. The value of the downstream electron temperature depends on the model taken for the wall losses – i.e. the h factor – and the type of collisionality – classical or instability-enhanced. The present model provides the correct orders of magnitude and the correct trends, but still has two main limitations:

1. The instability-enhanced collision frequency is taken from the study on the magnetized plasma column where the magnetic field and electron temperature gradients were neglected. Moreover, the direction of the instability changes with the magnetic field which is not accounted for in the present model;

2. Perhaps more importantly, the conductive heat flux Q is taken into account neither in the x direction, nor in the plane perpendicular to the simulation axis. We found that naive estimates of the radial heat flux as the ones used in global models yielded non-consistent results (the electron temperature drops to almost 0);

3. Finally, the 1D model does not allow one to account for the Hall effect, especially near the sheaths that develop in the (y, z) plane.

Some tests were also performed in the broader magnetic filter configuration for a maximum magnetic field of 40 mT. The predictions of the fluid model using classical and instability-enhanced transport theories are compared with the corresponding PIC simulation. The classical collision model grossly overestimates the upstream plasma density, while the yields a maximum plasma density only 10 % higher than the PIC simulation. The predicted electron temperature is also significantly closer to the PIC simulation results when an instability-enhanced collision frequency is used.

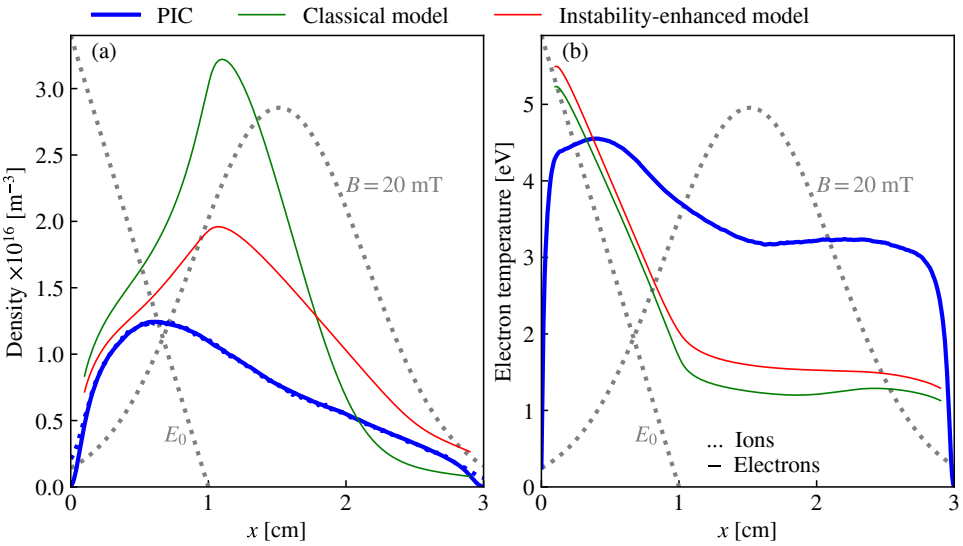

Figure 4.21: (a) Electron and ion densities and (b) electron temperature found by PIC simulation (thick lines) and with the 1D fluid model (thin line). The Gaussian magnetic field profile has a standard deviation $\varsigma = 0.2l_x$, and the peak magnetic field is 20 mT. The gas pressure is 12 mTorr.

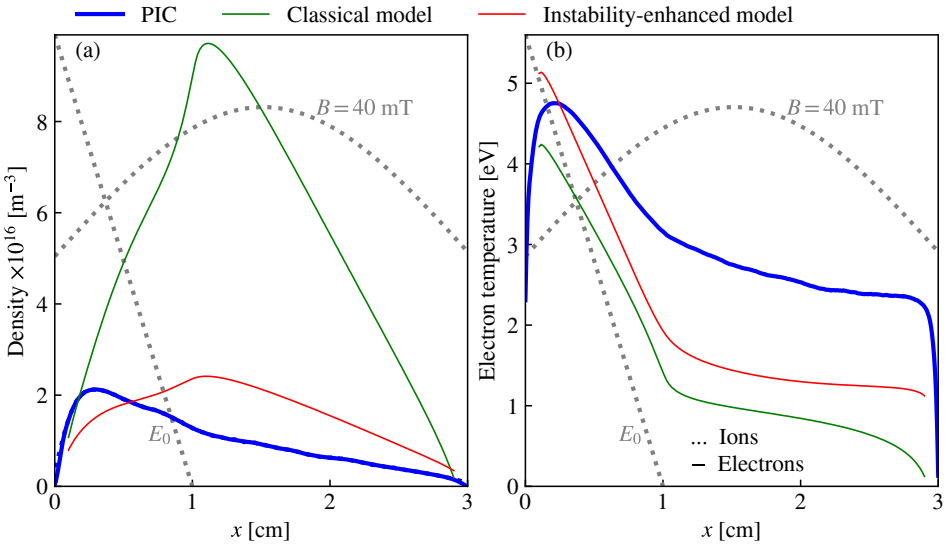

Figure 4.22: (a) Electron and ion densities and (b) electron temperature found by PIC simulation (thick lines) and with the 1D fluid model (thin line). The Gaussian magnetic field profile has a larger standard deviation $\varsigma = 0.5l_x$, and the peak magnetic field is 40 mT. The gas pressure is 12 mTorr.

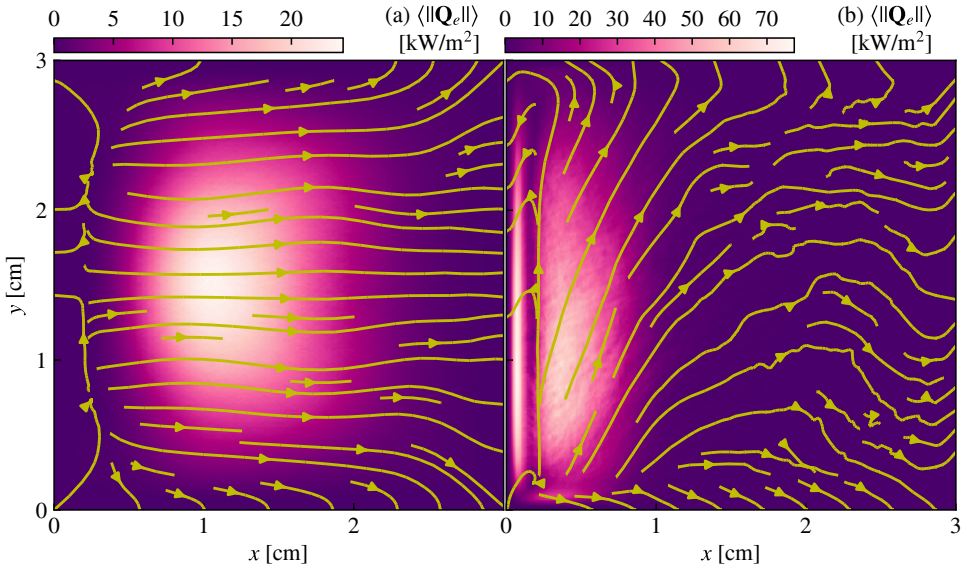

Figure 4.23: Mean electron heat fluxes found in the PIC simulations at 12 mTorr, at steady state. The absorbed power is 9.6 kW/m^3 and the amplitude of heating electric field decreases linearly with x from 0 to $l_x/3$. The arrows represent the streamlines. (a) No magnetic field. (b) Broad magnetic filter ($\varsigma = 0.5 l_x$) with a maximum at 40 mT.

Interestingly, the predicted plasma density is, in this case, closer to the PIC simulation than in the previous case at 20 mT with a narrower magnetic filter. This may be due to the fact that the instability is very similar to the resistive drift instability from which the instability enhanced collision frequency is derived, while in the narrow 20 mT filter configuration, the instability has a different aspect (see Fig. 4.8).

Nevertheless, as already observed in Fig. 4.21 the predicted electron temperature is lower than that found in the PIC simulation, and the location of the maximum plasma density is more on the RHS. Again, this suggests that the heat flux should be taken into account.

4.4.5 The Role of the Heat Flux

Heat Flux in the PIC Simulations

The heat flux was completely neglected in the previous paragraph. Fig. 4.23 shows the heat flux streamlines in the *LPPic* simulations, with no magnetic field, and in the broad magnetic filter configuration at 40 mT of maximum magnetic field. The heat flux should typically be compared to

$$n_e m_e {v_{Te}}^3. \tag{4.35}$$

For an electron temperature of 3 eV and a plasma density of 10^{16} m^{-3}, this is 3 kW/m^2 which is of the same order of magnitude as the typical values found in the PIC simulation. As a conclusion, the electron heat flux should not be neglected in fluid models, even at relatively low collisionality. Some work is on-going at LPP to add the heat flux in the 1D fluid simulation presented here. [3]

[3] The reader can refer to the master thesis of B. Estèves to be expected by October 2019 for more consistent estimates of the heat flux in the magnetic filter configuration.

Summary

This chapter was dedicated to the 2D PIC and 1D fluid simulations of the ionization and filtering stages of the PEGASES ion source operated with argon. A simulation in full geometry is performed and compared with former experimental results. Some of the characteristics of the filter are retrieved. The main characteristics of the PEGASES magnetic filter are retrieved: (i) The electron temperature decreases from 4 eV in the upstream region to less than 2 eV in the downstream region; (ii) the plasma is more localized in the upstream region; (iii) the plasma has a weak asymmetry in the y direction; and (iv) the EEDF is Maxwellian.

However, the downstream electron temperature found in the simulation is higher than in the experiments and it does not reach a plateau. Most likely, this is observed because the local heating power distribution, which is an input of the PIC simulation, does not match the experimental conditions. Furthermore, the simulation is very computationally expensive and is not converged. Multiple simulations were performed with reduced geometry and power to assess the influence of the control parameters on the performance of the filter. The filter efficiency is characterized by the electron cooling between the upstream and the downstream regions. Again, most of the trends found in the experiments were also found in the PIC simulation. The electron temperature gradient typically decreases with pressure and increases with the peak magnetic field strength and the width of the magnetic filter. Adding dielectric boundaries yields a higher plasma potential that may contribute to faster ion acceleration downstream. In general, the electron cooling found with the PIC simulation with reduced geometry and density is less pronounced than in experimental conditions.

Quantitative agreement with the experimental data is mainly limited by the uncertainty on the local power deposition. A 1D fluid model that was derived and implemented with the goal of reproducing both the experiments and the PIC simulation. Convergence is reached in about one minute using the explicit Steger-Warming flux vector splitting scheme, and the main trends of the plasma behavior through the filter are captured. The agreement with the PIC simulation results is improved when an instability-enhanced collision frequency is taken into account. Future work would involve a more thorough study of the heat flux, and a coupling to the downstream acceleration stage.

Chapter 5

SIMULATION OF IODINE DISCHARGES

Contents

The PEGASES thruster is ultimately made to operate with electronegative gases and not only with argon. Iodine has been identified in the past as a potential successor to xenon for space electric propulsion due to its high mass, and low ionization potential. Additionally, iodine can be stored in solid state which makes pressurized vessel unnecessary in iodine plasma thruster designs. Iodine is a halogen whose mass is 126.905 amu. It can, however, deposit on satellite surfaces, which can cause contamination. In this chapter, we first present a comprehensive CS set for the modeling and simulation of an ICP. Results of a global model, as well as PIC simulations of weakly ionized plasmas in 2D, are then presented.

Iodine is mostly available under the form of the I_2 molecule. In the PEGASES experiment carried out at LPP, the solid sample is heated up to approximately 70°C in order to be sublimated. A molecular gas of I_2 is injected in the discharge chamber, close to the antenna. The pressure inside the discharge chamber is controlled by a vacuum pump and measured by a gauge. More information on the experimental setup is available in the PhD thesis of the former students that worked on the PEGASES thruster in the past years. In particular, the experimental device operated with iodine is described in details in P. Grondein's PhD thesis (2016) [70]. P. Grondein has carried out probe experiments inside the PEGASES device and developed a global model of the discharge without the magnetic filter. More reactions are added to the model, and a minimal set of reactions was implemented in the *LPPic* code, to allow for 2D PIC simulations of iodine ICPs.

5.1 Iodine for Electric Space Propulsion

Iodine has been contemplated for space electric propulsion since the end of the 1990s as a possible alternative to xenon. The advantage of electric space propulsion, in general, is to feature a very good mass consumption efficiency, with high specific impulse designs. The mass of the full pressurized xenon tank on a typical geostationary Earth Orbit (GEO) spacecraft represents about 0.1% of the cost of the full system [160]. However, this may be significant for satellites that cost several hundred million euros. Pressurized vessels may not be optimal for simpler and more compact designs required for small satellites in low Earth orbit (LEO). Iodine is stored in solid state, so the storage tank of iodine EP systems can be lighter and does not need to be pressurized. This could be a great advantage for small satellites where the pressurized tanks have higher mass to volume ratios. Moreover, the xenon is quite expensive, and the supply is quite scarce, such that the price tends to fluctuate in time. One of the first studies on the potential of iodine for EP was performed by Dressler *et al.* [48]. In their study, the authors suggest that the performances of GIT or HT operated with iodine may be as good as equivalent designs with xenon. The authors propose a propellant handling system composed of a heating tank where iodine crystals are stored and vaporized, and a porous frit that filters out crystal particles. The gas enters the discharge chamber through a heated pipe to avoid deposition and a mass flow controller. The power consumption for the heating system is found to be negligible compared to the discharge power. Barnes and Kushner [8] performed optical measurements on low-pressure discharges in a mixture of xenon and iodine. More recently, Steinberger and Scime developed optical diagnostics to measure the proportions of various species inside an iodine plasma [144, 143].

At LPP, where the expertise on electronegative plasmas comes from the techniques developed for plasma etching and deposition with gases such as CF_4 / O_2 mixtures [18], chlorine [47] or sulfur hexafluoride (SF_6) [21, 22], the interest for

iodine electric propulsion systems is not only economical. The ultimate aim is to achieve new thruster designs where both positive and negative ions are extracted. This could allow for cathode-less thruster designs, and mutual recombination in the plume could generate a neutral beam that would be very focused (low plume angle), and that would not be deflected towards the charged surfaces of the satellite. The latter aspect is particularly important since surface reactivity is a potential issue for plasma thrusters operated with iodine. The first concepts and prototypes are described in details in G. Leray's thesis [97], as well as in the work of L. Popelier [119]. The extraction was investigated experimentally by Lafleur *et al.* [90, 95], and the acceleration by Rafalskyi *et al.* [122]. In 2016, P. Grondein [71] developed a global model of an iodine GIT. There was no magnetic field in the model, so the electronegativity derived from the model was quite low. The performances were comparable with those of the xenon model. Thanks to its affordable price and its compatibility with high specific impulse GIT designs, iodine is suitable for high Δv space missions, such as systematic space debris removal, for instance [107]. Future EP systems will also have to be compatible with space debris collision avoidance maneuvers [63, 106].

The extraction, the acceleration, and the plume recombination are not investigated here. We focus on the extension of the previous simulation cases of an argon plasma to the simulation of a realistic iodine discharge. The ultimate goal, that is only partially achieved here, is to simulate the formation of negative ions in the high magnetic field region of PEGASES. In the next sections, methods to simulate the inner part of a GIT operated with iodine are described.

5.2 A Collision Cross Section Set for the Simulation of Iodine Plasmas

Some of the fundamental data are missing for iodine and we do not pretend to describe the complete chemistry of an iodine plasma. All the assumptions made to gather the reaction set of Table 5.2 are made explicit in the text. Some of the assumptions come from comparisons with chlorine plasmas, but all the data are taken from the literature or dedicated computations made by Quantemol Ltd. The CSs and the reaction rates are shown in Figs. 5.1 to 5.3. The reactions that were not considered here are also presented in Table 5.3.

Compared to the global model developed by P. Grondein *et al.* [70], three new reactions are added:

$$\text{Electron impact dissociation of } I_2^+ \quad I_2^+ + e^- \longrightarrow I^+ + I + e^- \tag{5.1}$$

$$\text{Electron detachment from } I^- \quad I^- + e^- \longrightarrow I + 2e^- \tag{5.2}$$

$$I_2 - I^+ \text{ charge exchange} \quad I_2 + I^+ \longrightarrow I_2^+ + I \tag{5.3}$$

The main interest of this work is the implementation in the *LPPic* code.

I atom			
Mass	126.905	amu	[136]
Ionization potential	11.64	eV	[75]
Relative polarizability	27.0		[120]

I_2 molecule			
Mass	253.81	amu	[136]
Ionization potential	9.31	eV	[75]
Inter-atomic bond	2.7128×10^{-10}	m	[75]
Relative polarizability	69.7		[109]

Table 5.1: Physical properties of iodine

5.2.1 Plasma Species

Iodine is very reactive and can form a variety of species depending on electron temperature conditions. We follow here the work of P. Grondein [70] and we assume that there are only six species in the plasma

$$I_2,\ I,\ I_2^+,\ I^+,\ I^-,\ e^-$$

In general, the gas is injected under the form of molecular iodine I_2. The dissociation energy of I_2 is quite low (1.567 eV) such that I atoms will soon be present in the plasma. Moreover, dissociative attachment does not have a very large CS ($< 2 \times 10^{-21}\,m^2$) but no threshold, so I^- ions are also present in the mixture. Finally, electron impacts on I and I_2 cause I^+ and I_2^+ ions to form. All the processes considered will be described in the next paragraph with more details.

We are aware that other species may appear in the plasma. Henri (1972) [79] performed a study on mass spectrometers using electronegative plasmas, with relevant experimental results on iodine. The presence of I_3^+ and I_3^- ions was hence detected. Spencer and Smith found I_2^- ions as well [52]. Moreover, one can expect doubly-charged ions I^{2+} to form for high electron energies, as it is observed in Hall thrusters operated with xenon. The energy needed to form I^{2+} from the I^+ ion is 19.13 eV, which is slightly below the energy required to form Xe^{2+} from Xe^+ (20.98 eV) [136]. However, I^{2+} ions were not particularly observed in HTs operated with iodine [147]. In GITs, where the electron energy is lower, we do not expect any doubly-charged ions to form.

5.2.2 Electron-Neutral Reactions

The mechanisms that drive the balance of species in an iodine plasma are much more complex than in the case of a noble gas due to the species reactivity. The fundamental data are available on the NIST database [136] and the references therein. Iodine is an electronegative gas, and Biondi and Fox showed that dissociative attachment

$$I_2 + e^- \rightarrow I + I^- \tag{5.4}$$

was the main mechanism for electron losses in their experimental conditions [13]. They estimated the reaction CS in a microwave plasma afterglow at low electron temperature [56, 14]. Positive ions I^+ and I_2^+ are formed from I atoms and I_2 molecules with ionization energies of 11.64 eV and 9.31 eV respectively [3]. Some of the CSs for electron impact mechanisms were calculated by J. Hamilton [75] using the R-matrix method developed by J. Tennyson [151, 152]. This is the case for dissociative ionization

$$I_2 + e^- \rightarrow I + I^+ + 2e^-$$

that has a threshold energy of 10.75 eV, but the branching between electron impact ionization and dissociative ionization of the I_2 molecule was extrapolated from the mass spectra of Cl_2 and Br_2. The results of the R-matrix method were in agreement with experimental results [166] for elastic scattering of electrons on the I atom. The excitation states of the I atom are potentially very numerous, but all the excitation reactions are modeled with only one "superelastic" reaction, with a typical energy loss lower than 1 eV (0.953 eV). No excitations states of I_2 were found in the R-matrix calculation, due to the fact that the dissociation energy of the I_2 molecule is quite low (1.567 eV). As shown in Chapter 1, this reduction does not have a large influence on the EEDF. Finally, electron impact I_2 dissociation has a quite large CS (3.6×10^{-20} m^2 at 3.4 eV) and is generally as important as dissociative attachment for the equilibrium between I_2 and I.

5.2.3 Ion-Neutral Reactions

As for argon, the elastic collisions between ions and neutrals are split in two categories: isotropic scattering and backscattering. The fundamental data are sparse for noble gases and almost non-existent for iodine. The isotropic scattering was assumed to follow a Langevin capture CS, that can be computed from atomic and molecular polarizability [100]. The data is found in the book by Radzig and Smirnov [120] for I and in an article by Maroulis *et al.* for I_2 [109]. The numerical values are indicated in Table 5.1.

The resonant backscattering reaction between I and I^+ should follow the formula given by Sakabe *et al.* [130] (Eq. (1.28)), as it was done for krypton. The prediction of the Sakabe formula was compared to computations performed by Dressler *et al.* [48] based on a linear combination of atomic orbitals in Fig. 5.4. The latter computations were successfully compared to experimental data in the original

article. The Sakabe formula shows an agreement better than 6% with these computations in the range 10-1000 eV. However, the disagreement is higher at low energy, which suggests that one should not be too confident about the application of the Sakabe formula in the 0.026-10 eV energy range. Furthermore, it is assumed that the resonant charge exchange between I and I^- has the same CS, which is somewhat arbitrary and results mainly from a lack of fundamental data. However, Karmohapatro (1965) showed that the resonant charge exchange reaction between Cl and Cl^- had a CS only a few times higher than the resonant CS between Cl and Cl^+. We can, therefore, anticipate that the order of magnitude should be correct for iodine. The resonant charge exchange reactions between diatomic molecules and their positive ion counterpart were the focus of a theoretical article by Evseev *et al.* (1979), from which the CS for the reaction

$$I_2 + I_2^+ \rightarrow I_2^+ + I_2$$

could be estimated.

The non-resonant charge exchange reaction

$$I_2 + I^+ \rightarrow I_2^+ + I \tag{5.5}$$

should play a significant role in the equilibrium between I_2^+ and I^+ ions. Experimentally, it was suspected to cause a significant depletion of the I^+ population [79]. In a chlorine plasma, this reaction CS is twice lower than that of the resonant charge exchange reaction between Cl_2 and Cl_2^+. We made this assumption for iodine, and estimated that the CS for reaction (5.5) was half of the CS for resonant charge exchange between I_2 and I_2^+.

If the behavior is the same as for chlorine, the (non-resonant) charge exchange reaction between I and I_2^+, and the fragmentation reaction $I_2^+ + I_2 \rightarrow I_2 + I + I^+$ should both have thresholds higher than 1 eV and their influence can be neglected in a first approximation. Collisional detachment of electrons can also be important in some electronegative gases such as oxygen, but it is assumed to have a quite high threshold for iodine. Typically, the thresholds were estimated for chlorine by Huang and Gudmundsson [82] to 3.61 eV for $Cl^- + Cl_2 \rightarrow Cl + Cl_2 + e^-$ and 1.13 eV for $Cl^- + Cl \rightarrow Cl_2 + e^-$. The ion energies observed were mostly below 1 eV such that these reactions are neglected for iodine. Collisional detachment is an important mechanism for neutral beam generation in high energy ion sources. While it seems reasonable to neglect the four reactions mentioned above for the ionization and magnetic filtering stages of the PEGASES thruster, this assumption may not be valid for the acceleration stage, where the ions reach much higher energies. More insights about these reactions in a chlorine discharge can be found in an article by Huang and Gudmundsson [82], with relevant 1D PIC simulations of a chlorine CCP.

5.2.4 Ion Loss Mechanisms

At low ion energies, two mechanisms are mainly responsible for negative ion loss, that are two kinds of mutual neutralization. The recombination with I^+

$$I^- + I^+ \rightarrow 2I \tag{5.6}$$

was investigated in a article by Yeung (1957) [164], from which a recombination rate equal to 9.311×10^{-15} m^3/s could be found [71]. The recombination with I_2^+

$$I^- + I_2^+ \rightarrow I + I_2 \tag{5.7}$$

was studied by Greaves in the 1960s [69] and the author obtained a value of 1.22×10^{-13} m^3/s experimentally.

These reaction rates were shown to depend on the ion temperature in the articles cited above [164, 69] but these variations were neglected both in the global model and in the PIC simulation.

The electron detachment from I^-

$$I^- + e^- \longrightarrow I + 2e^- \tag{5.8}$$

is also investigated. The CS was computed by J. Hamilton [76] and a threshold at 2.18 eV of electron energy was found. For weakly ionized plasmas, this reaction is not dominant, and it was not implemented in the PIC simulation code. The electron impact dissociation of the I_2^+ molecular ion is also considered [76], with a threshold at 2.17 eV. Reactions (5.6), (5.7) and (5.8) are essential to balance negative ion production through dissociative attachment. Indeed, if no magnetic field is applied on the discharge, the negative ions are confined by the electric field of the sheath and cannot escape because $k_B T_n \ll e\phi_s$, T_n being I^- temperature. While the presence of the I^- ion recombination reactions are important, F. Marmuse has shown by uncertainty quantification methods that the value retained for the reaction rate was not critical, because it does not play a major role in the determination of the electron temperature.

Positive ions are destroyed by mutual neutralization with I^- but they are also lost at the walls, with a Bohm flux that needs to be corrected due to the presence of negative ions. The review article by Riemann (1991) [128] provides a quite general framework to apprehend the Bohm sheath criterion. The kinetic approach that is provided allows deriving a Bohm sheath criterion with potentially several positive ion species, both positive and negative. The condition for a collisionless sheath is always that the ion kinetic energy is of the order of $k_B T_e/2$ for a plasma where all the positive ions are singly charged, except when the electronegativity becomes high at the sheath edge. This was first shown experimentally by Braithwaite and Allen (1988) and explained in details by Sheridan *et al.* [137], and Franklin and Snell (1999) [57]. At high electronegativity, the kinetic energy of the ions becomes of the order of $k_B T_n/2$, and the flux of negative ions leaving the plasma cannot be neglected anymore.

Reaction		Process	Threshold [eV]	Model	Reference
Electron impact I					
$I + e^- \rightarrow$	$I + e^-$	Elastic	0	0D+PIC	[75]
$I + e^- \rightarrow$	$I + 2e^-$	Ionization	11.64	0D+PIC	[75]
$I + e^- \rightarrow$	$I^* + e^-$	Excitation	0.9529	0D+PIC	[75]
Electron impact I_2					
$I_2 + e^- \rightarrow$	$I_2 + e^-$	Elastic	0	0D+PIC	[75]
$I_2 + e^- \rightarrow$	$I_2^+ + 2e^-$	Ionization	9.31	0D+PIC	[75]
$I_2 + e^- \rightarrow$	$I^+ + I + 2e^-$	Dissociative ionization	10.75	0D+PIC	[75]
$I_2 + e^- \rightarrow$	$I^- + I$	Dissociative attachment	0	0D+PIC	[75]
$I_2 + e^- \rightarrow$	$2I + e^-$	Dissociation	1.567	0D+PIC	[75]
Electron impact dissociation of I_2^+					
$I_2^+ + e^- \rightarrow$	$I^+ + I + e^-$	Dissociation	2.17	0D	[76]
Electron detachment from I^-					
$I^- + e^- \rightarrow$	$I + 2e^-$	Detachment	2.1768	0D	[76]
Recombination					
$I^- + I_2^+ \rightarrow$	$I + I_2$	Mutual neutralization	0	0D+PIC	[69]
$I^- + I^+ \rightarrow$	$2I$	Mutual neutralization	0	0D+PIC	[164]
Isotropic scattering of ions					
$I + I^+ \rightarrow$	$I + I^+$	Elastic	0	PIC	Langevin
$I + I_2^+ \rightarrow$	$I + I_2^+$	Elastic	0	PIC	Langevin
$I + I^- \rightarrow$	$I + I^-$	Elastic	0	PIC	Langevin
$I_2 + I^+ \rightarrow$	$I_2 + I^+$	Elastic	0	PIC	Langevin
$I_2 + I_2^+ \rightarrow$	$I_2 + I_2^+$	Elastic	0	PIC	Langevin
$I_2 + I^- \rightarrow$	$I_2 + I^-$	Elastic	0	PIC	Langevin
Backscattering of ions					
$I + I^+ \rightarrow$	$I^+ + I$	Charge exchange	0	PIC	[130]
$I + I^- \rightarrow$	$I^- + I$	Charge exchange	0	PIC	[130]
$I_2 + I_2^+ \rightarrow$	$I_2^+ + I_2$	Charge exchange	0	PIC	[53]
$I_2 + I^+ \rightarrow$	$I_2^+ + I$	Charge exchange	0	0D+PIC	[130]+[82]
Surface recombination					
$I \rightarrow$	$\frac{1}{2}I_2$	Wall process	0	0D+PIC	[47]

Table 5.2: Reactions of a low temperature iodine plasma investigated in this work.

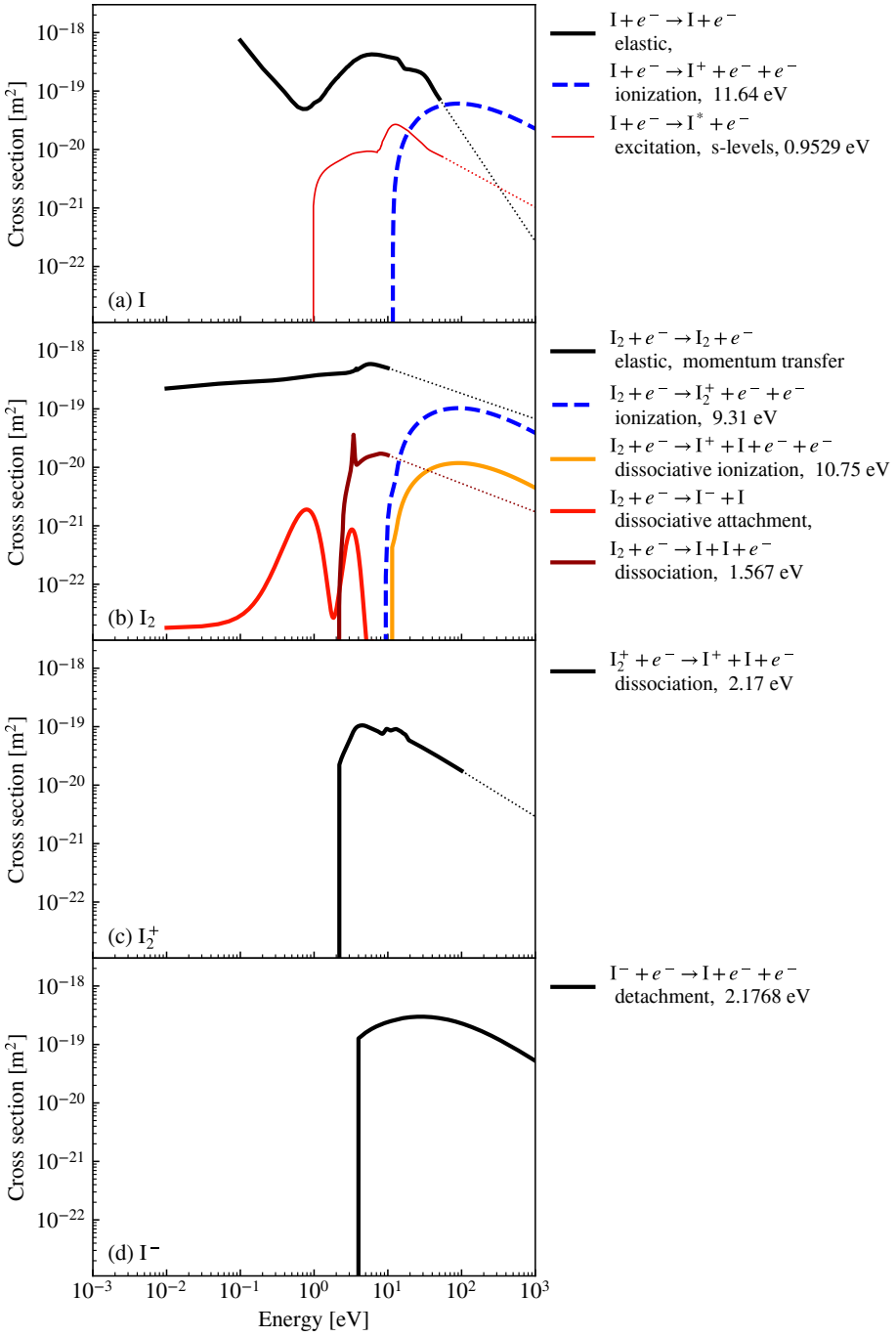

Figure 5.1: Electron-neutral collision CSs for iodine species I, I_2, I_2^+, and I^- computed by Quantemol. The dotted lines represents linear extrapolation in logarithmic scale.

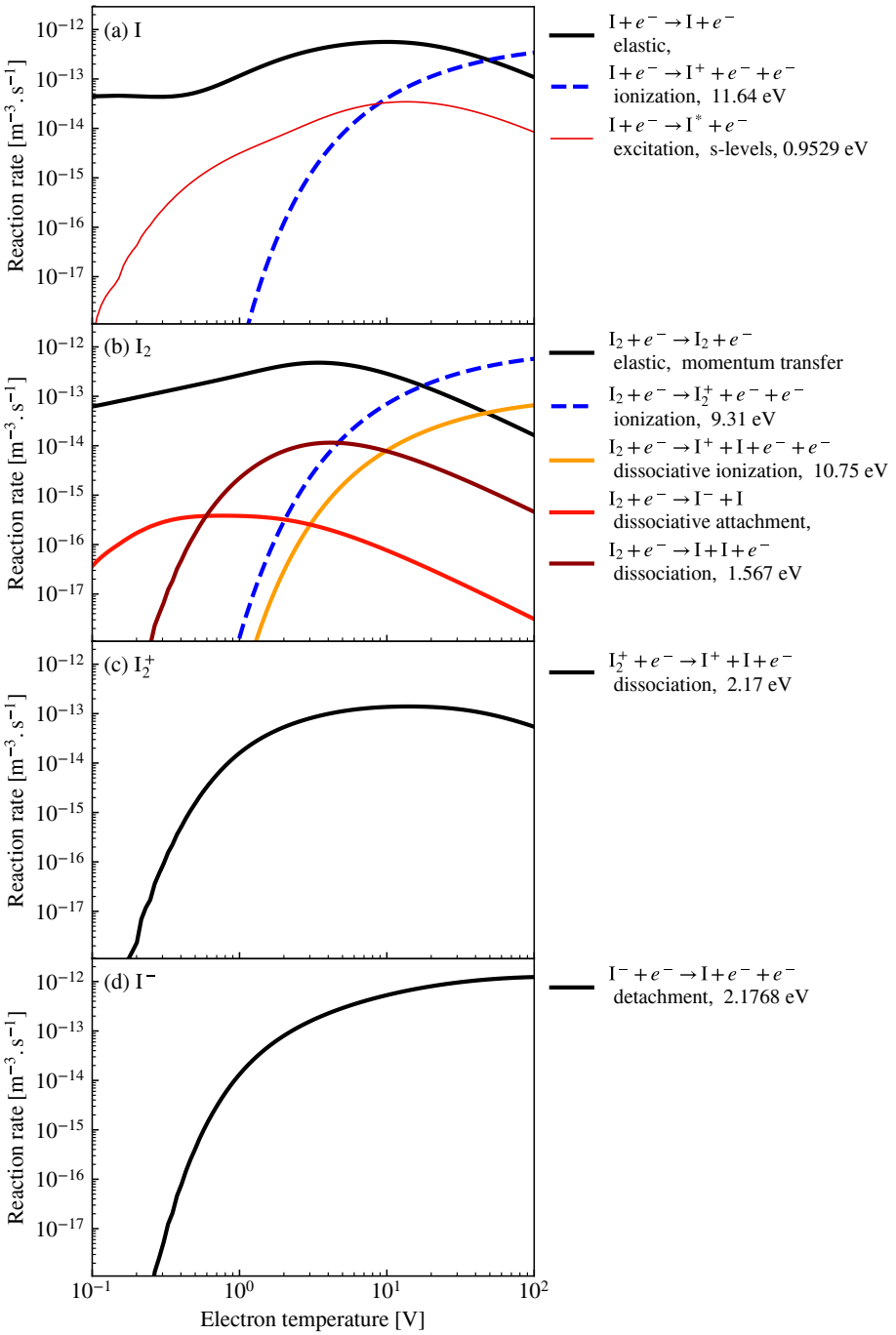

Figure 5.2: Electron-neutral reaction rates for a Maxwellian EEDF and neutral atoms at rest. Numerical integration was performed over the data of Fig. 5.1.

Reaction		Process	Reason	Reference
Electron impact				
$I_2 + e^- \longrightarrow$	$I_2^* + e^-$	Excitation	Threshold $> \mathcal{E}_{diss}$	[75]
$I_2 + e^- \longrightarrow$	$I^+ + I^- + e^-$	Polar dissociation	High threshold and low CS	[82, 79]
$I^- + e^- \longrightarrow$	$I^+ + 3e^-$	Electron impact detachment	Threshold $> 20\,\mathrm{eV}$	[82]
$I_2^+ + e^- \longrightarrow$	$2I$	Dissociative recombination	Weakly ionized	[82]
$I_2 + e^- \longrightarrow$	$2I^+ + 3e^-$	Dissociative double ionization	High threshold (22.5 eV)	[48]
Ion impact				
$I + I_2^+ \longrightarrow$	$I^+ + I_2$	Charge exchange	Threshold $> 1\,\mathrm{eV}$	[82]
$I_2^+ + I_2 \longrightarrow$	$I_2 + I + I^+$	Fragmentation	Threshold $> 1\,\mathrm{eV}$	[82]
$I^- + I_2 \longrightarrow$	$I + I_2 + e^-$	Detachment by I_2	Threshold $> 1\,\mathrm{eV}$	[82]
$I^- + I \longrightarrow$	$I_2 + e^-$	Detachment by I	Threshold $> 1\,\mathrm{eV}$	[82]

Table 5.3: Identified reactions that were neglected in the frame of this work.

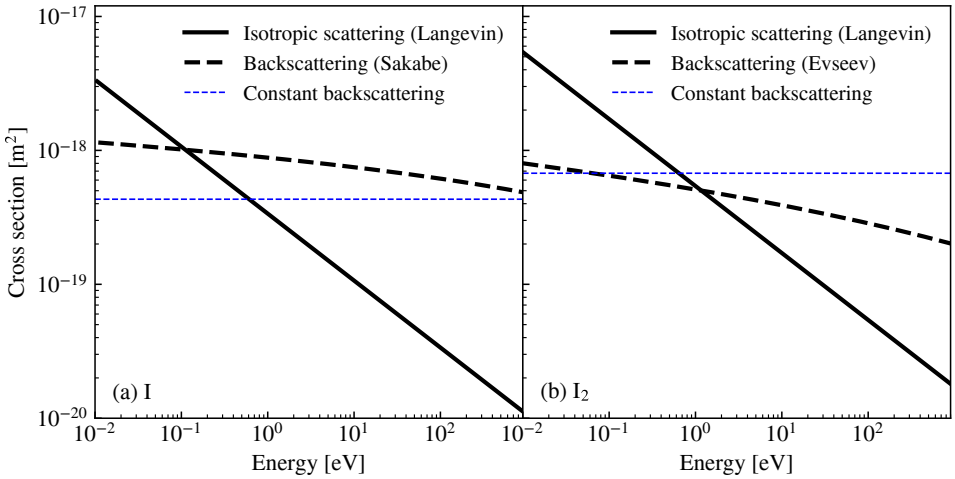

Figure 5.3: Ion-neutral collision CSs for iodine species. The Langevin capture CSs depend on the target only.

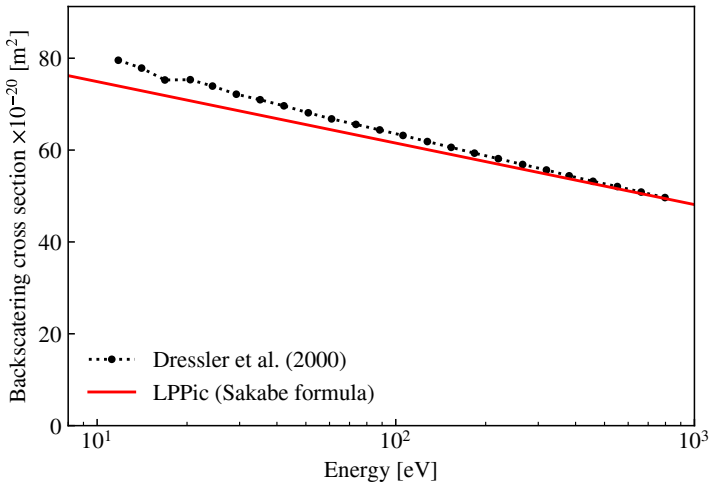

Figure 5.4: Comparison of CSs for the resonant charge exchange between I and I^+. The dotted line is the computation by Dressler *et al.* [48], and the solid line is the application of Eq. (1.28) [130] to atomic iodine. The latter is used in the *LPPic* code.

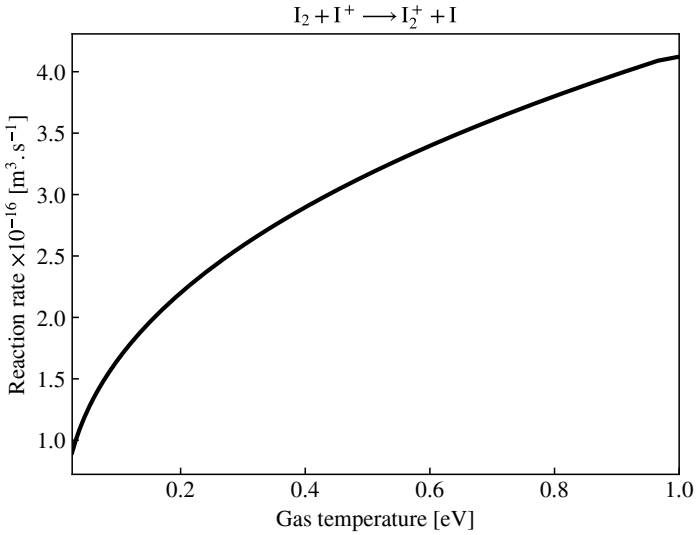

Figure 5.5: Reaction rate used in the global model for the non-resonant charge exchange reaction between I_2 and I^+ as a function of the gas temperature.

5.3 Electronegative Plasma Modeling

5.3.1 Main Modifications of the *LPPic* Code

Most of the reactions that were discussed above are necessary to model an iodine discharge via PIC simulation correctly. Only electron impact dissociation of I_2^+ and electron detachment from I^- were neglected because the results of the global model of P. Grondein *et al.* [71] did not show significant discrepancies when these reactions were added, for the range of parameters we are interested in. Some of these reactions can be easily adapted from the procedures used to model noble gas discharge, as described in V. Croes' thesis [41]. This is the case for elastic collisions, excitations, ionization and dissociative ionization reactions. The dissociative attachment is numerically treated as an ionization reaction, except that the electron is absorbed instead of producing two secondary electrons. Dissociation is treated as an excitation reaction from the point of view of the electron, with a threshold energy of 1.567 eV. However, the data structure of the *LPPic* code had to be changed in depth. Two main Fortran90 types were created, one for the population, and one for the gas. Since Fortran is not per say an object-oriented language, choices had to be made for the data structure of the various populations of super-particles. We chose to declare an array of fixed size `HSpecies` that contains all the populations of heavy particles tracked by the PIC algorithm:

```
integer, parameter                          :: N_HSpecies_max = 10
type(population), dimension(N_HSpecies_max) :: HSpecies
```

The maximum number of heavy species is hardcoded to 10 but can easily be changed if needed in a future version of the code. The `population` type contains mainly an allocatable array of `particle` objects. Its definition is:

```
type population
    real(dbleprc)                           :: mass = 1   ! mass of
        the particles (1 for elecs)
    integer                                 :: charge = 0 ! charge
        of the particles
    real(dbleprc)                           :: T_inj = -1 !
        injection temperature
    type(particle), dimension(:), allocatable :: part_tab
end type population
```

The `particle` type was not modified significantly from the previous versions of the code. Therefore, the number of allocatable arrays of particles corresponds only to the number of heavy species that are simulated, and wasted memory is limited.

The `gas` type is defined in a similar way, but it also contains all the grid diagnostics relative to the reactions, as well as the collision frequencies used for the Vahedi method of null reaction [161]. Its specification is given in Appendix E.

The implementation of these two Fortran types required to modify almost the entire code and makes it more suitable for the simulation of real noble gas plasmas, where multiple ions are generated, metastable species and fast neutrals may be important to take into account, as well as mixtures and molecular plasmas.

5.3.2 Discussion on the I/I_2 Gas Balance

The simulations that were performed still rely on the assumption of a weakly ionized plasma, because each gas is still treated as a uniform background, and local gas depletion is neglected. In particular, the neutral dynamics module developed by T. Charoy and D. Tordeux in 2018 was not coupled to the chemistry module. However, a gas balance equation is written globally to yield the correct fraction of I and I_2 in the gas. An effective dissociation rate was introduced such that the gas dynamics is decoupled from the ion dynamics. This dissociation rate $K_{\mathrm{diss,\,eff}}(T_e)$ should represent all the processes that may turn the I_2 molecule into two I atoms, directly or indirectly. The effective reaction writes

$$I_2 + e^- \underset{K_{\mathrm{diss,\,eff}}(T_e)}{\longrightarrow} 2I + e^- \tag{5.9}$$

The I atoms are repopulated by wall recombination. Indeed, wall recombination of atomic species has been identified as one of the main driver of the balance between gas species in electronegative plasmas [64]. Although the full derivation is made in an article by Chantry (1987) on diffusion theory involving wall reflection [34], we propose a slightly different approach of the phenomenon that might be more understandable in our specific context.

Wall recombination process is described by using a wall sticking coefficient γ_s for atomic iodine, that represents the probability for an iodine atom to be stuck at the wall after a wall collision. When two atoms are collected at the same place, which certainly happens after a long time, iodine is released under the form of a molecule I_2. Therefore, the flux of I_2 released in the discharge due to wall recombination $\Gamma_{I_2,rec}$ is related to the flux of iodine atoms stuck at the wall surface $\Gamma_{I,s}$ by

$$\Gamma_{I_2,rec} = \frac{\Gamma_{I,s}}{2} \tag{5.10}$$

The aim is now to determine $\Gamma_{I,s}$. The γ_s coefficient is the probability for an individual atom to be attached to the wall when a single collision occurs, but may not necessarily be the probability for a full population of particles, provided that some of them may perform several wall collisions before being absorbed. We will calculate a wall absorption frequency

$$\nu_s = \overline{v}_I / \langle \lambda \rangle_s \tag{5.11}$$

where $\langle \lambda \rangle_s$ is the average distance that an atom can go through before being attached to the wall, and $\overline{v}_I$ is the mean velocity of the iodine atoms. Let λ_0 be the *mean travel distance* between two wall reflections. In the low-pressure limit, the mean travel

distance to the wall is $\lambda_0/2$ [34]. After it is created, an atom, which is absorbed at the n^{th} wall collision, has traveled a distance

$$\lambda_n = \lambda_0/2 + (n-1)\lambda_0 \tag{5.12}$$

Moreover, the probability of being absorbed at the n^{th} wall collision is $(1-\gamma_s)^{n-1}\gamma_s$. Therefore,

$$\langle\lambda\rangle_s = \sum_{n=1}^{+\infty}(1-\gamma_s)^{n-1}\gamma_s\lambda_n \tag{5.13}$$

Series integration yields

$$\langle\lambda\rangle_s = \lambda_0\frac{2-\gamma_s}{2\gamma_s} \tag{5.14}$$

The wall absorption frequency is hence

$$\nu_s = \frac{\overline{v}_{\text{I}}}{\lambda_0}\frac{2\gamma_s}{2-\gamma_s} \tag{5.15}$$

This collision frequency comes from the perspective of a single atom. If N_{I} atoms are present in the domain, the flow of atoms collected at the walls is

$$\Gamma_{\text{I},s}S = N_{\text{I}}\nu_s \tag{5.16}$$

and $N_{\text{I}} = n_{\text{I}}V$ in a uniform gas density model, where S and V are respectively the surface area and the volume of the domain. It follows then that

$$\Gamma_{\text{I},s} = \frac{V}{S\lambda_0}n_{\text{I}}\overline{v}_{\text{I}}\frac{2\gamma_s}{2-\gamma_s} \tag{5.17}$$

At very *low pressure*, λ_0 is the *mean geometrical distance* between two points of the walls. In the case of a cosine angular distribution function, Case *et al.* (1953) showed that $\lambda_0 = 4V/S$ [26]. Therefore,

$$\Gamma_{\text{I},s} = \frac{1}{4}n_{\text{I}}\overline{v}_{\text{I}}\frac{2\gamma_s}{2-\gamma_s}. \tag{5.18}$$

The thermal flux

$$\Gamma_{\text{I},thermal} = \frac{1}{4}n_{\text{I}}\overline{v}_{\text{I}} \tag{5.19}$$

appears in this equation.

At low γ_s,

$$\Gamma_{\text{I},s} = \gamma_s\frac{1}{4}n_{\text{I}}\overline{v}_{\text{I}}. \tag{5.20}$$

In this case, the particles may come from all the directions after potentially multiple reflections. The mean velocity is hence the 3D thermal velocity

$$\overline{v}_{\text{I}} = \left(\frac{8k_BT_{\text{I}}}{\pi m_{\text{I}}}\right)^{1/2} \tag{5.21}$$

For chlorine, extensive measurements were performed to determine the recombination coefficient γ_s [88]. Values between 0.01 (silicon at room temperature) to 0.85 (stainless steel) were found, and dependence to the wall temperature was identified. Since the surface aspect is often unknown and subject to gas deposition, comparisons between ICP experiments and simulations are required. It was shown [81, 40] that a value of $\gamma_s \approx 0.02$ yielded better predictions of the discharge properties. No fundamental values were found for iodine. In the global model developed by Grondein *et al.* [71], the value of $\gamma_s \approx 0.04$ was retained.

Considering the uncertainty over the fundamental value of the sticking coefficient γ_s and the limitation of Chantry's model in the intermediate to high-pressure regimes, we used the simplified form of Eq. (5.20) for the flux of iodine atoms in the global model and the PIC code implementation. For both the global model and the PIC simulation, the default value is $\gamma_s = 0.04$. However, the PIC simulation results presented below were obtained for fixed I and I_2 densities. The values of I and I_2 densities used here come from the independent global model computation.

5.3.3 Results of a Global Model of an Iodine ICP

In this section, we model a 2D ICP of 3×3 cm of size based on the global model of Grondein *et al.* [71]. The gas pressure is controlled by a gas flow of I_2 of $2.93 \times 10^{18}\,s^{-1} = 6.53$ sccm and by a gas exhaust surface corresponding to 1.75% of the total discharge surface. The temperature of the gas and the ions is constant and kept to 300 K.

$$T_I = T_{I_2} = T_{I^+} = T_{I_2^+} = T_{I^-} = T_g = 300\ \text{K} \tag{5.22}$$

As this will be shown with the PIC simulations and as observed in experiments, this is not strictly the case, and gas heating may have some influence on the other discharge properties. In all the simulated conditions, the total gas pressure

$$p_g = k_B T_g (n_I + n_{I_2}) \tag{5.23}$$

is between 2.9 and 4.1 mTorr. The I atom and the I_2 molecule leave the discharge volume through the gas exhaust surface area with thermal fluxes $\frac{n_{I/I_2}\bar{v}_{I/I_2}}{4}$. The equilibrium between I and I_2 is mainly determined by the processes described in Section 5.3.2 but also account for all the electron processes summarized in Table 5.2.

The ions and electrons are generated in the discharge volume with the reaction rates given in Fig. 5.2 for Maxwellian EEDF. The positive ions are absorbed across the entire discharge boundary surface with the same Bohm flux

$$\Gamma_{I/I_2} = h n_{I/I_2} \left(\frac{k_B T_e}{m_I} \right)^{1/2} . \tag{5.24}$$

The effect of electronegativity is not included in the h coefficient and Eq. (2.130) is used. The negative ions are repelled by the positive space charge sheath such that

their flux to the walls is neglected. To preserve the global charge balance, the flux of electrons leaving the plasma is

$$\Gamma_e = \Gamma_{\mathrm{I}} + \Gamma_{\mathrm{I}_2} = h(n_{\mathrm{I}} + n_{\mathrm{I}_2}) \left(\frac{k_B T_e}{m_{\mathrm{I}}} \right)^{1/2} . \tag{5.25}$$

The power balance equation for the electrons is given by Eqs. (1.99) and (1.100) with uniform densities and temperatures across the volume. The power density w_{abs} is an input parameter that controls the power source term $\mathcal{W}_{\mathrm{abs}} = w_{\mathrm{abs}} V$. The main difference with the article by Grondein *et al.* [71] is that no ion acceleration is considered through the grid. Moreover, gas heating is neglected here. We also include three new reactions that can play a significant role on the plasma properties balance in some discharge conditions: electron impact dissociation of I_2^+ (Section 5.2), electron impact electron detachment from I^- (Section 5.2), and non-resonant charge exchange between I_2 and I^+ (Section 5.2).

The influence of these reactions in the model was assessed over the power range $0.4 - 100\,\mathrm{kW/m^3}$ and the results are plotted in Fig. 5.6. The set of temporal differential equations for the variables n_{I}, n_{I_2}, n_{I^+}, $n_{\mathrm{I}_2^+}$, n_{I^-}, n_e and T_e is integrated explicitly using the same 4^{th} order Runge-Kutta solver `odeint` from `scipy` as for the 1D model of the magnetic filter presented in Chapter 4. When the electron impact detachment of I^- is not included, the density of I^- remains almost constant with power for injected power densities higher than approximately $30\,\mathrm{kW/m^3}$. Conversely, when this reaction is taken into account, the increase of electron density with power causes the density of I^- to decrease by a factor 2 between 30 and $100\,\mathrm{kW/m^3}$. The non-resonant charge exchange reaction Section 5.2 tends to slightly increase the I_2^+ density and slightly decrease the I^+ density but has a minor role on the other characteristics of the discharge. The role is expected to be larger when the ionization fraction becomes equal to 1 or greater than 1, as the $\mathrm{I}^+/\mathrm{I}_2^+$ balance may become strongly coupled to the I/I_2 gas balance. The resonant charge exchange reactions were not taken into account in the global model as they do not affect the particle balance, but they should be included in the gas balance equation in the future.

Given the high uncertainty on the sticking coefficient γ_s, we found it useful to perform a parametric study where it is varied from 0 to 1. In Fig. 5.7(a), the absorbed power density is set to $10\,\mathrm{kW/m^3}$. In this case the electron temperature increases from 2.5 eV when $\gamma_s = 0$ to 2.7 eV when $\gamma_s = 1$. The electron and negative ion densities, and hence the plasma electronegativity, are only weakly impacted by a variation of the sticking coefficient. At $10\,\mathrm{kW/m^3}$, the discharge electronegativity is enhanced by less than a factor 2 when γ_s varies from 0 to 1. The variation is more significant at $100\,\mathrm{kW/m^3}$ since the I_2 density, and thus the I^- density, drop to almost 0 when γ_s is very small. As expected, the density of I_2 increases with the sticking coefficient and the density of I decreases. At $10\,\mathrm{kW/m^3}$, the ratio between I and I_2 densities is inverted when γ_s equals approximately 0.1. The densities of I_2^+ and I^+ follow the trends observed for I and I_2 at about three orders of magnitude below. As illustrated in Fig. 5.7(b) where the absorbed power density is set to $100\,\mathrm{kW/m^3}$, the

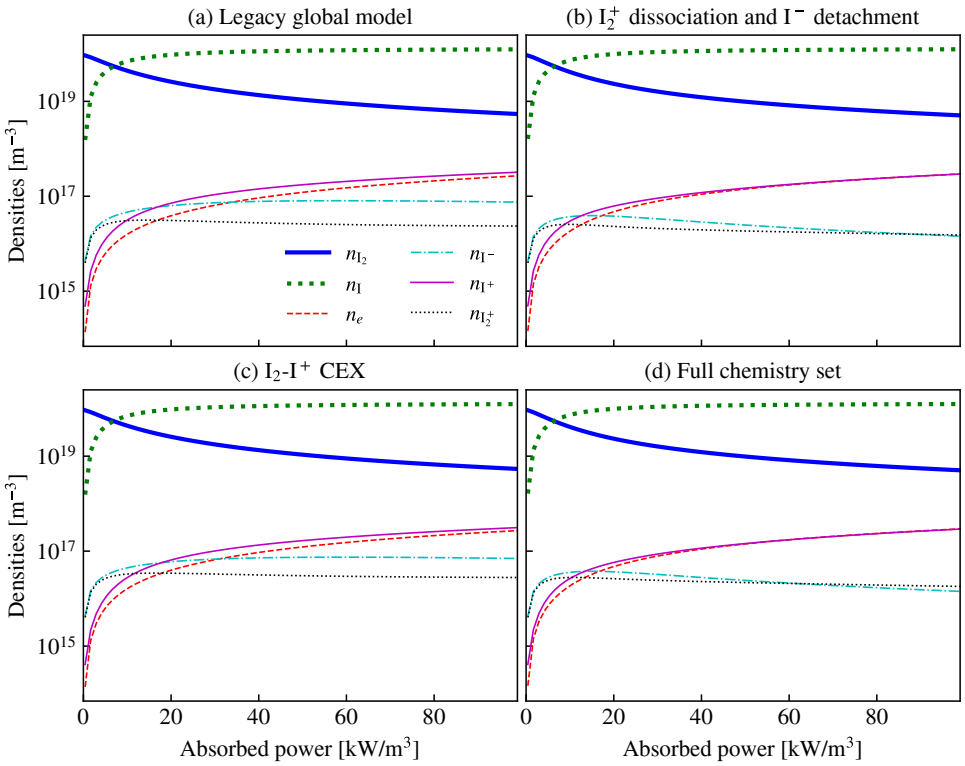

Figure 5.6: Equilibrium species densities predicted by the global model as a function of the power density absorbed for various chemical schemes. (a) legacy chemistry set (Grondein *et al.* [71]). The electron impact dissociation of I_2^+ and the detachment of I^- were added in (b), and the non-resonant charge exchange between I_2 and I^+ was added in (c). In (d), the full reaction set was used.

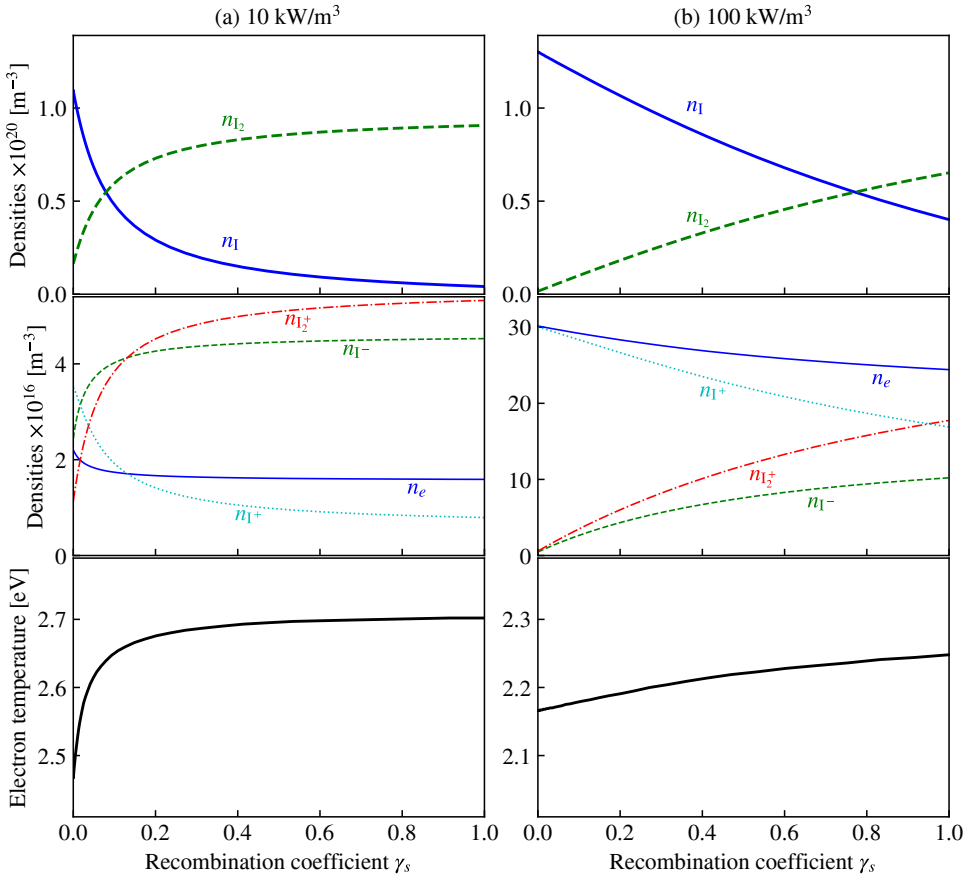

Figure 5.7: Equilibrium species densities and the electron temperature predicted by the global model as a function of the surface recombination coefficient between I and I_2 for (a) 10 kW/m^3 and (b) 100 kW/m^3 of power absorbed by the plasma. The full chemistry set is used here.

density of negative ions is much more sensitive to the value of the sticking coefficient at higher power. The electron temperature is slightly lower at higher power 100 kW/m^3 compared to the 10 kW/m^3 case, at about 2.2 eV.

(a)

Used for PIC simulation inputs		
p [mTorr]	n_{I_2} [m^{-3}]	n_I [m^{-3}]
3.609	4.128×10^{19}	7.397×10^{19}

(b)

To be compared with the PIC simulation outputs				
n_e [m^{-3}]	n_{I^-} [m^{-3}]	n_{I^+} [m^{-3}]	$n_{I_2^+}$ [m^{-3}]	T_e [eV]
1.864×10^{16}	3.583×10^{16}	2.656×10^{16}	2.792×10^{16}	2.603

Table 5.4: Outputs of the global models used to run the PIC simulation (top), and to be compared with the PIC simulation outputs (bottom). The absorbed power density is 10 kW/m^3. The discharge dimensions are 3×3 cm, and the third dimension is infinite.

5.4 Two-Dimensional PIC Simulation of an Iodine Discharge

5.4.1 Model Assumptions and Simulation Parameters

Since the gas balance is not so well determined because of the uncertainty on the sticking coefficient, we chose not to include it in the simulations presented in the following. The gas densities are computed from the global model with the same input parameters as in the PIC simulation and a sticking coefficient $\gamma_s = 0.04$ [47]. Again, the gas flow is 6.53 sccm, and the gas exhaust is 1.75 % of the discharge surface area.

The PIC model is valid for weakly ionized plasmas in the sense that the processes that involve charged species do not affect the densities of the neutral species that remain constant in time and space. The outputs of the global model are provided in Table 5.4. The densities found for I and I_2 are used as inputs and fixed throughout the PIC simulation.

The PIC simulation is started with a quite high density of 2.0×10^{16} m^{-3} for each charged species, such that the plasma is statistically quasineutral everywhere. This is of the same order of magnitude as the equilibrium values found by the global model. A large electron subcycling of 20 is used to reduce computational time. For comparison, a subcycling factor of 16 was used by Huang *et al.* [82] in the 1D PIC simulation of a chlorine CCP. Since the mass ratio between heavy species and electrons is larger for iodine, this should not cause a bigger error than in the former works on chlorine that were validated against experimental data [2]. All the grid data extracted from the PIC simulations are always averaged over 200 ns, which prevents to resolve fluctuations at frequencies higher than about 5 MHz. The numerical grid is the same as in the 2D simulations presented in Chapters 2 and 3. It is composed of a 400×400 uniform structured mesh, and each cell is 75 µm large. The time step is 25 ps and was chosen to resolve the electron plasma frequency safely, according

to Eq. (1.61). The heating electric field along the z direction has a frequency of 13.56 MHz, and its amplitude is uniform across the discharge. The absorbed power is 10 kW/m^3 which yields low ionization fraction and reasonable electronegativity. At initialization, the particles are loaded uniformly across the discharge. All the heavy species are loaded according to a 300 K Maxwellian distribution function, and the electrons are loaded with a Maxwellian distribution function at 4 eV.

The Poisson's equation is solved at each time step accounting for the updated distributions of electron super-particles (every time step) and ion super-particles (every 20 time steps) with Dirichlet boundary conditions ($\phi = 0$ at the boundaries). When an electron impact ionization occurs, the kinetic energy of each secondary electron is equal to half the kinetic energy of the primary electron minus the ionization energy. The procedure is the same for I and I_2 ionizations, and the dissociative ionization of I_2. The produced ions are released according to the assumed gas distribution function: a Maxwellian distribution function at 300 K. The same procedure is applied to negative ions produced by dissociative attachment. The energy transferred from the electron to the negative ion during the dissociative attachment process is hence neglected, which may be arguable.

As of July 2019, no algorithm has been implemented in the *LPPic* code to account rigorously for the reactions between super-particles. The only reactions involving multiple charged reactants are the ion recombination of I^- with I^+ and I_2^+. The reaction CSs are poorly known due to the lack of fundamental experimental data and calculations. A simplified algorithm was implemented to account globally for the ion losses through ion-ion-recombination: Every $N_{\text{average}} = 8\,000$ time steps, the number of positive and negative ions to be discarded is estimated through

$$\Delta_1 N_{I^+} = \Delta_1 N_{I^-} = K_{rec,I^+-I^-} q_f N_{\text{average}} \Delta t N_{I^+} N_{I^-} / (l_x l_y) \tag{5.26}$$

$$\Delta_2 N_{I_2^+} = \Delta_2 N_{I^-} = K_{rec,I_2^+-I^-} q_f N_{\text{average}} \Delta t N_{I_2^+} N_{I^-} / (l_x l_y) \tag{5.27}$$

$$\tag{5.28}$$

where N_X represents here the number of super-particles of species X and $\Delta_i N_X$ the number of super-particles of species X to be discarded due to the process indexed by i, and where

$$K_{rec,I^+-I^-} = 9.311 \times 10^{-15}\ \text{m}^3/\text{s} \tag{5.29}$$

$$K_{rec,I_2^+-I^-} = 1.22 \times 10^{-13}\ \text{m}^3/\text{s} \tag{5.30}$$

as said previously. The discarded super-particles are chosen randomly in the main table of the `population` data structure.

Kawamura *et al.* (2010) [84] have already performed 2D PIC simulations of an electronegative oxygen plasma with a transverse magnetic field. However, the chemistry set was simplified and rescaled to allow comparison with experimental plasmas with higher densities. In these simulations, the electronegativity α was of the order of 5 and the cross-field transport was found to be nearly classical. Nevertheless, the direction of a possible resistive drift wave instability was not simulated.

Physical parameters			
Gas type		I_2/ I	
Discharge size in x direction	l_x	30	mm
Discharge size in y direction	l_y	30	mm
Neutral total pressure	p	3.61	mTorr
Transverse magnetic field	$\boldsymbol{B}$	0	mT
Neutral density	n_{I}	7.397×10^{19}	m^{-3}
	n_{I_2}	4.128×10^{19}	m^{-3}
Neutral temperature	T_g	0.026	eV
Frequency	f_{RF}	13.56	MHz
Power density	w	10.0	kW/m^3
Physical time of the simulation	$t_{\mathrm{simulation}}$	> 100	µs
Averaging time	t_{average}	0.20	µs
Initial conditions			
Plasma density	$n_e = n_{\mathrm{I}^+} = n_{\mathrm{I}_2^+} = n_{\mathrm{I}^-}$	2×10^{16}	m^{-3}
Electron temperature	T_e [eV]	4.0	eV
Ion temperature	T_i [eV]	0.026	eV
Particles per cell (1 species)	$N_{part./cell}$	100	
Heating electric field amplitude	E_0	92.6	V/m
Numerical parameters			
Cell size	Δx	75	µm
Time step	Δt	2.5×10^{-11}	s
Steps to execute	$N_{simulation}$	$> 4 \times 10^6$	
Steps to average	N_{average}	8 000	
Weighting factor	q_f	1 125 000	m^{-1}
Number of CPU	N_{CPU}	240	
Initial number of super-particles	$N_{part,0}$	6.4×10^6	
Electron subcycling	$N_{subcycling}$	20	

Table 5.5: Main physical and numerical input parameters for iodine ICP 2D PIC simulation.

In this article, an iodine-like discharge was also simulated with CSs coming essentially from the data available for oxygen [84].

5.4.2 Relaxation Oscillations in an Iodine Plasma

Due to the quite high plasma density in the initial state, a density front develops and excites some modes of the discharge. In particular, we could observe mode propagation with quite clearly defined phase velocities propagating in both the x and y directions. Similar modes were observed experimentally in electronegative plasmas and are known as the fast modes and slow modes [158]. They were used to determine the electronegativity of plasma discharges experimentally [141, 138]. The method developed by Tuszevski and Gary [158] to predict the phase velocity of these waves was generalized to the case of plasmas with two positive ion species.

According to the analysis performed in Section 3.2, the susceptibility of each ion $i = \mathrm{I}^+, \mathrm{I}_2^+, \mathrm{I}^-$ is

$$\chi_i = \frac{\omega_{pi}^2}{k^2 {v_{Ti}}^2 - (\omega - k v_i)(\omega - k v_i + i\nu_i)} \tag{5.31}$$

where ion temperature $m_i {v_{Ti}}^2$ and ion drift v_i were taken into account, and where $\omega_{pi} = \left(\frac{n_i e^2}{m_i \epsilon_0}\right)^{1/2}$ is the ion plasma frequency of each species. Using a Boltzmann electron response to the electric field, the susceptibility of the electrons is

$$\chi_e = \frac{{\omega_{pe}}^2}{k^2 {v_{Te}}^2} \,. \tag{5.32}$$

The assumption of a Boltzmann electron response implies in particular that $\omega \ll k v_T$. Thanks to the parameters $\alpha = n_{\mathrm{I}^-}/n_e$ (electronegativity) and $\beta = n_{\mathrm{I}_2^+}/n_{\mathrm{I}^+}$, all the ion susceptibilities are expressed as functions of the electron density.

$$\begin{aligned}
\chi_{\mathrm{I}^+} &= {\omega_{pe}}^2 \frac{m_e}{m_{\mathrm{I}^+}} \frac{1+\alpha}{1+\beta} \left[k^2 v_{T\mathrm{I}^+}^2 - (\omega - k v_{\mathrm{I}^+})(\omega - k v_{\mathrm{I}^+} + i\nu_{\mathrm{I}^+})\right]^{-1} \\
\chi_{\mathrm{I}^+} &= {\omega_{pe}}^2 \frac{m_e}{m_{\mathrm{I}_2^+}} \frac{1+\alpha}{1+1/\beta} \left[k^2 v_{T\mathrm{I}_2^+}^2 - (\omega - k v_{\mathrm{I}_2^+})(\omega - k v_{\mathrm{I}_2^+} + i\nu_{\mathrm{I}_2^+})\right]^{-1} \\
\chi_{\mathrm{I}^-} &= {\omega_{pe}}^2 \frac{m_e}{m_{\mathrm{I}^-}} \alpha \left[k^2 v_{T\mathrm{I}^-}^2 - (\omega - k v_{\mathrm{I}^-})(\omega - k v_{\mathrm{I}^-} + i\nu_{\mathrm{I}^-})\right]^{-1}
\end{aligned} \tag{5.33}$$

The full dispersion relation is

$$1 + \chi_e + \chi_{\mathrm{I}^+} + \chi_{\mathrm{I}_2^+} + \chi_{\mathrm{I}^-} = 0 \tag{5.34}$$

but for electrostatic modes where $k\lambda_D \ll 1$, this becomes

$$\chi_e + \chi_{\mathrm{I}^+} + \chi_{\mathrm{I}_2^+} + \chi_{\mathrm{I}^-} = 0 \tag{5.35}$$

which is equivalent to

$$1 + V_{\mathrm{I}^+}^2 \left[k^2 v_{T\mathrm{I}^+}^2 - (\omega - k v_{\mathrm{I}^+})(\omega - k v_{\mathrm{I}^+} + i\nu_{\mathrm{I}^+})\right]^{-1} + V_{\mathrm{I}_2^+}^2 \left[k^2 v_{T\mathrm{I}_2^+}^2 - (\omega - k v_{\mathrm{I}_2^+})(\omega - k v_{\mathrm{I}_2^+} + i\nu_{\mathrm{I}_2^+})\right]^{-1} + V_{\mathrm{I}^-}^2 \left[k^2 v_{T\mathrm{I}^-}^2 - (\omega - k v_{\mathrm{I}^-})(\omega - k v_{\mathrm{I}^-} + i\nu_{\mathrm{I}^-})\right]^{-1} = 0 \tag{5.36}$$

where the ion acoustic velocities V_{I^+}, $V_{\mathrm{I}_2^+}$ and V_{I^-} are defined by

$$V_{\mathrm{I}^+}^2 = \frac{1+\alpha}{1+\beta} \cdot \frac{k_B T_e}{m_{\mathrm{I}^+}} \tag{5.37}$$

$$V_{\mathrm{I}_2^+}^2 = \frac{1+\alpha}{1+1/\beta} \cdot \frac{k_B T_e}{m_{\mathrm{I}_2^+}} \tag{5.38}$$

$$V_{\mathrm{I}^-}^2 = \alpha \cdot \frac{k_B T_e}{m_{\mathrm{I}^-}} \tag{5.39}$$

$$\tag{5.40}$$

In general, this gives a six order polynomial in ω whose roots can be found numerically. If the ion temperatures are neglected $v_{T\mathrm{I}^+} = v_{T\mathrm{I}_2^+} = v_{T\mathrm{I}^-} = 0$, if the drift velocities are assumed low, which is true near the discharge center, and collisions are neglected, then the dispersion relation yields a single phase velocity, in both directions

$$\boxed{v_\varphi = \omega/k = \pm\left(V_{\mathrm{I}^+}^2 + V_{\mathrm{I}_2^+}^2 + V_{\mathrm{I}^-}^2\right)^{1/2}} \tag{5.41}$$

Provided that $m_{\mathrm{I}^+} = m_{\mathrm{I}_2^+}/2 = m_{\mathrm{I}^-} = m_{\mathrm{I}}$, this is also

$$v_\varphi = \pm\frac{u_B}{\sqrt{1+\beta}}\left[1 + 2\alpha + (1+\alpha)\frac{\beta}{2}\right]^{1/2} \tag{5.42}$$

where the Bohm speed is here defined by $u_B = \left(k_B T_e/m_{\mathrm{I}}\right)^{1/2}$. This mode is called the *fast* mode [158] and was observed in the PIC simulation.

Simulating electronegative plasmas with a PIC method requires a very large number of integration time-steps. Huang and Gudmundsson [82] needed to simulate 1.1×10^7 time-steps or 405 µs of physical time in their 1D PIC simulation of a chlorine CCP. After 7.8×10^6 time-steps executed on 240 CPU over four weeks, and a physical time of about 200 µs, the simulation has not yet converged.

However, several oscillation patterns were observed in the transient state, which allows validating the model partially. The typical density profiles observed along x for $y = l_y/2$ are plotted in Fig. 5.8. At the beginning of the simulation, many different modes appear and high wavenumber structures are damped faster than lower wavenumbers. These oscillatory structures are present both in x and y directions and travel back and forth from the center of the discharge to the walls. In a few microseconds, we could retrieve the typical density profile of an electronegative plasma at moderate electronegativity [31]. From the center to the wall:

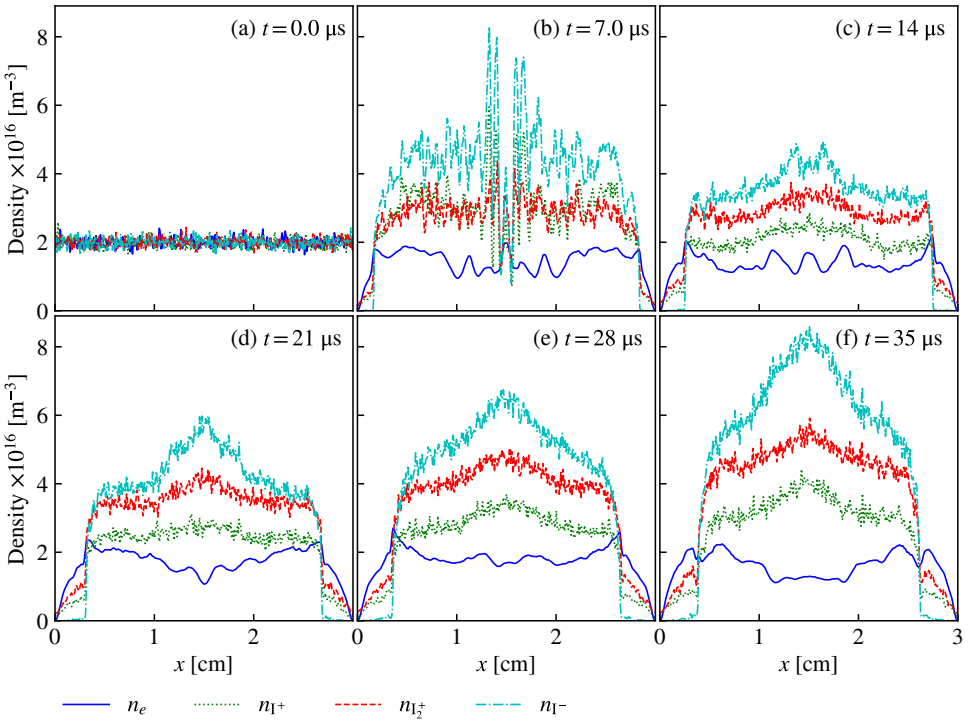

Figure 5.8: Density profiles at $y = l_y/2$ for the iodine ICP discharge in the transient regime.

1. A quasineutral core, with a relatively high electronegativity ($\alpha \approx 3$ here);
2. A quasineutral electropositive layer where the negative ion density drops to 0 very rapidly;
3. A positive space charge sheath where the electron density drops very fast.

The 2D structure of the discharge is illustrated in Fig. 5.9. The short wavelength structures are clearly visible in the map of electron density and I_2^+ density. The density maps of I_2^+, I^+ and I^- feature a cross shape suggesting that the 2D profile could be described by a convolution of 1D profiles. Due to this property, it seems relevant to investigate the oscillations along one of the symmetry axes of the discharge, for example, $y = l_y/2$.

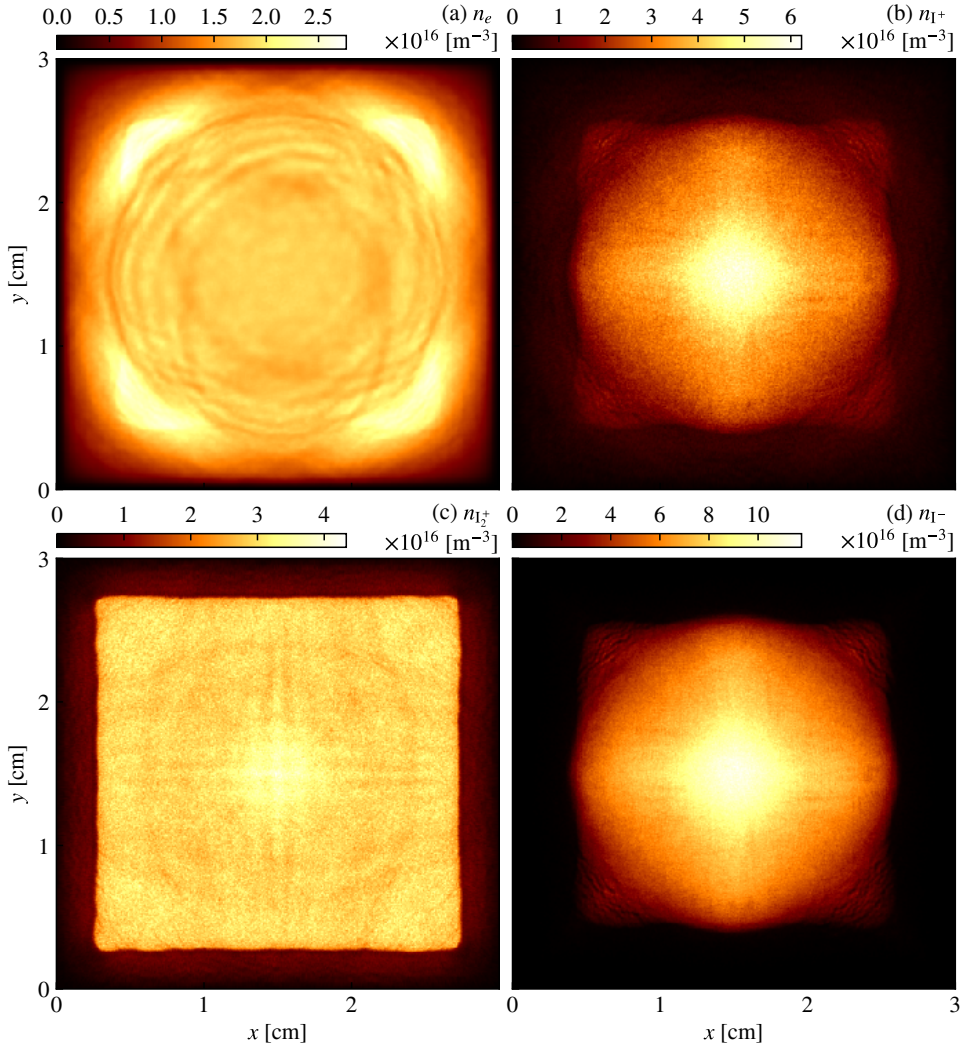

Figure 5.9: 2D maps of the densities of the various species present in the iodine plasma simulation. The snapshot performed at $t = 16.2\,\mu s$ corresponds to the transient and illustrates the wave perturbation.

The 2D FT of the electric field along x, E_x, is therefore performed in time and space, along the x direction, as shown in Fig. 5.10. The sheath effects were removed by taking into account only the region $x \in [2.5\,\text{mm}, 27.5\,\text{mm}]$. In order to obtain the temporal evolution of the spectrum, the signal was multiplied by Gaussian functions centered at different times, as in the wavelet transform algorithm. The standard deviation of the Gaussian is set to 3.53 µs. This standard deviation allows one to capture multiple oscillations, and to track the evolution of the phase velocity as the electronegativity evolves in time. The 2D FT reveals a quite clear phase velocity of the order of magnitude of the Bohm speed. This phase velocity tends to slightly increase in time, as the plasma electronegativity also increases. It is measured by estimating visually lower and upper bounds of the slope that relates ω with k. The estimated mean phase velocity is the average between the upper and lower bounds. The upper and lower values are used to generate the error bars plotted in Fig. 5.11. Between 13 and 25 µs, another mode is also visible with a phase velocity of the order of the ion thermal speed. This mode may be the slow mode formerly observed in experiments [158].

We could verify that the high phase velocity observed in Fig. 5.10 corresponds to the fast mode predicted by the theory. In Fig. 5.11, the phase velocity measured with the upper and lower bounds method is displayed with red triangles in Fig. 5.11 and compared with the predictions of the linear perturbation of fast waves. The blue circles correspond to the simplified model depicted by Eq. (5.42). It should match quite well the phase velocity of the wave at the discharge center where the ions do not drift. The electronegativity α and the $\beta = n_{\mathrm{I}_2^+}/n_{\mathrm{I}^+}$ are assessed by performing averages along the x axis, again for $x \in [2.5\,\text{mm}, 27.5\,\text{mm}]$. The measured phase velocity matches the simple fast wave theory with a 25 % error, and both curves show that the phase velocity should increase with electronegativity.

The first correction to the simple fast wave model consists in including finite drift velocity for both positive ion species. Indeed, the ion drift velocity of the positive ions may become quite large, especially near the sheath region where it should be approximately equal to the Bohm speed of each species. In red, the numerical solutions of the dispersion relation were computed for drift velocities equal to $\left(k_B T_e/m_{\mathrm{I}^+}\right)^{1/2}$, $\left(k_B T_e/m_{\mathrm{I}_2^+}\right)^{1/2}$ and 0 for I^+, I_2^+, and I^- respectively. The ion drift velocities are not uniform throughout the discharge, and the dispersion is applicable locally. However, the Fourier transform of the simulation data has to be performed over several spatial periods, over which the ion speeds vary. The velocties that were used in the dispersion relation should be seen as typical velocities. These values do not change the theoretical phase speed drastically, as illustrated by the blue and green curves in Fig. 5.11 The ion temperatures are also taken into account, again by performing a spatial average along x. This improved theoretical curve shows a quite good agreement with the phase velocity found in the PIC simulation. The high electronegativity measurements ($\alpha > 2.3$) where performed for $t > 20\,\mu\text{s}$ when the oscillations are already partially damped, so the estimate of the phase velocity is not so accurate anymore, as it is visible in Fig. 5.10(e) and (f). Moreover, the electroneg-

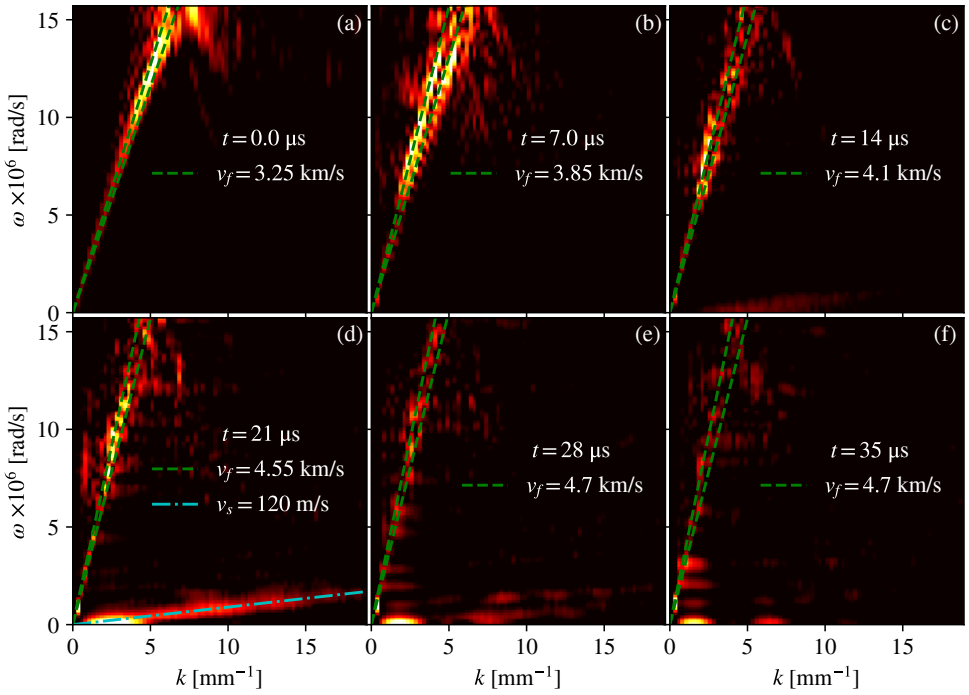

Figure 5.10: FT of the x component of the electric field in time and space, along x and for $y = l_y/2$, at several times. The fast mode (green dashed line) and the slow mode in (d) (cyan dashed-dotted line) are fitted manually to the 2D plot.

ative center tends to shrink when α increases so that the $x \in [2.5\,\text{mm}, 27.5\,\text{mm}]$ region might not be relevant to perform the analysis. Finally, spatial variations are neglected in the model, so a perfect agreement can not be reached with the PIC simulation anyway.

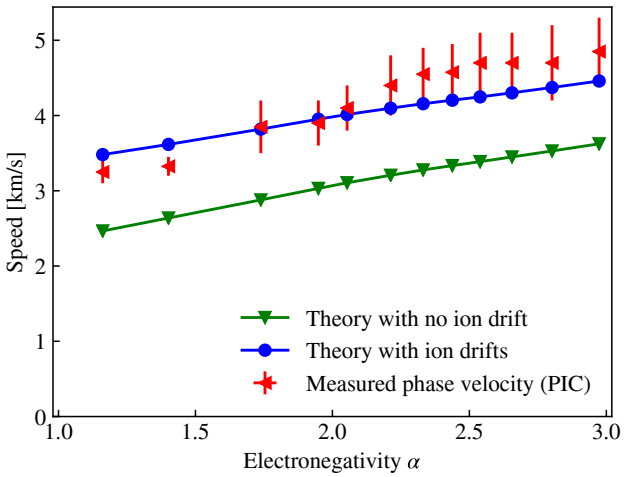

Figure 5.11: Comparison between the phase velocity measured in the PIC simulation (red triangles with error bars) with the fast modes predicted by the linear fluid theory, with no ion drift (green triangles), and with a Bohm speed for both positive ion species (blue circles).

5.5 Quasi-equilibrium

All the fast oscillations are eventually damped at $t = 65\,\mu s$. The plasma seems to converge towards some equilibrium, but the ion densities keep increasing slowly, while the number of electrons in the discharge seems stabilized. The density and temperature profiles at $t = 68.4\,\mu s$ are given in Fig. 5.12. The density profiles look similar to the typical solutions of 1D fluid simulations [29]. One of the advantages of the PIC method is that the kinetic temperatures of the charged species are computed at each grid point. We could observe that the temperature of the positive ions remains close to 300 K (0.026 eV) in the central region. Closer to the walls, the ion temperatures start increasing significantly from the region where the negative ion density is nearly 0. The ion temperature at the walls is about 690 K for I^+ and 830 K for I_2^+. On the contrary, the negative ions are significantly heated in the bulk plasma region and reach 460 K (0.04 eV) in the center. From the center to the walls, the negative ion temperature first decreases slightly and then increases violently in the pre-sheath region. This observation may come from the fact that the negative ions generated in the pre-sheath are strongly accelerated by the space charge electric field, and gain a large directional kinetic energy that is transferred to the thermal energy through collisions. However, the statistics are very poor in this region because almost no negative ions are present. The ion heating only comes from the electric field interaction and not from the chemistry, since the newly created ions are thermalized at 300 K, which may be a strong assumption for negative ions. Moreover, gas heating is neglected, which also causes the ion temperature to be underestimated with respect to experimental conditions. This discharge state looks quite realistic,

but the density of negative ions is higher than the global model predictions (see Table 5.4). However, equilibrium is not yet reached:

- As can be seen in Fig. 5.13(b), the negative ion density has not converged and keeps increasing slowly. This might be a clue that the recombination rate is too small. This needs to be checked.

- Soon after the high-frequency oscillations are damped, another oscillation develops at a lower frequency. This instability will be described in the following paragraph.

The first oscillation appears in the simulation at about 75 µs, when the electronegativity at the center is equal to 6 approximately. It seems to trigger from the center, and it affects the electron density the most. A soliton-like wave travels radially from the center to the walls. The wavelength is of the order of magnitude of the discharge size when it forms in the center, and the wavelength shrinks to about 2 mm at the sheath edge (see Fig. 5.13(a)). The electron density at the center varies from $6 \times 10^{15}\,\mathrm{m}^{-3}$ to $2.4 \times 10^{16}\,\mathrm{m}^{-3}$ within the instability cycle. The densities of the other charged species are also affected but the shapes of the profiles of n_{I^+}, $n_{I_2^+}$, and n_{I^-} do not vary significantly from what is shown in Fig. 5.12(a). The amplitude of the temporal fluctuations of n_{I^+}, $n_{I_2^+}$, and n_{I^-} at the center represents about 10 % of the time-averaged value. The measured frequency is 244 kHz. As shown in Fig. 5.13(c), the instability also affects to electron temperature by about 17 % in the center. The plasma potential is significantly affected as well, as illustrated in Fig. 5.13(e) and (f). The instability saturates in just a few cycles, and its amplitude and frequency do not seem to vary in time.

The observed instability looks similar to experimental measurements performed by Chabert *et al.* (2001) [32] in Ar/SF_6 mixtures. Experimentally, strong relaxation oscillations were observed in electronegative plasmas with frequencies ranging from 1 Hz to 900 kHz [101]. Similarly to the experiments performed in Ar/SF_6 mixtures, the discharge spends most of its time in the high electron density region. However, the instability amplitude is lower in the simulation than in the experiments, and the frequency is higher, for equivalent pressures.

In previous publications [101, 32, 33], it is shown that this type of oscillations can come from a hysteresis effect between the curve that relates the electron density with the power absorbed by the electrons. In these journal articles, the instability was related to a mode transition between inductive (H) and capacitive (E) modes in the experimental ICP reactor. However, Tuszewski and White (2003) [159] have shown that macroscopic instabilities in electronegative gases can as well come from the downstream instabilities, i.e., the slow modes that can be captured by the dispersion relation (5.36). These instabilities may form when the relative velocity between positive and negative ions becomes large. In our simulation, the instability triggers from an electrostatic potential drop in the central region of the discharge. It then travels towards the sheath and affects all the plasma properties locally. Smaller

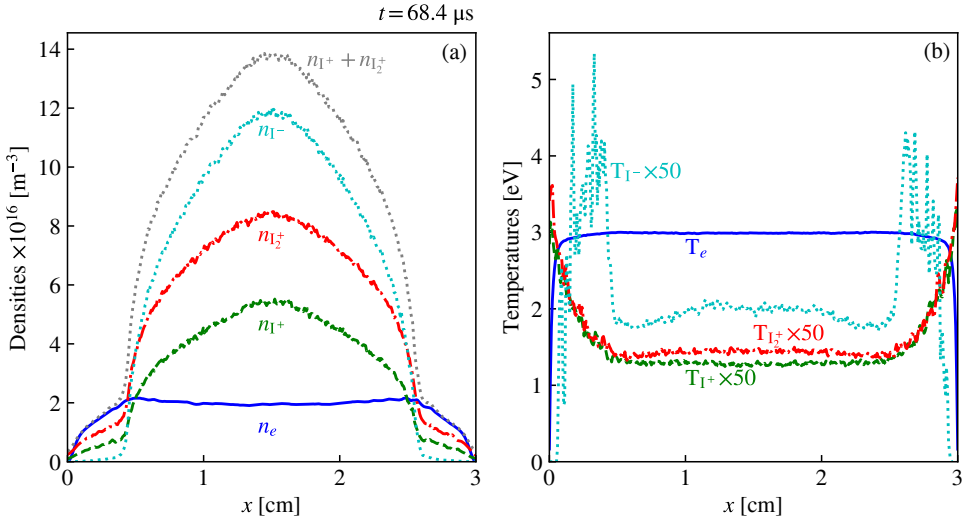

Figure 5.12: (a) Densities and (b) temperatures of charged species in the PIC simulation. The quantities are averaged over 18 cells at the vicinity of $y = l_y/2 = 1.5$ cm. On the LHS, the sum of the positive ion densities is plotted in gray dotted line. On the RHS, the ion temperatures are multiplied by a factor 50 to scale with the electron temperature.

wavelength structures appear closer to the sheath. The instability is not triggered downstream from the perspective of the ions.

Discussion on double layer formation and propagation

Several previous publications [117, 115, 116, 118] investigated similar oscillations in electronegative plasma discharges through the prism of double layer. A double layer is a region of the plasma where the sign of the charge density changes. Due to Maxwell-Gauss equation in 1D, at a double layer location, the electric field reaches an extremum. The oscillations that were observed in the PIC simulation described above affect all the plasma quantities, including the electric field, such that they can be interpreted as double layers. Interestingly, the criterion found for double layer formation in Meige *et al.* [111] is comparable to the slow mode instability criterion in Tuszewski and Gary [158], namely, the drift difference between positive and negative ions has to be of the order of the ion acoustic speed. Stationary double layers were even found by Sheridan *et al.* [137] with a fluid model where ion temperature is neglected. These are different specific interpretations of a family of plasma solutions that all emphasize the fact that low pressure electronegative discharges are usually unstable at moderate electronegativity.

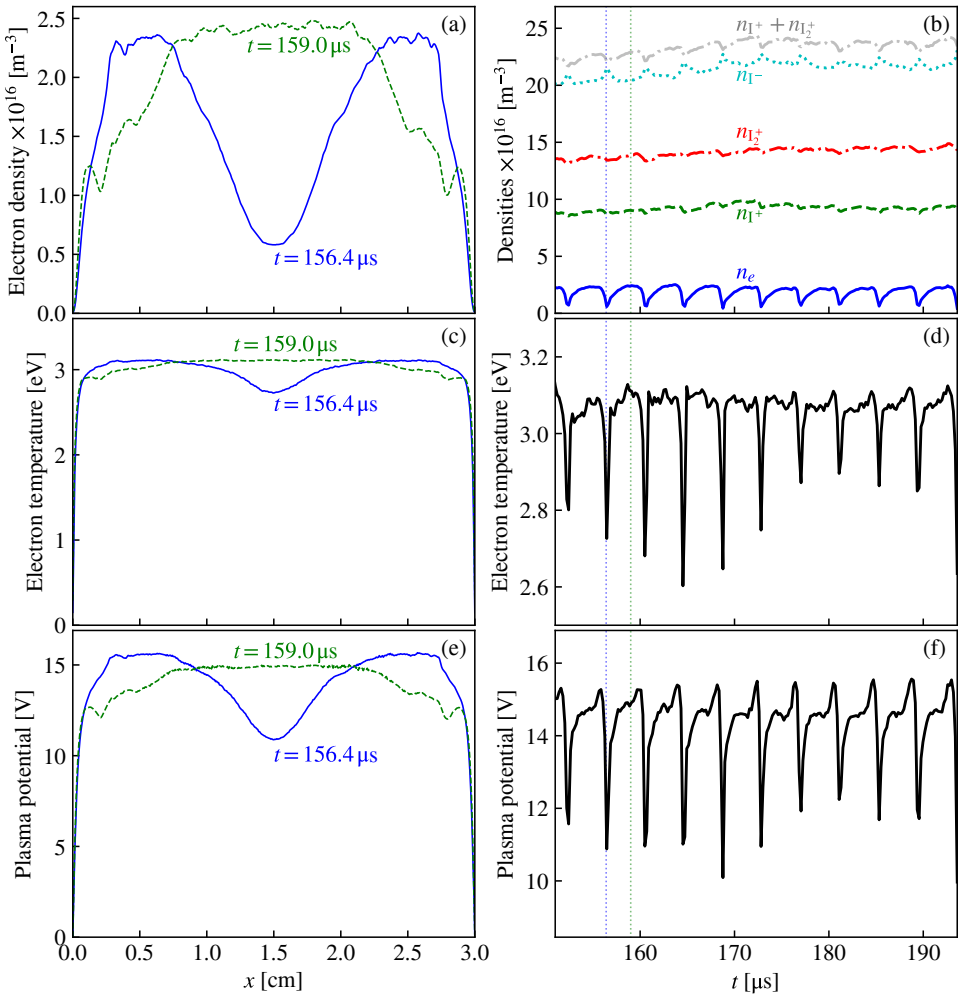

Figure 5.13: Low-frequency oscillations observed in the PIC simulations. (a) Electron density profiles along x at $y = l_y/2 = 1.5\,\mathrm{cm}$, at two times $t_1 = 156.4\,\mu\mathrm{s}$ and $t_2 = 159.0\,\mu\mathrm{s}$ (indicated in dotted lines in (b)) corresponding to a minimum (solid blue line) and a maximum (green dashed line) of the value at the center, respectively. (b) Temporal profiles of the densities of charged particles at the center between $t = 150\,\mu\mathrm{s}$ and $t = 194\,\mu\mathrm{s}$. The electron temperature and plasma potential profiles at t_1 and t_2 (for $y = l_y/2$) are shown in (c) and (e), and the corresponding temporal fluctuations in (d) and (e).

Summary

The physical properties of iodine make it a good candidate for future electric propulsion systems. Here, we have proposed a comprehensive CS set for iodine simulation, and we have performed the first 2D PIC simulations of an iodine discharge that include electron dynamics and that match experimental plasma densities. The model is limited to weakly ionized plasmas, and the gas balance is computed separately by an updated global model.

Using the global model, the influence of three reactions that were not considered previously was assessed: electron impact I_2^+ dissociation and I^- detachment, as well as non-resonant charge exchange between I and I_2^+. In the low power regime investigated with the PIC simulation (10 kW/m^3), these reactions play a minor role. However, they may be important at higher power densities, as electron detachment causes negative ion density to decrease with power. The balance between I and I_2 is greatly influenced by the wall recombination coefficient γ_s, which has not been measured experimentally, and which is expected to depend on the wall surface properties. The global model was run for the entire range of γ_s, between 0 and 1. At 10 kW/m^3, the I_2 density is of the same order of magnitude as the I density, even when there is no wall recombination because molecule dissociation is moderate. Therefore, although the value of γ_s has a significant influence on the predicted electron temperature and densities of charged particles, it is not as critical as it is at 100 kW/m^3.

The development of a PIC model for the simulation of a realistic iodine discharge in 2D is a challenge both from a scientific and a computer engineering point of view. The model that we developed paves the way to more specific simulations of the PEGASES thruster. Several well-known features of electronegative discharges, such as fast and slow waves, and relaxation instabilities, were already observed in the 2D PIC simulation. These first observations match previous experimental results qualitatively. The PIC simulation of an iodine discharge has provided valuable insights into these phenomena, and it could lead to a deeper understanding in the future. The oscillations that were observed with no magnetic field may also be present in the PEGASES thruster, and may affect particle transport and electron cooling. The full 2D kinetic simulation of the PEGASES thruster operated with iodine requires to combine the simulation cases of Chapter 4 with the chemistry set presented in this chapter, and has now been made possible.

CONCLUSION

Summary of the Thesis

The original name of the PhD project was *Simulation and Modeling of the PEGASES thruster operated with Iodine*. On our way to pursuing this goal, we found that a number of fundamental questions that needed to be addressed before producing any valuable model, even in the case of an apparently simple argon ICP discharge. The fundamentally 2D (if not 3D) geometry of the PEGASES experiment made us eager to understand the transport phenomena in multi-dimensional systems, starting with the non-magnetized configuration. The role of instabilities in the cross-field transport in magnetized plasmas was investigated with particular care. We have observed in 2D PIC simulations a variety of instabilities that can develop in a magnetic filter. One of them, the resistive instability related to the diamagnetic drift, is also the main driver of electron de-confinement in magnetized columns of weakly ionized plasma. A relevant dispersion relation is given and the solutions are successfully compared with the PIC simulations at saturated state. A formula was provided for the instability-enhanced collision frequency that can be used in simple fluid models.

Unlike non-magnetized plasmas, the localization of the power deposition plays an important role in the magnetized plasma properties. Therefore, self-consistent heating power source modeling or experimental data for the deposited power are vital to reach good quantitative agreement between simulations and experiments. Classical fluid models are unable to reproduce the PIC simulation data but the agreement becomes quite good when the instability-enhanced collision frequency is used.

The models that were developed and used within the project are summarized in Table 6. In this table, the models that were successfully investigated but for which no results were shown in the thesis are indicated in parenthesis. Modeling goes in pair with theory and physical understanding. The diagonal that goes from the top left corner to the bottom right corner in Table 6 is the natural path to gain a true physical understanding of the low-pressure plasma transport phenomena. In the table, the analytical models refer to Chapter 2, where the heating source term is uniform. In this case, and when the gas pressure is below typically 50 mTorr, even with a magnetic field, the electron temperature is uniform, and the problem of

		Fluid quasineutral		**Kinetic**
		Analytical (uniform power source)	Numerical	PIC
Ar	No B	0D, 1D, 2D, (3D)	(0D), (1D)	(1D), 2D
	Uniform B	0D, 1D, 2D-no E	(0D), (1D)	2D
	B gradients		1D	2D
I_2/I	No B		0D	2D

Physical understanding (↓)

Physical understanding (→)

Table 6: Summary of the ICP models developed and used within the frame of the project. The models that were investigated but not fully explained in this thesis are indicated in parenthesis.

plasma transport is reduced to only one equation for the electron temperature. This single variable scalar equation can easily be solved numerically, provided that the ionization rate is a known function of the electron temperature. In 2D, the resolution requires the assumption that the x and y variables can be separated. This assumption was verified with the PIC simulation. In 1D, analytical solutions exist for arbitrary values of the magnetic field, but in 2D, the assumption of a weak electric field, which is verified at high magnetic fields, is needed.

When the heating source term is not uniform, the electron heat equation has to be taken into account. In low-pressure non-magnetized plasmas, this is not a major problem as the plasma is still isothermal, and the analytical solutions are in good agreement with the PIC data. However, when a magnetic field is applied, the full set of Euler equations (continuity equation, momentum balance equation, and electron energy equation) has to be solved numerically. This was successfully implemented in a 1D model where the radial particle losses are accounted for using the h factor, and where the heat flux is neglected.

The PIC simulation tool *LPPic* is very powerful but is computationally expensive. All the simpler models mentioned above were always driven by and validated against the PIC simulations. Besides the simplified geometry, the current version of the code is electrostatic and cannot account for the inductive heating in a completely self-consistent and straight-forward fashion. Moreover, the PIC simulation is subject to numerical noise and numerical heating that can induce significant errors, especially when the plasma is unstable. Simulations of ICP with helium (see Section 1.4), xenon, and krypton gases were also performed, but most of them were not shown in the manuscript.

Preliminary results have shown that a better modeling of the heat flux was critical for a correct fluid simulation of the magnetic filter. In particular, the heat diffusion coefficient needs to be estimated with much care. Realistic PIC simulation of iodine discharges remains a challenge as consistent ion-ion recombination modeling has not been achieved, and discharge steady-state was not reached. Moreover, as gas depletion was not taken into account, the model is limited to weakly-ionized

plasmas. The balance between I and I_2 species depends on the wall recombination coefficient, which is provided as an input of the current models. Although wall recombination was identified among the key processes in more detailed studies on chlorine plasmas, its value remains essentially unknown for iodine.

Prospects

The chapters of the thesis are connected to one another, but each also contains results that could lead to further validations and improvements. In Chapter 2, the formula of the *collisionless ambipolar diffusion coefficient*, and its dependence on system geometry, could be verified experimentally. In Chapter 3, systematic numerical convergence with respect to the grid size should be done to improve the estimate of the ratio between the h factor at high magnetic fields and the non-magnetized h factor. Comparison between experimental data of a magnetized plasma column and predictions from a 0D or 1D model is on-going. The model would incorporate the instability-enhanced transport coefficients proposed in Chapter 3. The main difficulty lies in the correct modeling of local power deposition in magnetized plasmas, as was suggested in Chapter 4. We have seen that several types of instabilities form in the high magnetic field region of PEGASES. The influence of the spatial variations of the magnetic field on the dispersion relation could be investigated from a theoretical point of view, as it has been done in recent studies on HT. The EEDF found in the experiments and in our PIC simulations of the PEGASES thruster are Maxwellian with a very good approximation. This observation is only partially explained and could benefit from more theoretical investigations using kinetic or gyrokinetic theory.

The model of the PEGASES thruster operated with iodine contains a large number of parameters and assumptions. The chemistry set is not exhaustive and the accuracy of the reaction cross sections data used in this work was sometimes limited. Reactions between heavy species would require further investigations. In particular, isotropic scattering rely on Langevin capture cross sections while the backscattering cross sections are based on estimates made for resonant charge-exchange reactions at relatively high ion energies. These estimates could be challenged with more fundamental experiments and computations. Finally, ion-ion recombination cross sections are still poorly known and the implementation of such reactions should be improved in the PIC model.

Gas heating and neutral depletion are two important phenomena for experimental plasmas that were ignored here. Fluid models exist, but the dynamics of reactive gases may be challenging to couple to plasma chemistry. From a more general perspective, uncertainty quantification could help to identify the main variables of interest to focus on in order to improve the model. As the wall recombination coefficient depends on the wall surface properties and seems difficult to measure, a good approach is to measure directly the gas density, as it is currently being done

by F. Marmuse at LPP. In weakly ionized plasma conditions (at low power), the gas background can be frozen in the simulation, either PIC or multi-fluid, while the other parameters are varied. This type of techniques could be of great help for design optimization of NBI for fusion reactors (with hydrogen-deuterium mixtures), or future electric propulsion systems. Industrial systems of GIT or NBI are larger than what current PIC codes allow to simulate in 3D. However, the full simulation of the PEGASES thruster in 2D operated with iodine would allow validating simpler fluid models that could be of great assistance for industrial design and system optimization.

Appendix A

REFINED CROSS SECTION SETS FOR NOBLE GASES

The cross section set for electron-He reactions used for the run illustrated by the refined gas model in Fig. 1.8 is presented below. It comes from the Biagi Magboltz database on LXCat [11]. In Fig. A.1, analogous cross section sets also coming from the LXCat database for argon, krypton and xenon that can run in *LPPic* or in the global model are presented.

He

(1) $He + e^- \rightarrow He + e^-$ elastic, From Biagi's elastic momentum transfer.
(2) $He + e^- \rightarrow He^+ + e^- + e^-$ ionization,
(3) $He + e^- \rightarrow He^* + e^-$ excitation 1, EX 23S J=1 M ELVL=19.81961 eV.
(4) $He + e^- \rightarrow He^* + e^-$ excitation 2, EX 21S J=0 M ELVL=20.61577 eV.
(5) $He + e^- \rightarrow He^* + e^-$ excitation 3, EX 23P J= 1,0 ELVL=20.96409 eV.
(6) $He + e^- \rightarrow He^* + e^-$ excitation 4, EX 21P J=1 R ELVL=21.21802 eV.
(7) $He + e^- \rightarrow He^* + e^-$ excitation 5, EX 33S J=1 ELVL=22.71847 eV.
(8) $He + e^- \rightarrow He^* + e^-$ excitation 6, EX 31S J=0 ELVL=22.92032 eV.
(9) $He + e^- \rightarrow He^* + e^-$ excitation 7, EX 33P J= 1,0 ELVL=23.00707 eV.
(10) $He + e^- \rightarrow He^* + e^-$ excitation 8, EX 33D J=3, 1 ELVL=23.07365 eV.
(11) $He + e^- \rightarrow He^* + e^-$ excitation 9, EX 31D J=2 ELVL=23.07407 eV.
(12) $He + e^- \rightarrow He^* + e^-$ excitation 10, EX 31P J=1 R ELVL=23.08702 eV.
(13) $He + e^- \rightarrow He^* + e^-$ excitation 11, EX 43S J=1 ELVL=23.59396 eV.
(14) $He + e^- \rightarrow He^* + e^-$ excitation 12, EX 41S J=0 ELVL=23.67357 eV.
(15) $He + e^- \rightarrow He^* + e^-$ excitation 13, EX 43P J= 1,0 ELVL=23.70789 eV.
(16) $He + e^- \rightarrow He^* + e^-$ excitation 14, EX 41D J=2 ELVL=23.73633 eV.
(17) $He + e^- \rightarrow He^* + e^-$ excitation 15, EX 43D J=3, 1 ELVL=23.73609 eV.
(18) $He + e^- \rightarrow He^* + e^-$ excitation 16, EX 41F J=3 ELVL=23.73701 eV.
(19) $He + e^- \rightarrow He^* + e^-$ excitation 17, EX 43F J=3,4,2 ELVL=23.73701 eV.
(20) $He + e^- \rightarrow He^* + e^-$ excitation 18, EX 41P J=1 R ELVL=23.74207 eV.
(21) $He + e^- \rightarrow He^* + e^-$ excitation 19, EX 53S J=1 ELVL=23.97197 eV.
(22) $He + e^- \rightarrow He^* + e^-$ excitation 20, EX 51S J=0 ELVL=24.01121 eV.
(23) $He + e^- \rightarrow He^* + e^-$ excitation 21, EX 53P J= 1,0 ELVL=24.02822 eV.
(24) $He + e^- \rightarrow He^* + e^-$ excitation 22, EX 51D J=2 ELVL=24.04280 eV.
(25) $He + e^- \rightarrow He^* + e^-$ excitation 23, EX 53D J=3, 1 ELVL=24.04266 eV.

(26) $He + e^- \rightarrow He^* + e^-$ excitation 24, EX 513 J=3 ELVL=24.04315 eV.
(27) $He + e^- \rightarrow He^* + e^-$ excitation 25, EX 53F J=3,4,2 ELVL=24.04315 eV.
(28) $He + e^- \rightarrow He^* + e^-$ excitation 26, EX 51P J=1 R ELVL=24.04580 eV.
(29) $He + e^- \rightarrow He^* + e^-$ excitation 27, EX 63S J=1 ELVL=24.16900 eV.
(30) $He + e^- \rightarrow He^* + e^-$ excitation 28, EX 61S J=0 ELVL=24.19116 eV.
(31) $He + e^- \rightarrow He^* + e^-$ excitation 29, EX 63P J= 1,0 ELVL=24.20081 eV.
(32) $He + e^- \rightarrow He^* + e^-$ excitation 30, EX 63D J=3, 1 ELVL=24.20916 eV.
(33) $He + e^- \rightarrow He^* + e^-$ excitation 31, EX 61D J=2 ELVL=24.20925 eV.
(34) $He + e^- \rightarrow He^* + e^-$ excitation 32, EX 61P J=1 R ELVL=24.21100 eV.
(35) $He + e^- \rightarrow He^* + e^-$ excitation 33, EX 73S J=1 ELVL=24.28456 eV.
(36) $He + e^- \rightarrow He^* + e^-$ excitation 34, EX 71S J=0 ELVL=24.29828 eV.
(37) $He + e^- \rightarrow He^* + e^-$ excitation 35, EX 73P J= 1,0 ELVL=24.30429 eV.
(38) $He + e^- \rightarrow He^* + e^-$ excitation 36, EX 73D J=3, 1 ELVL=24.30954 eV.
(39) $He + e^- \rightarrow He^* + e^-$ excitation 37, EX 71D J=2 ELVL=24.30960 eV.
(40) $He + e^- \rightarrow He^* + e^-$ excitation 38, EX 71P J=1 R ELVL=24.31071 eV.
(41) $He + e^- \rightarrow He^* + e^-$ excitation 39, EX N3S SUM HIGH ELVL=24.35810 eV.
(42) $He + e^- \rightarrow He^* + e^-$ excitation 40, EX N1S SUM HIGH ELVL=24.36718 eV.
(43) $He + e^- \rightarrow He^* + e^-$ excitation 41, EX N3P SUM HIGH ELVL=24.37116 eV.
(44) $He + e^- \rightarrow He^* + e^-$ excitation 42, EX N1D SUM HIGH ELVL=24.37472 eV.
(45) $He + e^- \rightarrow He^* + e^-$ excitation 43, EX N3D SUM HIGH ELVL=24.37468 eV.
(46) $He + e^- \rightarrow He^* + e^-$ excitation 44, EX 81P J=1 R ELVL=24.37547 eV.
(47) $He + e^- \rightarrow He^* + e^-$ excitation 45, EX 91P J=1 R ELVL=24.41989 eV.
(48) $He + e^- \rightarrow He^* + e^-$ excitation 46, EX 101P J=1 R ELVL=24.45168 eV.
(49) $He + e^- \rightarrow He^* + e^-$ excitation 47, EX 111P J=1 R ELVL=24.47518 eV.
(50) $He + e^- \rightarrow He^* + e^-$ excitation 48, EX 121P J=1 R ELVL=24.49308 eV.
(51) $He + e^- \rightarrow He^* + e^-$ excitation 49, EX N1P SUM HI R ELVL=24.50708 eV.

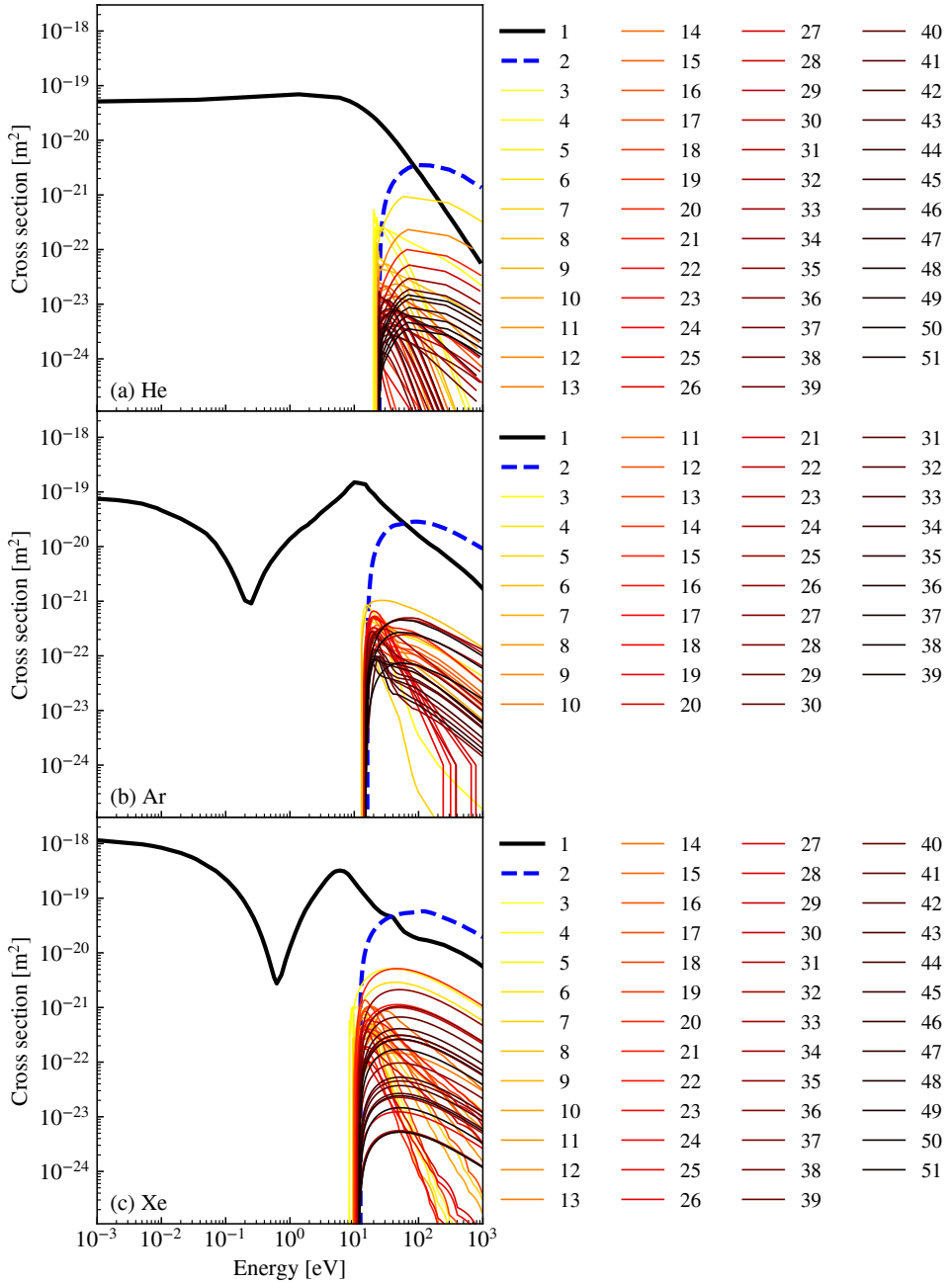

Figure A.1: Electron-neutral collision cross sections for helium, argon and xenon. [12, 6].

Appendix B

CONVERGENCE STUDY FOR THE MAGNETIZED COLUMN SIMULATION CASE

The PIC simulation relies on a number of numerical parameters that may affect the physical result. Here, we investigate the magnetized column simulation case at 3 mTorr for a domain of 3 $\times$ 3 cm. The magnetic field is uniformly equal to 20 mT and the mean absorbed power density is 9.6 kW/m^3. The influence of the number of particles, the ion subcycling and ion magnetization is investigated. The various simulation cases are summarized in Table B.1 and the electron density and electron temperature profiles are shown in Fig. B.1. We can see that the ion magnetization has only a minor influence on the discharge properties. The ion subcycling however seems to have a significant influence on the plasma density profile. The power losses seem lower when no ion subcycling is used which is quite unexpected. According to Fig. 3.23, this is always the case but the effect is more visible at higher magnetic field. The number of particles does not seem to play a critical role as the density profiles are statistically the same in cases 3, 4 and 5. However, the electron temperature seems to decrease slightly, and does not seem to be converged when the number of particles per cell at initialization is equal to 400.

The most critical effect that was observed is the influence of the discretization mesh. In case 6, the number of grid points in each direction is doubled (the number of cells is multiplied by four) and the time-step is multiplied by 2 as well to match the CFL criterion. The initial number of particles per cell is kept equal to 25. The electron temperature is found to be significantly lower than in the other cases and the plasma density is about 50 % higher in the center with a more peaked profile. This shows that the mesh discretization has a significant influence on the saturation mechanism and instability-enhanced transport. So most of the simulation results presented throughout where instabilities are present probably tend to underestimate the magnetic confinement.

	Initial # of part. per cell (1 species)	Ion magnetization	Electron subcycling	Cell size [μm]	Time step [ps]
Case 1	24	No	1	75	33
Case 1 bis	24	No	1	75	33
Case 2	24	Yes	10	75	33
Case 2 bis	24	Yes	10	75	33
Case 3	25	No	10	75	33
Case 4	100	No	10	75	33
Case 5	400	No	10	75	33
Case 6	25	No	10	37.5	16.5

Table B.1: Investigated numerical parameters for the study of the magnetized column at 3 mTorr and 20 mT.

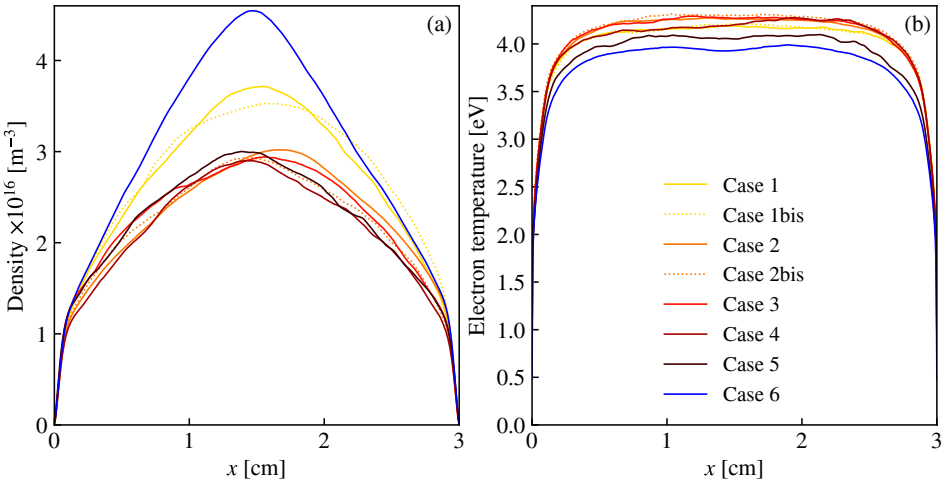

Figure B.1: Profiles of electron density (a) and temperature (b) found in the simulations of the magnetized plasma column at 3 mTorr and 20 mT with the numerical parameters described in Table B.1 .

Appendix C

SIMULATIONS AT HIGHER MAGNETIC FIELDS

Nothing should stop us from simulating argon plasmas at higher magnetic fields. The cell size is constrained by the Larmor radius, so the computation time is larger. As shown in Fig. C.1 (also used as a front picture), the structure of the plasma instability becomes different. The instability does not look like a wave that propagates but features smaller structures that spin and rotate with the diamagnetic drift. Fig. C.1 corresponds to a run at 3 mTorr with a uniform magnetic field of 100 mT. The simulation is not converged here, and the Larmor radius is poorly resolved ($\rho_{Le} \approx dX$). The spin motion of the small scale structure is very fast and would require finer time sampling, which would also require more particles to reduce the statistical noise. Overall, providing consistent and converged simulations in this range of magnetic fields would require special care for convergence studies and timely runs.

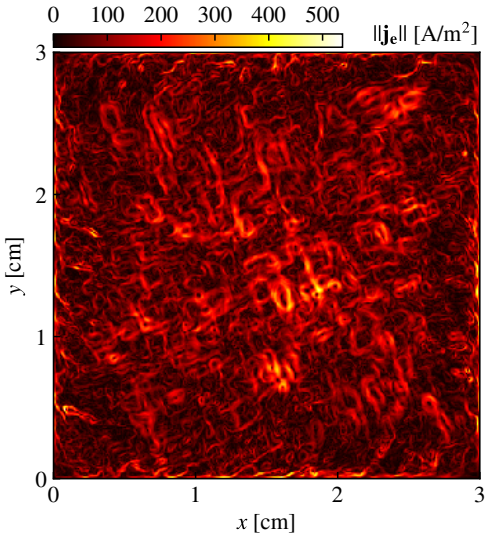

Figure C.1: Example of 2D PIC simulation at higher magnetic fields: B_z is here uniform and equal to 100 mT. The pressure is 3 mT. The electron current is extracted at $t = 5.7\,\mu s$ when the simulation is not converged.

Appendix D

MATHEMATICAL FUNCTIONS

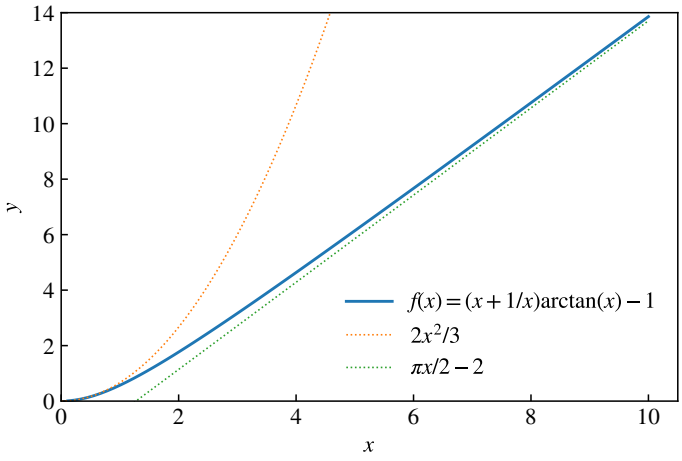

Figure D.1: Graph of the function $f : x \to \left(x + \frac{1}{x}\right)\arctan(x) - 1$ essential to solve the electron temperature equation for isothermal quasineutral plasma transport in Cartesian coordinates. See Chapter 2.

Appendix E

FORTRAN GAS TYPE DEFINTION

```
type gas
    character (LEN=9)                              :: formula     ! gas
        formula
    real(dbleprc)                                  :: mass
    character (LEN=256)                             :: lxcat_input_e !
        cross section file for elec
    character (LEN=256)                             :: lxcat_input_i !
        cross section file for ions
    real(dbleprc)                                  :: density=0.0d0
                ! density

    ! Number of reactions for each type of process
    !-------------------------------------------------------------------
    ! Electrons
    integer                                  :: ela_elec_nb=0 ! Elastic
    integer                                  :: exc_elec_nb=0 !
        Excitation
    integer                                  :: iz_elec_nb=0    !
        ionization
    ! Ions
    integer                                  :: i_n_nb=0 ! Elastic

    integer                                  :: e_react_nb=0 ! number
        of electron processes
    integer                                  :: i_react_nb=0 ! number
        of ion processes

    ! Data size for each process
    integer, allocatable, dimension(:)    :: len_ela_elec
    integer, allocatable, dimension(:)    :: len_exc_elec
    integer, allocatable, dimension(:)    :: len_iz_elec
    integer, allocatable, dimension(:)    :: len_i_n

    ! Cross section (cs) tables
    ! dim 1: number of reactions of the given type
```

```
    ! dim 2: size of the energy table
    ! dim 3: (1) energy [eV] / (2) cs [m^2]
    real(dbleprc), ALLOCATABLE, dimension(:,:,:) :: ela_elec  !
        electron elastic
    real(dbleprc), ALLOCATABLE, dimension(:,:,:) :: exc_elec  !
        electron excitation
    real(dbleprc), ALLOCATABLE, dimension(:,:,:) :: iz_elec   !
        electron impact ionization
    real(dbleprc), ALLOCATABLE, dimension(:,:,:) :: i_n       !
        ion-neutral

    ! grid values
    !
        ------------------------------------------------------------------
    ! Electron-gas reactions
    real(dbleprc), dimension(:,:), allocatable :: nu_ela_elec_temp !
        Elastic scattering
    real(dbleprc), dimension(:,:), allocatable :: nu_ela_elec
    real(dbleprc), dimension(:,:), allocatable :: nu_exc_elec_temp !
        Excitation
    real(dbleprc), dimension(:,:), allocatable :: nu_exc_elec
    real(dbleprc), dimension(:,:), allocatable :: nu_iz_elec_temp !
        Ionization
    real(dbleprc), dimension(:,:), allocatable :: nu_iz_elec
    real(dbleprc), dimension(:,:), allocatable :: nu_dat_elec_temp !
        Dissociative attachment
    real(dbleprc), dimension(:,:), allocatable :: nu_dat_elec
    real(dbleprc), dimension(:,:), allocatable :: nu_diz_elec_temp !
        Dissociative attachment
    real(dbleprc), dimension(:,:), allocatable :: nu_diz_elec
    ! Ion-gas reactions
    real(dbleprc), dimension(:,:), allocatable :: nu_iso_ion_temp !
        Isotropic scattering
    real(dbleprc), dimension(:,:), allocatable :: nu_iso_ion
    real(dbleprc), dimension(:,:), allocatable :: nu_bsc_ion_temp !
        Backscattering
    real(dbleprc), dimension(:,:), allocatable :: nu_bsc_ion

    ! Collision probability level for each reaction
    real(dbleprc), allocatable, dimension(:)   :: nu_e ! electrons
    real(dbleprc), allocatable, dimension(:)   :: nu_i ! ions

    ! Maximum collision probability including null collision
    real(dbleprc)                              :: nu_prime ! electrons
    real(dbleprc)                              :: nu_primi ! ions

end type gas
```

BIBLIOGRAPHY

[1] A. Aanesland, J. Bredin, P. Chabert, and V. Godyak. Electron energy distribution function and plasma parameters across magnetic filters. *Applied Physics Letters*, 100(4):044102, 2012.

[2] J. Adam, A. Gourdin Serveniere, and A. Langdon. Electron sub-cycling in particle simulation of plasma. *Journal of Computational Physics*, 47(2):229–244, 1982.

[3] M. A. Ali and Y.-K. Kim. Ionization cross sections by electron impact on halogen atoms, diatomic halogen and hydrogen halide molecules. *Journal of Physics B: Atomic and Molecular Physics*, 41(14):145202, 2008.

[4] J. E. Allen and J. T. Holgate. On the Bohm criterion in the presence of a magnetic field. *Nuclear Materials and Energy*, 2016.

[5] W. P. Allis, S. J. Buchsbaum, and A. Bers. *Waves in Anisotropic Plasmas*. The MIT Press, 2003.

[6] L. L. Alves. The IST-Lisbon database on LXCat. *Journal of Physics: Conference Series*, 012007(1), 2004.

[7] S. Balay, S. Abhyankar, M. F. Adams, J. Brown, P. Brune, K. Buschelman, L. Dalcin, A. Dener, V. Eijkhout, W. D. Gropp, D. Karpeyev, D. Kaushik, M. G. Knepley, D. A. May, L. C. McInnes, R. T. Mills, T. Munson, K. Rupp, P. Sanan, B. F. Smith, S. Zampini, H. Zhang, and H. Zhang. PETSc Web page. `https://www.mcs.anl.gov/petsc`, 2019.

[8] P. N. Barnes and M. J. Kushner. Reactions in the afterglow of time modulated inductive discharges of Xe and I2 mixtures. *Journal of Applied Physics*, 84(9):4727–4730, 1998.

[9] P. Bellan. *Fundamentals Of Plasma Physics*. Cambridge University Press, 2006.

[10] S. F. Biagi. Programm magboltz v7.1. cross section compilation. see www.lxcat.net. retrieved on November 16, 2016, 2004.

[11] S. F. Biagi. Programm magboltz v8.97. cross section compilation. see www.lxcat.net. retrieved on February 11, 2019, 2010.

[12] S. F. Biagi. Programm Magboltz v8.9. Cross section compilation. see www.lxcat.net. retrieved on February 12, 2019, 2015.

[13] M. A. Biondi. Dissociative Attachment of Electrons in Iodine. I. Microwave Determination of the Absolute Cross Section at 300°K. *Physical Review*, 109(6):2005–2007, 1958.

[14] M. A. Biondi and R. E. Fox. Dissociative Attachment of Electrons in Iodine. III. Discussion. *Physical Review*, 109(6):2012–2014, 1958.

[15] C. K. Birdsall, G. R. Brewer, and A. V. Haeff. The resistive-wall amplifier. *Proceedings of the IRE*, 41(7):865–875, 1953.

[16] C. K. Birdsall and A. B. Langdon. *Plasma Physics via Computer Simulation*. CRC Press, 2004.

[17] J. P. Boeuf, J. Claustre, B. Chaudhury, and G. Fubiani. Physics of a magnetic filter for negative ion sources. II. E × B drift through the filter in a real geometry. *Physics of Plasmas*, 19(11):113510, 2012.

[18] J.-P. Booth, C. S. Corr, G. A. Curley, J. Jolly, J. Guillon, and T. Földes. Fluorine negative ion density measurement in a dual frequency capacitive plasma etch reactor by cavity ring-down spectroscopy. *Applied Physics Letter*, 88(15):151502, 2006.

[19] J. P. Boris and R. A. Shanny. Relativistic Plasma Simulation - Optimization of a Hybrid Code. In *Proceedings of the Conference on the Numerical Simulation of Plasmas*, number 4th in AD-A023 511, Washington D.C., USA, 1970. NRL.

[20] J. Bredin. *Développement de diagnostics électrostatiques pour le filtrage magnétique et la formation du plasma ion-ion dans le propulseur PEGASES*. PhD thesis, École polytechnique, 2013.

[21] J. Bredin, P. Chabert, and A. Aanesland. Langmuir probe analysis of highly electronegative plasmas. *Applied Physics Letters*, 102(15):154107, 2013.

[22] J. Bredin, P. Chabert, and A. Aanesland. Langmuir probe analysis in electronegative plasmas. *Physics of Plasmas*, 21(12):123502, 2014.

[23] D. J. Campbell. Preface to Special Topic: ITER. *Physics of Plasmas*, 22(2):021701, 2015.

[24] J. Carlsson, I. Kaganovich, A. Powis, Y. Raitses, I. Romadanov, and A. Smolyakov. Particle-in-cell simulations of anomalous transport in a Penning discharge. *Physics of Plasmas*, 25(6):061201, 2018.

[25] J. Carlsson, A. Khrabrov, I. Kaganovich, T. Sommerer, and D. Keating. Validation and benchmarking of two particle-in-cell codes for a glow discharge. *Plasma Sources Science and Technology*, 26(1):014003, 2017.

[26] K. M. Case, F. de Hoffmann, and G. Placzek. *Introduction to the theory of neutron diffusion*. Los Alamos, N. M.,, 1953. Section 10.1.

[27] P. Chabert. *Étude d'un plasma de SF_6 créé dans un reacteur hélicon : application à la gravure du carbure de silicium*. PhD thesis, Paris 11, 1999.

[28] P. Chabert. Propulseur à Plasma électronégatif, 2005. French patent number 0512417.

[29] P. Chabert. An expression for the h_l factor in low-pressure electronegative plasma discharges. *Plasma Sources Science and Technology*, 25(2):025010, 2016.

[30] P. Chabert, J. Arancibia Monreal, J. Bredin, L. Popelier, and A. Aanesland. Global model of a gridded-ion thruster powered by a radiofrequency inductive coil. *Physics of Plasmas*, 19(7):073512, 2012.

[31] P. Chabert and N. Braithwaite. *Physics of Radio-Frequency Plasmas*. Cambridge University Press, 2011.

[32] P. Chabert, A. J. Lichtenberg, M. A. Lieberman, and A. M. Marakhtanov. Instabilities in low-pressure electronegative inductive discharges. *Plasma Sources Science and Technology*, 10(3):478, 2001.

[33] P. Chabert, A. J. Lichtenberg, M. A. Lieberman, and A. M. Marakhtanov. Dynamics of steady and unsteady operation of inductive discharges with attaching gases. *Journal of Applied Physics*, 94(2):831–843, 2003.

[34] P. J. Chantry. A simple formula for diffusion calculations involving wall reflection and low density. *Journal of Applied Physics*, 62(4):1141–1148, 1987.

[35] F. F. Chen. Excitation of drift instabilities in thermionic plasmas. *Journal of Nuclear Energy, Part C Plasma Physics*, 7(4):399, 1965.

[36] F. F. Chen. "Universal" Overstability of a Resistive, Inhomogeneous Plasma. *The Physics of Fluids*, 8(7), 1965.

[37] F. F. Chen. *Introduction to plasma physics and controlled fusion*. Plenum Press, New York, 2nd edition, 1984.

[38] R. Chodura. Plasma–wall transition in an oblique magnetic field. *Physics of Fluids*, 25(9):1628, 1982.

[39] E. Y. Choueiri. A Critical History of Electric Propulsion: The First Fifty Years (1906-1956). Technical Report 2004-3334, AIAA, 2004.

[40] C. S. Corr, E. Despiau-Pujo, P. Chabert, W. G. Graham, F. G. Marro, and D. B. Graves. Comparison between fluid simulations and experiments in inductively coupled argon/chlorine plasmas. *Journal of Physics D: Applied Physics*, 41(18):185202, 2008.

[41] V. Croes. *Plasma discharge 2D modeling of a Hall thruster*. PhD thesis, Université Paris-Saclay, 2017.

[42] V. Croes, T. Lafleur, Z. Bonaventura, A. Bourdon, and P. Chabert. 2D particle-in-cell simulations of the electron drift instability and associated anomalous electron transport in Hall-effect thrusters. *Plasma Sources Science and Technology*, 26(3):034001, 2017.

[43] V. Croes, A. Tavant, R. Lucken, T. Lafleur, A. Bourdon, and P. Chabert. Study of electron transport in a Hall effect thruster with 2D $r - \theta$ Particle-In-Cell simulations. In *IEPC*, volume 2017-57, Atlanta, USA, 2017.

[44] V. Croes, A. Tavant, R. Lucken, R. Martorelli, T. Lafleur, A. Bourdon, and P. Chabert. The effect of alternative propellants on the electron drift instability in Hall-effect thrusters: Insight from 2D particle-in-cell simulations. *Physics of Plasmas*, 25(6):063522, 2018.

[45] D. Curreli and F. F. Chen. Cross-field diffusion in low-temperature plasma discharges of finite length. *Plasma Sources Sci. Technol.*, 23(6):064001, 2014.

[46] D. Bohm. *The Characteristics of Electrical Discharges in Magnetic Fields*. R. K. Wakerling, A. Guthrie, Mcgraw-hill Book Company, Inc., first edition edition, 1949.

[47] E. Despiau-Pujo and P. Chabert. Global model of instabilities in low-pressure inductive chlorine discharges. *Plasma Sources Science and Technology*, 18(4):045028, 2009.

[48] R. Dressler, Y.-H. Chiu, and D. Levandier. Propellant alternatives for ion and Hall effect thrusters. *AIAA Paper*, 602:2000, 2000.

[49] J. P. J. Dubois, K. Achkasov, D. Kogut, A. Ahmad, J. M. Layet, A. Simonin, and G. Cartry. Negative-ion surface production in hydrogen plasmas: Determination of the negative-ion energy and angle distribution function using mass spectrometry. *Journal of Applied Physics*, 119(19):193301, 2016.

[50] L. Dubois, F. Gaboriau, L. Liard, D. Harribey, C. Henaux, and J. P. Boeuf. Ion acceleration through a magnetic barrier Toward an optimized double-stage Hall thruster concept. In *IEPC*, volume 2017-215, Atlanta, USA, 2017.

[51] V. Désangles. *Forçage à grande échelle d'une colonne de plasma faiblement magnétisée : influence d'une cathode émissive de grande taille*. PhD thesis, École Normale Supérieure de Lyon, 2018.

[52] K. G. Emeleus and G. A. Woolsey. *Discharges in Electronegative Gases*. Taylor and Francis Ltd, London, United Kingdom, 1970.

[53] A. V. Evseev, A. A. Radtsig, and B. M. Smirnov. Resonance charge exchange of diatomic molecular ions on molecules. *Soviet Physics. Journal of Experimental and Theoretical Physics*, 50(2):283, 1979.

[54] R. D. Falgout and U. M. Yang. Hypre: A Library of High Performance Preconditioners. In P. M. A. Sloot, A. G. Hoekstra, C. J. K. Tan, and J. J. Dongarra, editors, *Computational Science — ICCS 2002*, pages 632–641, Berlin, Heidelberg, Germany, 2002. Springer.

[55] U. Fantz, P. Franzen, W. Kraus, M. Berger, S. Christ-Koch, H. Falter, M. Fröschle, R. Gutser, B. Heinemann, C. Martens, P. McNeely, R. Riedl, E. Speth, A. Stäbler, and D. Wünderlich. Physical performance analysis and progress of the development of the negative ion RF source for the ITER NBI system. *Nuclear Fusion*, 49(12):125007, 2009.

[56] R. E. Fox. Dissociative Attachment of Electrons in Iodine. II. Mass Spectrographic Determination of the Energy Dependence of the Cross Section. *Physical Review*, 109(6):2008–2011, 1958.

[57] R. N. Franklin and J. Snell. The positive column with negative ions in a magnetic field at low pressure. *Journal of Physics D: Applied Physics*, 32(9):1031–1038, 1999.

[58] W. Frias, A. I. Smolyakov, I. D. Kaganovich, and Y. Raitses. Long wavelength gradient drift instability in Hall plasma devices. I. Fluid theory. *Physics of Plasmas*, 19(7):072112, 2012.

[59] A. Fruchtman, G. Makrinich, and J. Ashkenazy. Two-dimensional equilibrium of a low temperature magnetized plasma. *Plasma Sources Science and Technology*, 14(1):152, 2005.

[60] G. Fubiani. Modeling of the negative ion source and accelerator of the ITER Neutral Beam Injector, 2016. French *Habilitation à diriger des recherches*.

[61] G. Fubiani and J. P. Boeuf. Role of positive ions on the surface production of negative ions in a fusion plasma reactor type negative ion source—Insights from a three dimensional particle-in-cell Monte Carlo collisions model. *Physics of Plasmas*, 20(11):113511, 2013.

[62] R. Futtersack. *Modélisation fluide du transport magnétisé dans les plasmas froids*. PhD thesis, Université de Toulouse, Université Toulouse III-Paul Sabatier, 2014.

[63] P. Gavigan. Estimation of Minimum Required Thrust for Spacecraft Collision Avoidance, 2013. Master thesis. Defence R&D Canada.

[64] A. R. Gibson, M. Foucher, D. Marinov, P. Chabert, T. Gans, M. J. Kushner, and J.-P. Booth. The role of thermal energy accommodation and atomic recombination probabilities in low pressure oxygen plasmas. *Plasma Physics and Controlled Fusion*, 59(2):024004, 2017.

[65] R. H. Goddard. Method and Means for Producing Electrified Jets of gases, 1920. US patent number 1,363,037.

[66] V. A. Godyak. *Soviet Radio Frequency Discharge Research*. Delphic Associates, Inc., 1986.

[67] D. M. Goebel, G. Becatti, J. E. Polk, and P. Guerrero. Life Model for Lanthanum Hexaboride Hollow Cathodes for High-Power Hall Thrusters. In *IEPC-2017-276*, Atlanta, Georgia, U.S., 2017.

[68] D. M. Goebel and I. Katz. *Fundamentals of electric propulsion: ion and Hall thrusters*. John Wiley & Sons, 2008.

[69] C. Greaves. Ion-Ion Recombination in Iodine Afterglows†. *Journal of Electronics and Control*, 17(2):171–180, 1964.

[70] P. Grondein. *Investigation de l'iode comme propergol pour la propulsion ionique à grilles*. PhD thesis, École polytechnique, 2016.

[71] P. Grondein, T. Lafleur, P. Chabert, and A. Aanesland. Global model of an iodine gridded plasma thruster. *Physics of Plasmas*, 23(3):033514, 2016.

[72] G. J. M. Hagelaar, G. Fubiani, and J.-P. Boeuf. Model of an inductively coupled negative ion source: I. General model description. *Plasma Sources Sci. Technol.*, 20(1):015001, 2011.

[73] G. J. M. Hagelaar and N. Oudini. Plasma transport across magnetic field lines in low-temperature plasma sources. *Plasma Physics and Controlled Fusion*, 53(12):124032, 2011.

[74] G. J. M. Hagelaar and L. C. Pitchford. Solving the Boltzmann equation to obtain electron transport coefficients and rate coefficients for fluid models. *Plasma Sources Sci. Technol.*, 14(4):722–733, 2005.

[75] J. R. Hamilton. Iodine: I_2 molecule and I atom. Technical report, Quantemol Ltd, 2015.

[76] J. R. Hamilton. Consultancy project for LPP. I_2 and I^- data. Technical report, Quantemol Ltd, 2017.

[77] B. Heinemann, H. D. Falter, U. Fantz, P. Franzen, M. Froeschle, W. Kraus, C. Martens, R. Nocentini, R. Riedl, E. Speth, and A. Staebler. The negative ion source test facility ELISE. *Fusion Engineering and Design*, 86(6):768–771, 2011.

[78] H. W. Hendel, B. Coppi, F. Perkins, and P. A. Politzer. Collisional Effects in Plasmas-Drift-Wave Experiments and Interpretation. *Physical Review Letters*, 18(12):439–442, 1967.

[79] J. R. Henry. *Étude d'un plasma de gaz électronégatif. Spectrométrie de masse et propagation des ondes ioniques longitudinales*. PhD thesis, Université ParisVII, 1972.

[80] R. W. Hockney, J. W. Eastwood, and J. W. Eastwood. *Computer Simulation Using Particles*. CRC Press, 1988.

[81] C.-C. Hsu, M. A. Nierode, J. W. Coburn, and D. B. Graves. Comparison of model and experiment for Ar, Ar/O_2 and Ar/O_2 /Cl_2 inductively coupled plasmas. *Journal of Physics D: Applied Physics*, 39(15):3272–3284, 2006.

[82] S. Huang and J. T. Gudmundsson. A particle-in-cell/Monte Carlo simulation of a capacitively coupled chlorine discharge. *Plasma Sources Science and Technology*, 22(5):055020, 2013.

[83] S. Janhunen, A. Smolyakov, O. Chapurin, D. Sydorenko, I. Kaganovich, and Y. Raitses. Nonlinear structures and anomalous transport in partially magnetized $E \times B$ plasmas. *Physics of Plasmas*, 25(1):011608, 2018.

[84] E. Kawamura, A. J. Lichtenberg, and M. A. Lieberman. Two-dimensional particle-in-cell simulations of transport in a magnetized electronegative plasma. *Journal of Applied Physics*, 108(10):103305, 2010.

[85] G.-H. Kim, H.-C. Lee, and C.-W. Chung. Experimental investigation of edge-to-center density ratio in inductively coupled plasmas. *Physics of Plasmas*, 17(7):073504, 2010.

[86] S. Kolev, G. J. M. Hagelaar, G. Fubiani, and J.-P. Boeuf. Physics of a magnetic barrier in low-temperature bounded plasmas: insight from particle-in-cell simulations. *Plasma Sources Science and Technology*, 21(2):025002, 2012.

[87] S. Kolev, S. Lishev, A. Shivarova, K. Tarnev, and R. Wilhelm. Magnetic filter operation in hydrogen plasmas. *Plasma Physics and Controlled Fusion*, 49(9):1349–1369, 2007.

[88] G. P. Kota, J. W. Coburn, and D. B. Graves. The recombination of chlorine atoms at surfaces. *Journal of Vacuum Science & Technology A*, 16(1):270–277, 1998.

[89] T. Lafleur and A. Aanesland. Ambipolar and non-ambipolar diffusion in an rf plasma source containing a magnetic filter. *Physics of Plasmas*, 21(6):063510, 2014.

[90] T. Lafleur and A. Aanesland. Generalization of the Child-Langmuir law to the alternate extraction of positive and negative ions. *Physics of Plasmas*, 21(12):123506, 2014.

[91] T. Lafleur, S. D. Baalrud, and P. Chabert. Theory for the anomalous electron transport in Hall effect thrusters. I. Insights from particle-in-cell simulations. *Physics of Plasmas*, 23(5):053502, 2016.

[92] T. Lafleur, S. D. Baalrud, and P. Chabert. Theory for the anomalous electron transport in Hall effect thrusters. II. Kinetic model. *Physics of Plasmas*, 23(5):053503, 2016.

[93] T. Lafleur and R. W. Boswell. Particle-in-cell simulations of ambipolar and nonambipolar diffusion in magnetized plasmas. *Physics of Plasmas*, 19(5):053505, 2012.

[94] T. Lafleur and P. Chabert. Edge-to-center density ratios in low-temperature plasmas. *Plasma Sources Science and Technology*, 24(2):025017, 2015.

[95] T. Lafleur, D. Rafalskyi, and A. Aanesland. Alternate extraction and acceleration of positive and negative ions from a gridded plasma source. *Plasma Sources Science and Technology*, 24(1):015005, 2014.

[96] V. P. Lakhin, V. I. Ilgisonis, A. I. Smolyakov, E. A. Sorokina, and N. A. Marusov. Marginal stability, characteristic frequencies, and growth rates of gradient drift modes in partially magnetized plasmas with finite electron temperature. *Physics of Plasmas*, 25(1):012107, 2018.

[97] G. Leray. *PEGASES: Plasma Propulsion with Electronegative Gases*. PhD thesis, École Polytechnique, 2009.

[98] R. J. Leveque. *Finite Volume Methods for Hyperbolic Problems*. Cambridge University Press, 2002.

[99] L. Liard, J.-L. Raimbault, J.-M. Rax, and P. Chabert. Plasma transport under neutral gas depletion conditions. *Journal of Physics D: Applied Physics*, 40(17):5192–5195, 2007.

[100] M. A. Lieberman and A. J. Lichtenberg. *Principles of plasma discharges and materials processing*. Wiley-Interscience, 2nd edition, 2005.

[101] M. A. Lieberman, A. J. Lichtenberg, and A. M. Marakhtanov. Instabilities in low-pressure inductive discharges with attaching gases. *Applied Physics Letters*, 75(23):3617, 1999.

[102] R. Lucken. Simulation and Modelling of the Interaction between Spacecraft and Plasma Propulsion System, 2016. Master thesis of Université Paris-Saclay. Airbus Defence and Space (confidential).

[103] R. Lucken, A. Bourdon, M. A. Lieberman, and P. Chabert. Instability-enhanced transport in low temperature magnetized plasma. *Physics of Plasmas*, 26(7):070702, 2019.

[104] R. Lucken, V. Croes, T. Lafleur, J.-L. Raimbault, A. Bourdon, and P. Chabert. Global models of plasma thrusters: Insights from PIC simulation and fluid theory. In *IEPC*, volume 2017-323, 2017.

[105] R. Lucken, V. Croes, T. Lafleur, J.-L. Raimbault, A. Bourdon, and P. Chabert. Edge-to-center plasma density ratios in two-dimensional plasma discharges. *Plasma Sources Science and Technology*, 27(3):035004, 2018.

[106] R. Lucken and D. Giolito. Collision risk prediction for constellation design. *Acta Astronautica*, 161:492–501, 2019.

[107] R. Lucken, N. Hubert, and D. Giolito. Systematic space debris collection using Cubesat constellation. In *EUCASS*, volume 2017-678, Milan, Italy, 2017.

[108] R. Lucken, A. Tavant, A. Bourdon, M. A. Lieberman, and P. Chabert. Saturation of the magnetic confinement in weakly ionized plasma. *Accepted in Plasma Sources Science and Technology*, 2019.

[109] G. Maroulis, C. Makris, U. Hohm, and D. Goebel. Electrooptical Properties and Molecular Polarization of Iodine, I_2. *The Journal of Physical Chemistry A*, 101(5):953–956, 1997.

[110] R. Martorelli, T. Lafleur, A. Bourdon, and C. P. Comparison between ad-hoc and instability-induced electron anomalous transport in a 1D fluid simulation of Hall-effect thruster. *Accepted in Physics of Plasmas*, 2019.

[111] A. Meige, R. W. Boswell, C. Charles, and M. M. Turner. One-dimensional particle-in-cell simulation of a current-free double layer in an expanding plasma. *Physics of Plasmas*, 12(5):052317, 2005.

[112] S. Mochalskyy. *Modeling of the negative ion extraction from a hydrogen plasma source. Application to ITER Neutral Beam Injector*. PhD thesis, Université Paris-Sud, 2011.

[113] A. V. Phelps. The application of scattering cross sections to ion flux models in discharge sheaths. *Journal of Applied Physics*, 76(2):747–753, 1994.

[114] D. Piscitelli, A. V. Phelps, J. de Urquijo, E. Basurto, and L. C. Pitchford. Ion mobilities in Xe/Ne and other rare-gas mixtures. *Physical Review E*, 68(4), 2003.

[115] N. Plihon. *Stabilité et structure électrique d'une décharge inductive en gaz électronégatif*. PhD thesis, École polytechnique, 2004.

[116] N. Plihon and P. Chabert. Ion acoustic waves and double-layers in electronegative expanding plasmas. *Physics of Plasmas*, 18(8):082102, 2011.

[117] N. Plihon, P. Chabert, and C. S. Corr. Experimental investigation of double layers in expanding plasmas. *Physics of Plasmas*, 14(1):013506, 2007.

[118] N. Plihon, C. S. Corr, P. Chabert, and J.-L. Raimbault. Periodic formation and propagation of double layers in the expanding chamber of an inductive discharge operating in Ar/SF_6 mixtures. *Journal of Applied Physics*, 98(2):023306, 2005.

[119] L. Popelier. *Développement du propulseur PEGASES: source inductive à haute performance et accélération successive de faisceaux d'ions positifs et d'ions négatifs.* PhD thesis, École polytechnique, 2012.

[120] A. A. Radzig and B. M. Smirnov. *Reference Data on Atoms, Molecules, and Ions*. Number 31 in Chemical Physics. Springer, 1985.

[121] D. Rafalskyi and A. Aanesland. A Neutralizer-Free Gridded Ion Thruster Embedded Into a 1U Cubesat Module. In *IEPC*, volume 2017-94, Atlanta, Georgia, USA, 2017.

[122] D. Rafalskyi, L. Popelier, and A. Aanesland. Experimental validation of the dual positive and negative ion beam acceleration in the plasma propulsion with electronegative gases thruster. *Journal of Applied Physics*, 115(5):053301, 2014.

[123] J.-L. Raimbault and P. Chabert. Edge-to-center plasma density ratio in high density plasma sources. *Plasma Sources Science and Technology*, 18(1):014017, 2009.

[124] D. Rapp and W. E. Francis. Charge Exchange between Gaseous Ions and Atoms. *The Journal of Chemical Physics*, 37(11):2631, 1962.

[125] J.-M. Rax. *Physique des Plasmas*. Dunod, 2005.

[126] D. Renaud. *Caractérisation du propulseur PEGASES: diagnostics du filtre magnétique et du faisceau: optimisation de la géométrie*. PhD thesis, Université d'Orléans, 2016.

[127] D. Renaud and S. Mazouffre. Investigation of the PEGASES thruster magnetic filter via laser photodetachment experiments. In *IEPC*, volume 380, Kobe, Japan, 2015.

[128] K. U. Riemann. The Bohm criterion and sheath formation. *Journal of Physics D: Applied Physics*, 24(4):493–518, 1991.

[129] E. Rutherford. The Structure of the Atom. *The London, Edinburgh, and Dublin Philosophical Magazine and Journal of Science*, LVII-27(159):488–498, 1914.

[130] S. Sakabe and Y. Izawa. Simple formula for the cross sections of resonant charge transfer between atoms and their positive ions at low impact velocity. *Physical Review A*, 45(3):2086, 1992.

[131] G. Sary. *Modélisation d'une cathode creuse pour propulseur à plasma*. PhD thesis, Université de Toulouse, Université Toulouse III - Paul Sabatier, 2016.

[132] G. Sary, L. Garrigues, and J. P. Boeuf. Hollow cathode modeling: a first approach on scaling laws. In *IEPC-2015-14*, volume 14, Kobe, Japan, 2015.

[133] G. Schmidt. *Physics of High Temperature Plasmas: An Introduction*. Academic Press, 1966.

[134] W. Schottky. Diffusionstheorie der positiven Säule. *Physikalische Zeitschrift*, 25(635), 1924.

[135] G. Serianni, V. Toigo, M. Bigi, M. Boldrin, G. Chitarin, S. Dal Bello, L. Grando, A. Luchetta, D. Marcuzzi, R. Pasqualotto, N. Pomaro, P. Zaccaria, L. Zanotto, P. Agostinetti, M. Agostini, V. Antoni, D. Aprile, M. Barbisan, M. Battistella, M. Brombin, R. Cavazzana, M. Dalla Palma, M. Dan, A. De Lorenzi, R. Delogu, M. De Muri, S. Denizeau, M. Fadone, F. Fellin, L. Ferbel, A. Ferro, E. Gaio, G. Gambetta, F. Gasparini, F. Gnesotto, P. Jain, A. Maistrello, G. Manduchi, S. Manfrin, G. Marchiori, N. Marconato, M. Moresco, T. Patton, M. Pavei, S. Peruzzo, N. Pilan, A. Pimazzoni, R. Piovan, C. Poggi, M. Recchia, A. Rizzolo, G. Rostagni, E. Sartori, M. Siragusa, P. Sonato, E. Spada, S. Spagnolo, M. Spolaore, C. Taliercio, P. Tinti, M. Ugoletti, M. Valente, A. Zamengo, B. Zaniol, M. Zaupa, C. Baltador, M. Cavenago, D. Boilson, C. Rotti, P. Veltri, T. Bonicelli, F. Paolucci, S. Muriel, A. Masiello, A. Chakraborty, H. Patel, N. Singh, U. Fantz, B. Heinemann, W. Kraus, M. Kashiwagi, and K. Tsumori. SPIDER in the roadmap of the ITER neutral beams. *Fusion Engineering and Design*, 2019. in press.

[136] V. K. Shen, D. W. Siderius, W. P. Krekelberg, and H. W. Hatch. *NIST Standard Reference Simulation Website, NIST Standard Reference Database Number 173*. National Institute of Standards and Technology, Gaithersburg MD, 20899, 2019.

[137] T. E. Sheridan, P. Chabert, and R. W. Boswell. Positive ion flux from a low-pressure electronegative discharge. *Plasma Sources Science and Technology*, 8(3):457, 1999.

[138] M. Shindo, S. Uchino, R. Ichiki, S. Yoshimura, and Y. Kawai. Measurements of the negative ion density in SF_6/Ar plasma using a plane electrostatic probe. *Review of Scientific Instruments*, 72(5):7, 2001.

[139] A. I. Smolyakov, O. Chapurin, W. Frias, O. Koshkarov, I. Romadanov, T. Tang, M. Umansky, Y. Raitses, I. D. Kaganovich, and V. P. Lakhin. Fluid theory and simulations of instabilities, turbulent transport and coherent structures in partially-magnetized plasmas of $E \times B$ discharges. *Plasma Physics and Controlled Fusion*, 59(1):014041, 2017.

[140] E. Speth, H. Falter, P. Franzen, U. Fantz, M. Bandyopadhyay, S. Christ, A. Encheva, M. Fröschle, D. Holtum, B. Heinemann, W. Kraus, A. Lorenz, C. Martens, P. McNeely, S. Obermayer, R. Riedl, R. Süss, A. Tanga, R. Wilhelm, and D. Wünderlich. Overview of the RF source development programme at IPP Garching. *Nuclear Fusion*, 46(6):S220–S238, 2006.

[141] L. St-Onge, J. Margot, and M. Chaker. Characterization of the negative ion fraction in high-density SF6 magnetoplasmas using ion acoustic waves. *Applied Physics Letters*, 72(3):290–292, 1998.

[142] P. C. Stangeby. The Bohm–Chodura plasma sheath criterion. *Physics of Plasmas*, 2(3):702–706, 1995.

[143] T. E. Steinberger, M. T. Dufor, D. S. Thompson, and E. E. Scime. Zeeman splitting measurements of magnetic fields in iodine plasma. *Review of Scientific Instruments*, 89(10):10C113, 2018.

[144] T. E. Steinberger and E. E. Scime. Laser-Induced Fluorescence of Singly Ionized Iodine. *Journal of Propulsion and Power*, 34(5):1235–1239, 2018.

[145] N. Sternberg and V. Godyak. Two-dimensional cylindrical plasma for intermediate gas pressures. *Plasma Sources Sci. Technol.*, 20(1):015018, 2011.

[146] N. Sternberg, V. Godyak, and D. Hoffman. Magnetic field effects on gas discharge plasmas. *Physics of Plasmas*, 13(6):063511, 2006.

[147] J. Szabo, M. Robin, S. Paintal, B. Pote, V. Hruby, and C. Freeman. Iodine Propellant Space Propulsion. In *IEPC*, volume 2013-311, Washington D.C., USA, 2013.

[148] F. Taccogna and P. Minelli. PIC modeling of negative ion sources for fusion. *New Journal of Physics*, 19(1):015012, 2017.

[149] A. Tavant, V. Croes, R. Lucken, T. Lafleur, A. Bourdon, and P. Chabert. The effects of secondary electron emission on plasma sheath characteristics and electron transport in an exb discharge via kinetic simulations. *Plasma Sources Science and Technology*, 27(12):124001, 2018.

[150] A. Tavant, R. Lucken, A. Bourdon, and P. Chabert. Non-isothermal sheath model for low pressure plasmas. *Plasma Sources Science and Technology*, 28(7):075007, 2019.

[151] J. Tennyson, D. B. Brown, J. J. Munro, I. Rozum, H. N. Varambhia, and N. Vinci. Quantemol-N: an expert system for performing electron molecule collision calculations using the R-matrix method. *Journal of Physics: Conference Series*, 86:012001, 2007.

[152] J. Tennyson, S. Rahimi, C. Hill, L. Tse, A. Vibhakar, D. Akello-Egwel, D. B. Brown, A. Dzarasova, J. R. Hamilton, D. Jaksch, S. Mohr, K. Wren-Little, J. Bruckmeier, A. Agarwal, K. Bartschat, A. Bogaerts, J.-P. Booth, M. J. Goeckner, K. Hassouni, Y. Itikawa, B. J. Braams, E. Krishnakumar, A. Laricchiuta, N. J. Mason, S. Pandey, Z. L. Petrovic, Y.-K. Pu, A. Ranjan, S. Rauf, J. Schulze, M. M. Turner, P. Ventzek, J. C. Whitehead, and J.-S. Yoon. QDB: a new database of plasma chemistries and reactions. *Plasma Sources Science and Technology*, 26(5):055014, 2017.

[153] M. B. Thomas, D. Rafalskyi, T. Lafleur, and A. Aanesland. Experimental investigation of electron transport across a magnetic field barrier in electropositive and electronegative plasmas. *Plasma Sources Science and Technology*, 25(4):045018, 2016.

[154] V. Toigo, S. Dal Bello, E. Gaio, A. Luchetta, R. Pasqualotto, P. Zaccaria, M. Bigi, G. Chitarin, D. Marcuzzi, N. Pomaro, G. Serianni, P. Agostinetti, M. Agostini, V. Antoni, D. Aprile, C. Baltador, M. Barbisan, M. Battistella, M. Boldrin, M. Brombin, M. Dalla Palma, A. De Lorenzi, R. Delogu, M. De Muri, F. Fellin, A. Ferro, G. Gambetta, L. Grando, P. Jain, A. Maistrello, G. Manduchi, N. Marconato, M. Pavei, S. Peruzzo, N. Pilan, A. Pimazzoni, R. Piovan, M. Recchia, A. Rizzolo, E. Sartori, M. Siragusa, E. Spada, S. Spagnolo, M. Spolaore, C. Taliercio, M. Valente, P. Veltri, A. Zamengo, B. Zaniol, L. Zanotto, M. Zaupa, D. Boilson, J. Graceffa, L. Svensson, B. Schunke, H. Decamps, M. Urbani, M. Kushwah, J. Chareyre, M. Singh, T. Bonicelli, G. Agarici, A. Garbuglia, A. Masiello, F. Paolucci, M. Simon, L. Bailly-Maitre, E. Bragulat, G. Gomez, D. Gutierrez, G. Mico, J.-F. Moreno, V. Pilard, A. Chakraborty, U. Baruah, C. Rotti, H. Patel, M. Nagaraju, N. Singh, A. Patel, H. Dhola, B. Raval, U. Fantz, M. Fröschle, B. Heinemann, W. Kraus, R. Nocentini, R. Riedl, L. Schiesko, C. Wimmer, D. Wünderlich, M. Cavenago, G. Croci, G. Gorini, M. Rebai, A. Muraro, M. Tardocchi, and R. Hemsworth. The ITER Neutral Beam Test Facility towards SPIDER operation. *Nuclear Fusion*, 57(8):086027, 2017.

[155] L. Tonks and I. Langmuir. A General Theory of the Plasma of an Arc. *Phys. Rev.*, 34(876), 1929.

[156] M. M. Turner. Collisionless electron heating in an inductively coupled discharge. *Physical Review Letters*, 71(12):1844, 1993.

[157] M. M. Turner, A. Derzsi, Z. Donkó, D. Eremin, S. J. Kelly, T. Lafleur, and T. Mussenbrock. Simulation benchmarks for low-pressure plasmas: Capacitive discharges. *Physics of Plasmas*, 20(1):013507, 2013.

[158] M. Tuszewski and S. P. Gary. Downstream instabilities of electronegative plasma discharges. *Physics of Plasmas*, 10(2):539–545, 2003.

[159] M. Tuszewski and R. R. White. Instabilities of Ar/SF6 inductive plasma discharges. *Journal of Applied Physics*, 94(5):2858–2863, 2003.

[160] O. Tverdokhlebov and A. Semenkin. Iodine propellant for electric propulsion - To be or not to be. In *37th Joint Propulsion Conference and Exhibit*, Salt Lake City, USA, 2001. AIAA.

[161] V. Vahedi and M. Surendra. A Monte Carlo collision model for the particle-in-cell method: applications to argon and oxygen discharges. *Computer Physics Communications*, 87(1-2):179–198, 1995.

[162] J. Weiland. *Stability and Transport in Magnetic Confinement Systems*. Springer Series on Atomic, Optical, and Plasma Physics. Springer-Verlag, 2012.

[163] J. Yankun, Z. Xiu, L. Huiping, and Q. Minghui. Bohm Criterion in a Magnetized Plasma Sheath. *Plasma Science and Technology*, 13(5):519, 2011.

[164] T. H. Y. Yeung. Recombination coefficients for positive and negative ions. *Proceedings of the Physical Society*, 71(3):341, 1958.

[165] S. Yoshikawa and D. J. Rose. Anomalous Diffusion of a Plasma across a Magnetic Field. *The Physics of Fluids*, 5(3):334–340, 1962.

[166] O. Zatsarinny, K. Bartschat, G. Garcia, F. Blanco, L. Hargreaves, D. Jones, R. Murrie, J. Brunton, M. Brunger, M. Hoshino, and S. Buckman. Electron-collision cross sections for iodine. *Physical Review A*, 83(4):042702, 2011.

université PARIS-SACLAY | ÉCOLE DOCTORALE Ondes et Matière (EDOM)

Titre: THÉORIE ET SIMULATION DE PHÉNOMÈNES DE TRANSPORT DU PLASMA À BASSE PRESSION
Application au propulseur PEGASES
Mots clés: plasma basse pression, transport du plasma, instabilités, simulation PIC, propulsion électrique de satellite, iode

Résumé: Le domaine de la physique des plasmas froids a émergé avec les premières découvertes fondamentales en physique atomique et en physique des plasmas il y a plus d'un siècle. Toutefois, ce domaine a été rapidement orienté vers les applications. L'une des applications les plus importantes dans la première moitié du XX^{eme} siècle est le "Calutron" (California University Cyclotron), inventé par E. Lawrence à Berkeley, qui faisait partie du projet Manhattan, et utilisé comme un spectromètre de masse pour séparer les isotopes de l'uranium. Dans un rapport du projet Manhattan daté de 1949, D. Bohm fait deux observations qui sont fondamentales pour la physique des plasmas froids : (i) Les ions doivent avoir une énergie cinétique minimale lorsqu'ils entrent dans la gaine du plasma, estimée à $T_e/2$, T_e étant la température électronique en électron-volts. (ii) Le transport du plasma à travers un champ magnétique est augmenté par des instabilités.
La propulsion électrique par plasma est utilisée pour des satellites militaires et des sondes spatiales depuis les années 1960 et a suscité un intérêt grandissant ces vingt dernières années avec le développement des applications commerciales des technologies spatiales. Néanmoins, les mêmes questions que celles auxquelles D. Bohm était confronté, c'est-à-dire le transport multidimensionnel, l'interaction plasma-gaine, et les instabilités, se posent toujours. La théorie et les simulations sont d'autant plus importantes pour la conception des systèmes de propulsion électrique que les tests en conditions réelles nécessitent le lancement d'un satellite dans l'espace.
Dans ce travail, nous établissons les équations du transport multidimensionnel dans un plasma isotherme, nous proposons un critère de gaine qui permet de rendre compte de la saturation du champ magnétique dans un plasma froid et faiblement ionisé, et nous modélisons le refroidissement des électrons à travers le filtre magnétique du propulseur PEGASES (Plasma Propulsion with Electronegative Gases). Toutes les théories sont motivées et validées par un grand nombre de simulations particulaires PIC bi-dimensionnelles, en utilisant le code LPPic qui a été partiellement développé dans le cadre du projet. Enfin, les cas de simulation sont étendus à une décharge inductive à plasma dans l'iode, avec un nouvel ensemble de sections efficaces de réaction.

Title: THEORY AND SIMULATION OF LOW-PRESSURE PLASMA TRANSPORT PHENOMENA
Application to the PEGASES Thruster
Keywords: low-pressure plasma, plasma transport, instabilities, PIC simulation, satellite electric propulsion, iodine

Abstract: The field of low-temperature plasma physics has emerged from the first fundamental discoveries in atom and plasma physics more than a century ago. However, it has soon become driven by applications. In the first half of the XXth century, one of the most important application is the "Calutron" (California University Cyclotron) invented by E. Lawrence in Berkeley. It was part of the Manhattan project, and operated as a mass spectrometer to separate uranium isotopes. In a 1949 report of the Manhattan project, D. Bohm makes two observations that are fundamental for low-temperature plasma physics: (i) The ions must have minimum kinetic energy when they enter the plasma sheath estimated to $T_e/2$, T_e being the electron temperature in eV ; (ii) plasma transport across a magnetic field is enhanced by instabilities.
Plasma electric propulsion is used on military satellites and space probes since the 1960s and has gained more and more interest in the last twenty years as space commercial applications were developing. However, the same questions as the ones D. Bohm was faced with, namely multi-dimensional transport, plasma sheath interaction, and instabilities, arise. Theory and simulation are even more important for electric space propulsion systems design since testing in real conditions involves to launch a satellite into space.
In this work, (i) we derive the equations of the multi-dimensional isothermal plasma transport, (ii) we establish a sheath criterion that causes the magnetic confinement to saturate in low-temperature, weakly ionized plasmas, and (iii) we model the electron cooling through the magnetic filter of the PEGASES (Plasma Propulsion with Electronegative Gases) thruster. All the theories are driven and validated with extensive two-dimensional particle-in-cell (PIC) simulations, using the LPPic code that was partially developed in the frame of this project. Finally, (iv) the simulation cases are extended to an iodine inductively coupled plasma (ICP) discharge with a new set of reaction cross sections.

Université Paris-Saclay
Espace Technologique / Immeuble Discovery
Route de l'Orme aux Merisiers RD 128 / 91190 Saint-Aubin, France